TECHNISCHE UNIVERSITÄT MÜNCHEN

Lehrstuhl für Aerodynamik und Strömungsmechanik

Modeling and Simulation of Multiphase Phenomena with Smoothed Particle Hydrodynamics

Stefan Adami

Vollständiger Abdruck der von der Fakultät für Maschinenwesen der Technischen Universität München zur Erlangung des akademischen Grades eines

Doktor-Ingenieurs

genehmigten Dissertation.

Vorsitzender:		Univ.-Prof. Dr.-Ing. Thomas Sattelmayer
Prüfer der Dissertation:	1.	Univ.-Prof. Dr.-Ing. Nikolaus A. Adams
	2.	Prof. Joe J. Monaghan, Ph. D. Monash University, Australia

Die Dissertation wurde am 14.01.2014 bei der Technischen Universität München eingereicht und durch die Fakultät für Maschinenwesen am 26.03.2014 angenommen.

Stefan Adami
Elisabethstraße 83
80797 München
Germany

stefan.adami@tum.de

© Stefan Adami, 2014

All rights reserved. No part of this publication may be reproduced, modified, re-written, or distributed in any form or by any means, without the prior written permission of the author.

Released January 12, 2014
Typesetting LaTeX

ABSTRACT

Smoothed Particle Hydrodynamics (SPH) is a Lagrangian method where the field quantities are interpolated at individual discretization points (particles) that are advected with the local flow field. Independently proposed in 1977 by Lucy [76] and Gingold and Monaghan [49], SPH was first used for astrophysical problems where the gridless nature of the method has several advantages. First, different resolution lengths i.e. kernel-interpolation widths can be assigned to different particles allowing to simulate large variations in length-scales. Second, as particles are advected with the flow, the discretization does not need to cover the entire domain but only regions where gas or fluid is present. Finally, SPH is Galilean invariant which is a desirable property in astrophysics.

Since 1977, SPH was also successfully applied to fluid-mechanical as well as solid-mechanical problems. The very broad range of applications (free-surface flows, multiphase flows, non-Newtonian fluids, fluid-structure-interaction, elastic solids, brittle fracture) shows the generality and capabilities of SPH, yet its industrial relevance as tool for CFD (Computational Fluid Dynamics) simulations is still to be opened up. Possible reasons of the lack of commercial use are the higher computational cost compared to grid-based solvers and the need for case-dependent numerical parameter tuning. Also, still a strict mathematical proof for convergence and stability is missing as classical numerical analysis fails for randomly distributed and moving particles. Nevertheless, many examples of SPH applications for complex flows including sophisticated physical models have shown to give reasonable results especially for complex multiphase problems that are very challenging for grid-based methods.

This work presents several important improvements of the state-of-the-art of SPH with emphasis on generality and stability. The published developments on a general wall boundary condition for SPH, a modified advection scheme, a new surface-tension model and a conservative surfactant model are designed to be generally applicable to arbitrary domains and dimensions, and special attention is paid to computational simplicity.

A simple boundary condition for solid walls is proposed where the solid phase is discretized with Cartesian particles. Compared to existing body-fitted approaches the representation of curved interfaces is inferior. However, with increasing resolution the ”numerical roughness“ of non-straight walls vanishes and arbitrarily complex bodies can be easily discretized. A simple interpolation scheme for wall particles allows to model no-slip walls and to impose a von-Neumann condition for the pressure.

Currently available SPH methods rely on stabilization techniques such as artificial viscosity, density reinitialization or Shepard filtering to smooth the particle movement and

allow for stable simulations. Mostly, a combination of several corrections is applied and their numerical parameters are tuned to achieve correct results. Thus, the quality of SPH simulations is strongly dependent on the experience of the user. In this work, a new advection scheme for particles is presented that allows to simulate single- and multi-phase flows without additional numerical parameters. Therefore, to the best of our knowledge for the first time a black-box SPH method thus has become available that can be used to simulate flows at unprecedentedly high Reynolds numbers (Re=10000).

The interaction-based force calculation in SPH offers an implicit multi-phase modeling framework as interactions of different phases can be easily identified using integer identifiers for particles and complex interface models can be employed. Surface tension is modelled in SPH with roughly three different models. Most simple, inter-particle attraction forces similar to inter-molecular forces are introduced that result in qualitatively correct behaviour. Secondly, reconstructing the normals at the interface, surface tension can be considered macroscopically as capillary force proportional to the local curvature and the surface-tension coefficient. Finally, by reformulating surface tension as gradient of a surface stress, the calculation of the curvature can be omitted and the resulting method is momentum conservative. In this work, a modified capillary force model is presented with advantages for high density ratios. Partitioning the surface force according to the phase densities allows to use larger time-steps and reduces the computational cost.

Surfactants (surface active agents) are additives or impurities in a fluid that have the tendency to migrate to the interface and change locally the surface tension. The presence of surfactants in multi-phase systems can strongly alter the dynamics and introduce new physical effects such as the Marangoni effect (interfacial motion due to a surface tension gradient). Numerical modeling of surfactant dynamics is challenging as the interface singularity has to be discretized accurately and surfactant conservation is important for long-time simulations. In this work, an exactly conservative, fully coupled surfactant model is presented that accounts for interfacial diffusion, bulk diffusion and transport between the interface and the bulk (adsorption and desorption). When applied to SPH, complex surfactant induced interface deformations can be simulated without difficulty.

This cumulative thesis is structured as follows: in the first chapter a brief overview of numerical flow simulation in general and multi-phase modeling is given. The fundamental issues of SPH are introduced in the second chapter. Chapter 3 presents the main findings of this work with a literature review on each topic followed by a summary of the respective publication. A list of all publications that emerged from this work including journal publications, book contributions and conference talks/papers is presented in chapter 4. Finally, conclusions are given in chapter 5 and the main publications are attached in the appendix.

KURZFASSUNG

Smoothed Particle Hydrodynamics (SPH, ”geglättete Teilchen-Hydrodynamik“) ist eine Lagrangesche Diskretisierungsmethode bei der die Feldgrößen an den Knotenpunkten (Partikeln) interpoliert werden und diese mit dem lokalen Geschwindigkeitsfeld mitbewegt werden. SPH wurde 1977 von Lucy [76] und Gingold und Monaghan [49] unabhängig voneinander vorgeschlagen und wurde zunächst auf astrophysikalische Probleme angewendet, da besonders hier die gitterlose Beschreibungsweise vorteilhaft ist. Erstens können die Interpolationsradien, d.h. die Weite der Interpolationsfunktion (”Kernel“) individuell für einzelne Partikel variieren und somit große Längenskalen-Unterschiede abgebildet werden. Darüber hinaus liefert SPH aufgrund der Partikeladvektion mit der lokalen Strömung implizit eine adaptive Diskretisierung, das heißt Partikel müssen zu Beginn einer Simulation nur das mit Fluid ausgefüllte Volumen abdecken und nicht das gesamte Simulationsgebiet. Außerdem erfüllt SPH die Galilei Invarianz, eine besonders in der Astrophysik erwünschte Eigenschaft.

Seit 1977 wurde SPH darüber hinaus erfolgreich zur Lösung fluidmechanischer und strukturdynamischer Probleme eingesetzt. Die grundsätzlich flexible Einsatzmöglichkeit und die hohe Funktionalität von SPH wird deutlich anhand der breiten Anwendungsgebiete (freie Oberflächen-Strömungen, Mehrphasen-Strömungen, Nicht-Newtonsche Fluide, Fluid-Struktur-Interaktion, Elastische Körper, Rissbildung und Bruchentwicklung), dennoch ist SPH im industriellen Umfeld als Werkzeug für numerische Simulationen (CFD) immer noch unbedeutend. Mögliche Gründe dafür sind einerseits der erhöhte Rechenaufwand im Vergleich zu gitterbasierten Strömungslösern und die Abhängigkeit von fallspezifischer Anpassung der numerischen Stabilisierungsparameter. Darüber hinaus fehlt bis heute eine fundamentale, mathematische Analyse der Konvergenz und Stabilität des Verfahrens, da die klassischen numerischen Analysemethoden auf zufällig verteilte und bewegte Partikelkonfigurationen nicht allgemeingültig anwendbar sind. Trotzdem zeigen viele Beispiele komplexer Strömungen mit neuesten physikalischen Modellen sinnvolle bzw. mit Experimenten vergleichbare Ergebnisse, besonders für schwierige und mit existierenden gitterbasierten Methoden zum Teil unlösbare Probleme.

In dieser Arbeit werden mehrere wichtige Weiterentwicklungen für SPH vorgestellt, wobei der Fokus dabei auf Allgemeingültigkeit und Stabilität der Methode liegt. Die veröffentlichten Arbeiten zu einer generellen Wandmodellierung für SPH, einem modifizierten Advektionsschema, einem neuen Oberflächenspannungsmodell und einem konservativen Surfactant-Modell sind allesamt so formuliert, dass sie generell einsetzbar sind für beliebige Geometrien und Dimensionen und vor allem einfach umsetzbar sind.

Für feste Wände wird eine neue, einfach zu realisierende Randbedingung vorgeschlagen, unter Verwendung von kartesischen Partikeln innerhalb der Wand. Im Vergleich zu existierenden Kontur-angepassten Ansätzen ist die Darstellung von gekrümmten Wänden in dieser Form natürlich ungenauer. Aber mit steigender Auflösung verschwindet diese ”numerische Rauhigkeit“ von ungeraden Wänden, und beliebig komplexe Körper können einfach realisiert werden. Mittels eines trivialen Interpolationsschemas für die Eigenschaften der Wandpartikel kann die Haftbedingung an der Wand aufgeprägt werden und eine von-Neumann Druckrandbedingung abgebildet werden.

Derzeit verfügbare SPH-Ansätze benötigen numerische Stabilisierungen in Form von künstlicher Viskosität, Reinitialisierung der Dichte oder Shepard-Filtern zur Kontrolle der geordneten Partikelbewegung. Meistens wird dabei eine Kombination mehrerer Korrekturen verwendet, was allerdings eine Parameterjustierung nötig macht, um genaue Ergebnisse zu erzielen. Eine Konsequenz daraus ist die Abhängigkeit der Ergebnisqualität von der Erfahrung des Benutzers. Im Gegensatz dazu wird hier ein neues Advektionsschema vorgestellt, das ohne jeglichen numerischen Stabilisierungsparameter für ein- und mehrphasige Strömungen verwendet werden kann. Nach bestem Wissen der Autoren bietet diese Methode erstmals die Möglichkeit einer Black-box SPH-Simulation, die sogar für bisher unerreichbar hohe Reynoldszahlen (Re=10000) stabil ist.

Die interaktionsbasierte Berechnung der Kräftebilanz mit SPH ermöglicht eine implizite Mehrphasenmodellierung, da Interaktionen zwischen verschiedenen Phasen mittels Farbcodes der Partikel leicht zu identifizieren sind und komplexe Phasengrenzflächenmodelle eingesetzt werden können. Als Beispiel dafür kann Oberflächenspannung in SPH mittels drei verschiedenen Ansätzen berücksichtigt werden. Am einfachsten ist die Modellierung mittels zusätzlicher Anziehungskräfte zwischen Partikeln, die qualitativ ein Verhalten entsprechend einer Oberflächenspannung hervorrufen. Alternativ kann ein makroskopischer Ansatz basierend auf der Rekonstruktion der Normalenrichtung der Grenzfläche gewählt werden. Hier werden die Kapillarkräfte als Produkt aus Krümmung und lokalem Oberflächenspannungskoeffizienten berechnet. Außerdem kann die Oberflächenspannung direkt als Spannungstensor formuliert werden mit dem Vorteil, dass nicht erst die Krümmung einer Oberfläche berechnet werden muss und diese Methode exakt impulserhaltend ist. In dieser Arbeit wird eine Variante des Kapillarkraft-Modells vorgestellt, das besonders für Probleme mit hohen Dichtesprüngen über einer Phasengrenze geeignet ist. Mittels einer Gewichtung der Oberflächenspannungskraft entsprechend den Dichten der verschiedenen Phasen können größere Schrittweiten für die Zeitintegration verwendet werden und somit der Aufwand einer Simulation reduziert werden.

Surfactants (oberflächenaktive Substanzen) sind Additive oder Verunreinigungen in einem Fluid, die die Eigenschaft haben, sich an einer Grenzfläche anzusammeln und dort die lokale Oberflächenspannung zu verändern. Mehrphasen-Systeme unter Berücksichtigung von Surfactants können sich grundsätzlich anders verhalten als reine Gemische, da neue Effekte wie Marangoni-Kräfte (induzierte Grenzflächenbewegung aufgrund eines Oberflächenspannungsgradienten) auftreten können. Die numerische Modellierung von Surfactant-Verhalten ist herausfordernd, da einerseits die Singularität

der Grenzfläche numerisch genau abgebildet werden muss und die exakte Massenerhaltung des Surfactants besonders für Langzeitsimulationen essentiell ist. In dieser Arbeit wird ein exakt konservatives, voll gekoppeltes Surfactant Modell für SPH vorgestellt, das Diffusion entlang der Grenzfläche und im gelösten Medium sowie den Austausch zwischen gelöstem und an der Phasengrenze aktivem Surfactant berücksichtigt. In Kombination mit der Lagrangeschen Partikelbewegung können damit komplexe Surfactant-induzierte Grenzflächendeformationen simuliert werden.

Die vorliegende kumulative Dissertation ist wie folgt aufgebaut: im ersten Kapitel wird ein kurzer Überblick zu CFD und numerischer Mehrphasen-Modellierung gegeben. Anschließend werden im zweiten Kapitel die Grundzüge von SPH vorgestellt. Kapitel 3 beinhaltet die Ergebnisse dieser Arbeit. Jedes Thema wird begleitend mit einem diesbezüglichen Literaturüberblick motiviert und die entsprechende Veröffentlichung zusammengefasst. Eine komplette Liste der Veröffentlichungen, die im Rahmen dieser Arbeit entstanden sind (Journal Paper, Buchbeiträge und Konferenzbeiträge), ist in Kapitel 4 zu finden. Abschließend wird die Arbeit in Kapitel 5 zusammengefasst und die relevanten Veröffentlichungen sind im Anhang eingebunden.

DANKSAGUNG

Die vorliegende Arbeit entstand in den Jahren 2008 bis 2013 während meiner Zeit am Lehrstuhl für Aerodynamik und Strömungsmechanik an der Technischen Universität München. An dieser Stelle möchte ich einigen Personen meinen Dank aussprechen, die in besonderer Weise zum Gelingen meiner Arbeit beigetragen haben.

Ich möchte mich ganz besonders bei meinem Doktorvater, Prof. Dr.-Ing. N.A. Adams, für seine Betreuung und Unterstützung während meiner Zeit am Lehrstuhl bedanken. Sie haben mir stets die Möglichkeit gegeben, mich sowohl fachlich als auch persönlich in bestem Maße zu entfalten. Dank ihrer Unterstützung und Befürwortung konnte ich auch sehr bereichernde Auslandserfahrungen sammeln.

Special thanks to Dr. Xiangyu Hu, my supervisor and group leader of the complex fluids group at AER. It was a pleasure to work with you and I learned a lot from your research. I cannot tell how many times we discussed failed approaches, but with endless patience and seemingly without any frustration you always condensed the crucial message to immediately come up with a new idea.

I also want to thank Prof. J.J. Monaghan and his wife: Jenny and Joe, the time at Monash was such a great experience and a warm welcome such as yours is not a given. I'm very proud that you, Joe, agreed to co-examine my thesis.

Jules, Amelia, Ali, and Lorenzo: thank you all so much for the wonderful time Down Under. Hope to see you all soon again!

Natürlich möchte ich mich auch bei den zahlreichen netten Kollegen am Lehrstuhl in München bedanken. Selbst bei einer Promotion gibt es eine Work-Life-Balance (wenn auch verschoben) und ich hatte viele schöne Kaffeepausen, Grillfeiern, Geburtstagsfeiern und ESP's mit Euch.

Den vielleicht wichtigsten Anteil an meiner Arbeit habt ihr, Mama und Papa: ich danke Euch für Eure Unterstützung im Studium, die Ermutigung, meinen Interessen zu folgen,

Eure Liebe und Euer Vertrauen in mich und mein Werken. Nadine, herzlichen Dank für deine große Unterstützung bei der Korrektur meiner Arbeit!

An dieser Stelle möchte ich mich auch bei Margaret und Peter bedanken. Ihr habt mich in München mit offenen Armen empfangen, immer unterstützt und gerade in der Anfangszeit mir sogar ein Dach überm Kopf geboten.

Meine liebe Ehefrau, Nicole, leider hat das mit dem Doktor heiraten nicht geklappt - aber ohne Deine Unterstützung wäre auch kein verheirateter Doktor daraus geworden ☺! Vielen Dank für deine Unterstützung, Geduld und dein Verständnis, wenn meine Laune zwischenzeitliche Misserfolge widergespiegelt hat.

München, den 12.01.2014 Stefan Adami

TABLE OF CONTENTS

Abstract i

Kurzfassung iii

Danksagung vii

1. Motivation 1
- 1.1. Computational Fluid Dynamics . . . 3
- 1.2. Multi-phase modeling . . . 4

2. Smoothed Particle Hydrodynamics 7
- 2.1. Method details . . . 9
  - 2.1.1. Kernel function . . . 10
  - 2.1.2. Derivatives in SPH . . . 10
  - 2.1.3. Mass conservation . . . 11
  - 2.1.4. Momentum conservation . . . 12
- 2.2. Multi-phase SPH . . . 13
- 2.3. Computational aspects . . . 15

3. Accomplishments 17
- 3.1. Wall boundary condition . . . 18
- 3.2. Accuracy and stability . . . 21
- 3.3. Surface-tension modeling . . . 24
- 3.4. Surfactant dynamics . . . 28

4. List of publications 31
- 4.1. Peer-reviewed journal publications . . . 31
- 4.2. Book sections . . . 32
- 4.3. Conference proceedings . . . 32

5. Conclusions 35

A. Appendix 37
- A.1. A generalized wall boundary condition for smoothed particle hydrodynamics . . . 39
- A.2. A transport-velocity formulation for smoothed particle hydrodynamics . . . 65
- A.3. A new surface–tension formulation for multi–phase SPH . . . 87
- A.4. A conservative SPH method for surfactant dynamics . . . 105

B. Bibliography 129

NOMENCLATURE

ARDS	Acute Respiratory Distress Syndrom
BIM	Boundary-integral method
CAE	Computer Aided Engineering
CFD	Computational Fluid Dynamics
DEM	Discrete Element Method
DFG	Deutsche Forschungsgesellschaft (German Research Foundation)
EOS	Equation-of-State
FDM	Finite-Difference-Method
FEM	Finite-Element-Method
FSI	Fluid-Structure-Interaction
FVM	Finite-Volume-Method
GPU	Graphics Processing unit
ISPH	Incompressible SPH
LS	Level-Set
MD	Molecular Dynamics
MHD	Magnetohydrodynamics
PAR	Protective Artificial Respiration
PPE	Pressure-Poisson equation
PPM	Parallel Particle-Mesh Library
SPH	Smoothed Particle Hydrodynamics
VILI	Venilator induced lung injury

VOF	Volume-of-Fluid
WCSPH	Weakly-compressible SPH

1. MOTIVATION

This thesis gives on overview about my research in the field of Smoothed Particle Hydrodynamics (SPH). Over the past five years I have worked on the method development and improvement of SPH with emphasis on multi-phase modeling.

Originally, as sub-project of the *DFG* priority program “Protective Artificial Respiration” (PAR) the objective was a fundamental investigation on flow-induced stresses on epithelial lung cells in the alveolar airway ducts coupled with air-water interface dynamics and soft-tissue interaction. The long-term goal of this project is a better understanding of the human respiration system aiming for new developments of protective ventilation techniques. Intensive care medicine patients or patients suffering from the Acute Respiratory Distress Syndrom (ARDS) require artifical ventilation. Although this treatment currently is mostly without alternative, ventilator induced lung injuries (VILI) show a mortality rate on the order of 50% [118]. It is widely accepted that VILI originates from the fact that artificial ventilation reverses the physiological lung functionality by pumping air into the airways rather than air suction controlled by the diaphragm. However, a profound understanding of the lung injury is still missing and a key question in the medical community. Most probable is a combination of shear-induced mechanical stresses at the endothelial lung cells that cause alveolar overexpansion and mechanotransduction, i.e. inflammatory injuries due to mechanical stimulation of the cells.

In collaboration with the group of Prof. Dr. rer. nat. E. Koch (Klinisches Sensoring und Monitoring, Technische Universität Dresden) we worked both experimentally and

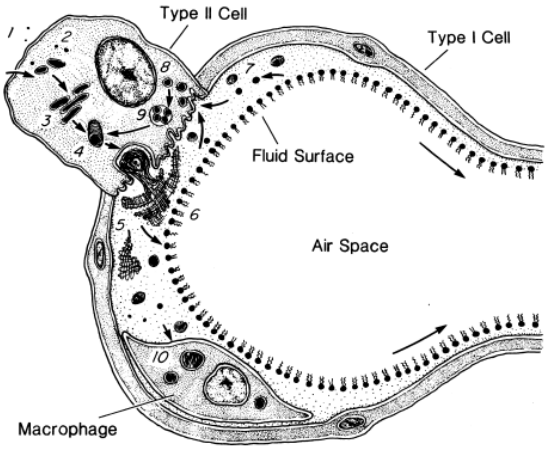

Figure 1.1.: Schematic diagram of a single alveolus with the surfactant system, taken from Hawgood and Clements [52].

numerically on the fundamental investigation of the pathogenesis mechanisms at the alveolar level. A schematic diagram of a single alveolus is given in Fig. 1. A liquid lining is coating the endothelial cells and serves as a buffer layer between the incoming air and the cells. This liquid layer is of special interest as its presence and properties strongly affect the dynamics of a single alveolus. In case of a film rupture the incoming air would get into direct contact with the endothelial cells and this might be one reason for inflammatory injuries. The film dynamics itself are a complex fluid mechanical problem as due to the length-scale of an alveolus ($\approx 100\ \mu m$), surface-tension effects are relevant at the liquid-air interface and additionally so-called “surfactants” (surface active agents) manipulate the film stability. In the absence of surfactants, the high surface-tension at the interface of the water-like liquid layer and the air would collapse the alveolus due to the high capillary pressure forces. In addition to immune function, the surfactant mainly takes effect in strongly reducing surface tension when adsorbed at the air-water interface, thus prevents the so-called atelectasis (collapse of the lung). Besides the general fact that surfactants are strongly necessary in mammal respiration systems, many questions are still open, e.g. the effect of mechanical stresses on the production rates of surfactant by the type II endothelial cells or the effect of varying surfactant properties in the fluid film and at the interface.

Numerical investigations of such complex problems are a challenging if not infeasible task. The difficulty arises from the fact that on one hand very sophisticated computational models are required to capture the relevant physical phenomena, and on the other hand many unknown parameters and uncertainties for example in the boundary conditions or surfactant properties occur in the system. Nevertheless, numerical simulations can provide detailed insight into complex problems under well-defined conditions. Unlike experiments, simulations allow for studying the effect of isolated parameters in the system or to manipulate individual characteristics to analyse their influence on the fully coupled problem.

Given the complexity of the problem (geometry, physics) standard grid-based computational tools are clearly inappropriate, and a main milestone of the original research

project was the development of a numerical method that can simulate air-water interface dynamics with emphasis on surfactant dynamics and surface-tension effects. Due to its promising properties with focus on multi-phase modeling, the smoothed particle hydrodynamics method (SPH) was chosen as numerical framework. This method is based on a gridless discretization using Lagrangian particles that are advected with the local flow and thus is particularly suitable for complex deforming geometries. Although conceptually promising, application of SPH to a complex problem as described above showed several limitations of the method that prompted us to focus on developing and improving the capabilites of SPH itself.

The following two sections give a short introduction on computational fluid dynamics in general and an overview of classical multi-phase modeling approaches. The subsequent chapter on Smoothed Particle Hydrodynamics summarizes the fundamental properties of the numerical method and deals with particular computational aspects of gridless schemes. Chapter 3 presents the four major improvements of the SPH method in this thesis prepended with a literature review on each topic, namely a new wall boundary condition for arbitrarily shaped geometries, a transport-velocity formulation that allows for accurate and stable simulations without artificial damping parameter, a surface-tension model for interfaces with high density ratios and, finally, a conservative formulation for surfactant dynamics including interfacial and bulk diffusion and an adsorption-desorption-based transport model. An overview of all publications related to this dissertation is provided in the next chapter, ordered by peer-reviewed journal publications, contributions to book sections and conference proceedings. The relevant journal publications together with the publisher agreement are attached in the original layout in Appendix A. Finally, chapter 5 gives a conclusion on the state of the method.

1.1. Computational Fluid Dynamics

Computational Fluid Dynamics (CFD) is the discipline of predicting fluid mechanics with computer simulations on the basis of mathematical models for the physical phenomenon of interest. The generic term *CFD* includes strictly speaking the entire process of abstracting a physical problem with a mathematical model and deriving the governing equations, discretizing the equations with the numerical method of choice, implementing the routines in a computer code, performing the simulations and finally postprocessing the data and visualizing the results. Commercial software packages are usually optimized for a limited range of applications and imply a specific implementation of an appropriate numerical method. Using such tools requires only generation of input data such as geometry and initial conditions, performing the simulation and analyzing and visualizing the results of the simulation.

As subgroup of computer aided engineering (CAE), CFD has gained industrial relevance over the past decades thanks to the increase of available computational resources (both resulting from cost reduction and performance increase). CFD as a design tool is for example already highly used in the automotive industry or the aerospace industry. Although simulations cannot replace real experiments completely, numerical

experiments can strongly reduce their necessity. Often, it is easier to study parameter variations or geometrical modifications using numerical simulations as state-of-the-art commercial CFD tools often predict qualitative trends reasonably well. Also, data acquisition from simulations is superior to experiments since any quantity can be monitored at any location and more complex derived variables can be evaluated easily. Another important field of operation for simulations are investigations at extreme conditions that are difficult or impossible to achieve in experiments. The overall trend is to include CFD in the product development as early as possible and finally only validate the observations from the simulations with a few experiments.

In the context of academic research the interest in CFD is, roughly speaking, threefold. Firstly, meeting industrial demands, the flow physics of a problem can be analyzed in detail using CFD to identify the relevant parameters and optimize e.g. the shape of an object with respect to drag reduction. Secondly, CFD offers the possibility to investigate the flow physics itself. That means by carefully analysing numerical simulation results it is possible to improve the understanding of the underlying physical phenomena. Microfluidics is a prime example where numerical simulations can give new insights when experiments are unfeasible. Given the small length-scales of these problems, quantitative measurements are extremely difficult and often inaccurate. Today still, in many cases prototypes of microfluidic applications (e.g. lab-on-a-chip, inkjet printhead) serve as proof-of-concept, but the development process follows mostly trial-and-error studies rather than well-directed research. With CFD it is possible to model such microfluidic flows and study their dynamics. In contrast to experiments, with numerical simulations it is possible to separate and investigate different physical phenomena individually. This decoupling often helps to understand the behavior of a complex system, hence opens up room for improvement. Thirdly, the research on numerical methods per se seems purely academic but helps to improve existing schemes (e.g. accuracy, computational cost) and can lead to new approaches that enable investigations of previously unfeasible problems.

The work presented in this thesis goes with both last two categories. As SPH is preferable for numerical studies of multi-phase problems with complex geometries and multiple physics it is the method of choice to address the challenging modeling of alveolar dynamics. On the other hand, although already available sporadically in particular commercial software, e.g. LS-DYNA [75], SPH is not yet well established in the CFD community mainly due to crucial limitations regarding stability, convergence or computational cost. Therefore, development and improvement of the method itself is necessary.

1.2. MULTI-PHASE MODELING

Multi-phase models in numerical methods are used to incorporate the physical effects caused by the presence of different phases. This requires on one hand algorithms that identify these phases, and on the other hand mathematical relations that describe the interfacial physics.

Grid-based continuum methods for multi-phase problems can be split into two groups according to the type of the interface representation. Lagrangian approaches explicitely discretize the interface singularity and allow for discontinuous physical quantities. In contrast, Eulerian approaches evolve field equations that are used to locate the interface. Examples for the first group are boundary-integral methods (BIM) [96] and front-tracking methods [119]. In the second group level-set methods (LS) [94, 93] and volume-of-fluid methods (VOF) [56] are commonly used.

In the boundary-integral method an interface is explicitely discretized with piecewise curved sections between marker points and the evolution of these markers follows the solution of an integral equation. More generally, front-tracking methods evolve the location of an interface ("front ") coupled with an underlying fluid solver. Similar to BIM, the interface is represented with Lagrangian marker points that are used to reconstruct the contact line between different phases. In addition, surface forces and other interfacial phenomena (surface diffusion, species transport) are fed back to the continuous phase equations and form a fully coupled system.

In the level-set method (LS) [94, 93] a signed distance function specifies the distance of a discretization point to a nearby interface. Hence, the zero-level set of this function defines the interface. This field function evolves over time according to an additional advection equation.

All previously mentioned methods approximate the interface singularity with a so-called sharp-interface or zero-thickness model. Contrarily, the volume-of-fluid method (VOF) [56] leads to a smeared interface approximation with a smooth transition between the opposing phases at an interface. For a two-fluid problem a scalar volume-fraction field or color-function is introduced to distinguish between the phases. This fraction defines the mixture of the two phases at any discretization point and varies from zero to one. Accordingly, the interface can be reconstructed from the iso-surface (in 2D it is a line) at one half of the volume-fraction. Except for the initial condition, where a sharp transition between the phases can be imposed, usually the color-function or volume-fraction gradually changes between the phases and gives a smoothed interface representation with a finite thickness on the order of the numerical resolution length. As a consequence, the governing equations are formulated for a single field using mixture properties and the mixture fraction (color-function) evolves according to an additional equation.

There exist many other approaches as well as modifications or combinations of the fundamental methods with higher complexity in literature [100, 127]. Here, only a brief survey of classical multi-phase methods is presented to recall the widely-used fundamental concepts in multi-phase modeling. It is difficult to discuss these approaches in terms of relevance or preferability since the method-of-choice for a specific problem is always case dependent. Each of the modeling attempts has several advantages and disadvantages that have to be taken into account when choosing a numerical framework for the application of interest. Front-tracking methods for example need a priori knowledge of the number of closed surfaces that might be unavailable for complex mixtures. Level-set methods without special treatment ensure a sharp interface discretization but might violate mass conservation.

Fundamentally different, Lagrangian particle methods offer a very powerful numerical framework especially for multi-phase problems as a number of the mentioned difficulties is omitted by the nature of the method. With Lagrangian discretization points that advect with the flow, it is possible to distinguish between different phases with the use of a simple integer identifier. For each point the single fluid equations can be solved according to a purely present phase and at the same time the interface can be discretized with a smooth surface delta-function with bounded thickness. These properties allow for modeling surface phenomena in conservative form and complex topological changes such as merging or breakup of interfaces can be handled implicitely.

Recently, Wörner [127] has given an overview on numerical modeling of multiphase flows in microfluidics. Interestingly, meshless particle-methods such as *Smoothed Particle Hydrodynamics* (SPH) were not considered as "[...] they have only limited application in microfluidics so far [...]" [127]. Given the potentials of Lagrangian methods especially for multi-phase problems, it is indeed surprising that these methods are still lacking broad acceptance and usage in the CFD community. Actually, many studies have already shown that particle methods can successfully simulate microfluidic problems ranging from wetting dynamics [115, 35] or droplet dynamics [43, 92, 59, 8] to porous transport phenomena [106] and coarse-grained multiscale problems [74, 66].

The focus of this work is on improving the capabilities of SPH for complex multi-phase problems (high density ratios, interfacial surfactant transport) and especially on increasing the accuracy and stability of the method. With the presented developments SPH can be used for a broad range of applications without the need for parameter calibration and highly diffusive stabilization techniques. Thus, for the first time a blackbox-type status of the method is achieved that is necessary to gain industrial relevance.

2. SMOOTHED PARTICLE HYDRODYNAMICS

SPH was introduced independently by Lucy [76] and Gingold and Monaghan [49] in 1977. Although Lucy did not call the method “SPH” and used the terminology “broadening function” rather than “kernel” or “smoothing function” as in [49], the basic principle of a Lagrangian particle method with finite range interactions resulting from a mollification function is similar in both methods.

In the beginning, SPH was applied to astrophysical problems such as the fission of a rapidly rotating star [49]. Although over the years SPH was extended to a broad range of fluid and solid mechanical problems, astrophysics still today is a classical field of research with SPH as it clearly benefits from the key features of the method. In SPH, “particles” represent discretization points where numerical solutions to the governing equations are calculated. When moving these particles with the local flow field, pure advection is treated exactly by the nature of the method and Galilean invariance is ensured. Being exact for SPH, even linear advection of a scalar field in diagonal direction on a Cartesian lattice can be approximated only with a modern finite-difference-method (FDM) or finite-volume-method (FVM). Next, as particles advect with the flow the discretization includes already adaptive capabilities since the computational domain can vary from the initialization of a simulation to the final configuration. This feature is maybe the most important advantage as it allows to simulate complex evolving flows as dambreaks or avalanches [34, 104]. With the use of particles the mesh generation is omitted and there is no need to discretize the entire domain a fluid might reach during

a simulation from the beginning. Also, variations in spatial and temporal resolution can be realized as different particles can have different interpolation length-scales. Useful for multi-phase problems, particles can be tagged with an identifier to distinguish different phases without the need for explicit front-tracking or front-capturing algorithms. Thus, complex interfacial phenomena can be modeled and e.g. different constitutive laws or governing equations for different sets of particles can be introduced.

From these properties it is clear that SPH has huge capabilities and potentials in many fields of research. Since 1977 the method was used and developed further for a large variety of complex phenomena. By no means exhaustive, the following overview is intended to show this versatility.

Taking advantage of the Lagrangian advection of particles and the simple discretization of complex domains, SPH can be used to simulate highly-violent free-surface flows such as dam breaks or coastal wave breaking events [34, 83, 77]. By assigning different properties to different particles it is straightforward to model multi-phase flows including surface tension effects [59, 51, 88, 92]. Ellero et al. and Vazquez-Quesada et al. [42, 121] have introduced more complex particle-particle interactions and showed that non-Newtonian fluid behavior can also be modeled with SPH. Recently, Pan et al. proposed a non-Newtonian SPH model to simulate ice-shelf dynamics [95]. Besides fluid mechanics, due to the flexibility in the constitutive equation for the stress tensor of a continuum phase, it is possible to simulate solid bodies and their interaction [25, 123, 72]. Benz and Asphaug [26] introduced a fracture model to study the propagation of cracks in loaded rods. Again, since Lagrangian particles by the nature of the method advect according to the local momentum it is possible to track and evolve fragments caused by brittle fracture of material or simulate impacting projectiles [37, 111]. Combining fluid and solid mechanics, SPH can be used to couple fluids and structures in a monolithic framework [24, 50, 124]. Although this elegant approach reduces the code complexity and simplifies the boundary conditions at solid-fluid interfaces, more recent attempts to simulate fluid-structure interactions (FSI) use SPH as fluid solver and couple it to well established structural finite-element-method (FEM) codes [101, 47]. The Lagrangian particle discretization also offers the possibility to change the behavior of individual particles as they evolve in time. Monaghan et al. [86] used this functionality to model solidification of a binary fluid system like freezing of a salt solution, but they used fixed particles and only propagated the front of the phase-change. More general, Tartakovsky et al. [116] proposed a SPH model for reactive transport and precipitation including particle motion. Rather new, the capability of SPH to simulate turbulent flows has been shown by several groups and especially this area of research is currently of high interest [125, 103, 110, 85]. Unchanged from the beginning, SPH is highly used in astrophysics to study e.g. the formation of stars [112] or magnetohydrodynamics (MHD) [98]. Apart from this collection SPH is more and more used for very complex and “exotic” applications where other methods fail or hardly give reasonable results. Hieber et al. [54] showed that with Lagrangian particle methods it is possible to simulate nonlinear soft tissue and they reproduced numerically the experimental results of an aspiration test on liver tissue. Another example is given by Van Liedekerke et al. [120], who proposed a plant cell model to simulate the dynamics of parenchyma cells and aggregates allowing for large deformations and

arbitrary shapes.

Although SPH is a promising method with large capabilities the industrial relevance is still marginal. One possible reason is that a strict mathematical proof for convergence and stability is missing. As the Lagrangian particles in general are strongly disordered, classical numerical analysis fails so that convergence and consistency can only be demonstrated empirically. Nevertheless, many examples have shown that SPH gives reasonable results especially for very complex problems.[1] Another handicap of the method is the computational cost. Due to the smoothing concept the resulting number of calculation operations per particle are much higher compared to a standard grid-based method and consequently simulation times are longer. However, as the general multi-particle SPH algorithm shows high parallelism it is well suited for GPU computing (graphics processing unit). Using this technology the performance of SPH codes can be strongly increased in terms of computational acceleration and acceptable simulation times are achieved, see e.g. Hérault et al. [53] or Domínguez et al. [40]. Last, still today SPH is not yet ready to be used as black-box tool and the quality of the results can strongly depend on the experience of the user. This is due to several parameter-dependent corrections that are necessary to allow for stable and accurate simulations. Since these corrections usually need case-specific tuning it is difficult to use SPH as design tool in an industrial environment. Yet, with the improvements presented in this thesis to the best knowledge of the author, for the first time SPH can be applied to various wall-bounded flows without any fitted adjustments (see Sec. 3.2 for details and validation).

The following three sections briefly review the fundamental SPH concept. The smoothing and gradient discretization is introduced and the governing equations for continuum mechanical problems are presented. At the end of this chapter a few practical issues specific to particle methods in general such as neighbor-search and interaction-lists are discussed.

2.1. METHOD DETAILS

SPH particles are discretization elements that move with the flow and carry certain properties such as mass or species concentrations. To calculate a field quantity ϕ as function of the coordinate $\mathbf{r}$ the interpolation integral

$$\phi(\mathbf{r}) = \int \phi(\mathbf{r}') W(\mathbf{r} - \mathbf{r}', h)\, d\mathbf{r}' \tag{2.1}$$

with the smoothing function W (or *kernel*) is introduced. The smoothing length h is a measure of the width of the kernel. A discrete form of eq. (2.1) for a set of particles at

[1] In computer games and for special effects in movies (see e.g. www.nextlimit.com) SPH is successfully used to simulate and visualize flows (in constrast to "animating" them).

positions $\mathbf{r}_j$ is

$$\phi(\mathbf{r}) = \sum_j \phi(\mathbf{r}_j) W(\mathbf{r} - \mathbf{r}_j, h) V_j \ . \tag{2.2}$$

The value of ϕ at the position $\mathbf{r}_i$ of particle i is obtained from a summation over all neighboring particles j with weight $W(\mathbf{r}_i - \mathbf{r}_j, h)$ multiplied by their respective volume elements V_j.

2.1.1. KERNEL FUNCTION

The radially symmetric smoothing or kernel function is required to satisfy the following requirements. In the limit of a vanishing smoothing length h the kernel should reduce to a delta function

$$\lim_{h \to 0} W(\mathbf{r} - \mathbf{r}', h) = \delta(\mathbf{r} - \mathbf{r}') \tag{2.3}$$

giving an exact integral interpolant in eq. (2.1). The partition of unity property

$$\int W(\mathbf{r} - \mathbf{r}', h) \, d\mathbf{r}' = 1 \tag{2.4}$$

is important to interpolate constants exactly and requires proper normalisation of the kernel. Compact support of the kernel, i.e. a vanishing kernel at finite distance, is favorable for efficiency but not necessary.

The SPH formulation is not specific to the choice of the kernel function and various choices for the smoothing can be found in literature. Among these the most used kernel functions are the Wendland kernels [126] or B-Splines [108]. Recently, Dehnen and Aly [39] showed that kernels with non-negative Fourier transform (such as the Wendland functions) are favorable as they prevent the particle pairing instability. More details on this instability are given in Sec. 3.2, where a new transport-velocity formulation is presented that suppresses this pairing and allows for using more accurate spline kernels without stability problems as well.

2.1.2. DERIVATIVES IN SPH

Derivatives of field quantities can be approximated in SPH by several ways. A comprehensive account of this issue is given in [84] or [99].

Starting from the SPH approximation, eq. (2.2), the gradient of ϕ at the position $\mathbf{r}_i$ of particle i is obtained as

$$\nabla \phi_i = \sum_j \frac{m_j}{\rho_j} \phi(\mathbf{r}_j) \nabla W_{ij} \ , \tag{2.5}$$

where m_j and ρ_j are the mass and density of neighboring particles j. Here, a differentiable kernel function W with compact support is assumed and the mass elements ρdV are replaced with the discrete particle mass. Note that the gradient of ϕ at particle i is

calculated from the field function ϕ itself at neighboring particles, and the gradient of the kernel function is an analytical expression. However, the discrete sum in eq. (2.5) is zero-order consistent only, i.e. the gradient of a constant field p is non-zero for a randomly distributed particle configuration.

It is straightforward to substract the first error term of a Taylor series about $\mathbf{r}_i$ to obtain a more accurate gradient approximation as

$$\nabla\phi_i = \sum_j \frac{m_j}{\rho_j} \left(\phi_j - \phi_i\right) \nabla W_{ij} \ . \tag{2.6}$$

Consequently, this form is first-order consistent. Further increasing the accuracy, a renormalization can be introduced to recover second-order consistency. The problem with these gradient approximations is that, when applied to the momentum balance equation, the resulting numerical discretization is non-conservative.

Using the identity

$$\nabla\phi = \varphi \left[\frac{\phi}{\varphi^2} \nabla\varphi + \nabla \left(\frac{\phi}{\varphi} \right) \right] \ , \tag{2.7}$$

another variant of the gradient discretization is obtained as

$$\nabla\phi_i = \varphi_i \sum_j m_j \left(\frac{\phi_i}{\varphi_i^2} + \frac{\phi_j}{\varphi_j^2} \right) \nabla W_{ij} \ , \tag{2.8}$$

where φ is a differentiable scalar quantity. As shown later in sec. 2.1.4, this anti-symmetric form conserves linear and angular momentum when applied to the pressure force in the momentum balance equation.

Comparing the two formulations eq. (2.6) and (2.8) it is interesting to note that the first discretization gives worse results compared to the second one although linear error analysis shows higher accuracy. The conservative formulation regularizes the particle configuration when applied to the equations of motion resulting in a more accurate approximation. This paradox is well explained in the section "*Why a bad derivative leads to good derivatives*" of Daniel Price's recent overview [99].

2.1.3. MASS CONSERVATION

In classical SPH mass conservation is intrinsically satisfied. Usually, each particle carries a constant portion of mass that does not change during a simulation. Thus, the total mass is exactly conserved. Two fundamentally different approaches exist for the evolution of density, the density evolution form and the density summation form.

According to mass conservation of a Lagrangian particle, the continuity equation

$$\frac{d\rho}{dt} = -\rho \nabla \cdot \mathbf{v} \tag{2.9}$$

relates the change of density to the divergence of the velocity field. For incompressible flows the divergence of the velocity field vanishes, hence $d\rho/dt = 0$. Solving the resulting pressure-Poisson equation (PPE) with SPH is non-trivial and computationally expensive since particles are randomly distributed and continuously move relative to each other even for a stationary flow. Methods for dealing with incompressible SPH (ISPH) can be found for example in [33, 61, 130]. Assuming a weakly-compressible fluid the density can be evolved according eq. (2.9), and incompressibility is approximately satisfied by limiting the density variation to 1%. One possible discretization of the continuity equation is

$$\frac{d\rho_i}{dt} = -\sum_j V_j \left(\mathbf{v}_i - \mathbf{v}_j\right) \cdot \nabla W_{ij} \ , \tag{2.10}$$

where ρ, V and $\mathbf{v}$ denote the density, volume and velocity of a particle and the subscript indicates particle i and its neighbors j. The density evolution approach can be applied directly to free-surface flows, where surface particles do not have full-support. The drawback of this form is that the total volume ($V = m/\rho$) can vary as errors in the density evolution may accumulate due to the symmetric term in the summation of Eq. (2.10).

Another way to calculate the density of a particle follows directly from the kernel interpolation and is given by

$$\rho_i = \sum_j m_j W_{ij} \ . \tag{2.11}$$

Here, the density of particle i is directly obtained from the actual particle configuration and requires full support for the summation. The total volume can vary with this summation form as well, but when applied to wall-bounded flows the particle motion is geometrically confined and the error in total volume is bounded during the simulation.

2.1.4. Momentum conservation

Momentum conservation of an isothermal fluid is expressed by the Navier-Stokes equation

$$\frac{d\left(\rho\mathbf{v}\right)}{dt} = -\nabla p + \eta\nabla^2\mathbf{v} + \rho\mathbf{g} + \mathbf{F}^{(s)} \ , \tag{2.12}$$

where p, η and $\mathbf{g}$ denote pressure, dynamic viscosity and bodyforce, respectively. The surface force $\mathbf{F}^{(s)}$ describes additional interfacial effects such as surface tension. Further details are given in the following section on multi-phase SPH. Using the weakly-compressible approach to simulate incompressible flow with SPH the pressure is related to density by an equation-of-state (EOS) in the form of

$$p = p_0 \left[\left(\frac{\rho}{\rho_0}\right)^\gamma - 1\right] + p_b \tag{2.13}$$

to close the system of governing equations. The reference pressure p_0, the exponent γ and the background-pressure p_b are numerical parameters that are chosen based on a scale analysis presented by Morris et al. [90] to limit the density variation to 1%. The artificial sound speed c_s determines the reference pressure

$$p_0 = \frac{\rho_0 c_s^2}{\gamma} \tag{2.14}$$

and is usually taken to be an order of magnitude larger than the reference velocity of the flow. This choice is a compromise between using the physical speed of sound that would strongly constrain the numerical time-step size and the threshold of the density variation. The background-pressure p_b sets the constant reference pressure level in the flow and is a case-dependent parameter that affects also the stability of standard SPH simulations. The effect of p_b and a new approach without case-dependent tuning is discussed in detail in Sec. 3.2.

Using SPH derivatives for the gradient operators in eq. (2.12) the acceleration of a Lagrangian particle is approximated as

$$\frac{d\mathbf{v}_i}{dt} = \mathbf{g}_i - \frac{1}{m_i} \sum_j \left(V_i^2 + V_j^2\right) \frac{\partial W}{\partial r_{ij}} \left[\widetilde{p}_{ij}\mathbf{e}_{ij} + \eta \frac{\mathbf{v}_i - \mathbf{v}_j}{r_{ij}}\right] . \tag{2.15}$$

Here, the gradient of the kernel is rewritten as $\frac{\partial W}{\partial r_{ij}}\mathbf{e}_{ij} = \nabla W\left(\mathbf{r}_i - \mathbf{r_j}\right)$ with the unit vector $\mathbf{e}_{ij}$ between two particles i and j. The inter-particle pressure $\widetilde{p}_{ij}$ for single-phase problems is simply $\frac{1}{2}\left(p_i + p_j\right)$.

It can be shown [99] that the SPH equations (without viscous term) form a Hamiltonian system and are Galilean invariant. Note, the discretization in eq. (2.15) conserves linear momentum exactly due to the anti-symmetric summation. Other formulations are available in literature [31, 60, 84] that introduce particle-particle interactions only on the centre-lines and conserve angular momentum as well. Finally, the velocity of a particle is evolved in time using the actual acceleration and the position of particles is updated with the equation of motion

$$\frac{d\mathbf{r}_i}{dt} = \mathbf{v}_i \ . \tag{2.16}$$

2.2. MULTI-PHASE SPH

With small modifications to the single-phase model SPH can handle multi-phase problems with complex physical phenomena effectively. Due to the interaction-based force calculation between different particles it is straightforward to handle interfaces implicitly. Each phase is tagged with an identifier to distinguish particles of different types. When two particles of the same type interact, the single-phase model is applied. At interfaces, the interaction naturally takes into account different properties of the fluids.

Hu and Adams [59] showed for the viscosity model used in eq. (2.15) that by replacing the single-phase viscosity η with a combined viscosity in the form

$$\widetilde{\eta}_{ij} = \frac{2\eta_i\eta_j}{\eta_i + \eta_j} \tag{2.17}$$

the shear stress and velocity across the interface are continuous. Note, if two particles belong to the same phase, this combined viscosity reduces exactly to the single-phase viscosity. Hence, this formulation can be generally applied to any type of interaction. In a similar way the pressure term is adapted to ensure a continuous gradient of $\nabla p/\rho$ even for discontinuous density fields [61]. The only difference is the form of the inter-particle pressure that is now given by

$$\widetilde{p}_{ij} = \frac{\rho_j p_i + \rho_i p_j}{\rho_i + \rho_j} \ . \tag{2.18}$$

As for the viscosity, this model reduces to the single-phase form when both particles belong to the same phase and can be generally applied. The evolution equation (2.10) for mass conservation takes into account the geometrical particle configuration and the volume contribution. Therefore this approach can be directly applied even to interfaces with large density discontinuities. For the density summation (2.11) Hu and Adams [59] proposed a marginal modification that allows to use this form for multi-phase flows. In their model, the particle density is obtained from

$$\rho_i = m_i \sum_b W_{ij} \ . \tag{2.19}$$

Since neighboring particles now only affect the specific volume of particle i, artificial mass transport across the interface is suppressed and the summation applies to arbitrary density ratios.

The integer phase identifier is advected with the flow field and is constant for a particle in the absence of a phase transition model. Together with the multi-phase model previously prescribed it is possible to incorporate interface effects implicitly in an elegant way without a special interface reconstruction scheme. Arbitrary interface shapes as well as complex deformations including interface breakup and merging can be considered.

To model additional interface phenomena such as surface tension a color-function c is introduced with a unit jump at a phase interface. This function assumes the value $c_l^k = 1$ if the k-th particle belongs to the phase of type l and $c_l^k = 0$ if not. Following Brackbill et al. [29], the surface delta function δ_Σ is approximated with the gradient of the color-function

$$\mathbf{n}\delta_\Sigma = \nabla c \tag{2.20}$$

and can be used to write the interfacial surface-tension force in volumetric form. Furthermore, by

$$\mathbf{n} = \frac{\nabla c}{|\nabla c|} \tag{2.21}$$

the normalized color-gradient gives the normal direction at the interface that is required e.g. to calculate the curvature of an interface or to correctly impose Robin boundary conditions [8, 105]. Fig. 2.2 shows a sketch of a two-fluid situation with the normal $\mathbf{n}$ and the surface-delta function δ_Σ to further illustrate the particle discretization of an interface.

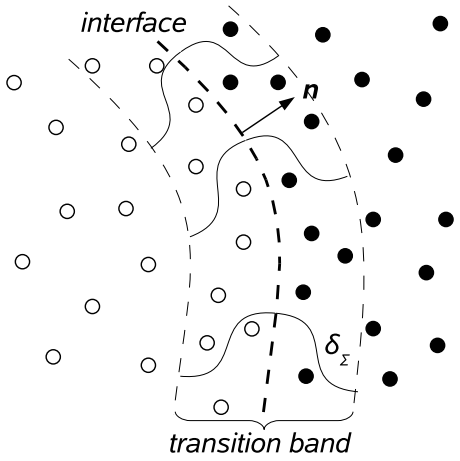

Figure 2.1.: Sketch of the transition band at an interface with the surface delta function δ_Σ, the normal $\mathbf{n}$ and particles of two different phases.

The combination of maintaining a sharp phase discontinuity and the smooth interface discretization using a surface delta function offers an enormous modeling potential for complex problems. A well-designed SPH implementation is furthermore attractive by its own, since simply exchanging, e.g., the constitutive law to calculate the stress tensor allows for simulating fluid-structure interactions within a monolithic approach.

2.3. COMPUTATIONAL ASPECTS

The discretization of the governing equations using a Lagrangian particle method results in a multi-body interaction scheme. Fundamentally different to grid-based methods, the *stencil* of a particle is not known a-priori and needs to be reconstructed at every time-step. As particles can move freely, the distance of interacting particles and therefore the weighting in the summation changes. In addition, particles might enter or leave the cutoff-range. The reconstruction of the interaction list requires approximately 5% of the computational time to calculate one numerical time step and contributes to the increase in computational complexity. However, the significant increase in computational cost compared to grid-based methods is due to the interaction-based discretization scheme itself. In SPH, using e.g. a quintic-spline kernel with a cutoff radius of three particle spacings $r_c = 3\Delta x$, the number of neighbors are on the order of $O\left(30\right)$

in 2D and $O(90)$ in 3D. Therefore it is very important to develop efficient algorithms to create the interaction lists and to calculate the change rates of the governing equations. Note, these algorithms are not specific to SPH but are shared by any particle method such as Molecular Dynamics (MD) or Discrete Element Method (DEM) that depend on a multiple-interaction scheme.

In 1989, Allen and Tildesley [23] have reviewed the cell-list approach using linked-lists to build up the particle-interaction lists efficiently. These algorithms are still today the state-of-the-art for particle methods. Without any presorting, the neighbor search for a particle in a randomly distributed cloud of particles requires $O(N^2)$ operations, where N is the total number of particles. With a given cutoff-radius r_c it is possible to presort particles in cells with a width of r_c. Consequently, particles with a distance smaller than the cutoff can only be located within the same cell or in the adjacent cell, i.e. the search can be limited to a field of 9 cells in 2D (or 27 cells in 3D). Furthermore, using linked lists all particles are reordered and assigned to their respective cell. With this approach it is straightforward to find the neighbors for any given particle i without sweeping over the entire set of particles. Verlet [122] proposed to use cells that are larger than the cutoff. As a consequence, distant interactions with effectively zero weighting are also included in the lists but the necessary frequency of reconstructing these so-called *Verlet lists* is reduced. Obviously, the increase in considered interactions versus the reduced cost of reconstructing the lists need to be properly tuned and can lead to a considerable increase in computational efficiency.

Concerning computational efficiency the creation of individual interaction lists for different phases and interfaces is beneficial, especially for multi-phase problems with complex physical phenomena. Instead of identifying each pairwise interaction and defining their relevant governing equations, it is profitable to create various lists first and then to directly apply the corresponding routines. In doing so, the calculation of forces e.g. due to surface tension effects is performed implicitly only for particles close to an interface.

The drawback of the cell-list approach is the Cartesian decomposition of the domain into cells, i.e. an arbitrarily complex geometry needs to be embedded in a rectangular computational box including empty or fractionally particle-filled cells. Furthermore, cell-lists are most efficient for kernels with a fixed cutoff radius. For weakly-compressible fluids this is no issue as they are modeled by a constant cutoff radius and marginal density variation. At the same time the cell-list decomposition of the domain enables a straightforward parallelization using MPI routines as the cells can be used directly as sub-domains to be distributed amongst individual processors. A very general framework for particle simulations offering all the necessary functionality ranging from domain decomposition to efficient communication in a parallel code was presented by Sbalzarini et al. [107]. They distributed a library called *PPM* that handles all challenging parallelization issues of a meshless numerical method where the user can focus on the modeling part. Using this library in this work allowed for highly efficient SPH simulations of millions of particles on the SuperMUC Petascale System at Leibniz-Rechenzentrum (Leibniz Supercomputing Centre) in Garching.

3. ACCOMPLISHMENTS

In this chapter the developed improvements of the SPH method are presented. Each work is motivated with a short literature review to demonstrate the state-of-the-art of each particular issue indicating the limitations that have been overcome by the respective research.

3.1. WALL BOUNDARY CONDITION

The correct imposition of boundary conditions in general, and wall-boundary conditions in particular, is of great importance for numerical methods. Yet, modeling of wall-boundary conditions is non-trivial especially for SPH and an established best-practice is not in place yet.

The SPH discretization relies on a kernel interpolation that requires full support to obtain an accurate approximation of the field quantities and derivatives. As an example, think of an uniform particle distribution within a wall-bounded box where the density of a particle close to the boundary is estimated using the density summation in eq. (2.11). Although particles are uniformly covering the fluid region, the density close to the walls drops and gives an unreasonable pressure field, as the support extends beyond the wall boundary.

Current wall-boundary treatments in SPH can be split into two fundamentally different concepts. Using particles within the wall to mimic a continuous particle distribution ensures full support of the summations in the fluid. However, additional interpolations are necessary. To accurately impose no-slip conditions on a wall, for example, the velocity field needs to be extrapolated beyond the wall boundary. The second concept accounts for the missing support of the kernel by estimating the non-vanishing surface-integral in the gradient approximation close to the boundary. Another variant is to add artificial repulsive forces that ensure the non-permeability of solid walls.

Various methods have been proposed following the first concept with different approaches to define the location of wall boundary particles. Libersky et al. [73] have used *ghost particles* to fill the boundary by simply mirroring real particles adjacent to the wall surface. Manipulating the velocities of the ghosts allows to mimic no-slip walls, free-slip walls and symmetry boundary conditions within the same framework. The two main drawbacks of this method are a) the need of recreation of ghost particles at every timestep and b) direct mirroring works only for simple (straight) wall geometries. The latter argument is significant since the method cannot be applied to arbitrarily complex geometries that occur in industrial applications. A more advanced wall-boundary model was proposed by Morris et al. [90] who used fixed wall particles and applied them also to curved surfaces. These wall particles are treated as real particles, i.e. their fluid quantities are evolved in time and they ensure full support for the particles in the fluid phase. The problem with this method is the velocity estimation for the wall particles. Although giving an accurate discretization of a no-slip condition, the velocity in the walls is calculated using a closed functional form of the exact geometry. Hence, this method can be used for geometries that can be represented by combination of a few generic forms (square, circle, sphere, ...) but again lacks generality. As a remedy, Colagrossi [32] uses a pointwise mirroring at the local tangent of the boundary for arbitrarily shaped walls to find the wall boundary particles. Here, the ghost particles need to be recreated every timestep. For complex geometries special care must be taken to maintain a uniform mass distribution of the ghost particles and to eliminate intersections at sharp corners. Hieber and Koumoutsakos [55] proposed another wall model based on the immersed-boundary method, but this method is currently limited to

remeshed smoothed particle hydrodynamics and therefore not considered here. To ensure full support close to the walls, in all previously presented methods the boundaries need to be discretized with several layers of particles. Thus, very complex geometries with small-scale features determine the necessary particle spacing to accurately represent the shape.

For the second concept of wall models the surface is discretized with only a single layer of particles that simplifies the handling of complex geometries. These methods differ mainly by the way the incomplete interpolation is corrected. DeLeffe et al. [38] propose a normal-flux method where the non-vanishing surface integral in the SPH summation close to a wall is considered. Testcases with straight walls show promising results but the application to complex geometries is not presented and seems rather difficult. A different approach to account for the presence of walls with non-full support is given by Ferrand et al. [45, 46]. Here, the smoothing and gradient calculation are renormalized to compensate for the missing particles in the wall. This renormalization introduces a new quantity that has to be evolved in time for every wall-near particle, thus requires additional computational effort. A very simple but still effective technique based on repulsive boundary particles is presented by Monaghan and Kajtar [87]. By the use of a Lennard-Jones-like potential, boundary particles cause an additional repulsion force to the momentum balance of a fluid particle to prevent penetration of the wall. Varying the magnitude of this force changes the repulsion between fluid and boundary particles and gives different inter-particle distances for different flow configurations. Hence, this model needs case-specific calibration and cannot be used as general black-box type model. Nevertheless, its simplicity and qualitatively correct behaviour are impressive.

The presented overview is not exhaustive and combinations or enhanced modifications are available. However, other approaches can be traced back to these concepts. Given the limitations of the available wall boundary methods a new generalized model has been proposed and is summarized here. Further details can be found in the paper attached in the appendix A.1.

S. Adami, X.Y. Hu and N.A. Adams (2012)
A Generalized Wall Boundary Condition for Smoothed Particle Hydrodynamics
J. Comput. Phys. **231**(21):7057-7075. [13]

In this paper a wall boundary condition for SPH is presented with emphasis on generality. Focusing on wall modeling, a standard weakly-compressible SPH model [84] is used for the fluid phase. To allow for free-surface simulations the density is evolved with the continuity equation and an artificial viscosity is used to stabilize the simulations. This artificial viscosity also takes effect as a real viscosity when its magnitude is properly calibrated [84]. The particles are evolved in time using a velocity-Verlet scheme [122] that is second-order accurate and reversible in time for inviscid flows. Solid walls are discretized with Cartesian particles of a separate phase to ensure full support for adjacent fluid particles. This simple procedure allows for discretizing complex geometries with particles without user interaction and without special treatments that are necessary for classical grid generators.

At the wall boundary free-slip or no-slip conditions for the velocity can be imposed. Free slip is realized by simply omitting the viscous interaction of fluid particles with wall boundary particles. For the no-slip condition the velocity of wall particles is extrapolated from the neighboring fluid particles and further modified to result in the correct shear force at the wall. The wall impermeability is implicitly enforced for both cases as approaching particles are compressed and the resulting increase in pressure force prevents penetration. To obtain quantitatively correct results it is important to accurately approximate the pressure gradient at the boundary. The pressure at wall boundary particles is extrapolated from neighboring fluid particles taking into account the acceleration of the wall and body force effects. Then, after rearranging the pressure equation-of-state the density of a wall particle is calculated with the extrapolated pressure. Together with the velocity, pressure and density approximation the walls contribute to the fluid phase as dummy particles of the same phase and ensure full support. The additional summation of particle interactions to calculate the wall quantities can be limited to pre-sorted interface particles only, thus the computational overhead is insignificant.

The wall boundary method is validated for two- and three-dimensional problems including channel flows and free-surface flows. Comparisons with analytical solutions and reference solutions from literature show that the proposed method can be applied to a broad range of problems without additional treatment. The flow examples over a backward-facing step or through a periodic lattice of cylinders show that the shear stress at the wall is accurately calculated and the correct velocity profiles are predicted. Hydrostatic tank simulations including complex wall geometries and multiple fluid phases demonstrate the correct imposition of the von-Neumann-boundary condition for the pressure. The last example shows the simulation of a rotating, partially-fluid filled rippled cylinder. This case includes complex moving boundaries with moving free-surfaces and illustrates the robustness and generality of this method.

My contribution to this work was the development of the method and the implementation in the in-house SPH code. I tested and validated the software, performed the numerical simulations and wrote the manuscript for the publication.

3.2. ACCURACY AND STABILITY

Since its first publication on astrophysical simulations [76, 49] SPH has been successfully applied to a broad range of fluid- and solid-mechanics-problems. Nevertheless, still today the method cannot be used as a blackbox simulation tool as numerical parameters need to be chosen carefully to allow for stable simulations. In addition, many correction or stabilization schemes violate the conservation properties, and the accuracy of the results can be unsatisfactory.

It is important to note that modifications of the method itself often result in counter-intuitive effects, especially compared to classical CFD experience. Although the continuous interpolation formulation is second-order accurate, in practice SPH results show grid-convergence rates less than second order. The reason is the strong dependency on the particle configuration, i.e. for non-homogeneous particle distributions the discrete field or gradient approximation is poor. Clearly, increasing the accuracy of the interpolation would be a straightforward advancement as presented e.g. by Chen et al. [30]. Based on a Taylor-series expansion, they expressed zero-, first- and second-order derivatives using higher order terms to end up with a more accurate SPH scheme. Not surprisingly, simple validation tests of heat conduction on static particles showed improved results as temperature gradients are calculated more accurately. However, besides the higher computational cost (in general, the method requires inversion of a matrix for each particle) the method is no longer conservative. Additionally, using higher-order derivative discretizations does not necessarily improve SPH results. Price [99] gives a clear explanation with examples on this aspect. The relevant message is that conservation is most important and numerical errors in SPH rearrange particles to regularize their distribution. Then, as a consequence and not by an enhanced method formulation, the gradient approximation becomes more accurate while conserving the total energy.

To simulate incompressible fluid dynamics with SPH there are two concepts available. Solving the truly incompressible Navier-Stokes equations with a zero-divergence constraint on the velocity leads to the ISPH method. Contrarily, allowing small density variations, in weakly-compressible SPH (WCSPH) the fluid is weakly-compressible and density and pressure are related with an equation-of-state. Choosing a proper sound-speed scale limits the density variations to an admissible threshold and the flow is quasi-incompressible. As many publications show, ISPH gives accurate results for free-surface and multi-phase flows [62, 33, 131, 70, 133]. However, solving the pressure Poisson equation is non-trivial for moving particles and special treatment for boundary-conditions is necessary. For reasons of simplicity and generality (in case of free-surfaces ISPH requires an interface reconstruction/detection), the focus here is on WCSPH.

Regardless of the quality of the results obtained with SPH, a significant challenge is the stability of simulations itself. When the particle motion is erroneous, often the problem is not an inaccurate result but an instability of the simulation. The classical instability is the so-called tensile instability [114]. Here, attractive forces e.g. due to negative pressures cause particles to lump. With decreasing distance between two particles

this attractive force further increases and triggers a numerical instability. Monaghan addressed this problem already in 1989 [82] and proposed to use a modified advection velocity for the particle movement. In this case, the advection velocity is a combination of the local momentum velocity and the smoothed velocity field using neighboring particles. As this blending is arbitrary, Monaghan himself called the correction *XSPH* denoting the unknown parameter. Effectively, XSPH smoothes the flow field and in turn particles move more regularly to avoid strongly disturbed configurations where negative pressures can occur. Alternatively and in practice additionally used, an artificial viscous term is added to the momentum equation to stop particles from approaching each other when they are very close [84]. For a given kernel this artificial viscosity can be translated into an effective physical viscosity [84] and is used to simulate viscous flows [31, 87, 95, 78, 32]. For high Reynolds number flows the necessary artificial viscosity to stabilize the simulations can exceed the physical viscosity and can strongly affect the results. In addition, state-of-the-art SPH codes also use Shepard filters and density re-initializations to smooth pressure oscillations and to stabilize the simulations.

SPH can be applied to many complex problems if the numerical parameters are chosen properly and all available corrections are used. However, quantitative results have to be cross-validated carefully. In this work, a fundamentally different approach is presented to overcome the stability problems of WCSPH and to allow non-experienced users to use SPH as a simulation tool for general purposes. Currently limited to internal flows, in the following publication a transport-velocity formulation is presented that is successfully applied to a broad range of challenging problems without difficulties and allows for simulating flows such as the lid-driven cavity at $Re = 10000$ that previously have been out of reach for SPH.

S. Adami, X.Y. Hu and N.A. Adams (2013)
A transport-velocity formulation for Smoothed Particle Hydrodynamics
J. Comput. Phys. **241**:292-307. [17]

In this paper, a new advection scheme for WCSPH is presented that allows for simulating high Reynolds number flows. Although the necessary modifications to the standard method are marginal, the resulting scheme is far more stable and accurate.

The improvement originates from the background-pressure dilemma of the WCSPH scheme. It is well-known that SPH suffers from the tensile-instability [114], and usually adjusting the equation-of-state to avoid negative pressures is sufficient to resolve it [63, 78]. On the other hand, the 0th-order consistency of SPH gives spurious pressure gradients for a formally constant field. Contrary to the theory of incompressible flow, a constant background-pressure affects the result and introduces additional numerical dissipation. In this work both effects are combined, i.e. the background-pressure effect regularizes the particle motion while artificial dissipation of momentum is decreased.

Similarly to XSPH, a modified advection velocity is introduced that leads to an additional stress term in the momentum balance equation. The method is still exactly conservative as the gradient of this stress term can be discretized in anti-symmetric form. The very simple but essential step now is to separate the constant background-pressure level from the EOS. For the momentum equation the classical relation without adding a constant pressure is used, i.e. for a particle at reference density the pressure is zero. To move the particles the momentum velocity is then corrected by the effect of the numerically non-vanishing gradient due to the constant background pressure.

The proposed method first is validated for classical low Reynolds number flows such as the flow around a periodic lattice of cylinders [90] or the two-dimensional Taylor-Green vortex. Comparisons with analytical solutions and reference results show excellent agreement for the new formulation. Secondly, the lid-driven cavity problem is simulated for Reynolds numbers up to $Re = 10000$ and velocity profiles along the horizontal and vertical centreline are compared to highly-resolved multi-grid finite-difference scheme results [48]. Surprisingly, at intermediate Reynolds numbers ($Re = 100,\ 1000$) the SPH results converge to the reference solution already at lower resolutions. Good agreement is found even for the large Reynolds number of $Re = 10000$. Note, to the best knowledge of the authors this is the first time that SPH can be used to simulate a wall-bounded flow at such a small physical viscosity. Finally, a Rayleigh-Taylor instability is simulated for both two and three dimensions. This example shows the capability to simulate multi-phase problems with the new method as well.

The transport-velocity formulation allows to simulate internal flows at high Reynolds numbers at high accuracy and stability. Most importantly, the numerical setup for all presented cases was identical. Thus, the new method is much more suitable for general purposes as the quality of results does not depend on numerical parameter adjustment of an experienced user.

My contribution to this work was the development of the method and the implementation in the in-house SPH code. I tested and validated the software, performed the numerical simulations and wrote the manuscript for the publication.

3.3. SURFACE-TENSION MODELING

Surface-tension modeling is challenging for numerical methods since the presence of an interface singularity can cause jumps in the field quantities, e.g. the pressure drop across an interface, and the evolution of the interface has to be tracked. The particle-particle interaction concept of SPH offers an implicit representation of interfaces since neighboring particles of different types indicate the presence of an interface and special forces/models can be applied locally. Over the last decade several surface tension models have been proposed for SPH that can be divided into two different concepts.

In the first group, microscopic inter-particle forces are considered that eventually take effect as a physical surface tension model. The difficulty for these models is the relation between the inter-particle forces and the resulting surface tension. So far there exists no closed formulation that relates both quantities and calibration of parameters is necessary.

From a macroscopic point of view the surface tension effect can be modeled as stress boundary condition that results in a singular force at the interface. This force is smoothed and reformulated to contribute to the volumetric momentum balance equation. While this approach recovers the prescribed surface tension, knowledge of the shape of the interface is necessary that requires detection or reconstruction methods.

Nugent and Posch [92] modeled a van der Waals fluid in two dimensions using basically standard SPH with a special equation-of-state for the pressure of particles. The resulting long-range attractive forces qualitatively give the same effect as surface tension. In the bulk of a fluid these forces cancel each other and only in the vicinity of a free surface the residue due to the missing full support gives an effective surface tension force. This model can be used to simulate a fluid phase surrounded by its vapour phase, i.e. a single phase with free surface produces stable drops. Note, a very similar modification of the equation-of-state is used by Colagrossi and Landrini [32] to prevent particle penetration at interfaces of multi-phase problems, the auxiliary effect is essentially an artificial surface tension. Nugent and Posch showed that the Laplace law for drops and the free oscillation of drops can be well reproduced. However, to supress numerical instabilities the range of the cohesive forces needs to be increased, thus the computational cost increases considerably. A very similar model was proposed by Tartakovsky and Meakin [115], but the interaction range of the proposed microscopic forces was explicitly designed not to exceed the underlying SPH smoothing range. Interestingly, they state that "*the exact form of the particle-particle interactions is not critical to the success of the simulations, but the interactions should be repulsive at short distances and attractive at large distances*" [115]. The calibrated model can be used to simulate the free oscillation of drops and even fluid-solid interactions that produce contact angles are recovered. Recently, Kordilla et al. [65] used this method to simulate three-dimensional droplet and film flow on smooth and rough fracture surfaces. This group of models is very attractive in terms of numerical simplicity since it only introduces an additional inter-particle force term without the need for detecting or reconstructing the shape of an interface and holds both for free-surface and multi-fluid situations. The main drawback is the lacking closed formulation for the

surface tension, i.e. numerical parameters need to be calibrated since the effective surface tension is not known beforehand.

Contrarily, macroscopic surface tension methods are based on an explicit interface representation and modify the momentum of particles in the vicinity of an interface. The basis for this group of methods goes back to Brackbill [29], who presented a volume reformulation of surface tension. In the so-called Continuum Surface Force (CSF) method the surface tension force is proportional to the curvature of the interface multiplied with the surface-tension coefficient. Then, using a surface-delta function the force is smoothed across the interface. This approach requires calculation of the normals and the curvature of the interface, which can be numerically difficult. The first implementation of the CSF method using SPH was proposed by Morris [89]. A color-function $0 \leq c \leq 1$ is introduced to define the two pure phases $c = 0$ and $c = 1$ with a smooth transition across the interface. The gradient of this color-function is aligned with the interface's normal direction and can thus be used to calculate the curvature of the interface. The magnitude of this gradient gives an approximation of the surface-delta function and is non-zero only within a narrow band region across the interface. As the color-function itself is smoothed across the interface, the color-gradient is non-zero within a band region of twice the cutoff range. Morris shows that this model accurately predicts the Laplace law and droplet oscillation, but to stabilize the simulations additional smoothing procedures are required. The problem occurs at the fringes of the interface band where the surface-delta function approaches zero. Here, the normalization of the gradient vectors is erroneous and the curvature calculation needs corrections. Still based on the CSF method, Zhang et al. [135] presented a surface-tension model for SPH where the interface is reconstructed. Therefore interface or boundary particles (in case of a free-surface) need to be detected and an interface curve is reconstructed from these particles using Lagrangian interpolation polynomials. Subsequently, the curvature and normal direction are calculated from the reconstructed curve and the resulting surface-tension force is added to the single layer of detected interface particles. The presented results of pressure drops, oscillations and drop collisions both in two and three dimensions illustrate the functionality of this method, but especially for three-dimensional problems the reconstruction is elaborate. Circumventing the curvature calculation, Hu and Adams [59] propose a multi-phase SPH method with surface tension effects based on the Continuum Surface Stress (CSS) method. This approach goes back to Lafaurie [67], who showed that surface tension can be formulated as gradient of a stress tensor depending on the surface-delta function, the interface normal direction and the surface-tension coefficient only. Furthermore, Hu and Adams introduce a sharp color function that can be easily tracked by tagging particles of different phases with constant integer identifiers. Consequently, the numerical width of the interface singularity is reduced. Using the stress-term formulation the particle interaction forces are pairwise anti-symmetric, thus the momentum is exactly conserved with this method. Here, the limitations are on one hand that drops with a free-surface cannot be handled directly and on the other hand that high density ratios give a strong numerical time-step limitation with an increase in computing time.

In literature, several other works on surface tension modeling with SPH exist, e.g. [51, 36, 69]. Here, the overview is intended to sketch the two main concepts of micro-

scopic and macroscopic models and their respective fundamental works are referred to in more detail. Modifications to the existing models do not present a significantly new modeling attempt so far but enhance the capabilities, accuracy or applicability of the model. The subsequently proposed surface-tension model is such a development based on the CSF method, where a new curvature approximation is presented and the difficulty for multi-phase problems with high density ratios is addressed.

S. ADAMI, X.Y. HU AND N.A. ADAMS (2010)
A new surface-tension formulation for multi-phase SPH using a reproducing divergence approximation
J. Comput. Phys. **229**(13):5011-5021. [9]

In the model of Morris [89] and Hu and Adams [59] the interface is represented with a symmetric surface-delta function. Consequently, the surface-tension force in both phases at an interface has the same magnitude. For strongly differing densities this induces much larger accelerations in the light phase that conversely restricts the numerical time-step based on the stability criterion.

The idea of this improvement is to partition the surface-tension force according to the density ratio to come up with accelerations in both phases of equal magnitude. Additionally, combining the sharp color-function as used in [59] with the CSF model [89] gives a surface-tension force with reduced interface thickness.

The color-function c has a unit jump at an interface. Using the standard SPH interpolation to approximate the color-gradient gives a delta-function-like distribution that is symmetric at the interface. This gradient estimation is modified using a density-weighted inter-particle average of c that takes into account the physical aspect that heavy liquid particles are much more prominent at an interface compared to an adjacent light phase, e.g. water and air. As the magnitude of the color-gradient approximates the surface-delta function, this ratio is reflected in the surface-tension force and the induced accelerations. Since the color-gradient is non-zero only within a band region with a width of the cutoff radius the curvature calculation using standard SPH approximations is erroneous. Therefore a new interpolation for the divergence of a vector is presented that does not require full support and is still exactly reproducing a linear field.

For a given surface-tension coefficient, the time-step criterion based on surface-tension can now be relaxed and depends only on the reference density (heavier phase) rather than taking the minimum for both phases. For an air-water problem this implies an increase in numerical time-step about 30 times compared to the formulation of Hu and Adams [59].

The proposed method is tested and validated with classical multi-phase test problems. The Laplace-law is recovered accurately for both drops (heavy drop in light ambient fluid) and bubbles (light bubble in heavy fluid) even for the physical water-air ratio. Although the surface-tension force in the CSF method acts like a body force, parasitic currents at the interface are of negligible magnitude. Further validations of free droplet oscillations show excellent agreement with analytical results and two-dimensional drop deformation simulations agree very well with previously published data and small-deformation theory predictions [117]. Finally, a drop deformation simulation in 3D is presented where the droplet is exposed to a strong shear and eventually breaks up.

My contribution to this work was the development of the method and the implementation in the in-house SPH code. I tested and validated the software, performed the numerical simulations and wrote the manuscript for the publication.

3.4. SURFACTANT DYNAMICS

Multi-phase flows can exhibit much more complex dynamics than single-phase flows and are of great importance for many industrial problems. Besides the possibility of discontinuous fluid properties, as e.g. for density or viscosity, additional physical effects can become relevant and new phenomena might occur. The classical multi-phase effect to consider when the characteristic length-scales are small is surface tension. Interfacial stresses may dominate inertial effects and the flow dynamics can be strongly altered. In many situations the surface tension can vary along the interface due to so-called *surfactants* (surface active agents). Either intentionally added as additives or present in a real fluid as impurities, surfactants change the local surface-tension coefficient by a constitutive law. Since surface tension is proportional to the curvature of the interface and the surface-tension coefficient, the presence of surfactants can cause non-uniform normal capillary forces along an interface. Additionally, surfactant-concentration gradients along the interface induce a gradient of the surface-tension coefficient in tangential direction that results in the so-called Marangoni force. This effect also occurs when the surface-tension coefficient varies with temperature in a heated environment [109]. By their nature, surfactants adhere to an interface to form a buffer zone that reduces the surface-tension coefficient, e.g. in water-air systems these molecules are partly hydrophobic and partly hydrophilic. At the interface, surfactants may diffuse along the interface and are advected with the interfacial motion. For soluble species the concentration field in the bulk is coupled with the interface by a transport mechanism (usually adsorption and desorption). Other effects of surfactants such as surface viscosity are neglected here, for more information refer e.g. to [41].

Numerical modeling of surfactant dynamics is a challenging task. The governing transport equations for the surfactant need to be solved on the interface singularity and need to be linked to the flow solver. Most important, mass conservation of the species is crucial for accurate long-term simulations, but only very few numerical models achieve exact conservation. Whilst early works are limited to insoluble surfactants that are present only at an interface, state-of-the-art methods include the fully coupled transport mechanism allowing also for multiple species forming a reaction-diffusion system.

Boundary-integral methods solve an integral equation for the interface singularity and can thus be used to incorporate directly surfactants present at the interface [113, 97, 81, 132, 44]. Mainly studying drop deformations with surfactant effects, the boundary-integral methods consider only surface diffusion of insoluble surfactants since by the nature of the method only the interface integral equation is solved and a full coupling with the bulk phase is impossible. Front-tracking methods can solve the fully coupled flow field allowing for soluble surfactants [134, 91, 1]. These methods are being applied to rather complex two- and three-dimensional flows but the mass of surfactant is not exactly conserved. Level-set methods [129, 128] either achieve mass conservation by rescaling the global surfactant mass or are limited to insoluble species. VOF methods are successfully extended to simulate insoluble surfactant dynamics on moving interfaces [64, 102] and a fully coupled three-dimensional model is proposed by Alke and Bothe [22]. Within the VOF-framework James and Lowengrub [64] propose

to track the surfactant mass instead of solving the evolution equation for the concentration. This concept enables exact conservation of surfactant mass and is adopted by most subsequent works. The problem with VOF models is the need for reconstruction, as the interface is tracked by the volume-fraction field. Surfactant models using immersed boundaries [68] or using finite-element methods [71, 79, 44] are available as well. However, again either mass conservation is violated or the models are limited to insoluble surfactants.

The advantages and disadvantages of each surfactant model are basically inherited from the underlying interface model since the discretization for the singularity defines the properties of the scheme. The two main aspects to consider are the exact conservation of species mass and the generality of the formulation, i.e. that arbitrary interface deformation can be handled. The particular method-of-choice might depend on the problem formulation, desired accuracy and computational cost. Here, the focus is on the development of a general multi-phase method that is capable of simulating surfactant dynamics in conservative form. Already shown earlier, SPH is capable of handling multi-phase problems with surface tension effects where strong deformations and break-up of interfaces occur. This method is extended for surfactant dynamics giving a fully coupled and exactly conservative method [8]. Note that almost at the same time Bergdorf et al. [27] have proposed a reaction-diffusion model based on remeshed SPH using level-sets to define interfaces and simulated deforming surfaces.

S. Adami, X.Y. Hu and N.A. Adams (2010)
A conservative SPH method for surfactant dynamics
J. Comput. Phys. **229**(5):1909-1926. [8]

The proposed conservative SPH method for surfactant dynamics is based on the multi-phase formulation by Hu and Adams [59]. In this work surface-tension is modeled following the CSF model. The surface force is expressed as gradient of the surface stress tensor. This approach is advantageous as the full stress tensor naturally incorporates tangential stresses so that surfactant-induced Marangoni forces are considered.

The evolution of surfactant on the interface is solved for particles with non-zero surface-delta function only, thus for the insoluble case the surfactant is implicitly bounded to the interface. Following the concept of James and Lowengrub [64], an evolution equation for the surfactant mass is solved. As particles can move freely there are rare events where particles leave the interfacial region and still carry a small amount of surfactant mass. This fraction of interfacial mass is mapped back to the neighbouring interface-particles to avoid artificial transport of adsorbed species into the bulk. As the numerical interface has a finite width, non-physical surfactant concentration profiles normal to the interface can occur. As a remedy, in addition to the tangential surface diffusion an artificial normal diffusion is solved to smoothen these profiles. Validation examples have shown that this directed-diffusion approach strongly decreases spurious concentration profiles and increases the accuracy especially at lower resolutions.

To account for soluble surfactants an additional bulk diffusion equation is solved. Exchange of surfactant between the interface and the dissolved species in the bulk is modeled with a conservative mass flux term. Here, the Langmuir kinetics [28] with competing adsorption and desorption rates are considered, but any source term can be used. A special treatment of this mass flux is necessary when surfactant is soluble only within one of the phases present at the interface. In that case, the smoothed interface representation requires interpolation of the bulk concentration field to the interface particles of the insoluble phase to accurately calculate the adsorption/desorption. Details of these mapping steps are given in the full article, most importantly to note is that the method still conserves exactly the surfactant mass in the system.

The surfactant model is first validated for stationary interfaces, i.e. particle motion is supressed and advective effects are neglected. Bulk and surface diffusion are validated separately. Comparisons with the analytical solution show second order convergence for bulk diffusion and first order convergence for surface diffusion. Note, although diffusion at the interface is tested on a circular drop that is discretized with Cartesian particles, the azimuthal concentration profiles are smooth and agree very well with the analytical solution. Surfactant transport coupled with bulk diffusion is also tested first on a non-moving circular interface showing exact conservation of global surfactant. Using the new method three dynamic examples show the capability to simulate fully coupled surfactant dynamics with SPH.

My contribution to this work was the development of the method and the implementation in the in-house SPH code. I tested and validated the software, performed the numerical simulations and wrote the manuscript for the publication.

4. LIST OF PUBLICATIONS

4.1. PEER-REVIEWED JOURNAL PUBLICATIONS

- S. ADAMI, X.Y. HU AND N.A. ADAMS (2013) A transport-velocity formulation for Smoothed Particle Hydrodynamics, J. Comput. Phys. **241**:292-307. [17]

- S. ADAMI, X.Y. HU AND N.A. ADAMS (2012) A Generalized Wall Boundary Condition for Smoothed Particle Hydrodynamics, J. Comput. Phys. **231**(21):7057-7075. [13]

- S. ADAMI, X.Y. HU AND N.A. ADAMS (2010) A new surface-tension formulation for multi-phase SPH using a reproducing divergence approximation, J. Comput. Phys. **229**(13):5011-5021. [9]

- S. ADAMI, X.Y. HU AND N.A. ADAMS (2010) A conservative SPH method for surfactant dynamics, J. Comput. Phys. **229**(5):1909-1926. [8]

4.2. BOOK SECTIONS

- S. ADAMI, X.Y. HU AND N.A. ADAMS (2012) Simulating 3D turbulence with SPH, in Proceedings of the 2012 Summer Program, Center for Turbulence Research, Stanford University. [16]
- S. ADAMI, X.Y. HU, N.A. ADAMS (2012) Numerical investigation of complex multiphase flows with Lagrangian particle methods. in High Performance Computing in Science and Engineering; S. Wagner, A. Bode, H. Satzger and M. Brehm (Eds.), Verlag der Bayerischen Akademie der Wissenschaften. [15]
- S. MEISSNER, L. KNELS, T. KOCH, E. KOCH, S. ADAMI, X.Y. HU AND N.A. ADAMS (2011) Experimental and numerical investigation on the flow-induced stresses on the alveolar-epithelial-surfactant-air interface, in Notes on numerical fluid mechanics and multidisciplinary design; M. Klaas, E. Koch and W. Schröder (Eds.), Springer. ISBN 978-3-642-20325-1. [80]

4.3. CONFERENCE PROCEEDINGS

- S. ADAMI, X.Y. HU AND N.A. ADAMS (2013) A transport-velocity formulation for Smoothed Particle Hydrodynamics, 8th SPHERIC workshop, Trondheim, Norway. [18]
- S. ADAMI, X.Y. HU AND N.A. ADAMS (2013) Simulating 3D turbulence with SPH, 8th SPHERIC workshop, Trondheim, Norway. [19]
- S. ADAMI, X.Y. HU AND N.A. ADAMS (2012) Contact line hydrodynamics with SPH, 7th SPHERIC workshop, Prato, Italy. [14]
- S. ADAMI, X.Y. HU, N.A. ADAMS, E.M. RYAN AND A.M. TARTAKOVSKY (2011) A fully coupled 3D transport model in SPH for multi-species reaction-diffusion systems, 6th SPHERIC workshop, Hamburg, Germany. [12]
- S. ADAMI, X.Y. HU AND N.A. ADAMS (2010) Tipstreaming of a drop in simple shear flow in the presence of surfactant, Gallery of Fluid Motion, 63rd Annual Meeting of the American Physical Society, Division of Fluid Dynamics, Long Beach, California, USA. [11]
- S. ADAMI, X.Y. HU AND N.A. ADAMS (2010) 3D drop deformation and breakup in simple shear flow considering the effect of insoluble surfactant, Euromech Fluid Mechanics Conference - 8, Bad Reichenhall, Germany. [6]
- S. ADAMI, X.Y. HU AND N.A. ADAMS (2010), A soft-tissue model coupled with fluid dynamics using SPH, 5th SPHERIC workshop, Manchester, UK. [10]
- S. ADAMI, X.Y. HU AND N.A. ADAMS (2010) 3D drop deformation and breakup in simple shear flow considering the effect of insoluble surfactant, 5th SPHERIC workshop, Manchester, UK. [7]

- S. ADAMI, X.Y. HU AND N.A. ADAMS (2009), Surfactant dynamics with SPH, 1st International Conference on Mathematical and Computational Biomedical Engineering, Swansea, UK. [5]
- X.Y. HU, S. ADAMI AND N.A. ADAMS (2009) Formulating surface tension with reproducing divergence approximation for multi-phase SPH, 4th SPHERIC workshop, Nantes, France [57]
- S. ADAMI, X.Y. HU AND N.A. ADAMS (2009) A conservative SPH method for interfacial flows with surfactant dynamics, 4th SPHERIC workshop, Nantes, France. [4]
- S. ADAMI, X.Y. HU AND N.A. ADAMS (2008) Simulations of multiphase phenomena using Smoothed Particle Hydrodynamics (SPH), Workshop on Turbulence and Hydrodynamical Instabilites, Excellence Cluster Universe, Garching. [3]
- S. ADAMI, X.Y. HU AND N.A. ADAMS (2008) Simulating dynamic surface tension of lung surfactant using SPH, Symposium on Protective Artificial Respiration, Aachen, Germany. [2]
- S. ADAMI, I. MAHLE, X.Y. HU, N.A. ADAMS AND M. WENDEL (2008) Simulating dynamic surface tension of lung surfactant using SPH, 3rd SPHERIC workshop, Lausanne, Switzerland. [21]
- X.Y. HU, S. ADAMI, I. MAHLE AND N.A. ADAMS (2008) Numerical modeling of the dynamic behavior of lung surfactant using smoothed particle dynamics, Workshop on Protective Artificial Respiration, Aachen, November 15, 2007 and World Congress of Computational Mechanics, Venice, Italy. [58]
- S. ADAMI AND H.J. KALTENBACH (2008) Sensitivity of the wave-steepening in railway tunnels with respect to the friction model, BBAA VI International Colloquium on: Bluff Bodies Aerodynamics & Applications, Milano, Italy. [20]

5. CONCLUSIONS

SPH is a Lagrangian particle method that uses moving discretization points with overlapping fluid volumes to represent a continuum. The governing equations are solved fo individual particles based on discrete particle-particle interactions. Moving these particles with the local flow, advection is exact. The absence of the convective derivative is advantageous as this term usually causes problems for grid-based methods and requires special treatments. An important field of application for SPH are multi-phase problems. Using integer identifiers, particles of different phases can be easily tracked and interfaces are captured implicitly without any additional detection scheme (front-capturing, -tracking or -reconstruction). Also, most problems can be formulated as multi-phase problem and therefore SPH offers a very general framework to handle multi-fluid- and fluid-structure-interactions. Without effort, the constitutive law to calculate the stress tensor can be adjusted to switch the particle behaviour from a fluid to an elastic solid. In spite of the huge potentials of SPH the general acceptance in the CFD community is for a number of reasons still poor and industrial applications are rare. Certainly, the considerable higher computational cost of SPH compared to grid-based solvers is an issue. Also, artificial numerical dissipation is necessary in many cases and often the available numerical models are tuned for a specific problem rather than a generalized formulation.

In this work, both improvements of existing models for stable multi-phase simulations and a new conservative surfactant model extending the capabilities of SPH are pre-

sented. The proposed modified advection scheme allows for simulating internal flows at large Reynolds numbers without any additional smoothing scheme or artificial viscosity. Besides excellent accuracy, this approach impresses by its simplicity as no numerical parameter had to be tuned for the broad range of considered validation examples.

Wall-boundary treatment in SPH is not a new topic. However, currently many models require exact knowledge of the solid wall interface in a closed form or use linear segments to construct the surface. For arbitrarily complex shapes this can be expensive or impossible. Here, a generalized method to impose wall-boundary conditions is presented that uses Cartesian particles to discretize a wall. Fluid properties as well as the flow field are extrapolated to these wall particles and free-slip or no-slip conditions can be imposed. The idea of this approach is to ensure full kernel support for fluid particles close to a wall, i.e. the only limitation for an accurate wall discretization is the minimal wall thickness $h_{min} = r_c$.

Furthermore, a modified surface-tension model based on the CSF model of Brackbill [29] is presented. A very similar SPH method was already proposed earlier, but here the efficiency for multi-phase problems with high density-ratios is strongly improved. Additionally, the width of the delta-function approximation for the interface singularity is reduced and a new, more accurate curvature calculation is presented.

The surfactant model for SPH is a new development and demonstrates the capabilities of the Lagrangian framework. Important for accurate long-time simulations, the species mass is exactly conserved with this method for both interfacial and bulk surfactant. Using an equation-of-state to relate the surfactant concentration at the interface to the local surface-tension coefficient, the fluid dynamics and surfactant dynamics are fully coupled. The transport model for exchange of surfactant between the interface and the bulk phase currently considers adsorption and desorption, but other relations can be easily incorporated.

Combining all models together, geometrically complex wall-bounded multi-phase flows can be simulated accounting for surface-tension effects and surfactant dynamics. The new SPH method was already successfully applied to challenging problems such as surfactant-induced tip-streaming of a drop in simple shear flow [11] or Lagrangian statistics in turbulent flows [16]. These examples demonstrate the significant progress in the state-of-the-art of SPH. The new transport-velocity formulation opens up a whole new range of applications since it allows for stable simulations of high Reynolds number flows at high accuracy.

A. Appendix

In the appendix, the four major publications are attached together with the publisher agreement notification to reuse the material for this cumulative thesis.

A.1. A GENERALIZED WALL BOUNDARY CONDITION FOR SMOOTHED PARTICLE HYDRODYNAMICS

Rightslink Printable License https://s100.copyright.com/App/PrintableLicenseFrame.jsp?publisherI...

ELSEVIER LICENSE
TERMS AND CONDITIONS

Feb 04, 2013

This is a License Agreement between Stefan Adami ("You") and Elsevier ("Elsevier") provided by Copyright Clearance Center ("CCC"). The license consists of your order details, the terms and conditions provided by Elsevier, and the payment terms and conditions.

All payments must be made in full to CCC. For payment instructions, please see information listed at the bottom of this form.

Supplier	Elsevier Limited The Boulevard,Langford Lane Kidlington,Oxford,OX5 1GB,UK
Registered Company Number	1982084
Customer name	Stefan Adami
Customer address	Technische Universität München Garching, 85748
License number	3081820343439
License date	Feb 04, 2013
Licensed content publisher	Elsevier
Licensed content publication	Journal of Computational Physics
Licensed content title	A generalized wall boundary condition for smoothed particle hydrodynamics
Licensed content author	S. Adami,X.Y. Hu,N.A. Adams
Licensed content date	30 August 2012
Licensed content volume number	231
Licensed content issue number	21
Number of pages	19
Start Page	7057
End Page	7075
Type of Use	reuse in a thesis/dissertation
Intended publisher of new work	other
Portion	full article
Format	both print and electronic
Are you the author of this Elsevier article?	Yes
Will you be translating?	No
Order reference number	
Title of your thesis/dissertation	Modeling and Simulation of Multiphase Phenomena with SPH
Expected completion date	Apr 2013
Estimated size (number of pages)	120

1 von 5 04.02.2013 10:32

Elsevier VAT number	GB 494 6272 12
Permissions price	0.00 EUR
VAT/Local Sales Tax	0.0 USD / 0.0 GBP
Total	0.00 EUR
Terms and Conditions	

INTRODUCTION

1. The publisher for this copyrighted material is Elsevier. By clicking "accept" in connection with completing this licensing transaction, you agree that the following terms and conditions apply to this transaction (along with the Billing and Payment terms and conditions established by Copyright Clearance Center, Inc. ("CCC"), at the time that you opened your Rightslink account and that are available at any time at http://myaccount.copyright.com).

GENERAL TERMS

2. Elsevier hereby grants you permission to reproduce the aforementioned material subject to the terms and conditions indicated.

3. Acknowledgement: If any part of the material to be used (for example, figures) has appeared in our publication with credit or acknowledgement to another source, permission must also be sought from that source. If such permission is not obtained then that material may not be included in your publication/copies. Suitable acknowledgement to the source must be made, either as a footnote or in a reference list at the end of your publication, as follows:

"Reprinted from Publication title, Vol /edition number, Author(s), Title of article / title of chapter, Pages No., Copyright (Year), with permission from Elsevier [OR APPLICABLE SOCIETY COPYRIGHT OWNER]." Also Lancet special credit - "Reprinted from The Lancet, Vol. number, Author(s), Title of article, Pages No., Copyright (Year), with permission from Elsevier."

4. Reproduction of this material is confined to the purpose and/or media for which permission is hereby given.

5. Altering/Modifying Material: Not Permitted. However figures and illustrations may be altered/adapted minimally to serve your work. Any other abbreviations, additions, deletions and/or any other alterations shall be made only with prior written authorization of Elsevier Ltd. (Please contact Elsevier at permissions@elsevier.com)

6. If the permission fee for the requested use of our material is waived in this instance, please be advised that your future requests for Elsevier materials may attract a fee.

7. Reservation of Rights: Publisher reserves all rights not specifically granted in the combination of (i) the license details provided by you and accepted in the course of this licensing transaction, (ii) these terms and conditions and (iii) CCC's Billing and Payment terms and conditions.

8. License Contingent Upon Payment: While you may exercise the rights licensed immediately upon issuance of the license at the end of the licensing process for the transaction, provided that you have disclosed complete and accurate details of your proposed use, no license is finally effective unless and until full payment is received from you (either by publisher or by CCC) as provided in CCC's Billing and Payment terms and conditions. If full payment is not received on a timely basis, then any license preliminarily

granted shall be deemed automatically revoked and shall be void as if never granted. Further, in the event that you breach any of these terms and conditions or any of CCC's Billing and Payment terms and conditions, the license is automatically revoked and shall be void as if never granted. Use of materials as described in a revoked license, as well as any use of the materials beyond the scope of an unrevoked license, may constitute copyright infringement and publisher reserves the right to take any and all action to protect its copyright in the materials.

9. Warranties: Publisher makes no representations or warranties with respect to the licensed material.

10. Indemnity: You hereby indemnify and agree to hold harmless publisher and CCC, and their respective officers, directors, employees and agents, from and against any and all claims arising out of your use of the licensed material other than as specifically authorized pursuant to this license.

11. No Transfer of License: This license is personal to you and may not be sublicensed, assigned, or transferred by you to any other person without publisher's written permission.

12. No Amendment Except in Writing: This license may not be amended except in a writing signed by both parties (or, in the case of publisher, by CCC on publisher's behalf).

13. Objection to Contrary Terms: Publisher hereby objects to any terms contained in any purchase order, acknowledgment, check endorsement or other writing prepared by you, which terms are inconsistent with these terms and conditions or CCC's Billing and Payment terms and conditions. These terms and conditions, together with CCC's Billing and Payment terms and conditions (which are incorporated herein), comprise the entire agreement between you and publisher (and CCC) concerning this licensing transaction. In the event of any conflict between your obligations established by these terms and conditions and those established by CCC's Billing and Payment terms and conditions, these terms and conditions shall control.

14. Revocation: Elsevier or Copyright Clearance Center may deny the permissions described in this License at their sole discretion, for any reason or no reason, with a full refund payable to you. Notice of such denial will be made using the contact information provided by you. Failure to receive such notice will not alter or invalidate the denial. In no event will Elsevier or Copyright Clearance Center be responsible or liable for any costs, expenses or damage incurred by you as a result of a denial of your permission request, other than a refund of the amount(s) paid by you to Elsevier and/or Copyright Clearance Center for denied permissions.

LIMITED LICENSE

The following terms and conditions apply only to specific license types:

15. **Translation**: This permission is granted for non-exclusive world **English** rights only unless your license was granted for translation rights. If you licensed translation rights you may only translate this content into the languages you requested. A professional translator must perform all translations and reproduce the content word for word preserving the integrity of the article. If this license is to re-use 1 or 2 figures then permission is granted for non-exclusive world rights in all languages.

16. **Website**: The following terms and conditions apply to electronic reserve and author websites:
Electronic reserve: If licensed material is to be posted to website, the web site is to be

password-protected and made available only to bona fide students registered on a relevant course if:
This license was made in connection with a course,
This permission is granted for 1 year only. You may obtain a license for future website posting,
All content posted to the web site must maintain the copyright information line on the bottom of each image,
A hyper-text must be included to the Homepage of the journal from which you are licensing at http://www.sciencedirect.com/science/journal/xxxxx or the Elsevier homepage for books at http://www.elsevier.com , and
Central Storage: This license does not include permission for a scanned version of the material to be stored in a central repository such as that provided by Heron/XanEdu.

17. **Author website** for journals with the following additional clauses:

All content posted to the web site must maintain the copyright information line on the bottom of each image, and the permission granted is limited to the personal version of your paper. You are not allowed to download and post the published electronic version of your article (whether PDF or HTML, proof or final version), nor may you scan the printed edition to create an electronic version. A hyper-text must be included to the Homepage of the journal from which you are licensing at http://www.sciencedirect.com/science/journal/xxxxx . As part of our normal production process, you will receive an e-mail notice when your article appears on Elsevier's online service ScienceDirect (www.sciencedirect.com). That e-mail will include the article's Digital Object Identifier (DOI). This number provides the electronic link to the published article and should be included in the posting of your personal version. We ask that you wait until you receive this e-mail and have the DOI to do any posting.

Central Storage: This license does not include permission for a scanned version of the material to be stored in a central repository such as that provided by Heron/XanEdu.

18. **Author website** for books with the following additional clauses:
Authors are permitted to place a brief summary of their work online only.
A hyper-text must be included to the Elsevier homepage at http://www.elsevier.com . All content posted to the web site must maintain the copyright information line on the bottom of each image. You are not allowed to download and post the published electronic version of your chapter, nor may you scan the printed edition to create an electronic version.

Central Storage: This license does not include permission for a scanned version of the material to be stored in a central repository such as that provided by Heron/XanEdu.

19. **Website** (regular and for author): A hyper-text must be included to the Homepage of the journal from which you are licensing at http://www.sciencedirect.com/science/journal/xxxxx. or for books to the Elsevier homepage at http://www.elsevier.com

20. **Thesis/Dissertation**: If your license is for use in a thesis/dissertation your thesis may be submitted to your institution in either print or electronic form. Should your thesis be published commercially, please reapply for permission. These requirements include permission for the Library and Archives of Canada to supply single copies, on demand, of the complete thesis and include permission for UMI to supply single copies, on demand, of the complete thesis. Should your thesis be published commercially, please reapply for permission.

21. **Other Conditions**:

v1.6

If you would like to pay for this license now, please remit this license along with your payment made payable to "COPYRIGHT CLEARANCE CENTER" otherwise you will be invoiced within 48 hours of the license date. Payment should be in the form of a check or money order referencing your account number and this invoice number RLNK500949016.
Once you receive your invoice for this order, you may pay your invoice by credit card. Please follow instructions provided at that time.

Make Payment To:
Copyright Clearance Center
Dept 001
P.O. Box 843006
Boston, MA 02284-3006

For suggestions or comments regarding this order, contact RightsLink Customer Support: customercare@copyright.com or +1-877-622-5543 (toll free in the US) or +1-978-646-2777.

Gratis licenses (referencing $0 in the Total field) are free. Please retain this printable license for your reference. No payment is required.

Author's personal copy

Journal of Computational Physics 231 (2012) 7057–7075

Contents lists available at SciVerse ScienceDirect

Journal of Computational Physics

journal homepage: www.elsevier.com/locate/jcp

A generalized wall boundary condition for smoothed particle hydrodynamics

S. Adami *, X.Y. Hu, N.A. Adams

Institute of Aerodynamics, Technische Universität München, 85748 Garching, Germany

ARTICLE INFO

Article history:
Received 31 May 2011
Received in revised form 13 March 2012
Accepted 5 May 2012
Available online 15 July 2012

Keywords:
Boundary condition
SPH
Solid walls

ABSTRACT

In this paper we present a new formulation of the boundary condition at static and moving solid walls in SPH simulations. Our general approach is both applicable to two and three dimensions and is very simple compared to previous wall boundary formulations. Based on a local force balance between wall and fluid particles we apply a pressure boundary condition on the solid particles to prevent wall penetration. This method can handle sharp corners and complex geometries as is demonstrated with several examples. A validation shows that we recover hydrostatic equilibrium conditions in a static tank, and a comparison of the classical dam break simulation with state-of-the-art results in literature shows good agreement. We simulate various problems such as the flow around a cylinder and the backward facing step at $Re = 100$ to demonstrate the general applicability of this new method.

© 2012 Published by Elsevier Inc.

1. Introduction

Gingold and Monaghan [1] and Lucy [2] presented in 1977, independently from each other, a gridless numerical method to simulate astrophysical problems such as e.g. the fission of a rapidly rotating star. Fundamentally different from gridbased methods, the so-called *smoothed particle hydrodynamics* (*SPH*) uses a kernel estimation at Lagrangian "grid" points (particles) to solve the governing equations of the system of interest. Moving the particles in time with a flow, pure advection is treated exactly. The rate of change of any conservative variable can be calculated from particle–particle interactions. For this reason SPH has a high potential especially for simulating multi-phase systems and can be applied to a broad variety of problems. Over the past three decades, SPH was successfully used to simulate complex problems ranging from magnetohydrodynamics [3] and solid mechanics [4–7] to fluid mechanics including free surfaces [8,9], surface tension [10,11] and transport phenomena [12,13].

Regardless of the application, boundary conditions are one of the key aspects of a numerical simulation and special attention should be paid to a correct and accurate representation of them. For the example of solid wall boundary conditions, we emphasize the particular importance of a proper formulation of boundary conditions for SPH, as this is crucial to achieve physically meaningful and quantitatively correct results. It is a misconception that SPH models of wall boundary conditions lead to correct results as long as the particle distribution is uniform and stable. Besides preventing particle penetration of the walls, a local force balance is essential to model solid boundaries accurately. We demonstrate the significance of this condition with a numerical freefall experiment in Section 7.1.

Generally, wall models for SPH simulations follow two basic concepts. One concept is to fill the walls with boundary particles to ensure that the support of the smoothing kernel near a wall is completely covered with particles. In the other

* Corresponding author.
E-mail address: stefan.adami@aer.mw.tum.de (S. Adami).

0021-9991/$ - see front matter © 2012 Published by Elsevier Inc.
http://dx.doi.org/10.1016/j.jcp.2012.05.005

Author's personal copy

concept, either the non-vanishing surface integral when smoothing the flow quantities close to the boundary is accounted for, or artificial repulsion forces are introduced to prevent that particles cross the interface.

Following the first concept [14], *ghost particles* as mirrors of real fluid particles along the surface are used to fill the solid wall domain. Depending on the velocity assigned to the ghost particle a slip or no-slip condition at the wall can be imposed. Similarly, ghost particles can be used to model symmetry and periodic boundary conditions, but in practice this method is limited to simple interfaces where fluid particles can be mirrored easily at the wall surface. Furthermore, ghost particles have to be created every timestep as mirrors of the evolving fluid particles. Without the need of recreating boundary particles, Morris et al. [15] use fixed wall particles to model curved surfaces and treat them as real particles. The density and the pressure of the boundary particles are evolved in time and they are considered in the continuity equation of the fluid phase. Consequently, the pressure field increases or decreases when particles move towards or away from the wall in order to prevent penetration. When fluid particles interact with boundary particles, the velocity of wall particles is chosen such that either a slip or no-slip condition is satisfied. The calculation of this velocity requires the knowledge of the shape of the wall surface in a closed functional form. Therefore this method cannot directly be applied for arbitrary geometries. Colagrossi [9] use a pointwise mirroring at the local tangent plane of the boundary for arbitrarily shaped walls and impose a free-slip condition at the wall. Density and pressure of these ghost particles are deduced from the fluid phase and the normal velocity component is flipped to ensure no penetration. This method also recreates ghost particles every timestep, and in case of complex geometries special care must be taken to maintain a uniform mass distribution of the ghost particles. Another boundary treatment requiring full support was proposed by Hieber and Koumoutsakos [16], who presented an immersed-boundary method in the context of remeshed smoothed particle hydrodynamics. There, a forcing term is added to the momentum equation such that effectively the no-slip condition is satisfied on a boundary.

The second concept has the advantage that only a single layer of boundary particles at the wall surface is required, i.e. complex geometries are rather easy to handle. DeLeffe et al. [17] account for the fact that the kernel support of fluid particles near walls extends beyond the wall in their so-called normal-flux method by evaluating the non-vanishing surface integral. They show that this method is suitable for testcases with straight walls but do not explain or show how it can be applied to complex geometries. Instead of calculating the surface integral close to the boundary, Ferrand et al. [18] renormalize the smoothing and gradient calculation with respect to the missing kernel support area. But as the geometrical quantities required for the renormalization are evolved in time, this method requires additional computational effort. A very simple technique based on repelling boundary particles is presented by Monaghan et al. [19]. They introduce a Lennard–Jones-like potential between fluid and wall particles to add a repulsion force normal to the boundary. When a fluid particle interacts with a wall particle, only the position of the boundary particle is used to calculate the repulsion force and all other quantities are taken from the fluid phase. But the magnitude of this force has to be calibrated in order to preserve the initial distance between fluid and wall particles on one hand and to prevent penetration on the other hand.

In this work we present a wall boundary formulation that can handle arbitrarily shaped geometries in two and three dimensions. We discretize a solid wall with *dummy* particles and do not evolve their quantities in time. Thus, our approach follows the first of the previously mentioned concepts for modeling solid wall boundaries with SPH. We use the dummy particles to ensure that the support of the kernel interpolants is fully contained within the fluid phase for density change and force calculation. The pressure at a wall particle position for the force calculation is calculated from the surrounding fluid particles with a boundary condition. Including the solid particles in the density change rate calculation ensures a pressure response when fluid particles approach a wall, i.e. the impermeability condition of solid walls is fulfilled. Our formulation is applicable for both stationary and moving walls.

We tested our method with two and threedimensional test cases and found excellent agreement with analytical results and state-of-the-art results in literature. At first, we validate our method with simple straight channel flows such as the Couette and Poiseuille flow. Then, a more complex separated flow past a backward facing step as well as a flow through a periodic lattice of cylinders is simulated, and both compare well with results available in literature. The correctness of our pressure boundary condition is proved with several hydrostatic tank simulations including complex wall geometries, multi-phase problems with different densities and a threedimensional example. A numerical freefall experiment shows the importance of the correct wall boundary formulation including the motion of the wall. We simulate the classical dambreak problem and show very good agreement with state-of-the-art results in literature. Finally, a rotating rippled cylinder simulation demonstrates the coupling of moving walls with complex geometry interacting with a free surface.

2. Governing equations

The governing equations for the motion of an isothermal fluid in a Lagrangian frame of reference are the continuity equation

$$\frac{d\rho}{dt} = -\rho \nabla \cdot \mathbf{v} \tag{1}$$

and the momentum equation

$$\rho \frac{d\mathbf{v}}{dt} = -\nabla p + \mathbf{F}^{(v)} + \rho \mathbf{g} \tag{2}$$

Author's personal copy

with $\rho, \mathbf{v}, t, p, \mathbf{F}^{(v)}$ and $\mathbf{g}$ denoting the density of a fluid, the velocity, the time, the pressure, the viscous force and a body-force, respectively.

Following the weakly-compressible approach [8,15,20] to simulate incompressible fluids with SPH, an equation of state is introduced to estimate the pressure from the density field via

$$p(\rho) = p_0\left[\left(\frac{\rho}{\rho_0}\right)^{\gamma} - 1\right] + \chi \tag{3}$$

The reference density ρ_0 is set to the initial density of the fluid phase so that the pressure field is initially equal to the background pressure χ. The stiffness of the equation of state can be adjusted with the two parameters p_0 and γ. For fluids it is common to use $\gamma = 7$, and the reference pressure is given by

$$p_0 = \frac{\rho_0 c^2}{\gamma} \tag{4}$$

The artificial sound speed c is chosen based on a scale analysis presented in Morris et al. [15] in order to limit the admissible density variation to 1%. When applied to free-surface flows, the background pressure χ in Eq. (3) is set to zero.

Assuming incompressibility of the fluid, the viscous force $\mathbf{F}^{(v)}$ simplifies to

$$\mathbf{F}^{(v)} = \eta\nabla^2\mathbf{v} \tag{5}$$

with the dynamic viscosity η.

3. Numerical method

The basic concept of SPH is to advect Lagrangian discretization points with a flow and to interpolate the quantities of these particles from its neighbors with a weighting function W. Generally, any kernel function that satisfies $\int W(\mathbf{r}, h)d\mathbf{r} = 1$ can be used, but due to numerical efficiency it is preferable to require compact support, see Monaghan [21]. Due to a compact kernel support particles which are further away from each other than the cutoff radius r_c do not interact with each other, i.e. $W(|\mathbf{r}| \geqslant r_c, h) = 0$. The relation of smoothing length h and cutoff radius r_c with $W(r_c = \kappa h) = 0$ is a measure of the smoothing property of the kernel function and the parameter κ varies with the chosen kernel function.

In this work a quintic spline kernel with a compact support of $3h$ is used, i.e. $\kappa = 3$, see Morris et al. [15]. The usage of this kernel is motivated by the work of Hongbin and Xin [22], who showed that the quintic spline or the Gaussian function are favorable for SPH simulations in terms of computational accuracy. Particles are initially placed at Cartesian grid points with a uniform distance Δx to fill the domain. Using Δx as the smoothing length h, in each coordinate direction approximately six particles are spread across the kernel. The volume of a particle V_a is given by $V_a = \Delta x^d$, where d is the number of spatial dimensions. Finally, the mass of each particle is set to $m_a = \rho_a V_a$ and is fixed during the entire simulation. Each particle is tagged with an integer flag to distinguish between fluid particles and solid particles. It is important to create three $(r_c/\Delta x)$ layers of dummy particles normal to the wall interface for representing the interface since an accurate integration of the field variables near the interface requires that the support of evolved particles is fully contained within the computational domain.

3.1. Continuity equation

The discretized form of the continuity Eq. (1) for particle a is [21]

$$\frac{d\rho_a}{dt} = \rho_a\sum_b \frac{m_b}{\rho_b}\mathbf{v}_{ab}\cdot\nabla_a W_{ab} \tag{6}$$

where m_b is the mass of particle $b, \mathbf{v}_{ab} = \mathbf{v}_a - \mathbf{v}_b$ is the relative velocity of particle a and $b, \nabla_a W_{ab} = \nabla_a W(\mathbf{r}_a - \mathbf{r}_b, h)$ is the gradient of the weight-function and the summation is performed with all neighboring particles b. Note, that in literature other discretizations of the continuity equation exist [21]. But here we use Eq. (6) since this form holds also for multi-phase problems. The summation over the neighboring particles takes only into account a volume contribution $(m_b/\rho_b = V_b)$ and therefore allows a stable simulation even when dealing with high density ratios.

3.2. Momentum equation

According to Hu and Adams [11], the acceleration of particle a due to a pressure gradient can be approximated as

$$\frac{d\mathbf{v}_a}{dt} = -\frac{1}{m_a}\sum_b \left(V_a^2 + V_b^2\right)\tilde{p}_{ab}\nabla_a W_{ab} \tag{7}$$

using the density-weighted inter-particle averaged pressure [23]

Author's personal copy

$$\tilde{p}_{ab} = \frac{\rho_b p_a + \rho_a p_b}{\rho_a + \rho_b} \tag{8}$$

and the volume of both particles V_a and V_b. This form conserves linear and angular momentum exactly as the force between particles a and b is anti-symmetric along the line of centers of the two particles.

The viscous force is derived from the inter-particle-averaged shear stress with a combined viscosity

$$\tilde{\eta}_{ab} = \frac{2\eta_a \eta_b}{\eta_a + \eta_b} \tag{9}$$

For incompressible flows, the acceleration of particle a caused by shear forces simplifies to

$$\frac{d\mathbf{v}_a}{dt} = \frac{1}{m_a} \sum_b \tilde{\eta}_{ab} \left(V_a^2 + V_b^2 \right) \frac{\mathbf{v}_{ab}}{r_{ab}} \frac{\partial W}{\partial r_{ab}} \tag{10}$$

with $\frac{\partial W}{\partial r_{ab}} = \nabla_a W(\mathbf{r}_a - \mathbf{r}_b, h) \cdot \mathbf{e}_{ab}$ and $r_{ab} = |\mathbf{r}_a - \mathbf{r}_b|$.

Monaghan and Gingold [24] added an artificial viscosity to the momentum equation to stabilize the numerical scheme. Amongst various formulations [21,3] for this dissipative term available in literature, we chose the form

$$\frac{d\mathbf{v}_a}{dt} = -\sum_b m_b \alpha h_{ab} c_{ab} \frac{(\mathbf{v}_a - \mathbf{v}_b) \cdot (\mathbf{r}_a - \mathbf{r}_b)}{\rho_{ab} (|\mathbf{r}_a - \mathbf{r}_b|^2 + \epsilon h_{ab}^2)} \nabla_a W_{ab} \tag{11}$$

as this term can be shown essentially to increase physical viscosity, see Monaghan [25]. The coefficients h_{ab}, c_{ab} and ρ_{ab} are the averages of the smoothing length, the sound speed and the density of the two particles a and b, respectively. The parameter ϵ is usually set to $\epsilon = 0.01$ and is included only to ensure a non-zero denominator. We empoly the artificial viscosity to reduce spurious flow oscillations, and therefore it is applied only for interactions between fluid particles, i.e. no artificial dissipation is introduced for the interaction of dummy particles and real particles. The parameter α is chosen such that the global solution is essentially unaffected by the artificial viscosity but also to ensure sufficient damping of spurious oscillations. When using an artificial viscosity in the form of Eq. (11) in the absence of a physical viscosity, an equivalent effective physical kinematic viscosity ν can be calculated from α [26,3] as

$$\nu = \frac{1}{2(d+2)} \alpha h_{ab} c_{ab} \tag{12}$$

In SPH simulations, a jump in initial data causes a transient behavior characterized by spurious high-frequency oscillations due to pseudo-sound waves travelling through the domain. Such artefacts can be reduced by the damping technique proposed by Monaghan et al. [19] during the initial transient of simulations. This damping smoothes the motion of otherwise impulsively accelerated particles. We define a damping time t_{damp} during which the acceleration of each particle due to the body force is mitigated by the factor ζ as follows

$$\zeta(t) = 0.5 \left[sin\left(\left(-0.5 + \frac{t}{t_{damp}} \right) \pi \right) + 1 \right], \quad t \leqslant t_{damp} \tag{13}$$

3.3. Time-stepping scheme

The equations of motion are integrated in time with a velocity-Verlet scheme [27]

$$\mathbf{v}_a^{n+\frac{1}{2}} = \mathbf{v}_a^n + \frac{\Delta t}{2} \left(\frac{d\mathbf{v}_a}{dt} \right)^n \tag{14}$$

$$\mathbf{r}_a^{n+\frac{1}{2}} = \mathbf{r}_a^n + \frac{\Delta t}{2} \mathbf{v}_a^{n+\frac{1}{2}} \tag{15}$$

$$\rho^{n+1} = \rho^n + \Delta t \frac{d\rho^{n+\frac{1}{2}}}{dt} \tag{16}$$

$$\mathbf{r}_a^{n+1} = \mathbf{r}_a^{n+\frac{1}{2}} + \frac{\Delta t}{2} \mathbf{v}_a^{n+\frac{1}{2}} \tag{17}$$

$$\mathbf{v}_a^{n+1} = \mathbf{v}_a^{n+\frac{1}{2}} + \frac{\Delta t}{2} \left(\frac{d\mathbf{v}_a}{dt} \right)^{n+1} \tag{18}$$

Although using a mid-point velocity, the force calculation to obtain the particle acceleration has to be performed only once per timestep. In the absence of viscous effects (where the force depends on the velocity) this scheme is second-order accurate and reversible in time.

The step size of the time integration is limited for stability reasons based on several criteria [21]. Here, the three relevant conditions are the CFL-condition based on the artificial sound speed c_{max} and the maximum flow speed

Author's personal copy

$$\Delta t \leqslant 0.25 \frac{h}{c_{max} + |\mathbf{v}_{max}|} \tag{19}$$

the viscous condition

$$\Delta t \leqslant 0.125 \frac{h^2}{\nu} \tag{20}$$

and the body force condition

$$\Delta t \leqslant 0.25 \left(\frac{h}{|\mathbf{g}|} \right)^{1/2} \tag{21}$$

The minimum of the three conditions is used as timestep to satisfy all conditions globally.

4. Solid wall boundary

Due to the special properties of SPH a whole range of different formulations to impose boundary data is possible. A proper formulation is essential for physically meaningful and quantitatively correct results. As particles approach a rigid boundary, the main problem arises from the fact that the support domain of the kernel is cut by the domain boundary. The question is then how to treat these particles and what boundary conditions have to be imposed. In our method we use dummy particles to approximate the interface between the fluid phase and the boundary, see Fig. 1. The main advantage of dummy particles compared to mirror particles is simplicity when using complex geometries, and that the boundary is well-described throughout the simulation once the particles have been initialized.

In Fig. 1, fluid particles (•) near the wall do interact with dummy particles representing the wall (o) according to the overlap of the kernel function. As the governing equations for the flow evolution apply only to the bulk phase wall-particle properties can be manipulated to mimic a continuous fluid phase for particles close to the boundary. Consequently, wall particles represent dummy fluid particles that contribute to the continuity and momentum evolution in the fluid phase. In the continuity equation, Eq. (6), the initial particle volume is used for the wall particles and $\mathbf{v}_b$ is set to the prescribed wall velocity. Thereby the density of a fluid particle increases when moving towards a wall and the resulting pressure force prevents particles from penetrating the walls. Hence, the impermeability condition of rigid walls, i.e. $\mathbf{v} \cdot \mathbf{n} = 0$, is implicitly enforced.

A free-slip or no-slip boundary condition at a wall can be imposed by the choice of the wall velocity used for the viscous interaction in Eq. (10). By simply omitting the viscous interaction of a fluid particle with adjacent dummy particles a free-slip wall boundary condition is applied. To impose a non-slip condition we first extrapolate the smoothed velocity field of the fluid phase to the dummy particle positions by

$$\tilde{\mathbf{v}}_a = \frac{\sum_b \mathbf{v}_b W_{ab}}{\sum_b W_{ab}} \tag{22}$$

Then, the velocity

$$\mathbf{v}_w = 2\mathbf{v}_a - \tilde{\mathbf{v}}_a \tag{23}$$

is assigned to the dummy particle in Eq. (10), where $\mathbf{v}_a$ is the prescribed wall velocity. Compared to the slightly more accurate approach of Morris et al. [15] our method does not require explicit information about the geometry of the boundary, and

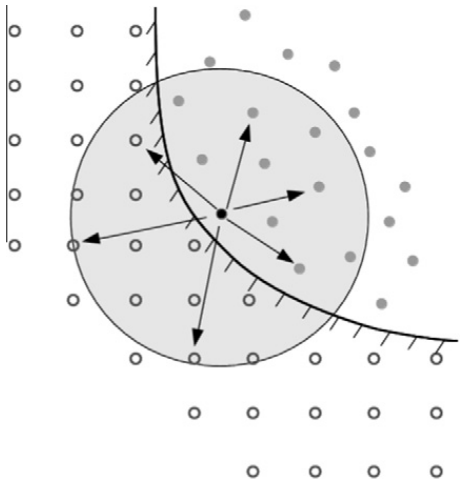

Fig. 1. Fluid particles (•) interact with cartesian dummy particles representing the wall (o) to ensure full support of the kernel interpolation.

Author's personal copy

as the calculation of the extrapolated velocities can be restricted to interface dummy particles the computational overhead is insignificant. Validation simulations for Poiseuille and Couette flows show that we recover the no-slip condition at walls with satisfactory accuracy.

Furthermore, the pressure of a wall particle has to be calculated from the fluid to accurately approximate the pressure gradient in the fluid phase near the boundary. A force balance at the wall interface gives

$$\frac{d\mathbf{v}_f}{dt} = -\frac{\nabla p_f}{\rho_f} + \mathbf{g} = \mathbf{a}_w \tag{24}$$

where the indices f and w refer to the fluid phase and the wall. Note, that here the more general formulation with moving walls is presented. A numerical freefall experiment (Section 7.1) shows that it is important to include the acceleration of the wall $\mathbf{a_w}$ when computing the boundary pressure. From a force balance along the centerline of a fluid-wall particle pair we find

$$\int \nabla p \cdot \mathbf{d}l = \rho_f \int (\mathbf{g} - \mathbf{a}_w) \cdot \mathbf{d}l \tag{25}$$

where $\mathbf{d}l$ is a vectorial length element along the centerline of the two particles and the indices f and w denote a fluid and a wall particle, respectively. The pressure of a wall particle due to the action of a single fluid particle can then be obtained from

$$p_w = p_f + \rho_f(\mathbf{g} - \mathbf{a_w}) \cdot \mathbf{r}_{wf} \tag{26}$$

where $\mathbf{r}_{wf} = r_{wf}\mathbf{e}_{wf}$. Since wall particles interact with several fluid particles, the resulting p_w is obtained by summation of all contributions of neighboring fluid particles f using the kernel function as weight

$$p_w = \frac{\sum_f p_f W_{wf} + (\mathbf{g} - \mathbf{a_w}) \cdot \sum_f \rho_f \mathbf{r_{wf}} W_{wf}}{\sum_f W_{wf}} \tag{27}$$

The calculation of the acceleration of a particle due to a pressure gradient in Eq. (7) uses a density-weighted inter-particle pressure. As we do not evolve the properties of dummy particles in a wall, we obtain its density from the pressure p_w as

$$\rho_w = \rho_{0,b}\left(\frac{p_w - \chi}{p_{0,b}} + 1\right)^{\frac{1}{\gamma}} \tag{28}$$

from the interacting fluid particle b.

5. Two-dimensional flow examples

The following two-dimensional examples show validation cases to demonstrate the performance of our method. Poiseuille and Couette flow are presented, and very good agreement with exact velocity profiles is found. A correct computation of these flows requires a correct no-slip boundary condition at the walls as the solution depends directly on wall friction. We simulate the laminar flow over a backward facing step at $Re = 100$ to show that seperated flows with rectangular walls can be well predicted. The last example, a flow around a cylinder, shows that the method can also handle curved wall boundaries. For all these flows we use a physical friction term in the fluid phase according to Eq. (10) and switch off the additional artificial viscosity term.

5.1. Poiseuille and Couette Flow

Our first examples are a Poiseuille flow and a Couette flow in a two-dimensional infinite channel with a distance between the walls of $L_y = 1$. The fluid phase is discretized with SPH particles at two different resolutions of $r_c = 0.1L_y$ and $0.05L_y$, i.e. 30 and 60 particles across the channel height, respectively. In x-direction we impose periodicity and simulate only a small section of width $L_x = 0.4L_y$. The viscosity and the density of the fluid are $\eta = 0.01$ and $\rho = 1$. The maximum velocity in both cases is $V_{max} = 1.25$, thus we use a sound speed of $c_s = 12.5$ and the Reynolds number of the flows is $Re = 0.0125$. The driving-force of the Poiseuille Flow is a body force $F = 0.1$ and for the Couette flow we move the upper wall with a constant velocity $v_w = 1.25$.

Fig. 2(a) shows a comparison of the SPH simulation with the analytic solution of the Poiseuille flow at $t = 2, 10, 20$ and 100 for two resolutions. Initially, the fluid is at rest and is accelerated by the body-force. At steady-state parabolic velocity profiles have developed and with increasing resolution the simulations converge to the analytical result. The average error of the velocity in flow direction at $t = 10$ for the two resolutions is 0.16% and 0.06%.

A comparison of the SPH simulation with the analytic solution of the Couette flow at $t = 2, 10, 20$ and 100 is shown in Fig. 2(b) for the two resolutions. The simulated profiles agree very well with the analytical results and converge for increasing resolution. Here, the average error of the velocity in flow direction at $t = 10$ for the two resolutions is 0.16% and 0.09%.

Author's personal copy

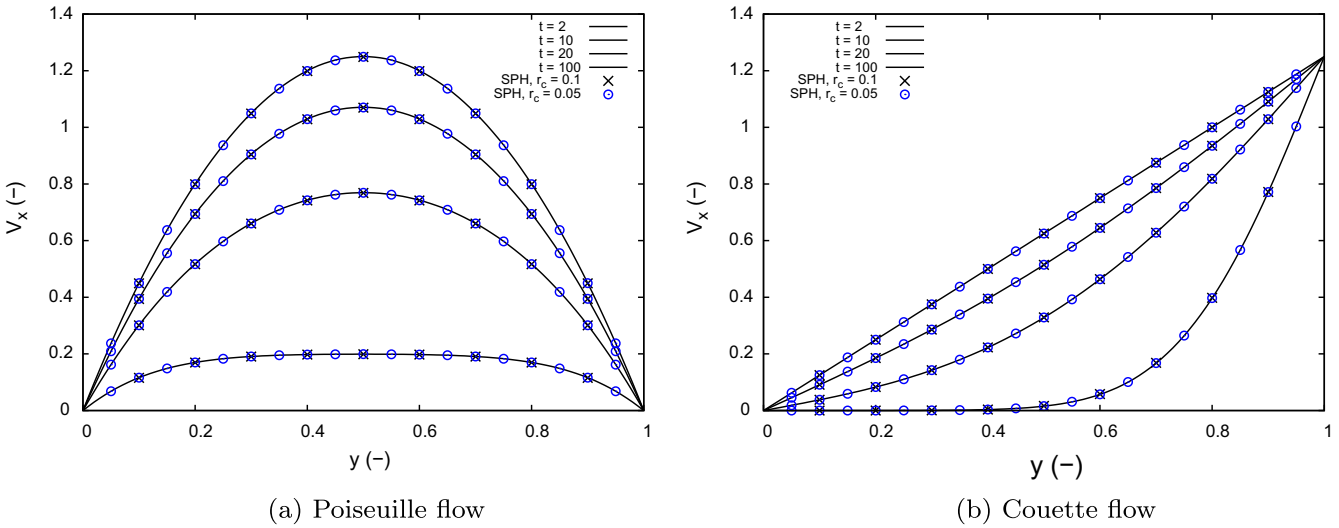

Fig. 2. Comparison of SPH simulations at two resolutions $r_c = 0.1L_y$ and $0.05L_y$ with the analytical solution for the Poiseuille flow (a) and the Couette flow (b).

5.2. Flow over a backward-facing step

We simulate the flow over a backward facing step in a periodic channel at $Re = 100$ and compare our results with the work of Issa et al. [28], who showed that this separated flow can be simulated using SPH. We use the same geometry as presented in [28], see Fig. 3 for a sketch and the dimensions of the problem. The marked positions P_1–P_4 show the locations where we compare the velocity profiles with the reference results. As there is no analytical solution for this example, the reference solution is obtained from a grid-based high-resolution simulation [29].

Instead of imposing a pressure gradient at the boundaries, we use a constant body force in x-direction to drive the flow in the periodic channel. The magnitude of the body force is adjusted to achieve a mean bulk velocity in the thinner channel above the step of $U = 0.14$. Using twice the channel height above the step as hydraulic diameter $D = 2H_1$, the kinematic viscosity of the fluid $\nu = 1.456 \times 10^{-2}$ follows from $Re = 100$. The sound speed used for this simulations is ten times the maximum velocity in the channel above the step, i.e. $c_s = 2.1$. Also, we have used a small background pressure of $\chi = 0.05p_0$ in the equation of state (3).

The result of the simulation of the flow over the backward-facing step is shown in Fig. 4 for two resolutions $r_c = 0.2S$ and $r_c = 0.1S$, where $S = 4.9$ is the step height. After an initial transient a steady flow field develops. Fig. 4(a) shows a snapshot at $t = 2000$ of a section of the channel. The fluid particles are colored with the axial velocity ranging from $v_x = -0.015$ (blue) to $v_x = 0.21$ (red). The contour lines are postprocessed after a projection of the particle data onto a Cartesian grid.

When the background pressure in Eq. (3) is omitted, we find large artificial void regions just behind the step similar as presented by Issa [29]. As a remedy, Issa showed that for his method only strongly increasing the speed of sound avoids the particle clumping, leading to a much smaller time step according to the CFL condition. In contrast, we have introduced a small background pressure ($\chi = 0.05p_0$) and maintain a sound speed for $Ma = 0.1$. We find that this constant background pressure is sufficient to prevent void regions in the fluid.

To analyze the quality of the simulation in more detail we plot the streamwise velocity over the channel height at four positions P_1–P_4 and compare the profiles with the reference results from [29], see Fig. 4(b). The instantaneous particle

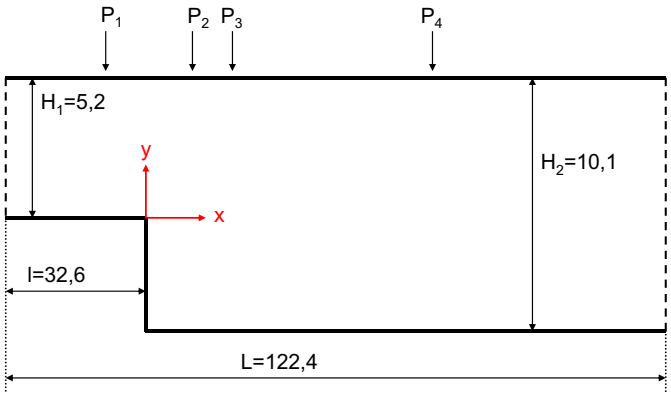

Fig. 3. Sketch of the backward-facing step.

Author's personal copy

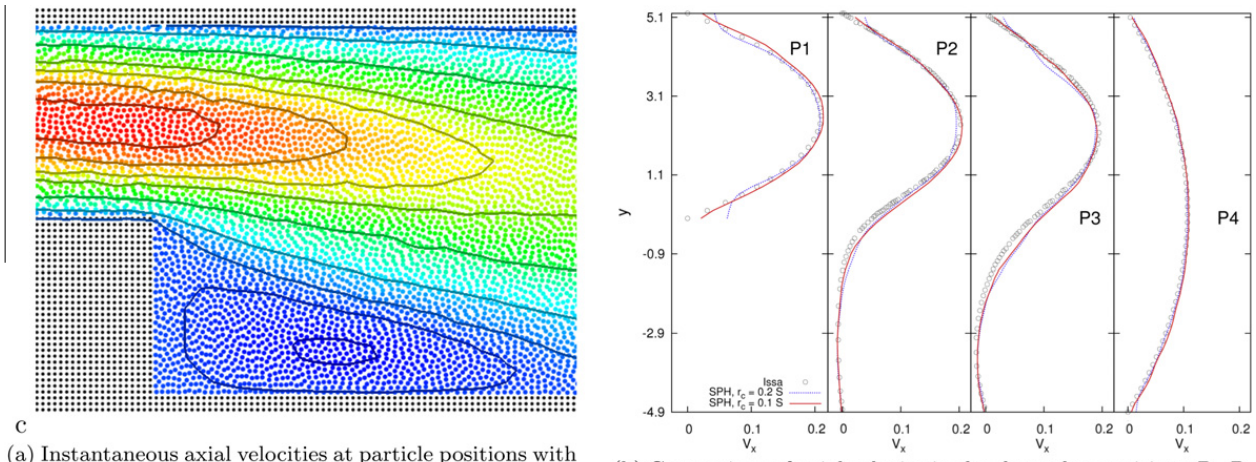

(a) Instantaneous axial velocities at particle positions with contour lines at $t = 2000$, the colormap range is from $v_x = -0.015$ (blue) to $v_x = 0.21$ (red).

(b) Comparison of axial velocity in the channel at positions P_1-P_4 with reference result for two resolutions $r_c = 0.2\ S$ and $r_c = 0.1\ S$.

Fig. 4. Simulation results of the laminar flow over a backward-facing step. (For interpretation of the references to colour in this figure legend, the reader is referred to the web version of this article.)

velocities are interpolated on a grid using the kernel W to obtain the smooth profiles. As the profile at P_1 was used to adjust the body force, the agreement with the reference solution at this position is very good. Note, the discrepancy especially for the lower resolution close to the wall is an artefact of the interpolation. The results at P_2 and P_3 show that also the recirculation bubble is well recovered, and in comparison to the SPH results of [28] we match the maximum velocity much better. Far behind the step, the flow field is again parabolic, see P_4.

5.3. Flow through a periodic lattice of cylinders

The previous examples have shown the validity of our method for a fluid flow confined by straight channel walls. Now we study the flow through a periodic array of cylinders to test the wall boundary condition for curved geometries. A solid cylinder of radius $R = 0.2$ is centered in a periodic box of size $L = 1$, and the driving pressure gradient for the flow is modeled by a constant body force $F = 1.5$ in x-direction. Following Morris et al. [15] we take the velocity scale to be $V_0 = 0.5$ and a sound speed of $c_s = 5.77$. Using the kinematic viscosity $\nu = 0.1$ in the fluid gives a Reynolds number of $Re = 1$.

The fluid phase is discretized with particles placed initially on a Cartesian lattice at two resolutions using $\Delta x = 0.02$ and $\Delta x = 0.01$. For the cylinder we placed particles on circular rings with the same spacing Δx to increase the smoothness of the solid boundary. This was done for the reason of a better representaion of the circular interface compared to using solid particles on a Cartesian lattice at the same resolution. Starting from rest the fluid phase is accelerated by the body force, and after about 5000 steps the particles are completely disordered and a steady flow field has developed. Fig. 5(a) shows the flow

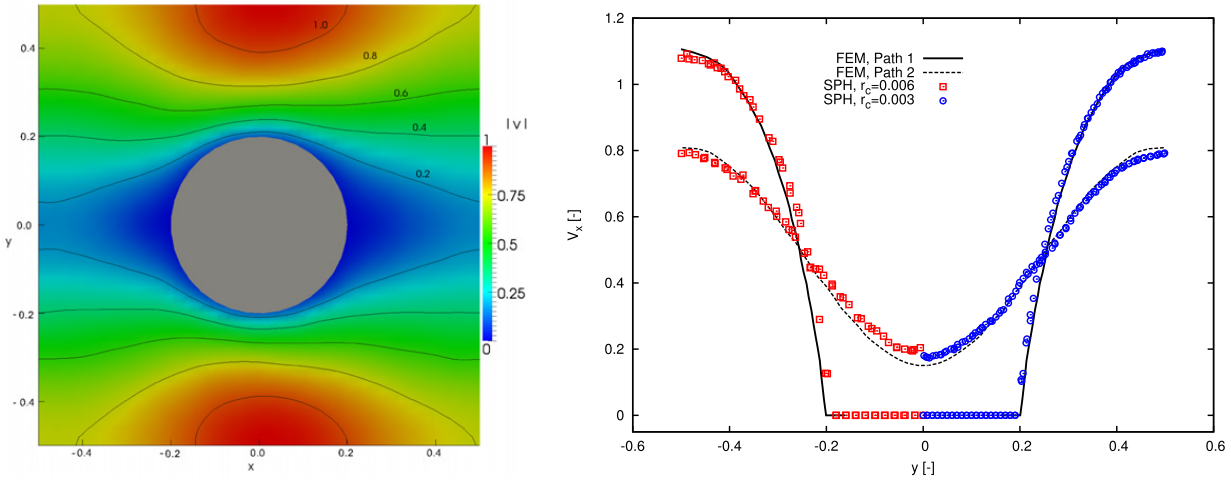

(a) Smoothed velocity field and contour lines for the flow around a cylinder at Re=1 using SPH at $\Delta x = 0.02$.

(b) Comparison of SPH and FEM [14] axial velocity profiles at the center of the cylinder and at the domain boundary.

Fig. 5. Simulation results of the flow through a periodic lattice of cylinders.

Author's personal copy

field and velocity contour lines in the steady state after projecting the particle data onto a Cartesian grid. The velocity magnitude was non-dimensionalized with twice the reference velocity scale $2V_0$. A comparison with the steady incompressible viscous flow using a finite element method (FEM) [15] is shown in Fig. 5(b). The streamwise velocities are plotted over the y-axis at the center of the cylinder and at the downstream domain boundary for particles within a layer of width $2\Delta x$ at these locations. The simulation results agree well with the reference profiles [15], and with increasing resolutions the SPH results converge to the FEM solution.

6. Hydrostatic examples

In this section we present several test cases to validate in particular the pressure boundary condition. The first example shows the development of a hydrostatic pressure field of a fluid in a tank under gravity. To show the robustness of our boundary condition we replace subsequently the simple straight wall on one side of the tank by a sharp wedge geometry. Next, the same setup is used to simulate the hydrostatic pressure field in a two-phase configuration where a stratified fluid with two different densities layered on top of each other is considered. Finally, a threedimensional cylinder example shows the versatility of our method. We use inviscid fluids in all hydrostatic examples, i.e. the physical viscosity is zero. For stabilization of the inviscid flows an artificial viscosity as given by Eq. (11) is necessary.

6.1. Hydrostatic tank

We simulate a two-dimensional cross-section of a rectangular tank with a water depth of $H = 0.9$. The width of the tank is $L_x = 2$ and the walls are about $L_y = 1$ high. Fig. 6(a) shows the initial setup with red particles denoting the wall boundary and blue particles showing the fluid phase. The initial distance between the particles in each direction is $\Delta x = 0.02$, thus a total of 5000 fluid particles is simulated. We chose the sound speed ten times bigger than the reference velocity $v_{ref} = \sqrt{gH}$ and use the artificial viscosity parameter $\alpha = 0.24$. According to Eq. (12) the effective kinematic viscosity corresponds to a Reynolds number of $Re = 100$. Note that we use the same setup as Monaghan et al. [19] in their first example in order to compare the effect of the different boundary condition formulations.

At $t = 0$ the particles are placed on a Cartesian lattice with the density equal to the reference density, thus zero pressure in the fluid phase. Accelerated by the gravity force g in negative y-direction, the particles move down, and due to the compression at the bottom wall their density increases. The pressure response creates a repulsive force, and finally the hydrostatic pressure field counterbalances the body force effect. Thus, after an initial transient phase the particles settle down with a steady and linear pressure field, see Fig. 6(a). We want to highlight the very ordered particle distribution in our simulation compared to previous works [17,19]. We do not see spurious currents in the corners of the tank or a separation of particles from the walls at the free surface. This shows the importance of proper boundary conditions formulated in terms of a force balance as presented in this work.

Fig. 7(a) shows the averaged pressure in the middle of the bottom wall over time, nondimensionalized with $p_{ref} = \rho g H$ and $t_{ref} = H/v_{ref}$. As intended by Monaghan et al. [19] when they introduced the smooth acceleration of particles, the initial damping according to Eq. (13) until $t = 1$ results in a smooth pressure rise and finally the exact value of $p = 1$ is achieved. The pressure profile in the water column is presented in Fig. 7(b). Here, the pressure profile is evaluated along the centerline of the tank by a simple SPH-average $p(y_i) = \sum_j p_j W_{ij} / \sum_j W_{ij}$ using the surrounding fluid particles j. A comparison with the exact linear hydrostatic profile shows very good agreement. Note, the damping technique to smoothly accelerate the particles due to gravity using Eq. (13) mimicks a slowly increasing gravitational acceleration. Thus, to compare the simulated pressure profile during this transient phase the actual gravity used to obtain the analytical hydrostatic profile is also scaled with the factor $\zeta(t)$. At each time instant during the transient period the profile is linear and agrees well with the effective gravitational acceleration.

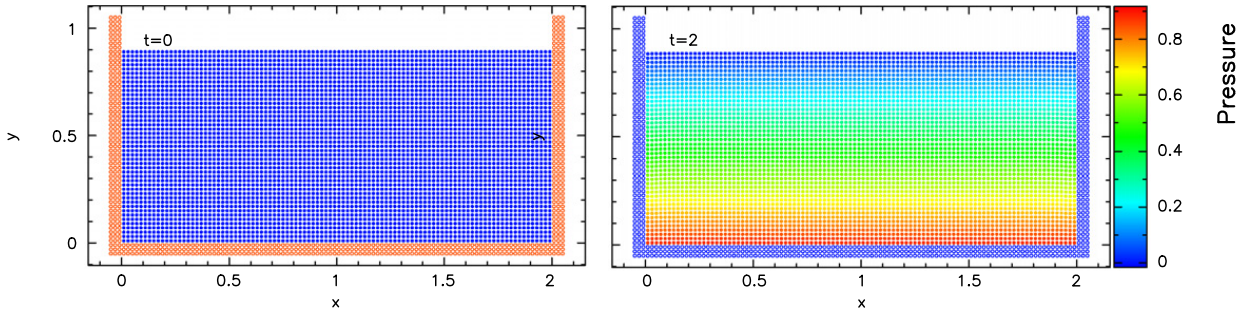

(a) Initial positions of wall (red) and fluid (blue) particles in the tank.

(b) Particle positions at $t = 2$, colored with the pressure field.

Fig. 6. Particle positions (a) and pressure field (b) in the cross-section of a rectangular tank with a water depth of $H = 0.9$ at $t = 0$ and $t = 2$. (For interpretation of the references to colour in this figure legend, the reader is referred to the web version of this article.)

Author's personal copy

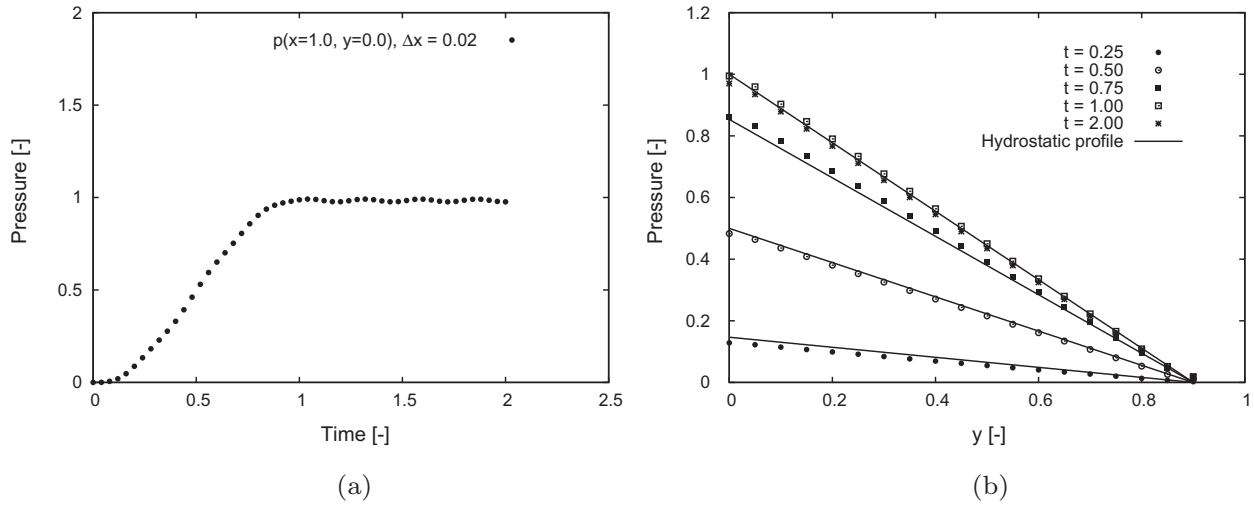

Fig. 7. Temporal (a) and spatial (b) pressure profile at the bottom wall and on the centerline of the hydrostatic tank.

6.2. Hydrostatic tank with complex geometry and two phases

The second example shows the capability of our method to simulate arbitrarily shaped geometries including multi-phase problems. Starting with the geometry of the previously presented cross-section of a watertank, the left wall of the tank is modified with a wedge according to the example presented by DeLeffe et al. [17]. This test demonstrates that even sharp corners in the domain do not cause stability problems and that the correct pressure profile develops in the fluid phase. In Fig. 8(a) the static wall particles are plotted in blue and the fluid particles are colored with the actual pressure at $t = 5$. Again, very good agreement with the analytical hydrostatic pressure profile is achieved and the particles are nearly at rest after the initial transient period.

At $t = 0$ particles are placed on a Cartesian lattice with density equal to the reference density and consequently the pressure is zero in the fluid. Due to the gravitational acceleration the particles move slightly and finally settle down when equilibrium between the external body force and the hydrostatic pressure field is achieved. Fig. 8(b) shows the velocity field in the fluid during the transient phase where particles rearrange under gravity. This snapshot was taken at $t = 0.3$ where the maximum velocity magnitude occured. The highest velocity magnitude occurs at the sharp corner, but note that it is on the order of only 1% of the reference velocity. At late times, particles are at rest in hydrostatic equilibrium. We compared this result with the results of DeLeffe et al. [17] who simulated this case using a much more complex normal-flux method at the boundaries. They show that the classical ghost particle technique produces a strong circulation zone close to the sharp wedge. Their normal-flux method apparently gives a stationary particle field, but it should be noted that the range of the velocities shown by the colormap in their Fig. 4 about seven times the range we show in Fig. 8(b). In fact, we achieve a very similar result with our rather simple method.

Now we further increase the complexity of this test and introduce a multi-phase problem, where two fluids of different density interact with the walls. Fig. 9(a) shows the initial condition with a resolution of $\Delta x = 0.02$. The heavy phase in the lower left corner ($l_x = 1,\ l_y = 0.5H$) has a density of $\rho = 1$ and the second fluid is four times lighter ($\rho = 0.25$). Due to gravity, the heavy patch of fluid sloshes against the right wall and displaces the light phase upward. Finally, the two fluids are on top

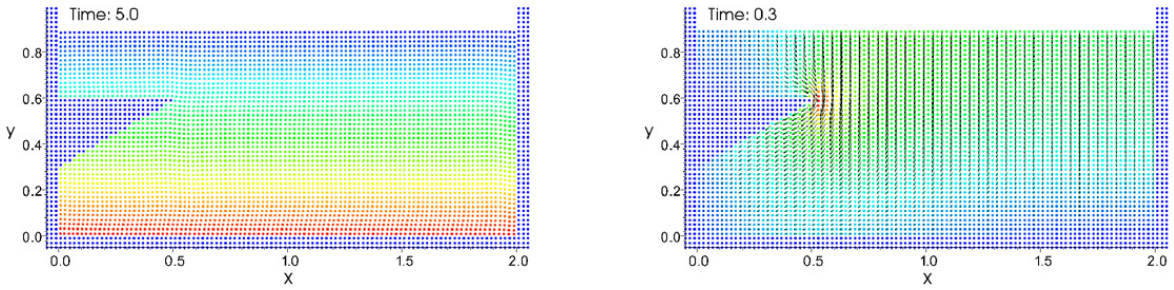

(a) Fluid particles are colored with the non-dimensionalized pressure, the colormap from blue to red denotes the range of the pressure between zero and one.

(b) This plot shows a snapshot of the velocity field when the velocities are biggest (t=0.3). Blue to red color shows the magnitude of the velocity in the range of $0 - 0.015 v_{rel}$.

Fig. 8. Pressure field (a) and spurious velocity field (b) for the hydrostatic tank problem with a wedge geometry at $t = 5$ and $t = 0.3$. (For interpretation of the references to colour in this figure legend, the reader is referred to the web version of this article.)

Author's personal copy

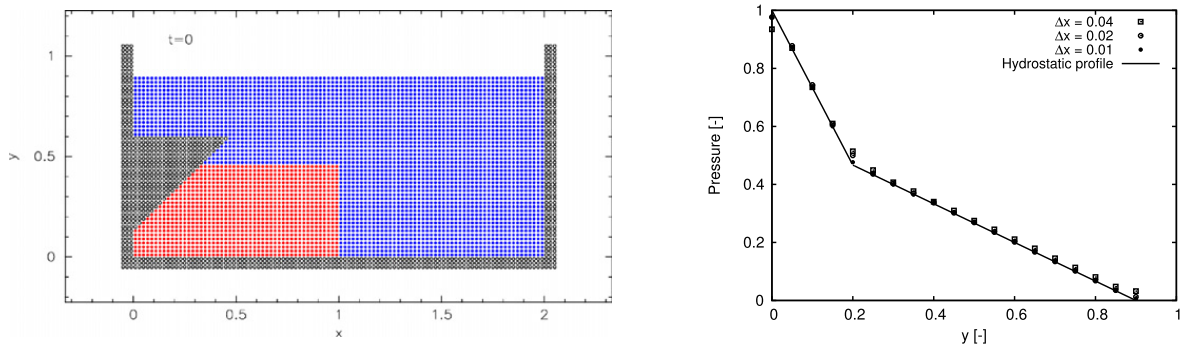

(a) Initial condition for the complex water tank with two phases. Red and blue particles denote the heavy phase with $\rho = 1$ and the light phase with $\rho = 0.25$, respectively. The resolution shown here is $\Delta x = 0.02$.

(b) Non-dimensional pressure profile in the center of the tank compared to piecewise linear analytic profile at $T = 30$.

Fig. 9. Initial condition (a) and final spatial pressure profile (b) in the complex water tank with two phases. (For interpretation of the references to colour in this figure legend, the reader is referred to the web version of this article.)

of each other in hydrostatic equilibrium. Due to the different densities, the pressure gradient in each phase is constant but discontinuous at the interface. The vertical pressure profile in the middle of the tank is plotted in Fig. 9(b) together with the piecewise linear analytical solution. The discrepancy between the exact solution and the numerical results close to the free-surface, the wall and near the phase interface comes from the fact that we used SPH interpolation of the pressure along the vertical line. This smoothes the pressure profile between the heavy and the light phase, and since we only use fluid particles for the interpolation it is obvious that the pressure close to the wall is underestimated, and it is overestimated near the free-surface. With increasing resolution these interpolation effects vanish and the results agree well with the analytical hydrostatic profile. Note that the artificial viscosity parameter α was adjusted for different resolutions following Eq. (12) to maintain a Reynolds number of $Re = 100$.

Several snapshots of the simulation at $t = 2, 4, 6, 8, 10$ and 30 are shown in Fig. 10 for two resolutions of $\Delta x = 0.02$ and $\Delta x = 0.01$. Due to the sloshing of the fluid the interface between the two fluids become distorted, and particles mix. Due to the different densities the phases separate at late times and the fluids settle forming two layers with the heavy phase on the bottom. Additionally, we have added a small constant background pressure to the lighter phase. Similarly to the modification of Colagrossi [9], who changed the pressure equation of state for the light phase, this attempt results in a soft artificial surface tension and suppresses strong mixing of particles of different phases at the interface.

6.3. Threedimensional cylinder

A last hydrostatic example shows the straight-forward application of the proposed method to a threedimensional problem. Now, we simulate a water column of height $H = 1$ in a cylinder with a radius of $R = 0.5$ under gravity. The artificial viscosity in this example is equivalent to a Reynolds number of $Re = 100$. Similar to the previous watertank example we smoothly increase the gravity to avoid strong oscillations in the water. Fig. 11(a) shows a snapshot of the simulation at $T = 2$ with static wall particles in grey and fluid particles colored with the pressure. Note, that the cylinder wall is cut only to visualize the fluid phase.

The reference pressure is $p_{ref} = \rho g H$ and consequently the non-dimensional pressure at the bottom of the cylinder is under hydrostatic equilibrium conditions equal to one, see the colormap in the figure. The pressure profile in the center of the cylinder over the water height is shown in Fig. 11(b). We have interpolated the pressure over the height in the center of the cylinder in z-direction from the particle values. Due to this averaging, the profile is flattened at the free-surface and at the bottom of the cylinder since only fluid particles are included in the summation. This artefact is purely caused by the post-processing and vanishes with increasing resolution. The simulated profile is almost indistinguishable from the analytic linear hydrostatic profile already at the low resolution shown here.

7. Dynamic examples

So far we have only presented simple test cases with stationary walls. Now we want to show the importance of considering the wall motion for the pressure estimation at the wall boundary particles. To the knowledge of the authors this is the first time that such an effect is discussed in terms of the SPH method, and we demonstrate the consequences with a numerical free-fall experiment. Furthermore, we have performed a typical highly dynamical dambreak simulation for which a comparison with results from literature shows good agreement. The final example of a rotating rippled cylinder includes both a quite complex shape and motion of the boundary, demonstrating the robustness and versatility of our method.

Author's personal copy

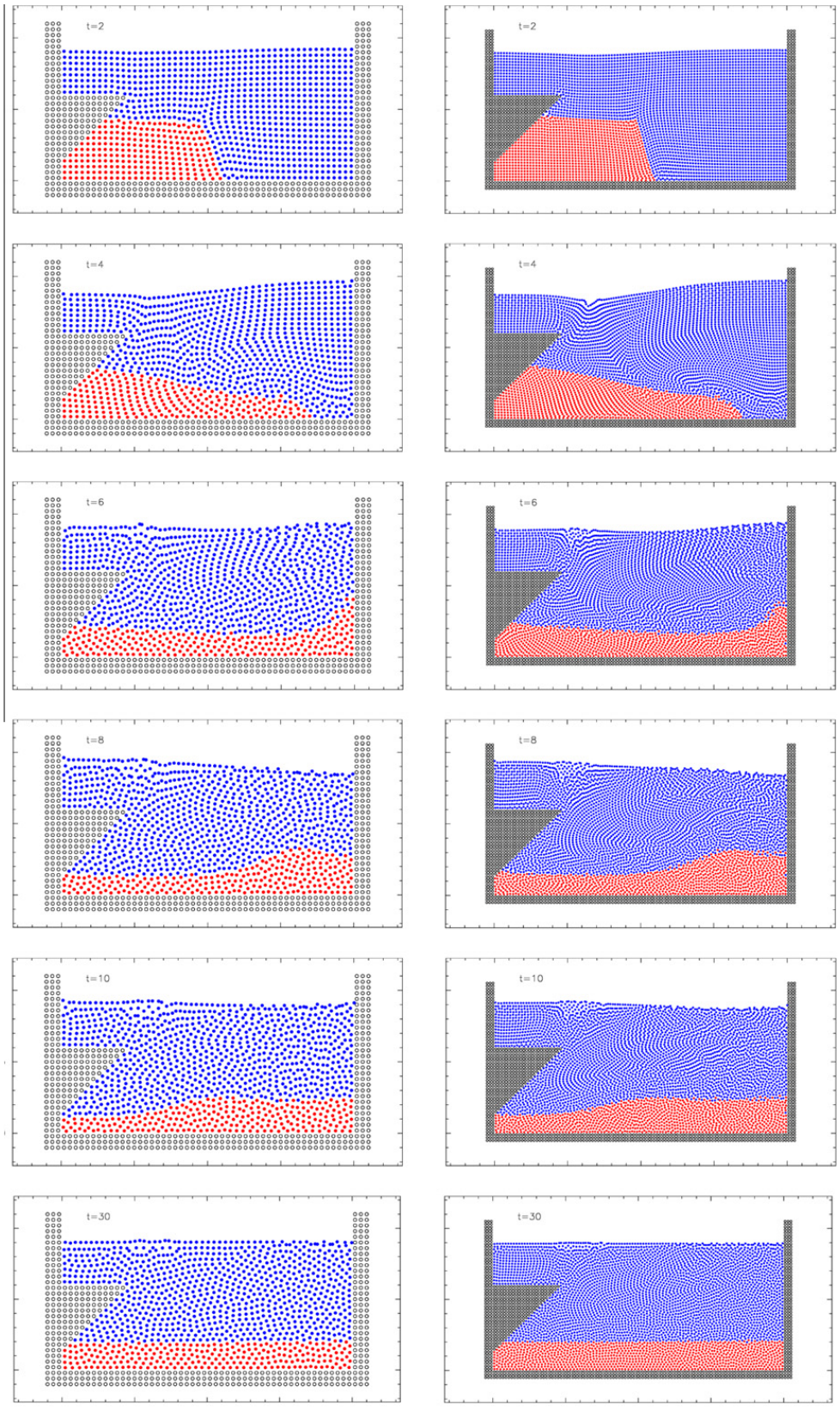

(a) Low resolution $\Delta x = 0.02$ (b) High resolution $\Delta x = 0.01$

Fig. 10. Snapshots of the two-phase sloshing in a tank with complex wall geometry for different resolutions at $t = 2, 4, 6, 8, 10$ and 30.

Author's personal copy

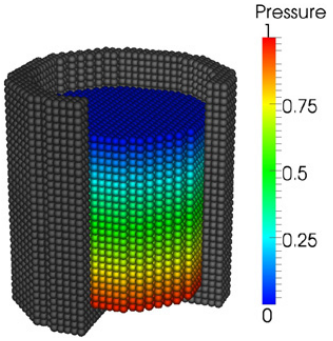

(a) Snapshot of the particles at $T = 2$ showing a section of the wall particles (grey) and the fluid particles coloured with the non-dimensional pressure.

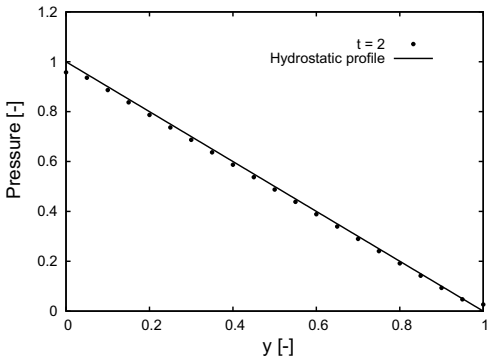

(b) Non-dimensional pressure over height in the cylinder compared to the linear analytic profile.

Fig. 11. Hydrostatic water column in a cylinder of radius $R = 0.5$ and water height $H = 1$. Particles are initially placed on cartesian coordinates with $\Delta x = 0.04$.

7.1. Freefall experiment

A rectangular two-dimensional tank with water is exposed to a gravity field with a constant acceleration of $g = 1$ in negative y-direction. The water depth in the tank is $H = 0.9$ and the side walls have a length of $L = 1$. We discretize the walls and the fluid phase with initially equidistant particles with $\Delta x = 0.04$ and assign a density of $\rho = 1$ to the water particles. At $T = 0$ the bottom wall is at $y = 5.5$ and due to the body force the tank is accelerated and moving down. Fig. 12 shows two snapshots of the simulation at $T = 1$ where particles are colored with the instantaneous pressure field.

The left snapshot is taken from a simulation where the boundary pressure is not corrected for the acceleration of the wall. That means the pressure in the solid phase contains only the hydrostatic term accounting for the height difference between the fluid and wall particles. Consequently, the pressure of solid particles is non-zero, and fluid particles are pushed off. Finally, fluid particles move relatively to the gravitationally imposed motion, and the noisy pressure field causes a collapse of the simulation. Note also the distortion and non-physical motion especially of the corner particles of the fluid phase in Fig. 12(a). In contrast, Fig. 12(b) shows the same simulation using the full boundary condition as given by Eq. (27). Due to the freefall of the entire body the pressure in the fluid is zero everywhere and particles are at rest relative to the tank motion.

7.2. Dambreak

Now we consider the collapse of a liquid column and compare our results with experimental data and SPH results from literature. First, we study the water-front propagation of a square patch of fluid of size $L = H = 1$ over a dry bed. The fluid

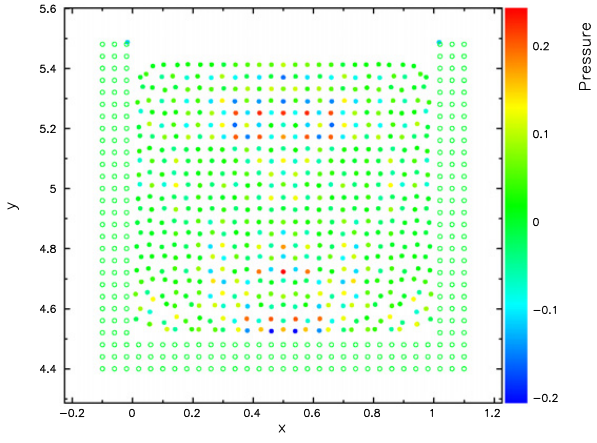

(a) The pressure at boundary particles is calculated from Eq. (27) but neglecting the wall acceleration $\mathbf{a}_\mathbf{w}$.

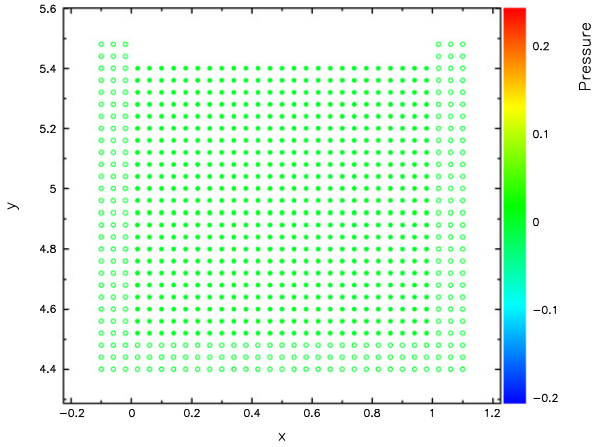

(b) The pressure at boundary particles is calculated from Eq. (27)

Fig. 12. Snapshot of the freefall test example at $T = 1$ for two different boundary particle treatments; particles are colored with local pressure.

Author's personal copy

phase of density $\rho = 1$ is discretized initially with equidistant particles at cartesian positions with Δx and the artificial viscosity parameter is chosen as $\alpha = 0.4$ to stabilize the simulation. Using $g = 1$ in negative y-direction, all quantities correspond to their non-dimensional variables. Since fluid particles interact with the walls only by the pressure force, the fluid phase is effectively inviscid and slip can occur at the walls. In Fig. 13(a) we monitor the front position of the water column over time in comparison with experimental data taken from Martin and Moyce [30]. At early times the results agree acceptably well, but from about $t > 1$ the simulation clearly overpredicts the speed of propagation of the front position. Due to several uncertainties in this example (effect of surface tension, effect of wall roughness, exact experimental setup) it is not clear what exactly causes the differences, but probably the major difference originates from the fact that the inviscid flow assumption is not appropriate. A rough estimate of the Reynolds number in the experiment gives $Re \approx 400$, thus the inviscid flow assumption at this moderate Reynolds number probably is not yet fully justified. Compared to an analytic water-front velocity derived for inviscid shallow-water conditions by Ritter [31], the simulated front propagation converges to that velocity at late times. We have checked the influence of the artificial viscosity parameter α to ensure that the fluid is unaffected by the numerical dissipation. To show convergence of the results we also have simulated the problem with a higher resolution, see Fig. 13(a). Colagrossi [9] studied the same case using mirror wall particles with free-slip, but imposed initially at $t = 0$ a pressure field in the fluid obtained from a Level-Set method at $t > 0$ to avoid high-frequency oscillations due to acoustic waves in the domain. Not shown here, we have also tested the influence of the initial condition and initialized the water column with a hydrostatic pressure field. As expected, the only difference was a much smaller pressure fluctuation in the fluid since we started the simulation from an equilibrium condition. The water-front propagation was unaffected.

The height of the water column in the simulation and in the experiment is compared in Fig. 13(b). As the velocity of the water-front is overpredicted in the numerical method, the height of the water column over time is slightly lower than in the experiment. The various simulations we have performed give more or less the same evolution of the water height. Again we conclude that the result is independent from the artificial viscosity and from the resolution. Comparing our simulations with results in literature [9,32] we find that our results for the evolution of the water front and height of the water column match with state-of-the-art weakly-compressible SPH simulations with different formulations for wall boundary conditions.

Now we modify the size of the water column and the tank to simulate the classical dam-break problem, as presented in Colagrossi [9]. In this case the water phase covers initially a rectangle of size $L = 2$ and $H = 1$, and the right wall of the tank is positioned at $L_{wall} = 5.366$. In Fig. 14 we show snapshots of two simulations at different resolution at $T = 1.7, 2.0, 4.8, 5.7, 6.2$ and 7.4. The color of the particles shows the local non-dimensional pressure between $p = 0$ (blue color) and $p = 1$ (red color). The two resolutions used in Fig. 14(k) and (l) are $\Delta x = 0.02$ and $\Delta x = 0.01$. Thus a total of 5000 and 20000 fluid particles was used, respectively. We want to highlight the very good agreement between the two resolutions. The high resolution simulation reproduces the pressure field and free surface of the reference case showing some more small structure, see for example the cavity at the right wall at the free surface at $t = 7.4$.

We compare our results with the simulation of a dam-break flow and impact against a vertical wall by Colagrossi [9]. The free-surface evolution of the breaking column agrees well with the snapshots of [9]. We observe a very similar roll-up and and second splash after the impact on the right wall. The main difference is in the pressure field of the fluid. We do not see a pressure distribution similar to a hydrostatic field in the fluid. Our converged results show traveling pressure waves during the highly dynamical collapse of the water column and pressure maxima at the impact positions with the wall. These pressure fluctuations are caused by the weakly-compressible nature of the method, and since viscous effects are small in this case, sound waves are very weakly damped in the simulations. Given the fact that we did not use a smoothed velocity to move the particles (XSPH, [33]) and did not renormalize the density as done in [9], the very good agreement with their results shows that our quite simple method is adequate to handle wall boundaries correctly. We have also confirmed the long-

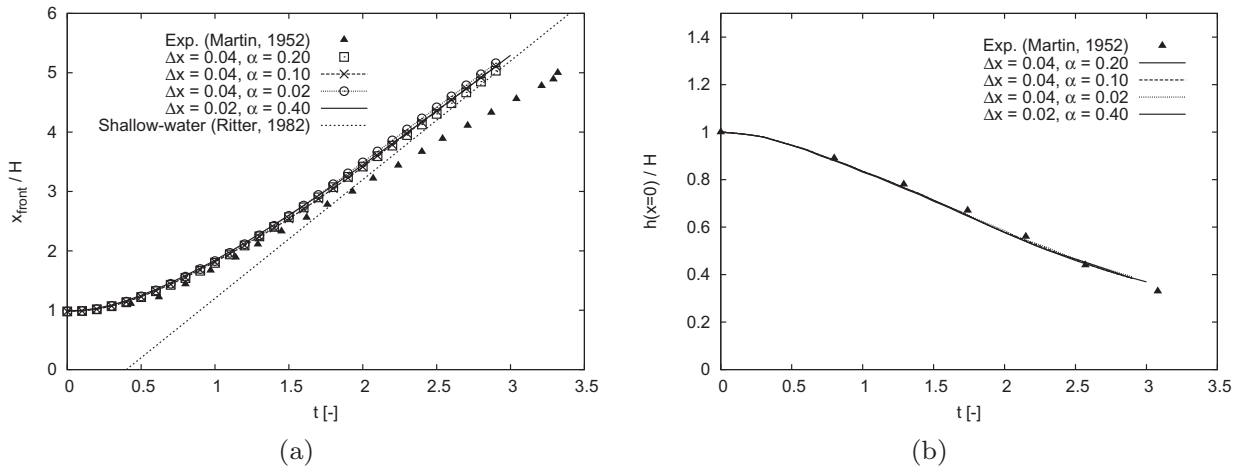

Fig. 13. Time evolution of the front (a) and the height (b) of a colapsing water column for varying parameter of α and Δx compared to experimental data [30].

Author's personal copy

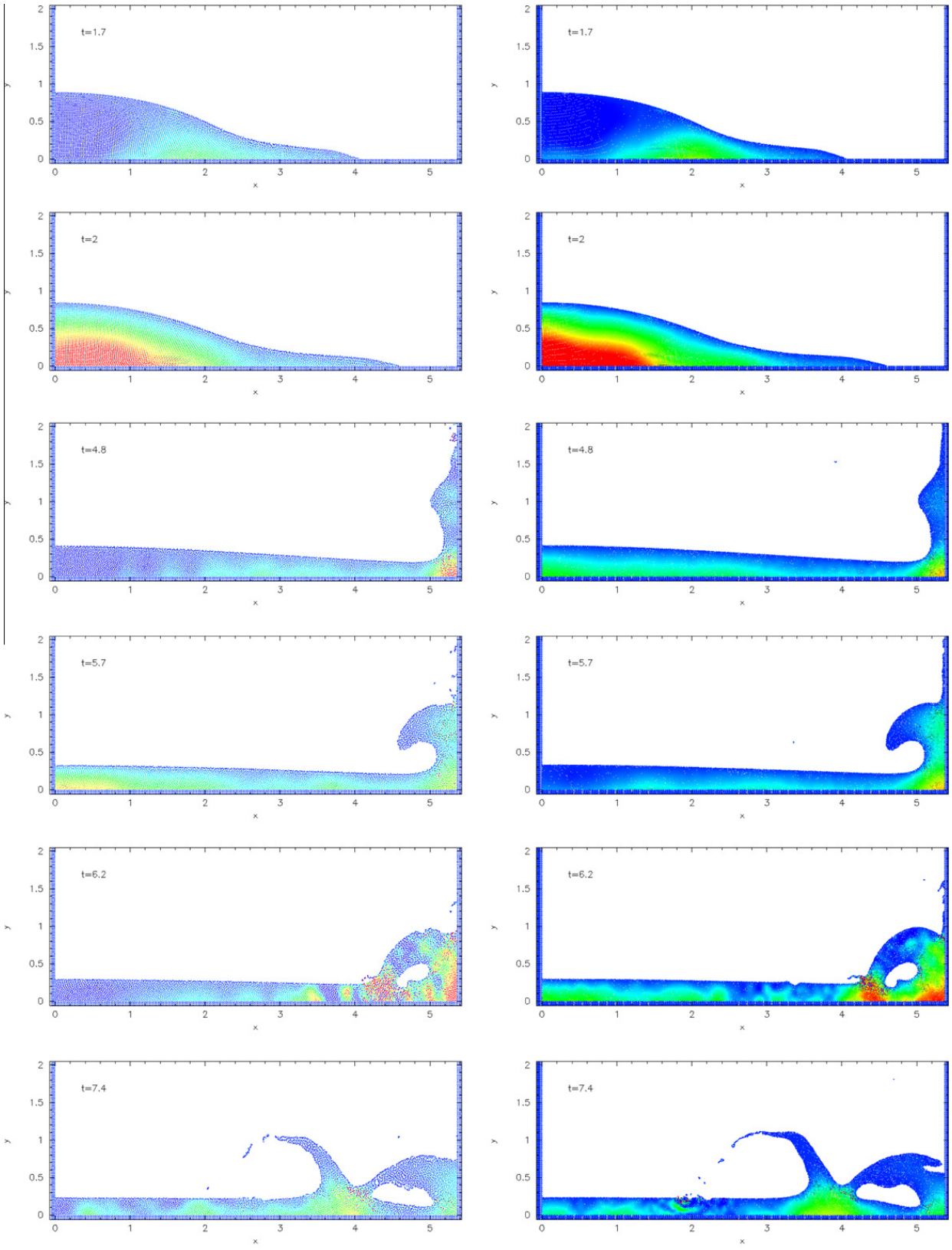

(k) $\Delta x = 0.02$, $\alpha = 0.1$, 5000 fluid particles (l) $\Delta x = 0.01$, $\alpha = 0.2$, 20000 fluid particles

Fig. 14. Snapshots of the dam-break simulation at $t = 1.7$, 2.0, 4.8, 5.7, 6.2 and 7.4 for two different resolutions.

time stability of our method by simulating six wave impacts at the end walls without facing numerical stablity problems, neither for the fluid nor for the boundary particles.

Author's personal copy

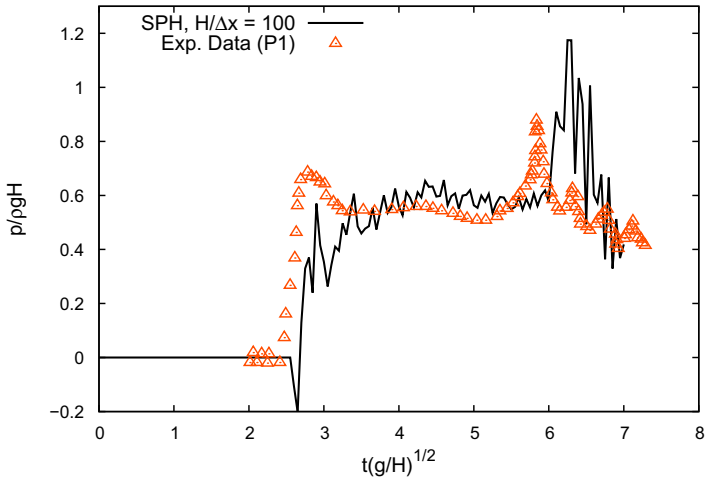

Fig. 15. Comparison of temporal pressure profile at $y/H = 0.2$ between experimental data [34] and SPH simulation with $H/r_c = 100$.

For a quantitative validation we compare the temporal pressure profile on the downstream wall with experimental data from Buchner [34] and the SPH result of Marrone et al. [35]. Fig. 15 shows the pressure on the right wall at $y/H = 0.19$ over time obtained from our simulation and measured data from the experiment [34]. The simulation results were interpolated on this wall position using the same SPH kernel as used in the corresponding calculation. Note, the probe position in the numerical setup does not exactly match the position in the experiment, but Greco [36] showed that this shift gives better agreement and reported several uncertainties in the measurements motivating this adjustment. As expected, the pressure profile obtained with our SPH simulation contains high frequency oscillations but the main pressure plateau is reasonably well captured. The strong peak at $t(g/H)^{1/2} = 6$ is caused by the plunging wave of the first roll-up after the flow hit the wall. As similarly presented already in [35] this peak occurs slightly delayed in the simulation since the air cushion effect is not captured with a mono-fluid simulation.

7.3. Rotating rippled cylinder

Finally, we simulate a cross-section of a partially filled rippled cylinder that is rotating about its own axis. The interface of the cylinder with radius $R = 0.7$ varies with a sinusoidal disturbance with an amplitude of $r_d = 0.1$ and eight periods along the circumference. The height of the water column is $H = 1.0$, measured from the lowest point of the interface. Particles are initially placed on a Cartesian lattice, and the thickness of the wall is equivalent to the cutoff radius r_c, see Fig. 16(a) for a snapshot of the initial setup with $r_c = 0.12$.

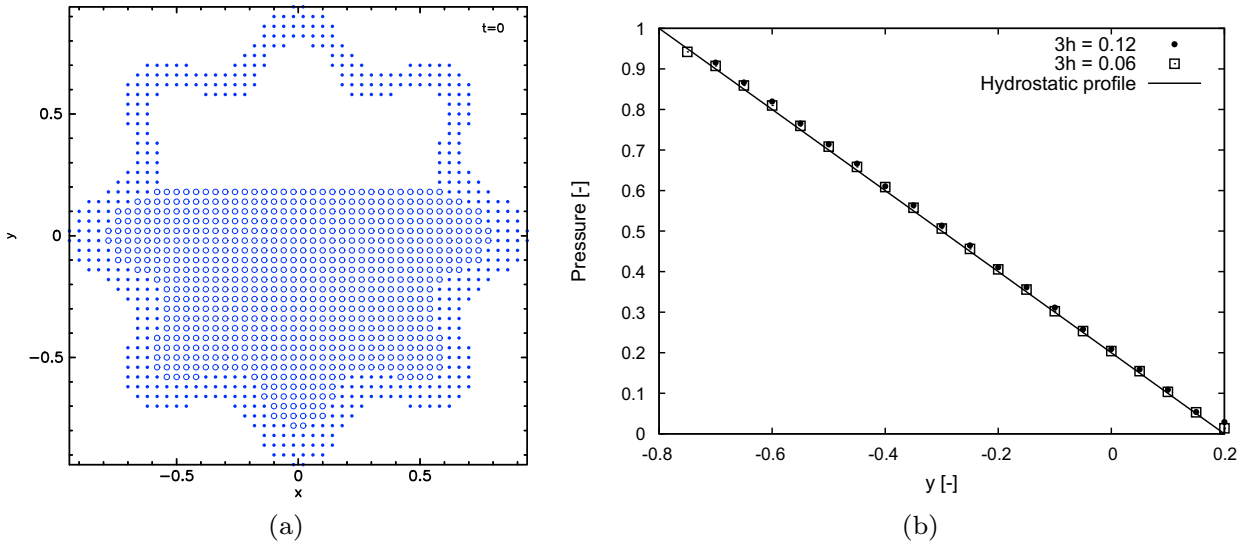

Fig. 16. Rotating rippled cylinder: (a) Initial position of wall (•) and fluid (o) particles using a cutoff radius of $r_c = 0.12$. (b) Pressure profile over the height in the center of the cylinder at $T = 18$ for two resolutions $r_c = 0.12$ and $rc_0.06$.

Author's personal copy

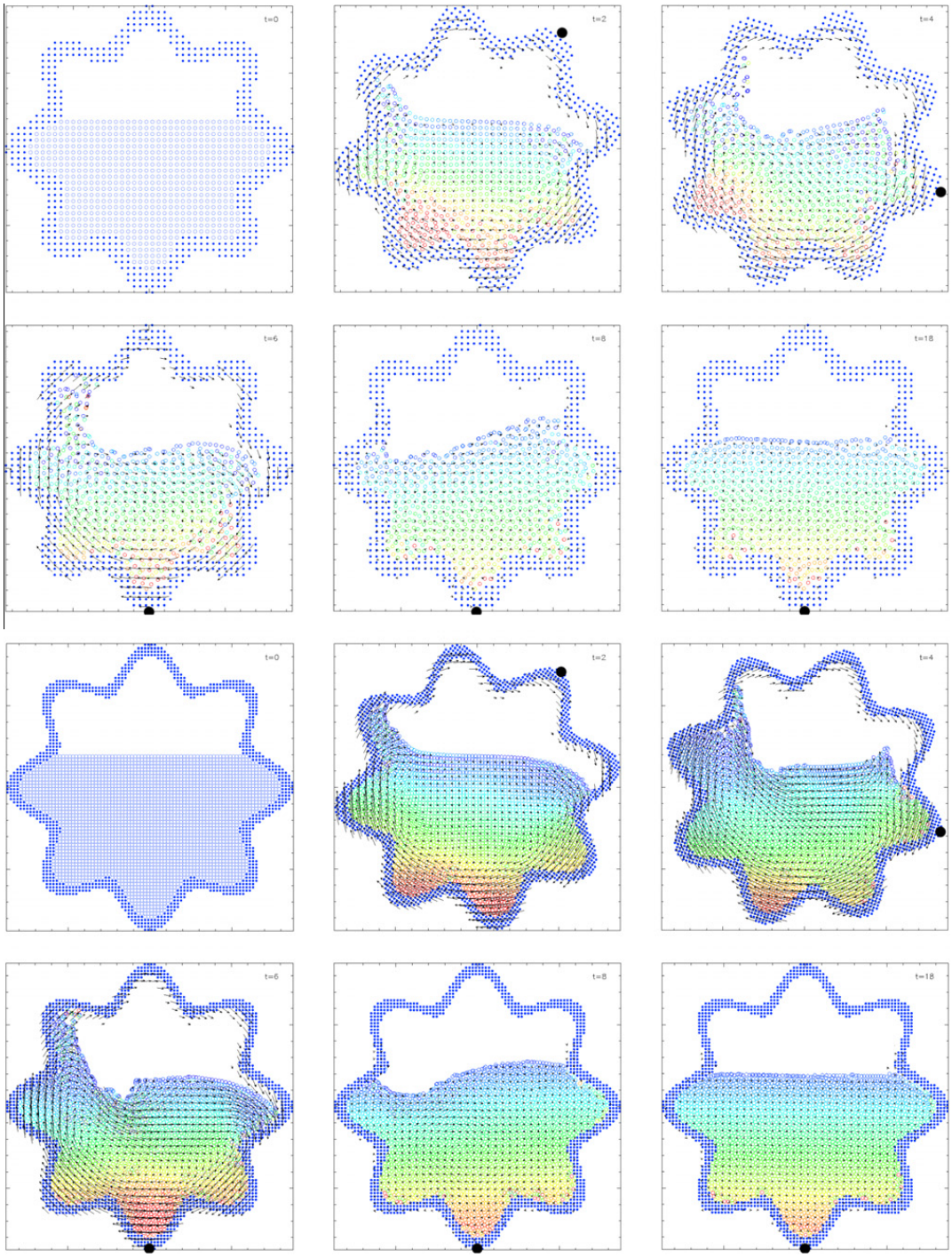

Fig. 17. Snapshots of the rotating cylinder with rippled wall for two resolutions $r_c = 0.12$ (upper half) and $r_c = 0.06$ (lower half). The fluid phase is colored with the pressure field in the range of $p = 0$ (blue) to $p = 1$ (red) and velocity vectors visualize the instantaneous flow field and the rotating cylinder wall. (For interpretation of the references to colour in this figure legend, the reader is referred to the web version of this article.)

First, the water column is exposed to a constant gravitational acceleration of $g = 1$ in negative y-direction. As for the hydrostatic tank simulations, we damp the motion of the fluid until $T = 1$ to smooth spurious oscillations caused by the initial gravitational acceleration. To stabilize the simulation we use a small artificial viscosity $\alpha = 0.1$ which according to Eq. (11) is equivalent to a Reynolds number of $Re = 200$. Then, we rotate the walls with an angular velocity of $\dot{\varphi} = 0.1$ for a half turn. The water column eventually settles in the cylinder with a hydrostatic pressure profile. Fig. 16(b) shows the pressure in the center of the cylinder along the y-axis from the bottom of the wall to the free surface at $T = 18$, where the fluid has settled again after the half turn. The linear slope of the pressure profile in the water column is well reproduced and with increasing resolution the pressure converges to the analytic solution.

Author's personal copy

A visualization of the flow field and pressure field in the fluid is shown in Fig. 17. The two columns show the result with different resolutions of $r_c = 0.12$ and $r_c = 0.06$ at $T = 2, 4, 6, 8$ and 18. After the initial damping time $T_{damp} = 1$ the cylinder is rotated with $\dot{\varphi} = 0.1$ until $T = 6$ for a half turn. To clarify the motion of the walls we tracked the initial tip of the cylinder wall with the black bold mark over time in the snapshots. The color in the fluid phase denotes the pressure field in the water in the range of $p = 0$ (blue) to $p = 1$ (red). We also show qualitatively the instantaneous velocity field with velocity vectors. The simulation shows a strong sloshing in the fluid phase due to the rotation of the walls and finally the fluid settles to a hydrostatic water column. With a higher resolution the free surface and flow field reproduce the results of the lower resolution and show some more details of the fluid phase during the sloshing phase. This case demonstrates the robustness of our method for simulating complex moving boundaries interacting with violently moving free-surfaces.

8. Conclusion

We have developed a new approach to simulate solid, non-permeable walls with SPH. Derived from a force balance at the wall boundary, this method incorporates external body forces such as gravitation in dynamical situations. Our proposed boundary particle treatment is simple and general. Solid walls are discretized with dummy particles in a layer of width r_c along the interface. The velocity at dummy particles is extrapolated from the adjacent fluid phase allowing for free-slip or no-slip boundary conditions and a pressure boundary condition prevents penetration of the wall. To calculate the velocity and pressure of dummy particles at the boundary an additional summation over its neighbors has to be performed. But as this operation is limited to interface particles only, i.e. particles that interact with other particles than of its own type/phase, the computational overhead is small. We have shown that our method is capable of simulating hydrostatic problems including complex and sharp wall geometries in two and three dimensions. A numerical freefall experiment demonstrates the relevance of the correct boundary condition for wall particles, and a comparison of the well-known dambreak simulation with results in the literature shows good agreement. The simulation of a rotating rippled cylinder shows that this method is capable of dealing with violent free-surface deformations interacting with moving complex boundaries. Another attractive feature of this wall boundary method is its straightforward extension to fluid–structure-interaction (FSI) problems. Since only geometric information is used, the dummy particles can represent real solid particles or can be evolved according to a separate material law.

Acknowledgments

The authors wish to acknowledge the shared funding of this work by the TUM Graduate School (Technische Universität München) and the German Research Foundation (DFG - Deutsche Forschungsgesellschaft) within the project AD 186/6–1. Computational resources have been provided by the LRZ (Leibniz - Rechenzentrum, computer center for Munich's universities) under Grant pr32ma. We acknowledge the work of Sbalzarini et al. [37] who provided the Parallel Particle Mesh (PPM) Library that we used to implement our model and enables us to perform large-scale simulations on parallel computer architectures. We also gratefully thank Daniel Price (School of Mathematical Sciences, Monash University, Australia) for his introduction and support with *Splash* [38] which was used to produce most of the figures in this paper and John Biddiscombe (CSCS, Swiss National Supercomputing Centre, Switzerland) for his help with *pv-meshless* [39]. Last but not least, sincere thanks go to the reviewers of this paper who ensured that our method is well described.

References

[1] R. Gingold, J. Monaghan, Smoothed particle hydrodynamics –theory and application to non-spherical stars, Mon. Not. R. Astron. Soc. 181 (1977) 375.
[2] L.B. Lucy, A numerical approach to the testing of the fission hypothesis, Astron. J. 82 (12) (1977) 1013.
[3] D.J. Price, Smoothed particle magnetohydrodynamics – IV. Using the vector potential, Mon. Not. Roy. Astron. Soc. 401 (3) (2010) 1475–1499.
[4] L.D. Libersky, A.G. Petschek, Smooth particle hydrodynamics with strength of materials, in: H. Trease, M. Fritts, W. Crowley (Eds.), Advances in the Free-Lagrange Method Including Contributions on Adaptive Gridding and the Smooth Particle Hydrodynamics Method, Lecture Notes in Physics, vol. 395, Springer Berlin Heidelberg, Berlin, Heidelberg, 1991, pp. 248–257.
[5] W. Benz, E. Asphaug, Simulations of brittle solids using smooth particle hydrodynamics, Comput. Phys. Commun. 87 (1–2) (1995) 253–265.
[6] J. Bonet, S. Kulasegaram, M.X. Rodriguez-Paz, M. Profit, Variational formulation for the smooth particle hydrodynamics (SPH) simulation of fluid and solid problems, Comput. Methods Appl. Mech. Engrg. 193 (12–14) (2004) 1245–1256.
[7] S.E. Hieber, P. Koumoutsakos, A Lagrangian particle method for the simulation of linear and nonlinear elastic models of soft tissue, J. Comput. Phys. 227 (21) (2008) 9195–9215.
[8] J.J. Monaghan, Simulating free surface flows with SPH, J. Comput. Phys. 110 (2) (1994) 399–406.
[9] A. Colagrossi, Numerical simulation of interfacial flows by smoothed particle hydrodynamics, J. Comput. Phys. 191 (2) (2003) 448–475.
[10] J.P. Morris, Simulating surface tension with smoothed particle hydrodynamics, Int. J. Numer. Methods Fluids 33 (3) (2000) 333–353.
[11] X.Y. Hu, N.A. Adams, A multi-phase SPH method for macroscopic and mesoscopic flows, J. Comput. Phys. 213 (2) (2006) 844–861.
[12] A.M. Tartakovsky, P. Meakin, T.D. Scheibe, R. Eichlerwest, R.M.E. West, Simulations of reactive transport and precipitation with smoothed particle hydrodynamics, J. Comput. Phys. 222 (2) (2007) 654–672.
[13] S. Adami, X. Hu, N. Adams, A conservative SPH method for surfactant dynamics, J. Comput. Phys. 229 (5) (2010) 1909–1926.
[14] L.D. Libersky, A.G. Petschek, T.C. Carney, J.R. Hipp, F.A. Allahdadi, High strain lagrangian hydrodynamics, J. Comput. Phys. 109 (1) (1993) 67–75.
[15] J.P. Morris, P.J. Fox, Y. Zhu, Modeling low reynolds number incompressible flows using SPH, J. Comput. Phys. 136 (1) (1997) 214–226.
[16] S. Hieber, P. Koumoutsakos, An immersed boundary method for smoothed particle hydrodynamics of self-propelled swimmers, J. Comput. Phys. 227 (19) (2008) 8636–8654.
[17] M. De Leffe, D. Le Touze, B. Alessandrini, Normal flux method at the boundary for SPH, in: Proceedings of the 4th SPHERIC Workshop, 2009, pp. 150–157.

Author's personal copy

[18] M. Ferrand, D. Laurence, B. Rogers, D. Violeau, Improved time scheme integration approach for dealing with semi analytic bounday conditions in SPARTACUS2D, in: Proceedings of the 5th SPHERIC Workshop, 2010, pp. 98–105.
[19] Monaghan, J.J. Monaghan, J.B. Kajtar, SPH particle boundary forces for arbitrary boundaries, Comput. Phys. Commun. 180 (10) (2009) 1811–1820.
[20] L.D.G. Sigalotti, J. Klapp, E. Sira, Y. Melen, A. Hasmy, SPH simulations of time-dependent poiseuille flow at low reynolds numbers, J. Comput. Phys. 191 (2) (2003) 622–638.
[21] J.J. Monaghan, Smoothed particle hydrodynamics, Ann. Rev. Astron. Astrophys. 68 (8) (2005) 1703–1759.
[22] J. Hongbin, D. Xin, On criterions for smoothed particle hydrodynamics kernels in stable field, J. Comput. Phys. 202 (2) (2005) 699–709.
[23] X.Y. Hu, N.A. Adams, An incompressible multi-phase SPH method, J. Comput. Phys. 227 (1) (2007) 264–278.
[24] J.J. Monaghan, R.A. Gingold, Shock simulation by the particle method SPH, J. Comput. Phys. 52 (2) (1983) 374–389.
[25] J.J. Monaghan, Smoothed particle hydrodynamic simulations of shear flow, Mon. Notices Roy. Astron. Soc. 365 (1) (2006) 199–213.
[26] X.Y. Hu, N.a. Adams, Angular-momentum conservative smoothed particle dynamics for incompressible viscous flows, Phys. Fluids 18 (10) (2006) 101702.
[27] L. Verlet, Computer experiments on classical fluids. I. Thermodynamical properties of Lennard–Jones molecules, Phys. Rev. 159 (1) (1967) 98.
[28] R. Issa, E.S. Lee, D. Violeau, D.R. Laurence, Incompressible separated flows simulations with the smoothed particle hydrodynamics gridless method, Int. J. Numer. Methods Fluids 47 (10–11) (2005) 1101–1106.
[29] R. Issa, Numerical assessment of smoothed particle hydrodynamics gridless method for incompressible flows and its extension to turbulent flows, Ph.d. thesis, University of Manchester, 2005.
[30] J.C. Martin, W.J. Moyce, Part IV. An experimental study of the collapse of liquid columns on a rigid horizontal plane, Philos. Trans. Roy. Soc. Lond. Ser. A 244 (882) (1952) 312–324.
[31] A. Ritter, Die Fortpflanzung der Wasserwellen, Z. Ver. deut. Ing. 36 (1982).
[32] J.P. Hughes, D.I. Graham, Comparison of incompressible and weakly-compressible SPH models for free-surface water flows, J. Hydraul. Res. 48 (2010) 105–107.
[33] J.J. Monaghan, On the problem of penetration in particle methods, J. Comput. Phys. 82 (1) (1989) 1–15.
[34] B. Buchner, Green water on ship-type offshore structures, Ph.D. thesis, Delft University of Technology, 2002.
[35] S. Marrone, M. Antuono, A. Colagrossi, G. Colicchio, D. Le Touzé, G. Graziani, δ-SPH model for simulating violent impact flows, Comput. Methods Appl. Mech. Eng. 200 (13–16) (2011) 1526–1542.
[36] M. Greco, A two-dimensional study of green-water loading, Ph.D. thesis, 2001.
[37] I.F. Sbalzarini, J.H. Walther, M. Bergdorf, S.E. Hieber, E.M. Kotsalis, P. Koumoutsakos, PPM A highly efficient parallel particlemesh library for the simulation of continuum systems, J. Comput. Phys. 215 (2) (2006) 566–588.
[38] D.J. Price, SPLASH: An interactive visualisation tool for smoothed particle hydrodynamics simulations, Publ. Astron. Soc. Aus. 24 (2007) 159–173.
[39] J. Biddiscombe, D. Graham, P. Maruzewski, R. Issa, Visualization and analysis of SPH data, ERCOFTAC Bull. 76 (2008) 9–12.

A.2. A TRANSPORT-VELOCITY FORMULATION FOR SMOOTHED PARTICLE HYDRODYNAMICS

Rightslink Printable License https://s100.copyright.com/App/PrintableLicenseFrame.jsp?publisherI...

ELSEVIER LICENSE
TERMS AND CONDITIONS

Mar 15, 2013

This is a License Agreement between Stefan Adami ("You") and Elsevier ("Elsevier") provided by Copyright Clearance Center ("CCC"). The license consists of your order details, the terms and conditions provided by Elsevier, and the payment terms and conditions.

All payments must be made in full to CCC. For payment instructions, please see information listed at the bottom of this form.

Supplier	Elsevier Limited The Boulevard,Langford Lane Kidlington,Oxford,OX5 1GB,UK
Registered Company Number	1982084
Customer name	Stefan Adami
Customer address	Technische Universität München Garching, 85748
License number	3110211105572
License date	Mar 15, 2013
Licensed content publisher	Elsevier
Licensed content publication	Journal of Computational Physics
Licensed content title	A transport-velocity formulation for smoothed particle hydrodynamics
Licensed content author	S. Adami,X.Y. Hu,N.A. Adams
Licensed content date	15 May 2013
Licensed content volume number	241
Licensed content issue number	
Number of pages	16
Start Page	292
End Page	307
Type of Use	reuse in a thesis/dissertation
Intended publisher of new work	other
Portion	full article
Format	both print and electronic
Are you the author of this Elsevier article?	Yes
Will you be translating?	No
Order reference number	
Title of your thesis/dissertation	Modeling and Simulation of Multiphase Phenomena with SPH
Expected completion date	Apr 2013
Estimated size (number of pages)	120

1 von 5 15.03.2013 14:07

Elsevier VAT number	GB 494 6272 12
Permissions price	0.00 EUR
VAT/Local Sales Tax	0.0 USD / 0.0 GBP
Total	0.00 EUR
Terms and Conditions	

INTRODUCTION

1. The publisher for this copyrighted material is Elsevier. By clicking "accept" in connection with completing this licensing transaction, you agree that the following terms and conditions apply to this transaction (along with the Billing and Payment terms and conditions established by Copyright Clearance Center, Inc. ("CCC"), at the time that you opened your Rightslink account and that are available at any time at http://myaccount.copyright.com).

GENERAL TERMS

2. Elsevier hereby grants you permission to reproduce the aforementioned material subject to the terms and conditions indicated.

3. Acknowledgement: If any part of the material to be used (for example, figures) has appeared in our publication with credit or acknowledgement to another source, permission must also be sought from that source. If such permission is not obtained then that material may not be included in your publication/copies. Suitable acknowledgement to the source must be made, either as a footnote or in a reference list at the end of your publication, as follows:

"Reprinted from Publication title, Vol /edition number, Author(s), Title of article / title of chapter, Pages No., Copyright (Year), with permission from Elsevier [OR APPLICABLE SOCIETY COPYRIGHT OWNER]." Also Lancet special credit - "Reprinted from The Lancet, Vol. number, Author(s), Title of article, Pages No., Copyright (Year), with permission from Elsevier."

4. Reproduction of this material is confined to the purpose and/or media for which permission is hereby given.

5. Altering/Modifying Material: Not Permitted. However figures and illustrations may be altered/adapted minimally to serve your work. Any other abbreviations, additions, deletions and/or any other alterations shall be made only with prior written authorization of Elsevier Ltd. (Please contact Elsevier at permissions@elsevier.com)

6. If the permission fee for the requested use of our material is waived in this instance, please be advised that your future requests for Elsevier materials may attract a fee.

7. Reservation of Rights: Publisher reserves all rights not specifically granted in the combination of (i) the license details provided by you and accepted in the course of this licensing transaction, (ii) these terms and conditions and (iii) CCC's Billing and Payment terms and conditions.

8. License Contingent Upon Payment: While you may exercise the rights licensed immediately upon issuance of the license at the end of the licensing process for the transaction, provided that you have disclosed complete and accurate details of your proposed use, no license is finally effective unless and until full payment is received from you (either by publisher or by CCC) as provided in CCC's Billing and Payment terms and conditions. If full payment is not received on a timely basis, then any license preliminarily

granted shall be deemed automatically revoked and shall be void as if never granted. Further, in the event that you breach any of these terms and conditions or any of CCC's Billing and Payment terms and conditions, the license is automatically revoked and shall be void as if never granted. Use of materials as described in a revoked license, as well as any use of the materials beyond the scope of an unrevoked license, may constitute copyright infringement and publisher reserves the right to take any and all action to protect its copyright in the materials.

9. Warranties: Publisher makes no representations or warranties with respect to the licensed material.

10. Indemnity: You hereby indemnify and agree to hold harmless publisher and CCC, and their respective officers, directors, employees and agents, from and against any and all claims arising out of your use of the licensed material other than as specifically authorized pursuant to this license.

11. No Transfer of License: This license is personal to you and may not be sublicensed, assigned, or transferred by you to any other person without publisher's written permission.

12. No Amendment Except in Writing: This license may not be amended except in a writing signed by both parties (or, in the case of publisher, by CCC on publisher's behalf).

13. Objection to Contrary Terms: Publisher hereby objects to any terms contained in any purchase order, acknowledgment, check endorsement or other writing prepared by you, which terms are inconsistent with these terms and conditions or CCC's Billing and Payment terms and conditions. These terms and conditions, together with CCC's Billing and Payment terms and conditions (which are incorporated herein), comprise the entire agreement between you and publisher (and CCC) concerning this licensing transaction. In the event of any conflict between your obligations established by these terms and conditions and those established by CCC's Billing and Payment terms and conditions, these terms and conditions shall control.

14. Revocation: Elsevier or Copyright Clearance Center may deny the permissions described in this License at their sole discretion, for any reason or no reason, with a full refund payable to you. Notice of such denial will be made using the contact information provided by you. Failure to receive such notice will not alter or invalidate the denial. In no event will Elsevier or Copyright Clearance Center be responsible or liable for any costs, expenses or damage incurred by you as a result of a denial of your permission request, other than a refund of the amount(s) paid by you to Elsevier and/or Copyright Clearance Center for denied permissions.

LIMITED LICENSE

The following terms and conditions apply only to specific license types:

15. **Translation**: This permission is granted for non-exclusive world **English** rights only unless your license was granted for translation rights. If you licensed translation rights you may only translate this content into the languages you requested. A professional translator must perform all translations and reproduce the content word for word preserving the integrity of the article. If this license is to re-use 1 or 2 figures then permission is granted for non-exclusive world rights in all languages.

16. **Website**: The following terms and conditions apply to electronic reserve and author websites:
Electronic reserve: If licensed material is to be posted to website, the web site is to be

password-protected and made available only to bona fide students registered on a relevant course if:
This license was made in connection with a course,
This permission is granted for 1 year only. You may obtain a license for future website posting,
All content posted to the web site must maintain the copyright information line on the bottom of each image,
A hyper-text must be included to the Homepage of the journal from which you are licensing at http://www.sciencedirect.com/science/journal/xxxxx or the Elsevier homepage for books at http://www.elsevier.com , and
Central Storage: This license does not include permission for a scanned version of the material to be stored in a central repository such as that provided by Heron/XanEdu.

17. **Author website** for journals with the following additional clauses:

All content posted to the web site must maintain the copyright information line on the bottom of each image, and the permission granted is limited to the personal version of your paper. You are not allowed to download and post the published electronic version of your article (whether PDF or HTML, proof or final version), nor may you scan the printed edition to create an electronic version. A hyper-text must be included to the Homepage of the journal from which you are licensing at http://www.sciencedirect.com/science/journal/xxxxx . As part of our normal production process, you will receive an e-mail notice when your article appears on Elsevier's online service ScienceDirect (www.sciencedirect.com). That e-mail will include the article's Digital Object Identifier (DOI). This number provides the electronic link to the published article and should be included in the posting of your personal version. We ask that you wait until you receive this e-mail and have the DOI to do any posting.

Central Storage: This license does not include permission for a scanned version of the material to be stored in a central repository such as that provided by Heron/XanEdu.

18. **Author website** for books with the following additional clauses:
Authors are permitted to place a brief summary of their work online only.
A hyper-text must be included to the Elsevier homepage at http://www.elsevier.com . All content posted to the web site must maintain the copyright information line on the bottom of each image. You are not allowed to download and post the published electronic version of your chapter, nor may you scan the printed edition to create an electronic version.

Central Storage: This license does not include permission for a scanned version of the material to be stored in a central repository such as that provided by Heron/XanEdu.

19. **Website** (regular and for author): A hyper-text must be included to the Homepage of the journal from which you are licensing at http://www.sciencedirect.com/science/journal/xxxxx. or for books to the Elsevier homepage at http://www.elsevier.com

20. **Thesis/Dissertation**: If your license is for use in a thesis/dissertation your thesis may be submitted to your institution in either print or electronic form. Should your thesis be published commercially, please reapply for permission. These requirements include permission for the Library and Archives of Canada to supply single copies, on demand, of the complete thesis and include permission for UMI to supply single copies, on demand, of the complete thesis. Should your thesis be published commercially, please reapply for permission.

21. **Other Conditions**:

v1.6

If you would like to pay for this license now, please remit this license along with your payment made payable to "COPYRIGHT CLEARANCE CENTER" otherwise you will be invoiced within 48 hours of the license date. Payment should be in the form of a check or money order referencing your account number and this invoice number RLNK500978202.
Once you receive your invoice for this order, you may pay your invoice by credit card. Please follow instructions provided at that time.

Make Payment To:
Copyright Clearance Center
Dept 001
P.O. Box 843006
Boston, MA 02284-3006

For suggestions or comments regarding this order, contact RightsLink Customer Support: customercare@copyright.com or +1-877-622-5543 (toll free in the US) or +1-978-646-2777.

Gratis licenses (referencing $0 in the Total field) are free. Please retain this printable license for your reference. No payment is required.

Author's personal copy

Journal of Computational Physics 241 (2013) 292–307

Contents lists available at SciVerse ScienceDirect

Journal of Computational Physics

journal homepage: www.elsevier.com/locate/jcp

A transport-velocity formulation for smoothed particle hydrodynamics

S. Adami *, X.Y. Hu, N.A. Adams

Institute of Aerodynamics, Technische Universität München, 85748 Garching, Germany

ARTICLE INFO

Article history:
Received 27 September 2012
Received in revised form 30 January 2013
Accepted 31 January 2013
Available online 14 February 2013

Keywords:
Weakly-compressible SPH
Background pressure
Internal flows

ABSTRACT

The standard weakly-compressible SPH method suffers from particle clumping and void regions for high Reynolds number flows and when negative pressures occur in the flow. As a remedy, a new algorithm is proposed that combines the homogenization of the particle configuration by a background pressure while at the same time reduces artificial numerical dissipation. The transport or advection velocity of particles is modified and an effective stress term occurs in the momentum balance that accounts for the difference between advection velocity times particle density and actual particle momentum. The present formulation can be applied for internal flows where the density summation is applicable. A wide range of test cases demonstrates unprecedented accuracy and stability of the proposed modification even at previously infeasible conditions.

© 2013 Elsevier Inc. All rights reserved.

1. Introduction

Smoothed particle hydrodynamics (SPH) is a fully Lagrangian, mesh-free method that was proposed 1977 independently by Lucy [1] and Gingold and Monaghan [2]. Originally, SPH was used to simulate astrophysical problems as its meshless nature and the exact advection are very attractive for these kind of problems. The key idea of SPH is to use a smoothing kernel to approximate field quantities at arbitrarily distributed discretization points (particles) and move these points with their local velocity. As a result of this smoothing technique, spatial derivatives are calculated only from interactions with any neighboring particles. In practice, the smoothing kernel has compact support to limit the number of interacting particles and the width of this kernel represents the discretization length scale of SPH.

In the past, SPH has been applied successfully to a broad range of problems beyond its original purpose. Different equations of motion can easily be incorporated by modifying the interactions between different particles, thus almost any continuum system that can be formulated in terms of partial differential equations can be discretized by SPH. A comprehensive overview of the capabilities of SPH is presented in the review article of Monaghan [3], where the principles of the method to simulate compressible flows (astrophysical problems) and incompressible fluid dynamics as well as solid mechanics within a unified framework are described.

Compared to mesh-based methods the evolution of a system in a Lagrangian framework offers many important advantages. Most obviously, advection is treated exactly by a Lagrangian particle method and exact conservation of mass and momentum is ensured in a straightforward way. Furthermore, for multi-phase problems the interaction-based force calculation allows for a modeling of very complex physical phenomena at phase interfaces without the need of additional surface-front detection algorithms. Large deformations and complex geometry changes such as fragmentation can be treated implicitly with SPH and the required preprocessing of a simulation is small.

* Corresponding author. Tel.: +49 89 28916122.
E-mail address: stefan.adami@tum.de (S. Adami).

0021-9991/$ - see front matter © 2013 Elsevier Inc. All rights reserved.
http://dx.doi.org/10.1016/j.jcp.2013.01.043

Author's personal copy

When solving incompressible fluid dynamics with SPH there are mainly two basic strategies, namely a true incompressible formulation (ISPH) and the weakly compressible model (WCSPH). In the former method a pressure Poisson equation is solved and the divergence condition for the velocity field is enforced, see e.g. [4–6]. This approach was shown to give accurate results for free-surface and multiphase flows but the computational complexity is high. The latter approach treats the fluid as weakly compressible with an equation of state that relates the fluid density to a hydrodynamic pressure. Given that the magnitude of the speed of sound and the characteristic flow velocities are well separated, density fluctuations remain small and the fluid behaves quasi-incompressible. Due to its simplicity and lower computational cost this method is widely used for various kinds of problems, see e.g. [7–11].

In this work we propose a new transport-velocity formulation for weakly-compressible SPH that resolves an important dilemma of the classical WCSPH scheme. According to the theory of incompressible flow, the pressure in the fluid takes effect merely by its gradient. Therefore, the flow is invariant of a superimposed constant background pressure field, i.e. it is gauge invariant. However, since the standard SPH is not 0th-order consistent, gauge invariance is not recovered numerically, leading to a spurious pressure gradient from a formally constant pressure field. Hence, the simulation results change with different background pressures. Ideally, no background pressure should need to be added to the system. On the other hand, when a low (zero) background pressure is imposed, SPH suffers from the so-called tensile instability. This instability is caused by particle clumping due to attraction forces between neighboring particles with effectively negative pressures. A possible solution to this problem is to increase the background pressure that ensures non-negative pressures in the entire domain, but as mentioned before this introduces additional numerical viscous dissipation that can be comparable to the physical viscous dissipation. Thus, increasing the background pressure effectively changes the Reynolds number of the flow, and consequently the application of SPH to practical industrial applications is substantially impeded. Note that our method mainly addresses the tensile instability problem, a "cousin of the pairing instability" with the same symptoms [12]. As a side-effect we found that with the new method the pairing instability [13] does not occur either. Alternatively the latter instability could also be circumvented by using kernels that have non-negative kernel Fourier transforms [12,14].

In 1989 Monaghan [15] addressed the problem of penetration in particle methods and proposed a modified advection velocity based on a smoothing of the velocity field. This so-called XSPH correction can improve the smoothness of the flow field, but, strictly speaking, the smoothing is arbitrary involving an unknown parameter. Another classical workaround for the clumping problem is to use an artificial viscosity that stops particles approaching each other when they are very close, e.g. Monaghan [3]. Whilst this artificial dissipation can be shown to take effect as a physical viscosity, and thus is used to simulate real flows at finite Reynolds numbers, at the same time the numerical dissipation required to stabilize the simulation of high Reynolds number flows can become comparable to the physical viscosity and of course strongly affects the results.

For truly incompressible SPH methods the particle clumping problem is easily suppressed as the divergence-free condition for the velocity field and the constant-density condition can be enforced separately. Hu and Adams [4] use a fractional time-step integration with an intermediate projection step and experienced no problems with particle penetration. Xu et al. [6] proposed an ISPH method that takes advantage of an additional diffusion-based particle shifting scheme ensuring well homogenized particle configurations at all times. Very recently, Lind et al. [16] extended this approach for free-surface problems where the standard method failed due to the incomplete kernel support of particles at the free surface. Additionally, they use the kernel gradient normalization and approximate the shifted particle quantities by a Taylor series to improve the accuracy of the scheme.

As a new, fundamentally different approach, we present here a simple and effective algorithm based on the classical WCSPH without need for additional parameters and involving only a marginally small computational overhead. The new method is characterized by the different utilization of a background pressure on computing the particle momentum velocity and the particle advection velocity. As a consequence of the new advection velocity, an additional term appears in the momentum equation that accounts for the difference between the motion of a particle and its averaged momentum. In more detail, the particle advection velocity is obtained from the momentum velocity corrected for the effect of a constant background pressure. Thus, regularization of the particle motion is achieved by the background pressure but the particle momentum is unaffected, i.e. no artificial dissipation of momentum occurs. The correction term in the momentum equation due to the different velocities acts as an effective stress and can be discretized in conservative form. While this correction is negligible when the flow is well resolved with the given size of a particle, it has considerable effects when the flow is not well resolved, e.g. for huge Reynolds numbers, and helps to prevent particle clustering. We point out that the present method is currently limited to internal flows. Free surfaces and inner surfaces of breaking waves for example would be treated as empty space and be filled with particles. An extension of this method for such cases requires the incorporation of suitable boundary conditions at the free surface and is subject of current work.

After describing our new method in detail in Section 2 we present many classical test problems of SPH in Section 3. The results show that our scheme prevents voids and particle clustering while strongly reducing numerical dissipation compared to standard WCSPH. Allowing for stable simulations at high Reynolds numbers, this method strongly extends the capabilities of SPH to simulate real applications. Finally, concluding remarks are given in Section 4.

Author's personal copy

2. Method

In this section we present our method in detail and focus on the new particle transport or advection velocity. We initialize all our simulations with Cartesian particles using a constant particle spacing Δx. Each particle is assigned a constant mass and the density is calculated using the density summation at every time step. Thus, mass conservation is satisfied exactly. We solve the incompressible Navier–Stokes equations in a Lagrangian frame and consider external body forces, viscous forces and pressure forces. Note, our general formulation holds for multi-phase problems as well (see the Rayleigh–Taylor instability in Section 3.6), but in the current work we do not include surface-tension effects. Fluids are treated as weakly compressible using an equation-of-state to relate the pressure to the density, and viscous effects are incorporated with a physical viscosity model [8] rather than an artificial viscosity.

In XSPH [15] particles are moved with a smoothed velocity field to prevent particle penetration. Here, we do not advect particles with the momentum velocity but use an advection velocity $\widetilde{\mathbf{v}}$ which is defined as the momentum velocity corrected by a pressure force due to an arbitrary but constant pressure field. Effectively, this advection velocity maintains a homogeneous particle distribution while it avoids the classical background-pressure problem in the momentum equation. Introducing the modified advection velocity into the conservation law for the momentum of a Lagrangian particle, for clarity using index notation, we obtain

$$\frac{\partial(\rho v_i)}{\partial t} + \widetilde{v}_j \frac{\partial(\rho v_i)}{\partial x_j} - \widetilde{v}_j \frac{\partial(\rho v_i)}{\partial x_j} + v_j \frac{\partial(\rho v_i)}{\partial x_j} = [\cdots]_i - \rho v_i \frac{\partial v_j}{\partial x_j}, \tag{1}$$

where $[\cdots]_i$ is short for the other components of the right-hand-side (pressure force, viscous force and body force). Defining the material derivative of a particle moving with the modified advection velocity $\widetilde{\mathbf{v}}$ as

$$\frac{\widetilde{d}(\bullet)}{dt} = \frac{\partial(\bullet)}{\partial t} + \widetilde{\mathbf{v}} \cdot \nabla(\bullet) \tag{2}$$

we rearrange the momentum equation to obtain

$$\frac{\widetilde{d}(\rho v_i)}{dt} = [\cdots]_i + \frac{\partial}{\partial x_j}\left(\rho v_i(\widetilde{v}_j - v_j)\right) - \rho v_i \frac{\partial \widetilde{v}_j}{\partial x_j}. \tag{3}$$

By the weakly compressible approximation the divergence of the advection velocity $\widetilde{\mathbf{v}}$ is approximately zero and thus can be neglected. Hence, the final form of the momentum equation for a Lagrangian particle moving with $\widetilde{\mathbf{v}}$ is

$$\frac{\widetilde{d}(\rho \mathbf{v})}{dt} = -\nabla p + \eta \nabla^2 \mathbf{v} + \rho \mathbf{g} + \nabla \cdot (\rho \mathbf{v}(\widetilde{\mathbf{v}} - \mathbf{v})). \tag{4}$$

The last term on the right-hand-side is a consequence of the modified advection velocity and can be interpreted as the convection of momentum with the relative velocity $(\widetilde{\mathbf{v}} - \mathbf{v})$. In the following we use the tensor $\mathbf{A} = \rho \mathbf{v}(\widetilde{\mathbf{v}} - \mathbf{v})$ for this term. Note the relation to the concept of Lagrangian mean motion [17]

2.1. Density summation

The density of each particle is calculated from a summation over all neighboring particles j

$$\rho_i = m_i \sum_j W_{ij}, \tag{5}$$

where ρ_i and m_i denote the density and mass of particle i. As kernel function $W_{ij} = W(\mathbf{r}_i - \mathbf{r}_j, h)$ we use the quintic spline function [18] with the smoothing length h set equal to the initial particle distance Δx. Note that the use of the density summation allows for density discontinuities, and, as the particle mass m_i does not change during a simulation, total mass is conserved exactly.

2.2. Conservation of momentum

The conservation equation for the momentum (4) is discretized following the standard SPH methodology in conservative form, i.e. using symmetric inter-particle pair forces. The properties $\mathbf{v}, p, v, \mathbf{g}$ and t in Eq. (4) are the particle velocity, pressure, kinematic viscosity, external body force and time, respectively. Using the inter-particle-averaged shear viscosity ($\eta = \rho v$)

$$\widetilde{\eta}_{ij} = \frac{2\eta_i \eta_j}{\eta_i + \eta_j}, \tag{6}$$

together with the density-weighted pressure,

$$\widetilde{p}_{ij} = \frac{\rho_j p_i + \rho_i p_j}{\rho_i + \rho_j} \tag{7}$$

Author's personal copy

the discretized momentum equation allowing for multi-phase problems is given by [8,19]

$$\frac{\widetilde{d}\mathbf{v}_i}{dt} = \frac{1}{m_i}\sum_j \left(V_i^2 + V_j^2\right)\left[-\widetilde{p}_{ij}\frac{\partial W}{\partial r_{ij}}\mathbf{e}_{ij} + \frac{1}{2}\left(\mathbf{A}_i + \mathbf{A}_j\right)\cdot\frac{\partial W}{\partial r_{ij}}\mathbf{e}_{ij} + \widetilde{\eta}_{ij}\frac{\mathbf{v}_{ij}}{r_{ij}}\frac{\partial W}{\partial r_{ij}}\right] + \mathbf{g}_i. \tag{8}$$

Here, $\mathbf{v}_{ij} = \mathbf{v}_i - \mathbf{v}_j$ is the relative velocity of particle i and j, r_{ij} is the distance $|\mathbf{r}_i - \mathbf{r}_j|$ between two interacting particles and $\frac{\partial W}{\partial r_{ij}}\mathbf{e}_{ij}$ is the kernel-function gradient $\nabla W(\mathbf{r}_i - \mathbf{r}_j, h)$. The additional term on the right-hand-side approximates the divergence of the tensor $\mathbf{A}$ using simply the average of both interacting particles i and j. Generally, the momentum equation can be discretized with SPH in various forms but we favor the above realization since due to the anti-symmetry the linear momentum is conserved exactly.

In the classical weakly-compressible SPH method the pressure of a fluid particle is obtained from the density by an equation of state in the form

$$p = p_0\left[\left(\frac{\rho}{\rho_0}\right)^{\gamma} - 1\right] + \chi, \tag{9}$$

where p_0, ρ_0 and χ are the reference pressure, reference density and background pressure, respectively. Following Morris et al. [18] the reference pressure $p_0 = \gamma c^2/\rho_0$ is calculated with an artificial speed of sound c and the exponent $\gamma = 7$ to limit the density variation to 1%. Usually, the speed of sound is chosen at least one order of magnitude larger than the reference velocity to limit the effect of compressibility on the flow. With our new scheme we suggest to use $\gamma = 1$ and $\chi = 0$, i.e.

$$p = c^2(\rho - \rho_0) = p_0\left(\frac{\rho}{\rho_0} - 1\right), \tag{10}$$

which reduces significantly the magnitude of spurious pressure.

2.3. Particle advection velocity

The key element in our proposed method is the modification of the particle advection velocity. Different from moving the particles with the momentum velocity we define a transport or advection velocity $\widetilde{\mathbf{v}}$ that is used to evolve the position of particles from one time step to the next by

$$\frac{d\mathbf{r}_i}{dt} = \widetilde{\mathbf{v}}_i. \tag{11}$$

Using a constant background pressure field p_b, the particle motion takes advantage of the regularization and anti-clumping effect when advecting with the transport velocity $\widetilde{\mathbf{v}}$. In particle notation, this velocity is obtained at every time-step δt from

$$\widetilde{\mathbf{v}}_i(t + \delta t) = \mathbf{v}_i(t) + \delta t\left(\frac{\widetilde{d}\mathbf{v}_i}{dt} - \frac{1}{\rho_i}\nabla p_b\right), \tag{12}$$

Note that although $\nabla p_b = 0$, the SPH discretization of ∇p_b following Eq. 13 below is not 0th-order consistent and therefore generates a non-vanishing contribution. By simply calculating this discrete gradient of a constant pressure field p_b we incorporate the effect of the actual particle distribution to the motion of the fluid. The discretized form of Eq. (12) is obtained from the standard pressure term discretization using only the position information of the neighbors of particle i. Thus, the background pressure p_b defines the magnitude of this force and occurs as a prefactor in Eq. (13). Using this relation it is straightforward to model multi-phase problems allowing for different reference pressures in different phases. The resulting discrete pressure forces are non-vanishing and create a more uniform pressure distribution. Also, attractive forces between particles with negative pressures from the equation of state are counterbalanced, and tensile instability is suppressed. In the same time we avoid using a background pressure directly in the momentum equation that can lead to pressure-driven instabilities or freezing of particles under very high background pressure conditions [20]. Another important aspect is that the shifting velocity is not decoupled from the momentum velocity since we only modify the momentum velocity by the discrete background-pressure gradient at each time-step. For a uniform particle distribution these contributions would cancel out so that in regions where the flow field is smooth and particles are uniformly distributed the two velocities are almost identical. But in regions with strong flow distortions where particles exhibit an inhomogeneous distribution the trajectory velocity is corrected by the background pressure effect and void regions are inhibited.

In discretized form the trajectory velocity of a particle i reads

$$\widetilde{\mathbf{v}}_i(t + \delta t) = \mathbf{v}_i(t) + \delta t\left(\frac{\widetilde{d}\mathbf{v}_i}{dt} - \frac{p_b}{m_i}\sum_j \left(V_i^2 + V_j^2\right)\frac{\partial W}{\partial r_{ij}}\mathbf{e}_{ij}\right). \tag{13}$$

We use a background pressure p_b which is on the order of the reference pressure p_0. Generally, this pressure could be chosen arbitrarily large as long as the time-step criterion is adjusted properly as a large p_b can cause high accelerations. Note that

Author's personal copy

the additional force in Eq. (13) can be calculated simultaneously with the right-hand-side of the momentum equation so that the additional computational cost of this step is marginal.

2.4. Time-integration scheme

To integrate the equation of motion and the momentum equation in time we adopt the so-called kick-drift-kick scheme as presented by Monaghan [3]. First, the intermediate momentum velocity and the shifting velocity are calculated for each particle using the pressure force $\mathbf{f}_{(p)}$, the viscous force $\mathbf{f}_{(\eta)}$, the body force $\mathbf{g}$ and the background pressure force $\mathbf{f}_{(p_b)}$

$$\mathbf{v}^{n+\frac{1}{2}} = \mathbf{v}^{n} + \frac{\delta t}{2m}\left(\mathbf{f}_{(p)}^{n-\frac{1}{2}} + \mathbf{f}_{(\eta)}^{n-\frac{1}{2}} + \mathbf{g}\right), \tag{14}$$

$$\widetilde{\mathbf{v}}^{n+\frac{1}{2}} = \mathbf{v}^{n+\frac{1}{2}} + \frac{\delta t}{2m}\mathbf{f}_{(p_b)}^{n-\frac{1}{2}}. \tag{15}$$

This step is referred to as the kick step, as only velocities are updated. Using the advection velocity we shift the particles to their new positions by

$$\mathbf{r}^{n+1} = \mathbf{r}^{n} + \delta t\,\widetilde{\mathbf{v}}^{n+\frac{1}{2}}. \tag{16}$$

Now, the density at the new time step $n+1$ is calculated from the updated positions using Eq. (5). At this stage the new inter-particle forces $\mathbf{f}_{(p)}^{n+\frac{1}{2}}$, $\mathbf{f}_{(\eta)}^{n+\frac{1}{2}}$ and $\mathbf{f}_{(p_b)}^{n+\frac{1}{2}}$ are calculated with the intermediate momentum velocity and the new positions. Finally, the velocity at the full time-step is obtained from

$$\mathbf{v}^{n+1} = \mathbf{v}^{n+\frac{1}{2}} + \frac{\delta t}{2m}\left(\mathbf{f}_{(p)}^{n+\frac{1}{2}} + \mathbf{f}_{(\eta)}^{n+\frac{1}{2}} + \mathbf{g}\right). \tag{17}$$

Note, with this scheme the force calculation is performed only once per time-step since in the first sub-step the forces from the second sub-step of the previous time step are used.

For stability reasons the global time-step δt is taken as the minimum of the CFL-condition based on the artificial speed of sound c and the maximum flow speed U

$$\delta t \leqslant 0.25\frac{h}{c + |U|}, \tag{18}$$

the viscous condition

$$\delta t \leqslant 0.25\frac{h^2}{\nu} \tag{19}$$

and the body-force condition

$$\delta t \leqslant 0.25\sqrt{h/|\mathbf{g}|}. \tag{20}$$

2.5. Boundary conditions

Symmetric and periodic boundary conditions are enforced by the use of mirror or ghost particles [21], respectively. These virtual points inherit the fluid properties from their corresponding real particle and are included in the force calculation to ensure full support of the kernel. Furthermore, in case of a symmetry condition the normal velocity component is flipped to mimic a symmetric velocity field. Solid walls are represented with real fixed particles where a Neumann-boundary condition for the pressure is imposed. The velocity at these particles $\mathbf{v}_{solid}$ is interpolated from the adjacent fluid phase and adjusted to enforce the no-slip condition by

$$\mathbf{v}_{solid} = 2\mathbf{v}_{wall} - \mathbf{v}_{fluid}. \tag{21}$$

For details of this boundary treatment we refer the reader to our previous work [22].

3. Numerical examples

We use our proposed method to simulate a broad range of classical SPH test cases, including the challenging Taylor–Green vortex flow or the lid-driven cavity problem. We want to emphasize that the current formulation does not require any additional parameters that need to be adjusted for each problem. The same numerical setup is used for all cases. More precisely, in all examples the speed of sound is chosen ten times larger than the characteristic reference velocity of the problem, and as background pressure for the advective acceleration we use the reference pressure p_0 from the equation of state.

Author's personal copy

3.1. Flow around a periodic lattice of cylinders

In the following example we study the flow through a periodic lattice of cylinders as presented in Morris et al. [18]. In this example all data are given in dimensional form as in the reference. A cylinder of radius $R = 0.02$ m is placed in a square box with length $L = 0.1$ m and the driving body force in x-direction is $g = 1.5 \times 10^{-7}$ m/s^2. The fluid is characterized by $\rho = 1000$ kg/m^3 and $\nu = 10^{-6}$ m^2/s and taking the velocity scale to be $U_{ref} = 5 \times 10^{-5}$ m/s gives a Reynolds number of one. We apply periodic boundary conditions at all boundaries to represent the periodic lattice of cylinders. If this case is simulated with the classical SPH method it is necessary to use a suitably adjusted constant background pressure in the equation of state to avoid void regions without particles in the wake behind the cylinder. The proposed method, however, works well without background pressure in the equation of state. The advective background pressure p_b is fixed as described above and does not require problem-specific adjustment.

The described geometry is discretized with Cartesian particles with an initial spacing of $\Delta x = 0.002$ m and 0.001 m in both directions, thus a total of 2500 particles and 10,000 particles is used, respectively. We compare our results with the finite element method (FEM) reference results of this problem given in [18]. Fig. 1(a) shows two velocity profiles of the axial velocity component $V_x(y)$ as function of the height of the periodic box for the two resolutions. The profiles are taken along vertical lines at $x = L/2$ (Path 1) and $x = L$ (Path 2), i.e. through the center of the box and at the exit of the domain. We find very good agreement in the presented velocity profiles indicating that we obtained converged results. The discrepancy of the velocity profile close to the cylinder surface is caused by the smoothing of the results due to interpolating the particle data onto the vertical lines. With increasing resolution this interpolation error vanishes, see the results at the higher resolution.

Morris et al. [18] also present contour plots of the velocity magnitude in the periodic box. In Fig. 1(b) we superpose their FEM reference results with the flow field extracted from our high-resolution simulation (red lines) using the same velocity scale ($V_{ref} = 10^{-4}$ m/s) for non-dimensionalization and find excellent agreement.

3.2. Channel flow through periodic array of cylinders

To further validate our method we analyze the drag on a cylinder in a periodic channel. The drag is an integrated quantity over the cylindrical surface and is therefore a suitable parameter to quantify the accuracy of a numerical simulation. Different from the previous example, the flow is now wall-bounded at the upper and lower boundaries with a channel height of $H = 4R$, where $R = 0.02m$ is the radius of the cylinder. The cylinder is placed on the centerline of the channel and the total length of the periodic channel segment is $L = 0.12$ m, thus the inter-cylinder distance is $6R$. The liquid has a density and viscosity of $\rho = 1000$ kg/m^3 and $\eta = 0.1$ kg/(ms), respectively. A very detailed study of this problem using standard weakly-compressible SPH is presented in Ellero and Adams [23]. Different to their approach, here we do not adjust the body force in time to achieve a specified, constant mass flux but use a constant driving force $g = 2.5 \times 10^{-4}$ m/s^2 in x-direction that yields an average flow velocity of similar magnitude as their imposed flow ($\langle v \rangle = 1.2 \times 10^{-4}$ m/s). Note that, as we are com-

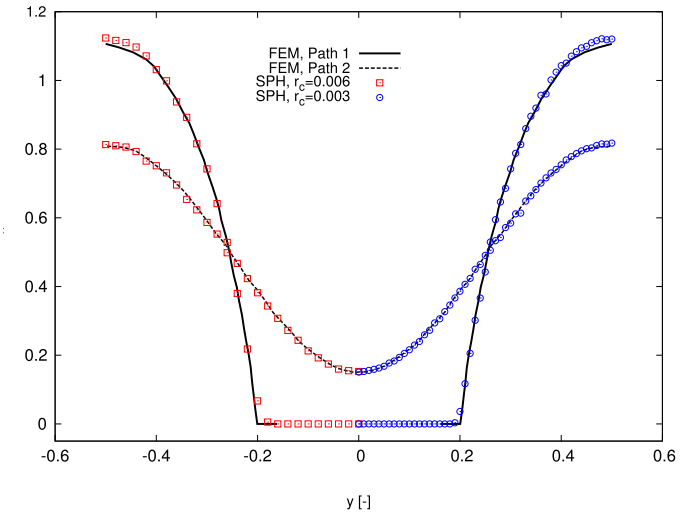

(a) Velocity profiles $V_x(y)$ at $x = L/2$ (Path 1) and $x = L$ (Path 2)

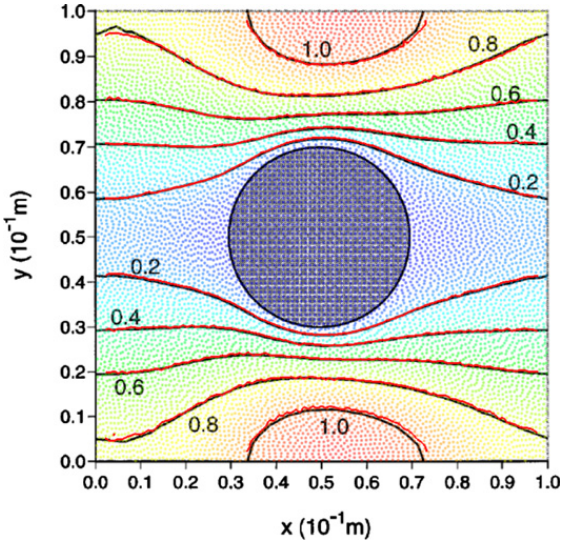

(b) Contour plots of velocity magnitude scaled with $10^{-4} m/s$.

Fig. 1. Comparison of SPH results with FEM reference results [18] for the flow through a periodic lattice of cylinders at $Re = 1$, references reproduced with permission of Elsevier.

Author's personal copy

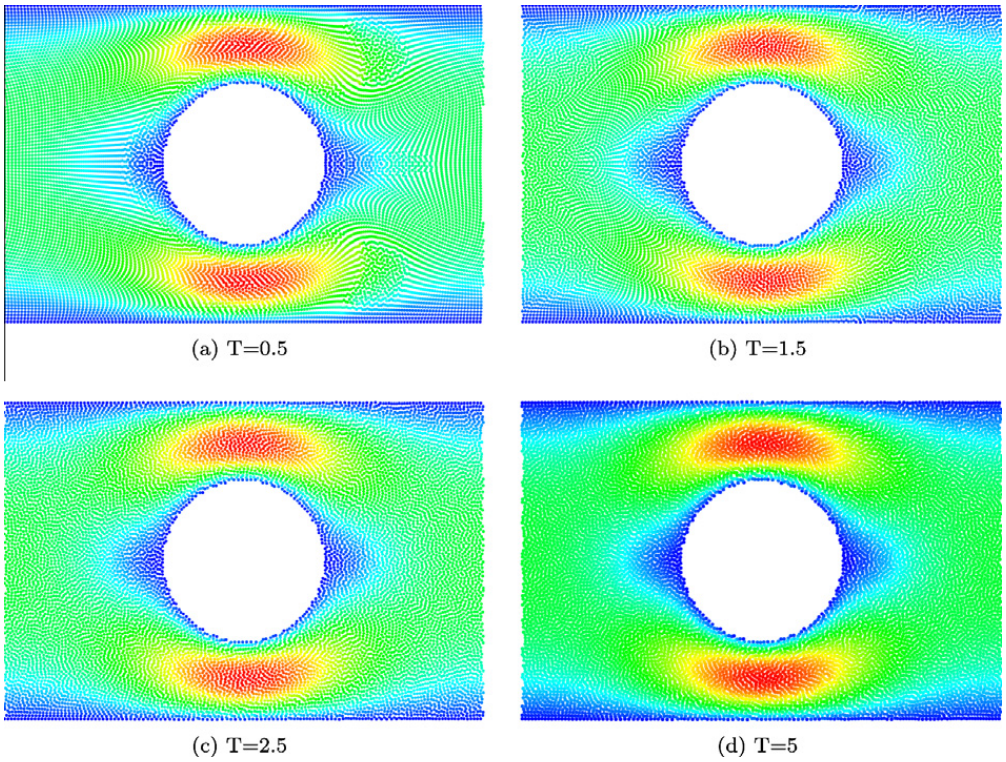

Fig. 2. Snapshots of the particles at various time steps colored with the magnitude of the velocity in the range between 0 (blue) and $3\langle v\rangle$ (red) using 96 particles spanning the channel height.

paring non-dimensional results, the exact flow rate is not important as long as the flow characteristics are similar (the Reynolds number in our simulation differs only by about three percent from $Re = 2.4 \times 10^{-2}$ given by Ellero and Adams [23]). For this example the dominating criterion for determining the speed of sound is the body-force scale and we use $c = 0.1\sqrt{|\mathbf{g}|R} = 2.236 \times 10^{-4}$ m/s. As shown before, with the proposed method the region behind the cylinder is filled with particles immediately after starting the flow, unlike standard SPH that requires a specifically adjusted background pressure in the equation of state to avoid void regions.

As example, Fig. 2 shows several snapshots of the flow using 96 particles spanning the channel height, i.e. a total of 13,824 particles is used in this case. The particles are colored with the magnitude of the local velocity where the colormap ranges from 0 (blue)[1] to $3\langle v\rangle$ (red). The time is scaled with the reference time $t_0 = R/\langle v\rangle$ to indicate the initial transient phase in terms of the characteristic time of the flow.

As we start the simulation from a lattice configuration, i.e. particles are initialized on nodes of a regular Cartesian lattice, it takes several characteristic times to obtain a homogenous particle distribution. After $T = 2.5$ the particle distribution is fully homogeneous. Steady-state quantities are extracted thereafter. The drag coefficient is defined as

$$C_D = \frac{F_D}{\eta\langle v\rangle}, \tag{22}$$

where F_D is the drag force exerted on the cylinder by the fluid. Note that due to symmetry in y-direction with respect to the center of the cylinder the only unbalanced force on the cylinder is F_D in x-direction. Instead of integrating the total stress along the cylinder surface, with particle methods it is straightforward to add all the force interactions between fluid and cylinder-wall particles in order to calculate the resulting drag on the cylinder [23].

Fig. 3 shows the temporal evolution of the drag coefficient obtained from SPH simulations using three resolutions with $\Delta x = H/48$, $\Delta x = h/96$ and $\Delta x = H/192$. The black dashed line denotes the reference result of Liu et al. [24], who obtained a drag coefficient of 106.76 for this case using a FEM code.

At early times, the extracted drag coefficient shows strong variations due to the rearrangement of particles from the initial lattice configuration, as can be seen from the particle snapshots. Later, only small fluctuations around the steady-state can be observed, and with increasing resolution the magnitude of these fluctuations decreases. The agreement with the reference value is very good and with increasing resolution we observe convergence to the exact value.

[1] For interpretation of color in Figs. 1–3, 5, and 7–13 the reader is referred to the web version of this article.

Author's personal copy

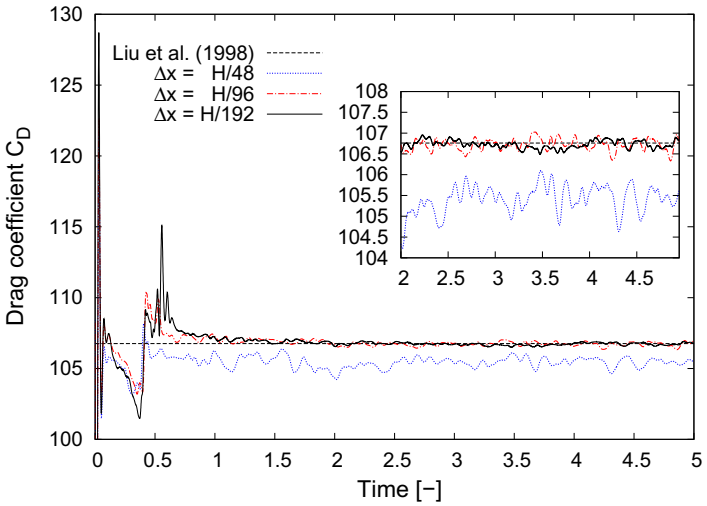

Fig. 3. Drag coefficient evolution: comparison of SPH results at three resolutions and the steady-state results of Liu et al. [24].

3.3. Taylor–Green vortex at $Re = 100$

We simulate the two-dimensional Taylor–Green flow at $Re = 100$ to show that our new approach does not suffer from particle clustering. The analytical solution of the incompressible Navier–Stokes equation for this periodic array of vortices is given by

$$u(x,y,t) = -Ue^{bt}\cos(2\pi x)\sin(2\pi y) \tag{23}$$

$$v(x,y,t) = Ue^{bt}\sin(2\pi x)\cos(2\pi y). \tag{24}$$

It is used as initial velocity distribution at $t = 0$ and as reference solution to check the accuracy of our simulations. The decay rate of the velocity field b is $-8\pi^2/Re$, where $Re = \rho UL/\eta$ is the Reynolds number obtained from the maximum initial velocity U, the density and viscosity of the fluid ρ and η and the length of the periodic vortex array L. In our simulations we use a domain with unit length $L = 1$ and apply periodic boundary conditions in both coordinate directions. At $t = 0$ we initialize the velocity of the particles with the analytical solution using a reference velocity of $U = 1$. We vary the initial particle spacing to study the influence of the resolution and use $\Delta x = 0.02$ (50×50 particles), $\Delta x = 0.01$ (100×100 particles) and $\Delta x = 0.005$ (200×200 particles).

Fig. 4 shows several snapshots of the particle distribution for the Taylor–Green vortex at $Re = 100$ using 2500 particles (50×50). At $t = 0.2$ it is clearly visible that some particles are aligned with the stagnation lines of this flow. Standard SPH applied to this case starting from a regular lattice particle distribution results in a wrong decay of the vortex. Our current method does not suffer from such an error, produces a homogeneous particle distribution and predicts the correct decay rate.

A comparison of the decay of the maximum velocity is shown in Fig. 5, where the decay and error of the maximum velocity over time are shown. Using a log scale the analytical maximum velocity decays linearly with the slope $-b$. Our simulation results show the correct decay rate but with a small shift in the absolute magnitude of the vortex velocity, see Fig. 5(a). This difference is due to the rearrangement of the particles at early times ($t < 0.5$) which causes the small peak and subsequent decrease of the maximum velocity. To show the improvement of our new scheme we also plot the result obtained from the standard weakly-compressible SPH approach, see the crosses in the figure. With the standard SPH method the maximum velocity decay is largely overpredicted and does not converge to the analytic solution (not shown here). The new proposed

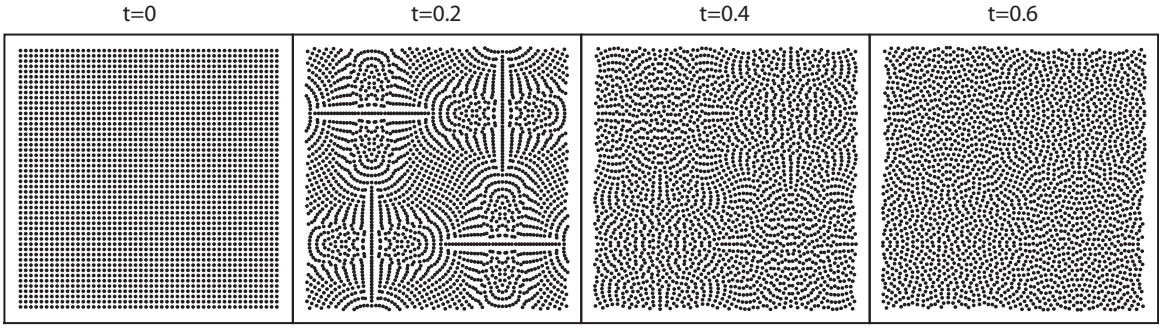

Fig. 4. Particle snapshots for the Taylor–Green problem at $Re = 100$ with a resolution of 50×50 particles.

Author's personal copy

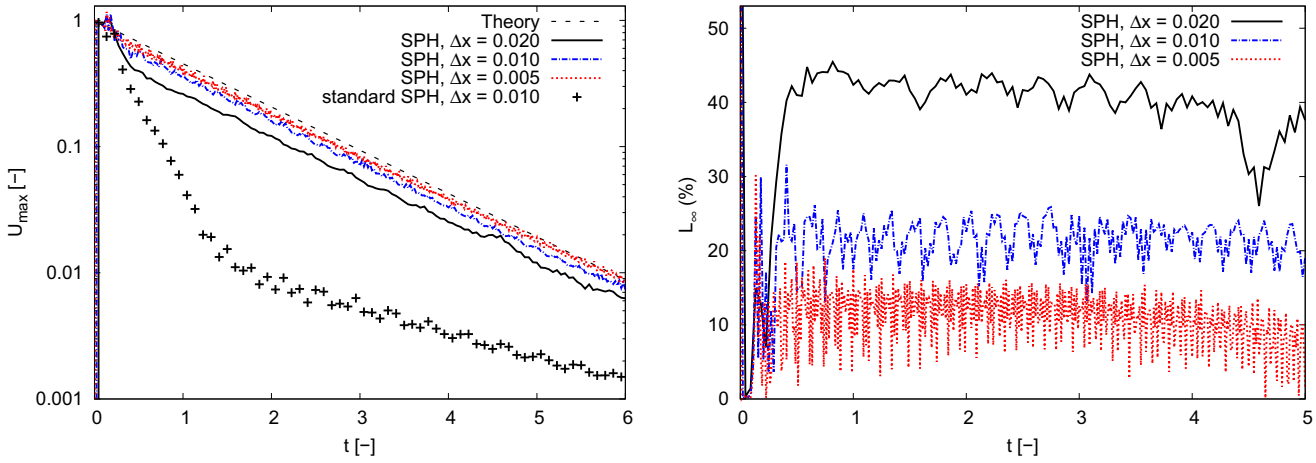

(a) Decay of maximum velocity (b) Relative error of maximum velocity

Fig. 5. Simulation results for the Taylor–Green problem at $Re = 100$ with particles initially on a Cartesian lattice.

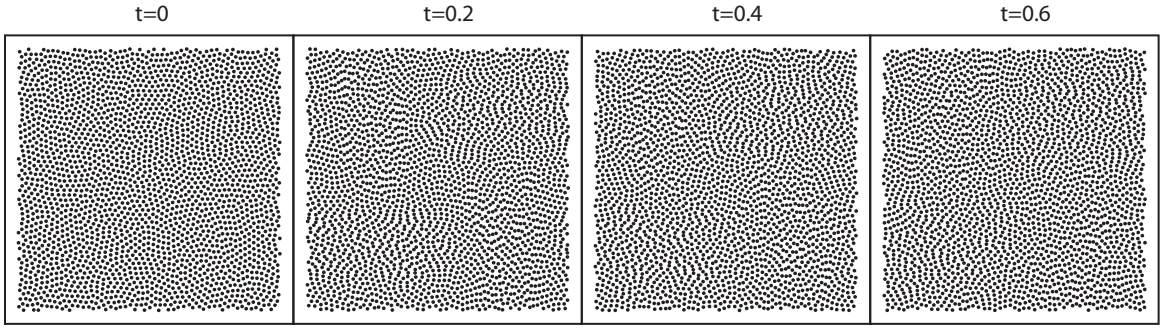

Fig. 6. Particle snapshots for the Taylor–Green problem at $Re = 100$ using 2500 particles.

method shows satisfactory agreement with the analytical decay rate and we find first-order convergence in the relative error of the maximum velocity $L_\infty(t)$, see Fig. 5(b). The error norm $L_\infty(t)$ is defined as

$$L_\infty(t) = \left| \frac{max(|\mathbf{v}_i(t)|) - Ue^{bt}}{Ue^{bt}} \right|. \tag{25}$$

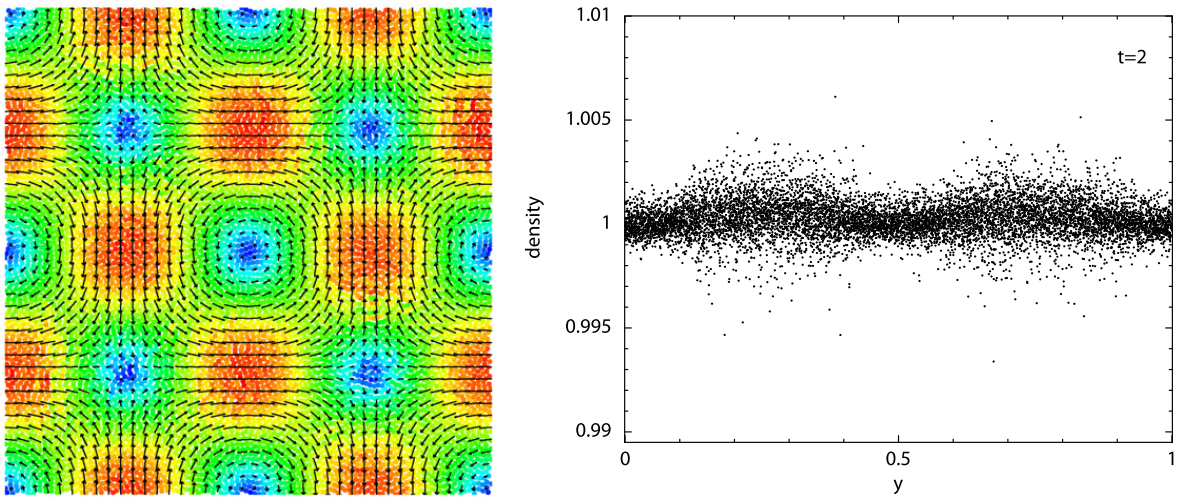

(a) Velocity field and velocity vectors (b) Spatial density variation

Fig. 7. Instantaneous velocity field and spatial density variation at t = 2 for the Taylor–Green flow at $Re = 100$.

Author's personal copy

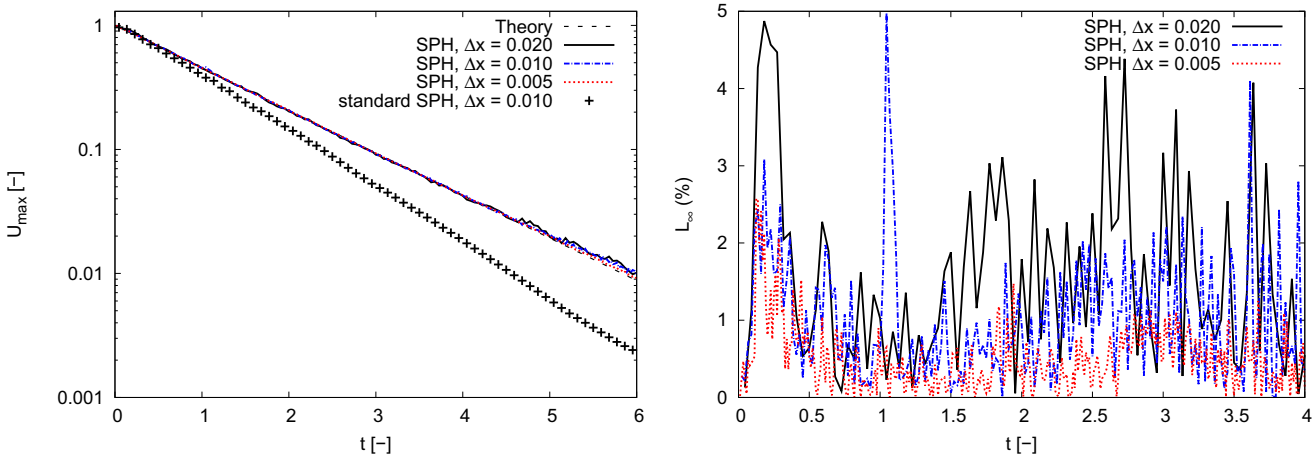

(a) Decay of maximum velocity (b) Relative error of maximum velocity

Fig. 8. Simulation results for the Taylor–Green problem at $Re = 100$ using a relaxed initial particle distribution.

To avoid the particle rearrangement at the beginning which causes the shift in the maximum velocity, we use the final particle distribution of the previously presented results as initial condition and impose the analytical velocity profile at $t = 0$. Now, the particles are uniformly distributed during the entire simulation as shown in Fig. 6.

We also show the absolute velocity field with velocity vectors for this case at $t = 2$ in Fig. 7(a). Here, the colormap ranges from 0 (blue) to $U_{max}(t = 2)$ (red). Velocity vectors are scaled to clearly show the structure of the flow. At this point we want to highlight the smoothness of the velocity field and remember that we do not use any additional smoothing, reinitialization, or remeshing scheme in our method. Supporting this fact, Fig. 7(b) shows the density of all particles at $t = 2$ simply plotted as function of the y-coordinate. The small scattering regions occur in the vicinity of the stagnation points, note however, that the total density variation is well below one percent.

The decay of the maximum velocity over time and the relative error for the Taylor–Green flow at $Re = 100$ using a relaxed particle distribution at $t = 0$ is shown in Fig. 8. The strong particle rearrangement as for the lattice setup case is avoided, and the initial overshoot in maximum velocity does not occur. The results for the three resolutions shown in Fig. 8(a) are almost identical and agree well with the analytical decay. Similarly to the previous case, from error plot we find approximately first-order convergence. The maximum error is remarkably reduced below five percent even for the lowest resolution of 50×50 particles. We also show the decay rate obtained with standard SPH in Fig. 8(a). The result with the standard SPH also shows now a linear decay when starting from a relaxed particle configuration, but the decay rate is strongly overestimated.

To the knowledge of the authors this is the first time that a weakly-compressible SPH method gives consistently correct results at different resolutions for the Taylor–Green vortex problem with a fully explicit scheme. Especially the accuracy of simulations starting from an initial Cartesian lattice particle configuration shows a strong improvement by the current approach. Note that for practical applications such an initial particle configuration is much more convenient than relaxed configurations that require pre-runs.

3.4. Lid-driven cavity

Another well-known and challenging test-case for SPH is the lid-driven cavity problem. A rectangular cavity with side length $L = 1$ is filled with a fluid, and the top wall moves at a constant speed $U_{max} = 1$. We simulate the flow in the cavity for three Reynolds numbers $Re = 100$, $Re = 1000$ and $Re = 10{,}000$ by adjusting the viscosity of the fluid accordingly, while fixing the density to $\rho_0 = 1$. The speed of sound for the equation of state is taken equal to $c = 10U_{max}$.

Two main difficulties arise in the lid-driven cavity problem. First, two singularities occur at the upper corners due to the moving lid on the horizontal wall boundary and the no-slip condition on the vertical walls. Second, strong velocity gradients are present in the flow at $Re = 10{,}000$ and several secondary vortices occur. As there exists no analytical solution for this problem we use as a reference the results of Ghia et al. [25], who simulated this case with a highly-resolved multi-grid finite-difference scheme on a 257×257 mesh. We simulate all three variations with 50×50, 100×100 and 200×200 particles initially placed on a regular Cartesian lattice, to check for convergence of our results and compare them with the reference. Different from previous SPH results of this problem, we do not use a background pressure in the equation of state (compare de Leffe et al. [26]) nor do we need to impose a very high sound-speed (Lee et al. [27] use $c = 100U_{max}$). We consider the results once the steady-state of the flow has been reached. We have checked for the steadiness by monitoring that the total kinetic energy in the system remains constant in time.

A visualization of the steady velocity field at $Re = 100$ is shown in Fig. 9(a). The colormap shows the magnitude of the velocity ranging from zero (blue) to U_{max} (red), and the velocity vectors visualize the structure of the flow. Essentially, a single core vortex develops in the upper half of the cavity due to the shear force at the moving wall, and the fluid in the lower

Author's personal copy

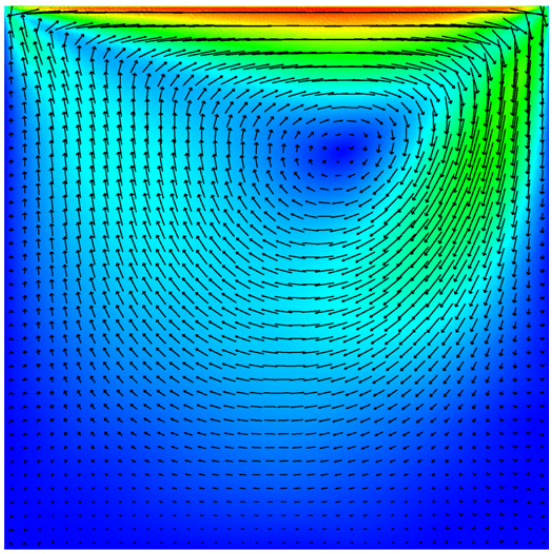

(a) Velocity field with vectors (200×200 particles)

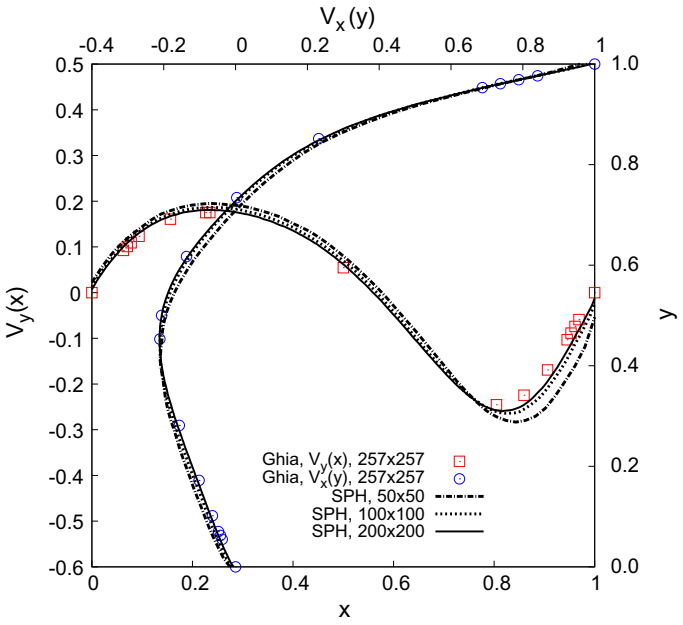

(b) Velocity profiles on the horizontal and vertical centerline.

Fig. 9. Lid-driven cavity at $Re = 100$.

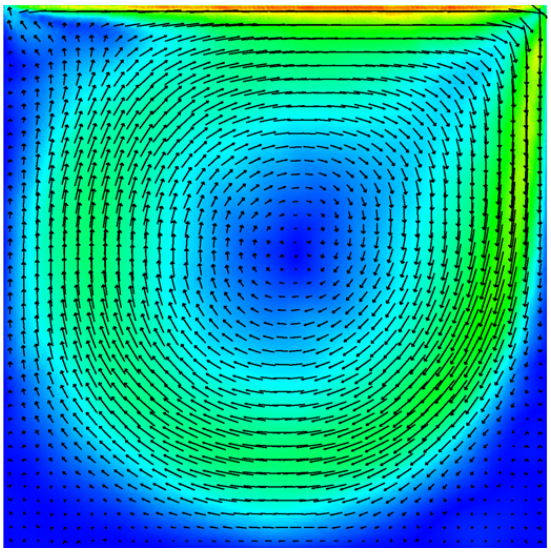

(a) Velocity field with vectors (200×200 particles)

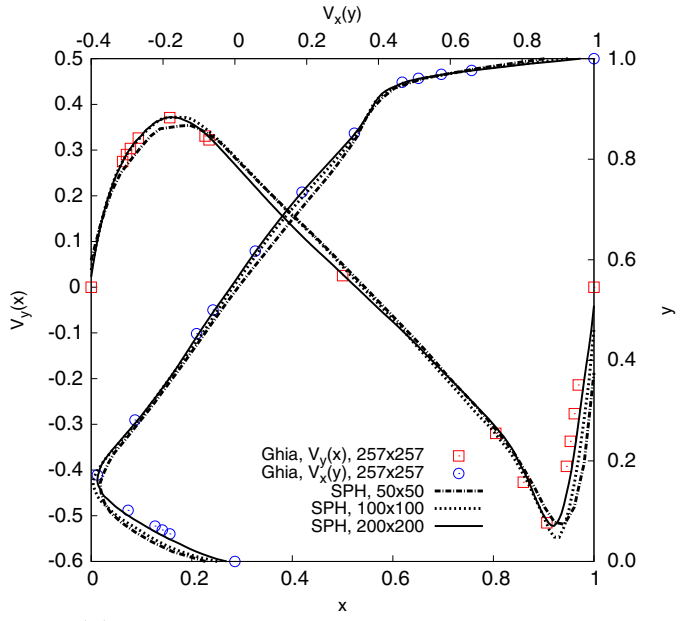

(b) Velocity profiles on the horizontal and vertical centerline.

Fig. 10. Lid-driven cavity at $Re = 1000$.

part of the cavity moves only slowly. A quantitative comparison with the reference is shown in Fig. 9(b), where the velocities in x and y-direction are plotted along the vertical and horizontal centerline, respectively. The reference results by Ghia et al. [25] are denoted by the colored symbols (□ for the velocity in y-direction along the horizontal centerline $V_y(x)$ and ⊙ for the velocity in x-direction along the vertical center line $V_x(y)$). The simulated profiles agree well with the reference results and the two higher resolutions show only marginal difference, thus converged results were obtained. For such a low Reynolds number already the lowest resolution using 50×50 particles gives satisfactory results.

The following Figs. 10 and 11 show the corresponding analysis for $Re = 1000$ and $Re = 10{,}000$. From the flow field we observe that the core vortex is more centered with increasing Reynolds number and the intensity of the vortex increases. Furthermore, in agreement with Ghia et al. [25] we find secondary vortices in the two lower and the upper left corner, but due to

Author's personal copy

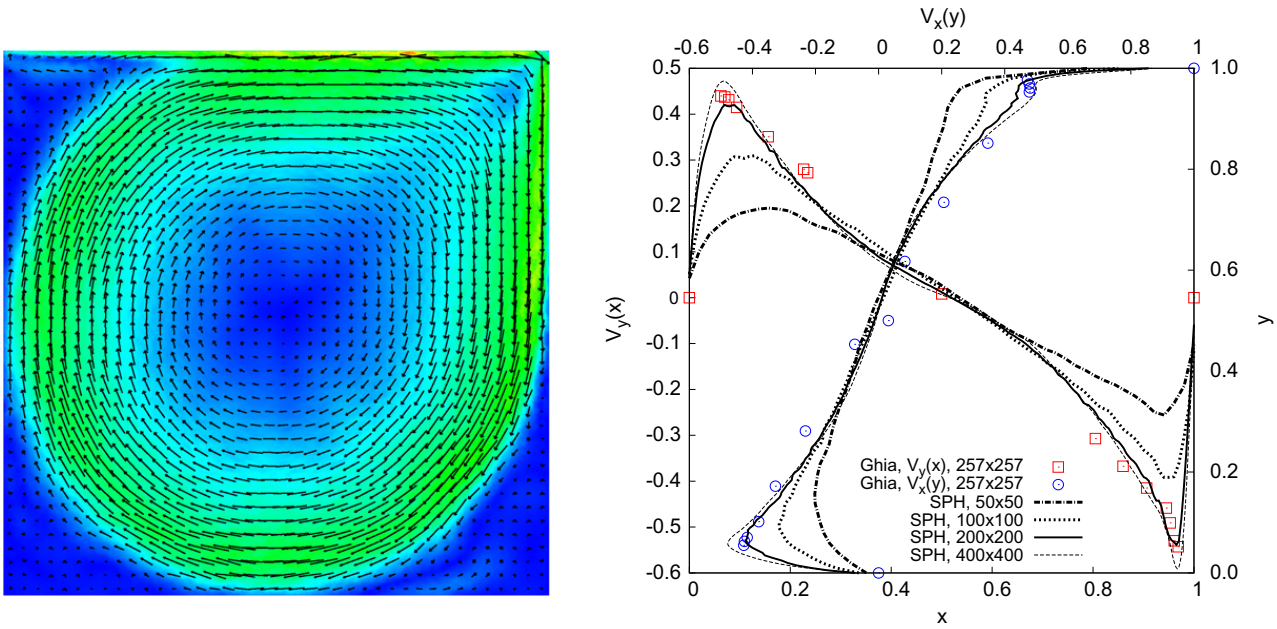

(a) Velocity field with vectors (200× 200 particles)

(b) Velocity profiles on the horizontal and vertical centerline.

Fig. 11. Lid-driven cavity at *Re* = 10,000.

the scale of the velocity vectors they are hardly visible in the presented figures. At *Re* = 1000 the velocity profiles along the centerlines match the reference results at all three resolutions. With higher resolutions we find a more accurate flow prediction in regions with strong velocity gradients (wall-near regions) but the core flow is approximated accurately even at the lowest resolution.

At *Re* = 10,000 a much larger resolution is required to converge to the reference results, see Fig. 11. As mentioned earlier, the core vortex at this Reynolds number is almost centered in the cavity and secondary vortices develop. With the lower resolutions we underestimate the intensity of the center vortex. At the highest resolution presented here (200 × 200 particles) the agreement with the reference result is satisfactory, especially the modified velocity profile in the thin boundary layer at the upper wall is already captured nicely. Note that the reference results were obtained with a resolution of 257 × 257 grid points.

The lid-driven cavity example demonstrates that our proposed method with the wall boundary formulation of our previous work [22] can be used to simulate accurately shear-driven flows with stagnation points at high Reynolds numbers.

3.5. Flow over a backward-facing step

Another wall-bounded flow driven by an external body force is the flow over a backward-facing step in a spanwise periodic channel. Fig. 12 shows a sketch and the dimensions of the geometry as presented in the work of Issa et al. [28]. The marked positions P_1—P_4 show the locations where we compare velocity profiles with the reference results. As there is no analytical solution for this example, the reference solution is obtained by a grid-based high-resolution simulation using *FLUENT* [28] (note, the resolution of the simulation using the Eulerian Finite-Volume method is not given in the reference).

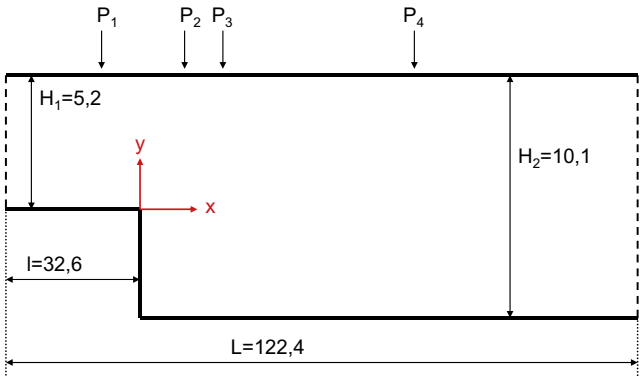

Fig. 12. Sketch of the backward-facing step, lengths are given in mm.

Author's personal copy

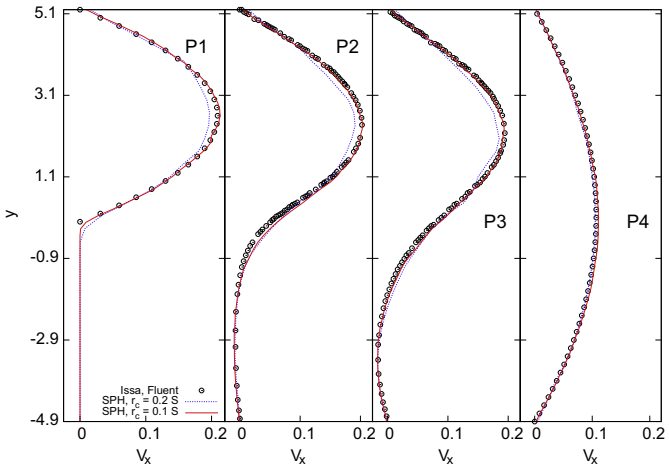

(a) Comparison of axial velocity in the channel at positions $P_1 - P_4$ with reference result for two resolutions $r_c = 0.2\ S$ and $r_c = 0.1\ S$.

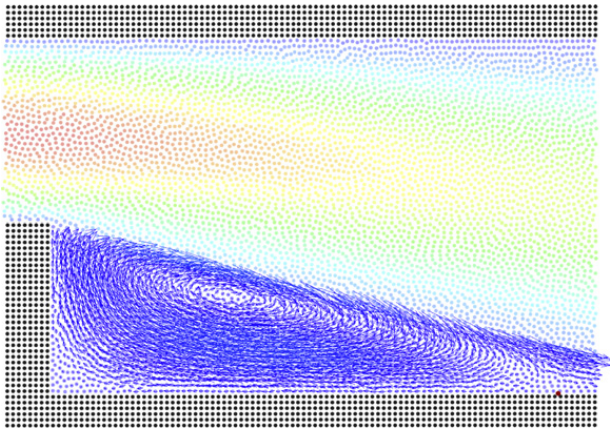

(b) Flow visualization at steady-state behind the step, particles are colored with the velocity magnitude in the range of $|\mathbf{v}| = 0.$ (blue) to $|\mathbf{v}| = 0.21$ (red).

Fig. 13. Simulation results of the laminar flow over a backward-facing step.

The incompressible fluid is characterized by a density of $\rho = 1$ and a kinematic viscosity of $\nu = 1.456 \times 10^{-2}$. Using twice the channel height above the step as hydraulic diameter $D = 2h$ and a mean bulk velocity in the thinner channel above the step of $U = 0.14$ gives a Reynolds number of $Re = 100$. The mean flow is driven by a constant body force in x-direction that was adjusted to achieve the specified mean bulk velocity. The speed of sound used for this simulation is ten times the maximum velocity in the channel above the step, i.e. $c_s = 2.1$.

Fig. 13(a) shows a comparison of the streamwise velocity over the channel height at four positions P_1—P_4 with the reference results from [28]. We plot the steady-state results of the flow field at two resolutions $r_c = 0.2S$ and $r_c = 0.1S$, where $S = 4.9$ is the step height. The instantaneous particle velocities were interpolated on a grid using the kernel W to obtain smooth profiles.

With the proper driving body force for the high resolution case to obtain the specified mean bulk flow at P_1, the agreement with the reference solution is very good. The results at P_2 and P_3 show that the recirculation bubble is well recovered, and far behind the step, the flow field again becomes parabolic, see P_4. Instead of fitting the driving force for each simulation we use the parameter from the highest-resolution case for all other simulations. Thus, the flow at $r_c = 0.2S$ is slightly underpredicted but the overall agreement with the reference solution is still satisfactory. Also, this underprediction is reflected systematically in the consecutive profiles and shows that this effect could be scaled out by increasing the driving force.

Fig. 13(b) shows a snapshot of the simulation at steady-state in the vicinity of the backward-facing step. Particles are colored with the magnitude of the velocity in the range of $|\mathbf{v}| = 0.$ (blue) – $|\mathbf{v}| = 0.21$ (red) and only in the recirculation bubble we visualize the flow with velocity vectors. There are no void regions behind the step and the flow is well captured with the SPH method. The bold red dot in the figure denotes the reattachment point of the flow at the lower channel wall and is located at $x_R = 6.2S$. Issa [28] presents the reattachment point positions for the *FLUENT* and SPH results at $x_R = 6.3S$ and $x_R = 6.0S$. Thus, our results agree well with the high-resolution grid data and the accuracy of the proposed SPH method is improved.

3.6. Rayleigh–Taylor Instability

We mainly applied our method to single fluid problems, but this last example shows that the modification of the particle advection velocity can also be used to simulate multi-phase problems. The Rayleigh–Taylor instability develops under the action of gravity when two fluids of different density are in contact and the heavier phase is on top of the lighter phase. We consider a rectangular domain of size $L_x = 1$ and $L_y = 2$ and use Cartesian particles to initialize the geometry. The density of the fluid in the lower part of the domain is set equal to one and above that phase the density is $\rho_u = 1.8$. To induce a well-defined instability the interface between the lighter and heavier phase is slightly disturbed following $y > 1 - 0.15\sin(2\pi x)$. Gravity acts in negative y-direction and the Froude number is set to $Fr = 1$. The Reynolds number based on the reference velocity $v_{ref} = \sqrt{L_y/2g}$ is $Re = 420$ and defines the kinematic viscosity. Initially, all the particle velocities are zero and we use a resolution of 60×120 particle for the fluids. The wall boundaries are modeled with non-moving SPH particles to enforce the no-slip boundary condition [22].

Fig. 14 shows the particles of the heavy phase for the Rayleigh–Taylor instability at three time instants $t = 1, 3$ and 5. Starting from the initial perturbation of the interface, initially two big plumes develop and the heavier and lighter phase are accelerated in opposite directions. Due to the relative motion shear forces act on the interface and produce interface roll-up.

Author's personal copy

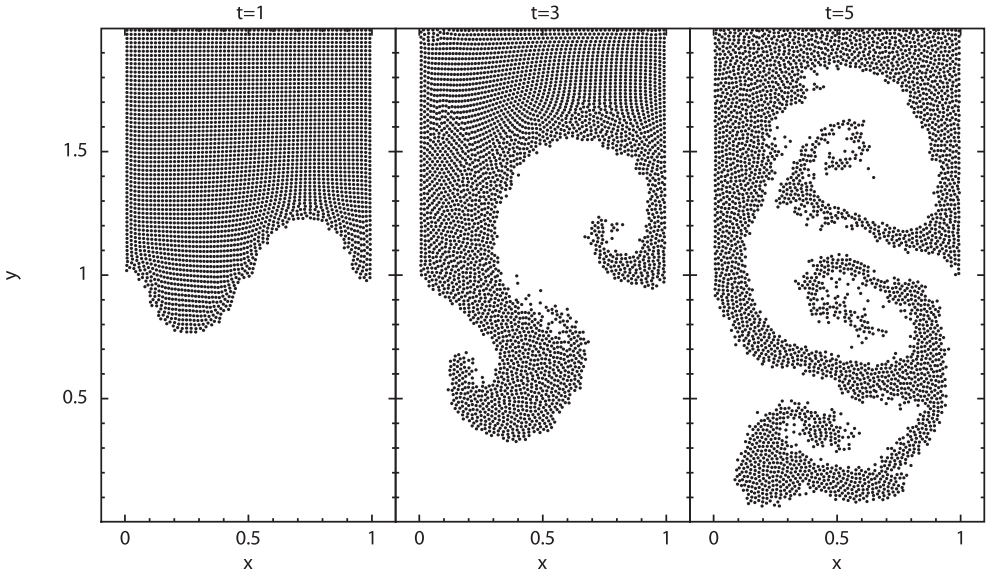

Fig. 14. Snapshots of the heavy-phase particles for the Rayleigh–Taylor instability using 60×120 particles at $t = 1,\ 3$ and 5.

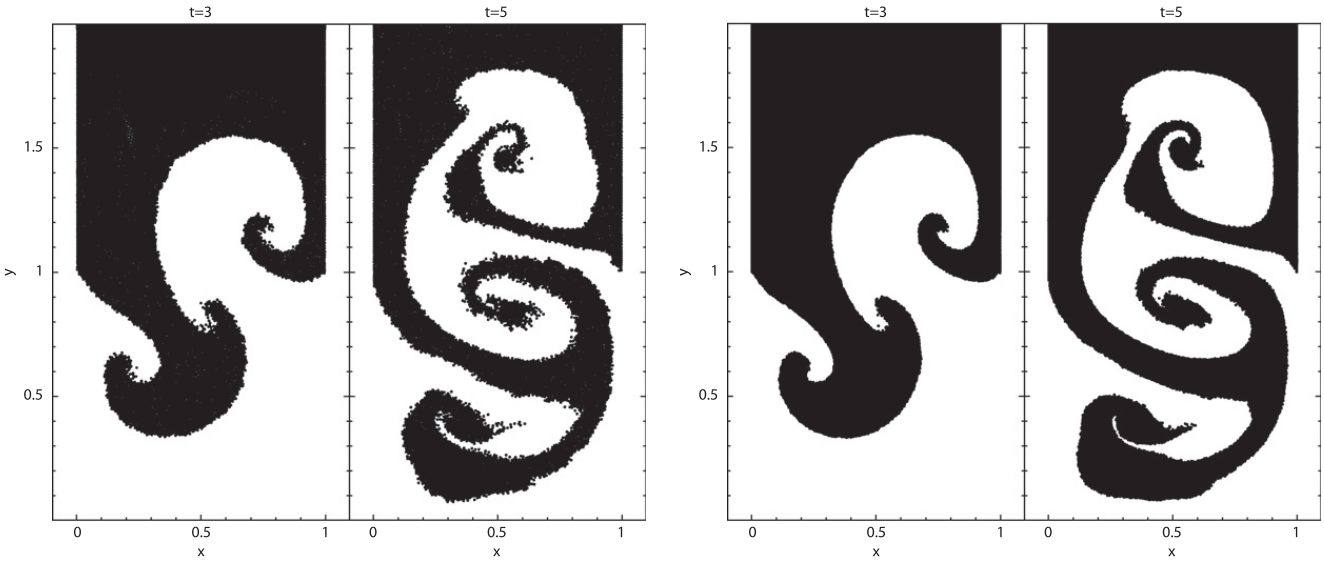

(a) Resolution: 120×240 particles (b) Resolution: 240×480 particles

Fig. 15. Snapshots of the heavy-phase particles for the Rayleigh–Taylor instability at $t = 1,\ 3$ and 5.

Fig. 15 shows the simulation results at $t = 3$ and $t = 5$ for two higher resolutions, each increased by a factor of two in both coordinate directions. Comparing all three cases we find that the main roll-up is well-captured at all resolutions and the shape of the main plumes at $t = 3$ is converged. At later times, we observe similar secondary plumes as presented in Hu and Adams [4], who used an incompressible SPH method to simulate this case.

Finally, we present a high-resolution simulation of a three-dimensional Rayleigh–Taylor instability in a periodic box of size $1 \times 1 \times 2$ using $120 \times 120 \times 240$ particles, i.e. a total of about 3.5×10^6 particles was used. The initial interface perturbation is now $y < 1 - 0.15 \sin(4\pi x) \sin(4\pi y)$ and gravity acts in negative z-direction. Fig. 16 shows the evolution of the volume-rendered lighter phase at $t = 0, 2, 4$ and 6. Note that here we only visualize 1.5 wavelengths but the domain covered two wavelengths of the disturbance. The initial interface disturbances grow with time and the plumes rise to the top of the container. Due to shear-forces the interfaces roll up and produce the well-known three-dimensional mushroom-shape structures. In the last frame of Fig. 16 the lighter phase reaches the upper wall and the remaining liquid pushes upwards through the liquid bridges that have developed.

Author's personal copy

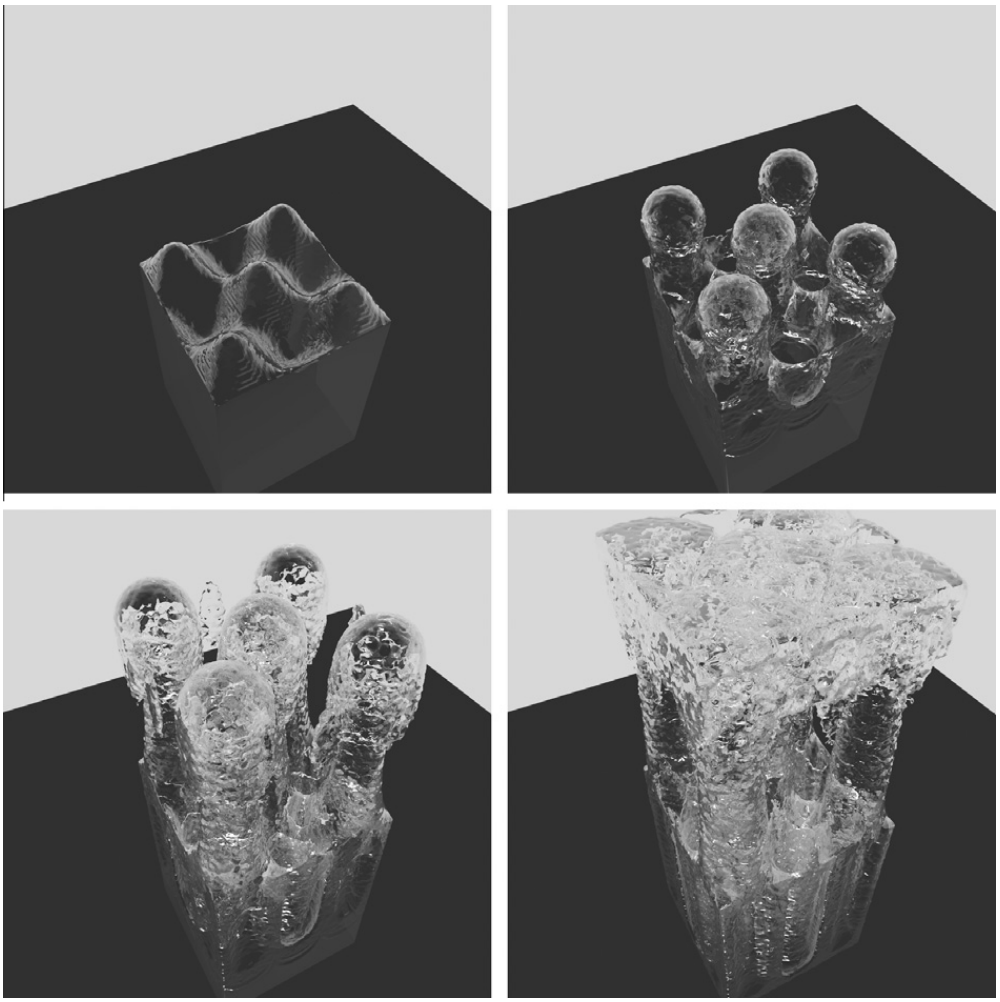

Fig. 16. 3D Rayleigh–Taylor instability.

4. Conclusions

We have presented a simple modification of the advection scheme for SPH particles that allowed us to simulate many challenging problems that so far have suffered from the well-known tensile instability or the creation of void regions in the flow when computed by standard SPH. Due to the modification of the advection velocity an additional term appears in the momentum equation that is added to the standard method without any difficulties. This extra term and the modified advection velocity are the only necessary changes of the standard weakly-compressible SPH method as presented by Monaghan [3], without additional smoothing schemes or artificial viscosities. In all our problems we were able to use exactly the same setup, thus no empirical parameter has to be adjusted with this method. The main advantage of this method is its generality and simplicity while achieving unprecedented accuracy and stability properties even for flows at large Reynolds numbers. Extensions of this method to two-phase flows and free-surface flows are subject of ongoing research.

Acknowledgments

The authors gratefully acknowledge the postprocessing-tool *splash* from Daniel J. Price [29] which was used to produce some of the figures presented in this article. Furthermore we want to thank J. Biddiscombe [30] for the *pv-meshless*-plugins of Paraview that were also used for visualization purposes. Computational resources have been provided by the Leibniz Supercomputing Center (LRZ, High Performance Computing in Bavaria) under Grant *pr32ma*. Finally, we acknowledge the work of Sbalzarini et al. [31] who provided the Parallel Particle Mesh (PPM) Library that we used to implement our model and enables us to perform large-scale simulations on parallel computer architectures.

References

[1] L.B. Lucy, A numerical approach to the testing of the fission hypothesis, The Astronomical Journal 82 (12) (1977) 1013–1024.
[2] R. Gingold, J. Monaghan, Smoothed particle hydrodynamics – Theory and application to non-spherical stars, Monthly Notices of the Royal Astronomical Society 181 (1977) 375.

Author's personal copy

[3] J.J. Monaghan, Smoothed particle hydrodynamics, Reports on Progress in Physics 68 (8) (2005) 1703–1759.
[4] X. Hu, N. Adams, A constant-density approach for incompressible multi-phase SPH, Journal of Computational Physics 228 (6) (2009) 2082–2091.
[5] S.J. Cummins, M. Rudman, An SPH projection method, Journal of Computational Physics 152 (2) (1999) 584–607.
[6] R. Xu, P. Stansby, D. Laurence, Accuracy and stability in incompressible SPH (ISPH) based on the projection method and a new approach, Journal of Computational Physics 228 (18) (2009) 6703–6725.
[7] A. Colagrossi, Numerical simulation of interfacial flows by smoothed particle hydrodynamics, Journal of Computational Physics 191 (2) (2003) 448–475.
[8] X. Hu, N. Adams, A multi-phase SPH method for macroscopic and mesoscopic flows, Journal of Computational Physics 213 (2) (2006) 844–861.
[9] S. Marrone, M. Antuono, A. Colagrossi, G. Colicchio, D. Le Touzé, G. Graziani, δ-SPH model for simulating violent impact flows, Computer Methods in Applied Mechanics and Engineering 200 (13–16) (2011) 1526–1542.
[10] A.M. Tartakovsky, P. Meakin, T.D. Scheibe, R. Eichlerwest, R.M.E. West, Simulations of reactive transport and precipitation with smoothed particle hydrodynamics, Journal of Computational Physics 222 (2) (2007) 654–672.
[11] S. Adami, X. Hu, N. Adams, A conservative SPH method for surfactant dynamics, Journal of Computational Physics 229 (5) (2010) 1909–1926.
[12] W. Dehnen, H. Aly, Improving convergence in smoothed particle hydrodynamics simulations without pairing instability, Monthly Notices of the Royal Astronomical Society 15 (June) (2012) 1–15.
[13] D.J. Price, Smoothed particle hydrodynamics and magnetohydrodynamics, Journal of Computational Physics 231 (3) (2012) 759–794, http://dx.doi.org/10.1016/j.jcp. 2010.12.011.
[14] J. Monaghan, A turbulence model for smoothed particle hydrodynamics, European Journal of Mechanics – B/Fluids 30 (4) (2011) 360–370.
[15] J.J. Monaghan, On the problem of penetration in particle methods, Journal of Computational Physics 82 (1) (1989) 1–15.
[16] S. Lind, R. Xu, P. Stansby, B. Rogers, Incompressible smoothed particle hydrodynamics for free-surface flows: a generalised diffusion-based algorithm for stability and validations for impulsive flows and propagating waves, Journal of Computational Physics 231 (4) (2012) 1499–1523.
[17] D.D. Holm, Fluctuation effects on 3D Lagrangian mean and Eulerian mean fluid motion, Physica D: Nonlinear Phenomena 133 (1–4) (1999) 215–269.
[18] J.P. Morris, P.J. Fox, Y. Zhu, Modeling low Reynolds number incompressible flows using SPH, Journal of Computational Physics 136 (1) (1997) 214–226.
[19] X. Hu, N.A. Adams, An incompressible multi-phase SPH method, Journal of Computational Physics 227 (1) (2007) 264–278.
[20] O. Kum, W. Hoover, H. Posch, Viscous conducting flows with smooth-particle applied mechanics, Physical Review E 52 (5) (1995) 4899–4908.
[21] P.W. Randles, L.D. Libersky, Smoothed particle hydrodynamics: some recent improvements and applications, Computer Methods in Applied Mechanics and Engineering 139 (14) (1996) 375–408.
[22] S. Adami, X. Hu, N. Adams, A generalized wall boundary condition for smoothed particle hydrodynamics, Journal of Computational Physics 231 (2012) 7057–7075.
[23] M. Ellero, N. Adams, SPH simulations of flow around a periodic array of cylinders confined in a channel, International Journal for Numerical Methods in Engineering 86 (8) (2011) 1027–1040.
[24] A.W. Liu, D.E. Bornside, R.C. Armstrong, R.A. Brown, Viscoelastic flow of polymer solutions around a periodic, linear array of cylinders: comparisons of predictions for microstructure and flow fields, Journal of Non-Newtonian Fluid Mechanics 77 (3) (1998) 153–190.
[25] U. Ghia, K. Ghia, C. Shin, High-Re solutions for incompressible flow using the Navier–Stokes equations and a multigrid method, Journal of Computational Physics 48 (3) (1982) 387–411.
[26] M. de Leffe, D. Le Touzé, B. Alessandrini, A modified no-slip condition in weakly-compressible SPH, in: T. Rung, C. Ulrich (Eds.), Proceedings of the Sixth SPHERIC Workshop, Hamburt, 2011, pp. 291–298.
[27] E. Lee, C. Moulinec, R. Xu, D. Violeau, D. Laurence, P. Stansby, Comparisons of weakly compressible and truly incompressible algorithms for the SPH mesh free particle method, Journal of Computational Physics 227 (18) (2008) 8417–8436.
[28] R. Issa, Numerical assessment of smoothed particle hydrodynamics gridless method for incompressible flows and its extension to turbulent flows, Ph.D. Thesis, University of Manchester, 2005.
[29] D.J. Price, SPLASH: An Interactive Visualisation Tool for Smoothed Particle Hydrodynamics Simulations, Publications of the Astronomical Society of Australia, 2007. vol. 24, pp. 159–173.
[30] J. Biddiscombe, D. Graham, P. Maruzewski, Visualization and analysis of SPH data, ERCOFTAC Bulletin 76 (2008) 9–12.
[31] I.F. Sbalzarini, J.H. Walther, M. Bergdorf, S.E. Hieber, E.M. Kotsalis, P. Koumoutsakos, PPM A highly effcient parallel particlemesh library for the simulation of continuum systems, Journal of Computational Physics 215 (2) (2006) 566–588.

A.3. A NEW SURFACE–TENSION FORMULATION FOR MULTI– PHASE SPH USING A REPRODUCING DIVERGENCE APPROXIMATION

Rightslink Printable License https://s100.copyright.com/App/PrintableLicenseFrame.jsp?publisherI...

ELSEVIER LICENSE
TERMS AND CONDITIONS

Feb 04, 2013

This is a License Agreement between Stefan Adami ("You") and Elsevier ("Elsevier") provided by Copyright Clearance Center ("CCC"). The license consists of your order details, the terms and conditions provided by Elsevier, and the payment terms and conditions.

All payments must be made in full to CCC. For payment instructions, please see information listed at the bottom of this form.

Supplier	Elsevier Limited The Boulevard,Langford Lane Kidlington,Oxford,OX5 1GB,UK
Registered Company Number	1982084
Customer name	Stefan Adami
Customer address	Technische Universität München Garching, 85748
License number	3081820423378
License date	Feb 04, 2013
Licensed content publisher	Elsevier
Licensed content publication	Journal of Computational Physics
Licensed content title	A new surface-tension formulation for multi-phase SPH using a reproducing divergence approximation
Licensed content author	S. Adami,X.Y. Hu,N.A. Adams
Licensed content date	1 July 2010
Licensed content volume number	229
Licensed content issue number	13
Number of pages	11
Start Page	5011
End Page	5021
Type of Use	reuse in a thesis/dissertation
Intended publisher of new work	other
Portion	full article
Format	both print and electronic
Are you the author of this Elsevier article?	Yes
Will you be translating?	No
Order reference number	
Title of your thesis/dissertation	Modeling and Simulation of Multiphase Phenomena with SPH
Expected completion date	Apr 2013
Estimated size (number of pages)	120

1 von 5 04.02.2013 10:33

Elsevier VAT number	GB 494 6272 12
Permissions price	0.00 EUR
VAT/Local Sales Tax	0.0 USD / 0.0 GBP
Total	0.00 EUR
Terms and Conditions	

INTRODUCTION

1. The publisher for this copyrighted material is Elsevier. By clicking "accept" in connection with completing this licensing transaction, you agree that the following terms and conditions apply to this transaction (along with the Billing and Payment terms and conditions established by Copyright Clearance Center, Inc. ("CCC"), at the time that you opened your Rightslink account and that are available at any time at http://myaccount.copyright.com).

GENERAL TERMS

2. Elsevier hereby grants you permission to reproduce the aforementioned material subject to the terms and conditions indicated.

3. Acknowledgement: If any part of the material to be used (for example, figures) has appeared in our publication with credit or acknowledgement to another source, permission must also be sought from that source. If such permission is not obtained then that material may not be included in your publication/copies. Suitable acknowledgement to the source must be made, either as a footnote or in a reference list at the end of your publication, as follows:

"Reprinted from Publication title, Vol /edition number, Author(s), Title of article / title of chapter, Pages No., Copyright (Year), with permission from Elsevier [OR APPLICABLE SOCIETY COPYRIGHT OWNER]." Also Lancet special credit - "Reprinted from The Lancet, Vol. number, Author(s), Title of article, Pages No., Copyright (Year), with permission from Elsevier."

4. Reproduction of this material is confined to the purpose and/or media for which permission is hereby given.

5. Altering/Modifying Material: Not Permitted. However figures and illustrations may be altered/adapted minimally to serve your work. Any other abbreviations, additions, deletions and/or any other alterations shall be made only with prior written authorization of Elsevier Ltd. (Please contact Elsevier at permissions@elsevier.com)

6. If the permission fee for the requested use of our material is waived in this instance, please be advised that your future requests for Elsevier materials may attract a fee.

7. Reservation of Rights: Publisher reserves all rights not specifically granted in the combination of (i) the license details provided by you and accepted in the course of this licensing transaction, (ii) these terms and conditions and (iii) CCC's Billing and Payment terms and conditions.

8. License Contingent Upon Payment: While you may exercise the rights licensed immediately upon issuance of the license at the end of the licensing process for the transaction, provided that you have disclosed complete and accurate details of your proposed use, no license is finally effective unless and until full payment is received from you (either by publisher or by CCC) as provided in CCC's Billing and Payment terms and conditions. If full payment is not received on a timely basis, then any license preliminarily

granted shall be deemed automatically revoked and shall be void as if never granted. Further, in the event that you breach any of these terms and conditions or any of CCC's Billing and Payment terms and conditions, the license is automatically revoked and shall be void as if never granted. Use of materials as described in a revoked license, as well as any use of the materials beyond the scope of an unrevoked license, may constitute copyright infringement and publisher reserves the right to take any and all action to protect its copyright in the materials.

9. Warranties: Publisher makes no representations or warranties with respect to the licensed material.

10. Indemnity: You hereby indemnify and agree to hold harmless publisher and CCC, and their respective officers, directors, employees and agents, from and against any and all claims arising out of your use of the licensed material other than as specifically authorized pursuant to this license.

11. No Transfer of License: This license is personal to you and may not be sublicensed, assigned, or transferred by you to any other person without publisher's written permission.

12. No Amendment Except in Writing: This license may not be amended except in a writing signed by both parties (or, in the case of publisher, by CCC on publisher's behalf).

13. Objection to Contrary Terms: Publisher hereby objects to any terms contained in any purchase order, acknowledgment, check endorsement or other writing prepared by you, which terms are inconsistent with these terms and conditions or CCC's Billing and Payment terms and conditions. These terms and conditions, together with CCC's Billing and Payment terms and conditions (which are incorporated herein), comprise the entire agreement between you and publisher (and CCC) concerning this licensing transaction. In the event of any conflict between your obligations established by these terms and conditions and those established by CCC's Billing and Payment terms and conditions, these terms and conditions shall control.

14. Revocation: Elsevier or Copyright Clearance Center may deny the permissions described in this License at their sole discretion, for any reason or no reason, with a full refund payable to you. Notice of such denial will be made using the contact information provided by you. Failure to receive such notice will not alter or invalidate the denial. In no event will Elsevier or Copyright Clearance Center be responsible or liable for any costs, expenses or damage incurred by you as a result of a denial of your permission request, other than a refund of the amount(s) paid by you to Elsevier and/or Copyright Clearance Center for denied permissions.

LIMITED LICENSE

The following terms and conditions apply only to specific license types:

15. **Translation**: This permission is granted for non-exclusive world **English** rights only unless your license was granted for translation rights. If you licensed translation rights you may only translate this content into the languages you requested. A professional translator must perform all translations and reproduce the content word for word preserving the integrity of the article. If this license is to re-use 1 or 2 figures then permission is granted for non-exclusive world rights in all languages.

16. **Website**: The following terms and conditions apply to electronic reserve and author websites:
Electronic reserve: If licensed material is to be posted to website, the web site is to be

password-protected and made available only to bona fide students registered on a relevant course if:
This license was made in connection with a course,
This permission is granted for 1 year only. You may obtain a license for future website posting,
All content posted to the web site must maintain the copyright information line on the bottom of each image,
A hyper-text must be included to the Homepage of the journal from which you are licensing at http://www.sciencedirect.com/science/journal/xxxxx or the Elsevier homepage for books at http://www.elsevier.com , and
Central Storage: This license does not include permission for a scanned version of the material to be stored in a central repository such as that provided by Heron/XanEdu.

17. **Author website** for journals with the following additional clauses:

All content posted to the web site must maintain the copyright information line on the bottom of each image, and the permission granted is limited to the personal version of your paper. You are not allowed to download and post the published electronic version of your article (whether PDF or HTML, proof or final version), nor may you scan the printed edition to create an electronic version. A hyper-text must be included to the Homepage of the journal from which you are licensing at http://www.sciencedirect.com/science/journal/xxxxx . As part of our normal production process, you will receive an e-mail notice when your article appears on Elsevier's online service ScienceDirect (www.sciencedirect.com). That e-mail will include the article's Digital Object Identifier (DOI). This number provides the electronic link to the published article and should be included in the posting of your personal version. We ask that you wait until you receive this e-mail and have the DOI to do any posting.

Central Storage: This license does not include permission for a scanned version of the material to be stored in a central repository such as that provided by Heron/XanEdu.

18. **Author website** for books with the following additional clauses:
Authors are permitted to place a brief summary of their work online only.
A hyper-text must be included to the Elsevier homepage at http://www.elsevier.com . All content posted to the web site must maintain the copyright information line on the bottom of each image. You are not allowed to download and post the published electronic version of your chapter, nor may you scan the printed edition to create an electronic version.

Central Storage: This license does not include permission for a scanned version of the material to be stored in a central repository such as that provided by Heron/XanEdu.

19. **Website** (regular and for author): A hyper-text must be included to the Homepage of the journal from which you are licensing at http://www.sciencedirect.com/science/journal/xxxxx. or for books to the Elsevier homepage at http://www.elsevier.com

20. **Thesis/Dissertation**: If your license is for use in a thesis/dissertation your thesis may be submitted to your institution in either print or electronic form. Should your thesis be published commercially, please reapply for permission. These requirements include permission for the Library and Archives of Canada to supply single copies, on demand, of the complete thesis and include permission for UMI to supply single copies, on demand, of the complete thesis. Should your thesis be published commercially, please reapply for permission.

21. **Other Conditions**:

v1.6

If you would like to pay for this license now, please remit this license along with your payment made payable to "COPYRIGHT CLEARANCE CENTER" otherwise you will be invoiced within 48 hours of the license date. Payment should be in the form of a check or money order referencing your account number and this invoice number RLNK500949018.
Once you receive your invoice for this order, you may pay your invoice by credit card. Please follow instructions provided at that time.

Make Payment To:
Copyright Clearance Center
Dept 001
P.O. Box 843006
Boston, MA 02284-3006

For suggestions or comments regarding this order, contact RightsLink Customer Support: customercare@copyright.com or +1-877-622-5543 (toll free in the US) or +1-978-646-2777.

Gratis licenses (referencing $0 in the Total field) are free. Please retain this printable license for your reference. No payment is required.

Author's personal copy

Journal of Computational Physics 229 (2010) 5011–5021

Contents lists available at ScienceDirect

Journal of Computational Physics

journal homepage: www.elsevier.com/locate/jcp

A new surface-tension formulation for multi-phase SPH using a reproducing divergence approximation

S. Adami *, X.Y. Hu, N.A. Adams

Institute of Aerodynamics, Technische Universität München, 85748 Garching, Germany

ARTICLE INFO

Article history:
Received 26 June 2009
Received in revised form 5 February 2010
Accepted 16 March 2010
Available online 18 March 2010

Keywords:
Multi-phase flows
Surface tension
Particle method

ABSTRACT

In this paper, we propose a new surface-tension formulation for multi-phase smoothed particle hydrodynamics (SPH). To obtain a stable and accurate scheme for surface curvature, a new reproducing divergence approximation without the need for a matrix inversion is derived. Furthermore, we introduce a density-weighted color-gradient formulation to reflect the reality of an asymmetrically distributed surface-tension force. We validate our method with analytic solutions and demonstrate convergence for different cases. Furthermore, we show that our formulation can handle phase interfaces with density and viscosity ratios of up to 1000 and 100, respectively. Finally, complex three-dimensional simulations including breakup of an interface demonstrate the capabilities of our method.
© 2010 Elsevier Inc. All rights reserved.

1. Introduction

Surface-tension effects are important for many multi-phase flow phenomena. Especially when the characteristic length scales of the investigated system are sufficiently small, the surface-tension forces become relevant compared to inertia effects and affect the flow field. Many industrial applications include multi-phase flow systems and encounter problems such as drop deformation and breakup in rather simple shear flows, wetting effects or Marangoni-force driven motion of interfaces. Therefore the accurate simulation of flows with complex interfaces is an interesting problem with practical relevance and motivates our work.

There are mainly two approaches for the numerical solution of the governing equations of the flow system, either using a grid-based method with a Eulerian formulation or a meshless method from a Lagrangian point of view. In this paper, we employ smoothed particle hydrodynamics (SPH) [10] due to its conceptual advantages for modeling of complex multi-phase flows. With this Lagrangian particle method, material interfaces are represented self-adaptively without the need for complex interface-capturing or front-tracking algorithms. By the use of a color function each particle is assigned to a single phase throughout a simulation. In doing so, interfaces can easily be followed and strong deformations and even breakup can be handled.

With SPH there are generally two ways to model the surface-tension effect: one is based on microscopic inter-phase attractive potentials [13,16]; the other one is based on a macroscopic surface-tension model [11,6]. Although the implementation of an inter-phase attractive potential is straightforward, one of the difficulties is that the resulting surface tension needs to be calibrated. Furthermore, with given parameters, the surface tension is resolution-dependent and does not converge to a fixed value with increasing resolution. On the other hand, the approach using a macroscopic surface-tension model recovers the prescribed surface tension and converges to the exact value with increasing resolution. Usually, this model is implemented in SPH by the continuum surface force (CSF) method of Brackbill et al. [1]. In this method, a color function is used to describe different phases, and the interface is defined as a finite transitional band, where the color gradient does not vanish. Within this band, the surface tension is approximated as a continuous force.

* Corresponding author.
E-mail address: stefan.adami@aer.mw.tum.de (S. Adami).

0021-9991/$ - see front matter © 2010 Elsevier Inc. All rights reserved.
doi:10.1016/j.jcp.2010.03.022

Author's personal copy

The surface-tension model for multi-phase SPH of Morris [11] uses a smoothed color function and has difficulties in predicting the surface curvature, i.e. the divergence of the unit interface-normal direction. One difficulty arises from the fact, that the standard SPH approximation of the divergence requires full support of the kernel function, which cannot be satisfied within the transitional band. Another problem is the color gradient near the edge of the transition band, which has small magnitude and may lead to an erroneous direction. In the work of Hu and Adams [6] a sharp color function with a discontinuity at the interface is used directly. The calculation of the surface curvature is circumvented by introducing a surface-stress tensor which only depends on the color gradient. Furthermore, since the magnitude of the surface-stress tensor is proportional to the magnitude of the color gradient, the contribution of a small color gradient vanishes hence does not introduce numerical difficulties.

In realistic configurations the surface force may not be distributed uniformly on each side of the interface. For example at an air–water interface, the surface force is dominantly acting on the water side. In all current approaches the surface force modeled by SPH is assumed to be distributed uniformly across the interface. Not only being nonphysical, this assumption can also introduce numerical problems. For example, in an air–water interface flow the surface force on the air side can introduce an acceleration about 1000 times higher than that on the water side. Consequentially, the stiffness of the equation of motion increases dramatically, and the step-size for time integration is strongly limited.

In this work, we revisit the formulation of surface curvature based on a sharp color function. To obtain a stable and accurate surface-curvature calculation without full support of the kernel function, a new reproducing divergence approximation is derived. Unlike previous formulations, which calculate the divergence from reproducing gradient approximations, the new approximation does not require a matrix inversion. Furthermore, we have not found notable effects caused by the errors due to small color-gradient values at the fringes of the transitional band. To reflect the reality of non-uniformly distributed surface forces, a new density-weighted color-gradient formulation is used. Several numerical tests on static water drops, oscillating drops, drop deformation and splitting in shear flow are carried out to demonstrate the potential of the present method. The results show that we achieve a comparable accuracy as with the formulation of Hu and Adams [6]. But as we can relax the dominating surface-tension based time-step criterion in the lighter phase, the computational effort of our new formulation is significantly smaller, especially for problems with large density ratios.

2. Governing equations

The isothermal Navier–Stokes equations are solved in a moving Lagrangian frame

$$\frac{d\rho}{dt} = -\rho\nabla\cdot\mathbf{v}, \tag{1}$$

$$\frac{d\mathbf{v}}{dt} = \mathbf{g} + \frac{1}{\rho}[-\nabla p + \mathbf{F}^{(v)} + \mathbf{F}^{(s)}], \tag{2}$$

where $\rho,\ p,\ \mathbf{v}$ and $\mathbf{g}$ are material density, pressure, velocity and body force, respectively. $\mathbf{F}^{(v)}$ denotes the viscous force and $\mathbf{F}^{(s)}$ is the interfacial surface force.

With SPH incompressible flow is usually modeled by the weakly-compressible approach in which a stiff EOS is used to relate the pressure to the density, i.e.

$$p = p_0\left[\left(\frac{\rho}{\rho_0}\right)^{\gamma} - 1\right] + \chi, \tag{3}$$

with $\gamma = 7$, the reference pressure p_0, the reference density ρ_0 and the background pressure χ. These parameters and the artificial speed of sound are chosen following a scale analysis presented by Morris et al. [12] which limits the threshold of the admissible density variation usually to 1%.

The viscous force $\mathbf{F}^{(v)}$ simplifies to the incompressible formulation

$$\mathbf{F}^{(v)} = \eta\nabla^2\mathbf{v}, \tag{4}$$

where η is the dynamic viscosity. Following the CSF model of Brackbill et al. [1] for constant surface tension, the surface force can be expressed as a volumetric force using the surface delta function δ_Σ by

$$\mathbf{F}^{(s)} = -\alpha\kappa\mathbf{n}\delta_\Sigma. \tag{5}$$

The capillary force $\alpha\kappa\mathbf{n}\delta_\Sigma$ is calculated with the curvature κ, the normal vector of the interface $\mathbf{n}$ and the surface-delta function δ_Σ. This expression describes the pressure-jump condition normal to an interface. In this work we focus only on the case where the interfacial surface tension is constant. Hence, the Marangoni force $\nabla_s\alpha\delta_\Sigma$ has no influence on the interface dynamics since the interfacial gradient of the surface tension $\nabla_s\alpha$ is zero.

3. Numerical method

The governing equations are discretized by the multi-phase SPH method presented in Hu and Adams [6]. Each particle represents a Lagrangian element of fluid, carrying all local phase properties. With updating the positions of the particles this

Author's personal copy

method accounts for advection as the governing equations are formulated in terms of material derivatives. For implementation we employ the Parallel Particle-Mesh (PPM) Library [15] which allows for large-scale particle simulations on parallel computer architectures.

3.1. Multi-phase flow solver

According to Hu and Adams [6] we calculate the density of a particle i at each time-step from a summation over all neighboring particles j

$$\rho_i = m_i \sum_j W_{ij} = \frac{m_i}{V_i}. \tag{6}$$

Here, m_i denotes the particle mass, $W_{ij} = W(\mathbf{r}_i - \mathbf{r}_j, h)$ is a kernel function with smoothing length h, and V_i is the volume of particle i. This summation allows for density discontinuities and conserves mass exactly.

The interpolation kernel function W can be any function which satisfies

$$\int W(\mathbf{r}, h) d\mathbf{r} = 1 \tag{7}$$

and has the Dirac delta-function property

$$\lim_{h \to 0} = W(\mathbf{r}, h) = \delta(\mathbf{r}). \tag{8}$$

Furthermore, according to Monaghan [10] a suitable kernel function should also have compact support to allow for numerically efficient approximations of the field quantities and gradients. Here, we use the quintic spline function presented by Morris et al. [12] with a compact support of $3h$. This kernel satisfies the above mentioned criteria, and Hongbin and Xin [5] showed that among 10 proposed kernels the quintic spline function or the Gaussian function are favorable in terms of computational accuracy.

The pressure term in the momentum equation is approximated as

$$\frac{d\mathbf{v}_i^{(p)}}{dt} = -\frac{1}{\rho_i}\nabla p_i = -\frac{1}{m_i}\sum_j \left(V_i^2 + V_j^2\right)\tilde{p}_{ij}\frac{\partial W}{\partial r_{ij}}\mathbf{e}_{ij}, \tag{9}$$

with the weight-function gradient $\frac{\partial W}{\partial r_{ij}}\mathbf{e}_{ij} = \nabla W(\mathbf{r}_i - \mathbf{r}_j)$ and the inter-particle pressure

$$\tilde{p}_{ij} = \frac{\rho_i p_j + \rho_j p_i}{\rho_i + \rho_j}. \tag{10}$$

In the case of interacting particles of the same phase this form of $\tilde{p}_{ij}$ recovers the simple midpoint-averaged pressure between the two particles. But when two particles of different phases interact, the density-weighted inter-particle pressure from Eq. (10) ensures that $\nabla p/\rho$ is continuous even for a discontinuous density field, see [8].

The viscous force is derived from the inter-particle-averaged shear stress with a combined viscosity. A simplification for incompressible flows gives

$$\frac{d\mathbf{v}_i^{(v)}}{dt} = \nu_i \nabla^2 \mathbf{v}_i = \frac{1}{m_i}\sum_j \frac{2\eta_i\eta_j}{\eta_i + \eta_j}\left(V_i^2 + V_j^2\right)\frac{\mathbf{v}_{ij}}{r_{ij}}\frac{\partial W}{\partial r_{ij}}, \tag{11}$$

where $\nu_i = \eta_i/\rho_i$ is the local kinematic viscosity of particle i, $\mathbf{v}_{ij} = \mathbf{v}_i - \mathbf{v}_j$ is the relative velocity of particle i and j and $r_{ij} = |\mathbf{r}_i - \mathbf{r}_j|$ is the distance of the two particles. This form of the viscous force conserves linear momentum. Angular conservation can be achieved using other formulations such as presented by Hu and Adams [7].

To distinguish between particles of different phases we use integer identifiers. Without a phase transition model this identifier is constant for a particle i during the entire simulation and is advected with the flow field. Introducing special interactions between particles of different phases, interface effects are incorporated within our method adaptively without the need of special interface reconstruction schemes. Therefore we can handle arbitrary interface shapes as well as breakup or merging of phases.

To calculate surface-tension forces between particles of different phases we introduce a color function c as

$$c_l^k = \begin{cases} 1, & \text{if the } k\text{th particle does not belong to the phase of particle } l, \\ 0, & \text{if the } k\text{th particle belongs to the phase of particle } l. \end{cases} \tag{12}$$

This color function has a unit-jump at a phase interface. Consequently, the gradient of the color function has a delta-function-like distribution and gives an approximation of the surface-delta function δ_Σ in Eq. (5). Furthermore, the normal direction at the interface can be obtained from the color gradient by

$$\mathbf{n} = \frac{\nabla c}{|\nabla c|}. \tag{13}$$

Author's personal copy

To further illustrate the transition region with a non-zero color gradient and the normal direction, Fig. 1 shows a sketch of the particles near an interface with the surface-delta function δ_Σ.

In this work, we do not use the color-gradient formulation of Hu and Adams [6], but introduce a new density-weighted summation. Physically, at an air–water interface the surface-tension forces in the liquid phase are much more prominent than those in the gas phase. Consequently, the interfacial motion is mainly driven by the water phase. Reflecting this behavior, we formulate the gradient of the color function as

$$\nabla c_i = \frac{1}{V_i}\sum_j [V_i^2 + V_j^2]\tilde{c}_{ij}\frac{\partial W}{\partial r_{ij}}\mathbf{e}_{ij} \tag{14}$$

using the inter-particle average

$$\tilde{c}_{ij} = \frac{\rho_j}{\rho_i+\rho_j}c_i^i + \frac{\rho_i}{\rho_i+\rho_j}c_j^i. \tag{15}$$

Note that for a density ratio $\Phi_\rho = \rho_1/\rho_2 = 1$ between the two phases, this expression is equal to the midpoint average of two particles i and j of Hu and Adams [6]. Fig. 2(a) shows the situation when two particles of different phase but with the same density interact. Here, the surface-delta function is symmetric since $\tilde{c}_{ij} = \tilde{c}_{ji} = 0.5$. For density rations Φ_ρ different from one the density-weighted inter-particle average Eq. (15) leads to a discontinuous color gradient as shown in Fig. 2(b).

It is important to note, that with the assumption of incompressibility of both phases and given the fact that $\tilde{c}_{ij} + \tilde{c}_{ji} = 1$, this new color gradient distribution maintains the property

$$\int_{-\infty}^{+\infty}\delta_\Sigma(\mathbf{r})d\mathbf{r} = \int_{-\infty}^{+\infty}|\nabla c(\mathbf{r})|d\mathbf{r}, \tag{16}$$

thus we can replace the surface-delta function in the surface-force term, Eq. (5), with the weighted color gradient, Eq. (14). In doing so, the resulting surface-tension force distribution along the interface is physically more sensible than for previous approaches.

To calculate the interface curvature within the transition band, we present a new reproducing divergence approximation without the need for the full support of the kernel function to be contained in the transition band. Starting from a Taylor series of a continuous vector field φ about the ith particle, we multiply the equation with the gradient of the kernel function

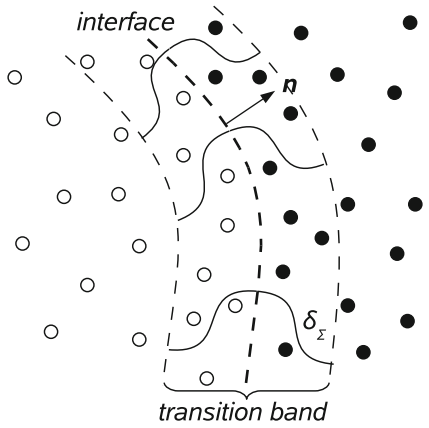

Fig. 1. Sketch of the transition band at an interface with the surface delta function δ_Σ, the normal **n** and particles of two different phases.

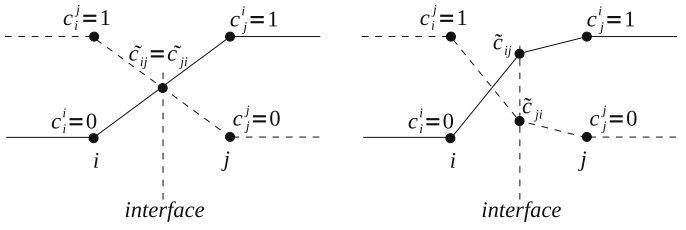

(a) Symmetric surface delta function $|\nabla c|$ (b) Non-symmetric surface delta function $|\nabla c|$

Fig. 2. Sketch of the color function and surface-delta function between two particles i and j of different phases with density ratio (a) $\rho_i/\rho_j = 1$ and (b) $\rho_i/\rho_j \gg 1$.

Author's personal copy

and integrate over the entire domain. Neglecting second and higher order terms, we obtain the summation form of the corrected gradient as

$$\nabla\varphi_i = \left[\sum_j \varphi_{ji} \otimes \nabla W(\mathbf{r}_{ji}) V_j\right]\left[\sum_j \mathbf{r}_{ji} \otimes \nabla W(\mathbf{r}_{ji}) V_j\right]^{-1}. \tag{17}$$

This formulation is very similar to the reproducing gradient approximation of Chen et al. [2]. One way to obtain the reproducing divergence approximation is to take the trace of Eq. (17). But since the denominator is a $d \times d$ matrix, where d is the number of spatial dimensions, this matrix must first be constructed and then inverted. To avoid this additional computational work, we further approximate the denominator of the formulation given above by two identities presented in Español and Revenga [3]

$$\int \mathbf{r} \otimes \nabla W(\mathbf{r}) d\mathbf{r} = -\mathbf{I}, \int \mathbf{r} \cdot \nabla W(\mathbf{r}) d\mathbf{r} = -d \tag{18}$$

with $\mathbf{I}$ being the unit matrix, as

$$\sum_j \mathbf{r}_{ji} \otimes \nabla W(\mathbf{r}_{ji}) V_j \approx \frac{\mathbf{I}}{d}\left(\sum_j \mathbf{r}_{ji} \cdot \nabla W(\mathbf{r}_{ji}) Vj\right). \tag{19}$$

Combining Eqs. (17) and (19) and taking the trace, we find that the approximated divergence can be written as

$$\nabla \cdot \varphi_i = d \frac{\sum_j \varphi_{ij} \cdot \mathbf{e}_{ij} \frac{\partial W}{\partial r_{ij}} V_j}{\sum_j r_{ij} \frac{\partial W}{\partial r_{ij}} V_j}. \tag{20}$$

Now only two simple summations are required to approximate the divergence for a particle i. Furthermore, for a linear field $\varphi = A\mathbf{r}$ with A being a constant, Eq. (20) gives Ad, hence reproduces the divergence of a linear field. Note, that Eq. (20) reproduces the divergence even when there is no full support of the kernel function of a particle contained within the transition band.

Using the above formulation to calculate the curvature of the interface, i.e. the divergence of the interface-normal direction, we finally obtain the acceleration of an interface particle by surface tension as

$$\frac{d\mathbf{v}_i^{(s)}}{dt} = -\frac{\alpha_i}{m_i} \kappa_i \nabla c_i. \tag{21}$$

Unlike the formulation in Hu and Adams [6] Eq. (21) takes effect as a body force, hence does not exactly conserve the total momentum of the system. Note, that when the density ratio Φ_ρ at the interface is large, according to Eq. (14) the surface force on the heavier phase is Φ_ρ-times of that on the lighter phase, thus both phases obtain accelerations with the same magnitude.

3.2. Time-step criteria

The equations presented above are integrated in time with the velocity Verlet scheme. For stability reasons the maximum time-step is chosen based on several time-step criteria [10,18]. Within the weakly-compressible SPH formulation, the time-step must satisfy the CFL-condition based on the maximum artificial sound speed and the maximum flow speed

$$\Delta t \leqslant 0.25 \frac{h}{c_{\max} + |u_{\max}|}, \tag{22}$$

the viscous condition

$$\Delta t \leqslant 0.125 \frac{h^2}{\nu}, \tag{23}$$

the body force condition

$$\Delta t \leqslant 0.25 \left(\frac{h}{|\mathbf{g}|}\right)^{1/2}, \tag{24}$$

and the surface-tension condition

$$\Delta t \leqslant 0.25 \left(\frac{\rho h^3}{2\pi\alpha}\right)^{1/2}. \tag{25}$$

For satisfying all conditions the global time-step is taken as minimum of Eqs. (22)–(25). Note that the surface-tension condition for the time-step constraint is based on the reference density. Hence, the admissible step-size of the time integration for a surface-tension dominated flow problem can be much larger than obtained with the formulation of Hu and Adams [6].

Author's personal copy

4. Numerical examples

In the following section we validate our surface-tension model by comparison to analytic solutions of two-dimensional problems for steady and unsteady problems. We demonstrate the capabilities of our method by simulating the breakup of a three-dimensional drop in a shear flow. For all cases we use ghost particles to impose the boundary conditions, see [14]. The mirror-particle technique is well suited for simple geometries with straight walls and allows for symmetry and no-slip conditions. Except for the last numerical example we use symmetry conditions at the boundaries and enforce a Neumann boundary condition for the pressure. Additionally, for walls we adjust the velocity of a mirrored ghost wall particle to $\mathbf{v}_{\text{virtual}} = 2\mathbf{v}_{\text{wall}} - \mathbf{v}_{\text{real}}$.

4.1. Square-droplet deformation

In our first test, we investigate the surface-tension driven deformation of an initially square droplet. We place a square patch of fluid "1" with an edge length of $l_x = l_y = 0.6$ into a box of fluid "2" with a domain size of $L_x = L_y = 1$. The density of both phases is $\rho = 1$, and we use a dynamic viscosity of $\eta = 0.2$. The surface-tension coefficient is set to $\alpha = 1$. Fig. 3(a) shows the initial particle positions of the two fluids of same density. After $t = 1$ a circular droplet is formed and the particles are at rest, see Fig. 3(b).

From the Laplace-law we find that the pressure within the droplet must be higher than that of the surrounding fluid. In two-dimensions the pressure drop across the interface must satisfy the condition

$$\Delta p = \frac{\alpha}{R} = \frac{\alpha\sqrt{\pi}}{l_x}, \tag{26}$$

where R is the final radius of the drop. In Fig. 4(a) the pressure profiles of two different initial square droplets of size $l_x = 0.4$ and 0.6 each with two different resolutions ($3h = 0.06$ and 0.03) are plotted against the radial coordinate. The dotted lines represent the analytic solutions for the two cases. The calculated pressure profiles agree well with the Laplace-law and convergence is demonstrated for both cases. Note also the thinning of the transition region at the interface with increasing resolution.

For our non-conservative surface-tension formulation we expect good stability properties with only small parasitic currents at the interface. Evidence is provided by the kinetic-energy evolution, Fig. 4(b), for an initially square droplet of size $l_x = 0.6$ and two resolutions $3h = 0.06$ and $3h = 0.03$. As a reference, we also computed the same case with the method of Hu and Adams [6], see the dashed line in the figure. At early stages, the surface-tension force produces interfacial motion deforming the square droplet, which is reflected by the peak in the logarithmic kinetic energy plot. At approximately $t = 1$ a circular droplet is formed and the particles are nearly at rest, i.e. the kinetic energy is very low. The energy-decrease at later times indicates the stability of the circular droplet configuration. Comparing our result with the simulations performed with the conservative method, good agreement is found for both resolutions. Consequently, our method neither introduces nor dissipates noticeable energy to a significant amount into the system. As the maximum velocity in the system at later times is on the order of $O(10^{-3})$ for both methods, parasitic currents are of negligible magnitude.

We also tested the square-droplet deformation with different densities for the two phases. Fig. 5 shows the pressure drop for density ratios ranging from $\Phi_\rho = \rho_1/\rho_2 = 0.001$ to $\Phi_\rho = 1000$. These ratios represent the situation of an air bubble in

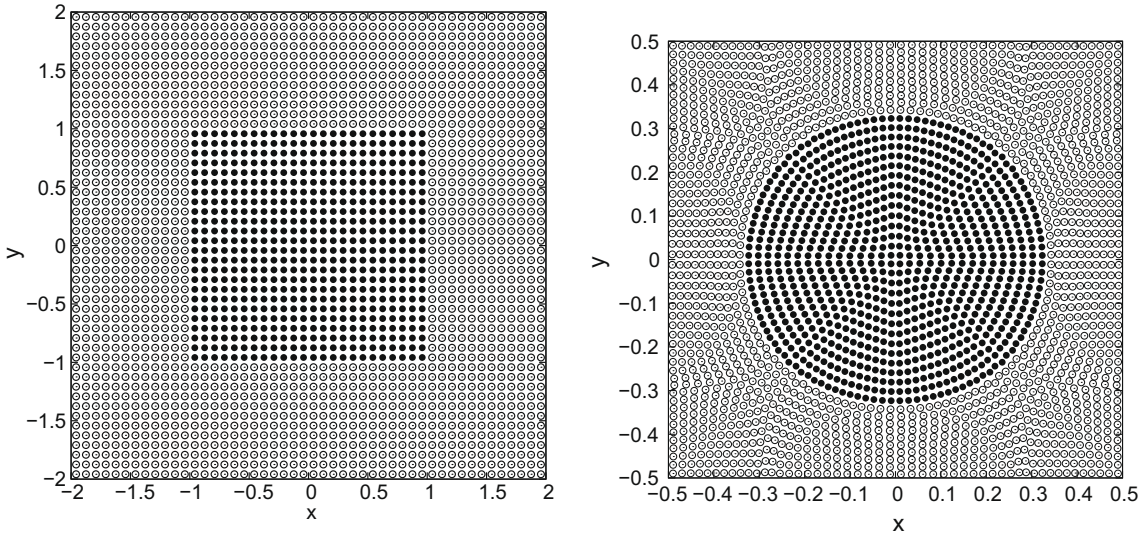

Fig. 3. Particle positions of the two fluids at (a) $t = 0$ and (b) $t = 1$.

Author's personal copy

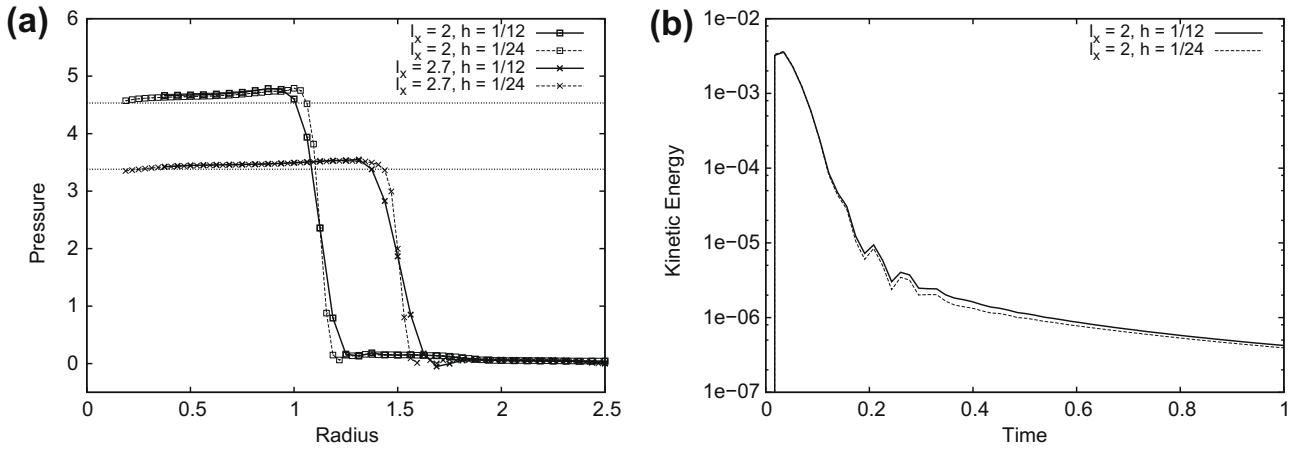

Fig. 4. Results of the simulation of the square-droplet deformation. (a) Pressure profiles vs. radial coordinate at $t = 1$ for $l_x = 0.4$ and 0.6. (b) Temporal evolution of the kinetic energy for $l_x = 0.6$ with two different resolutions $3h = 0.06$ and 0.03.

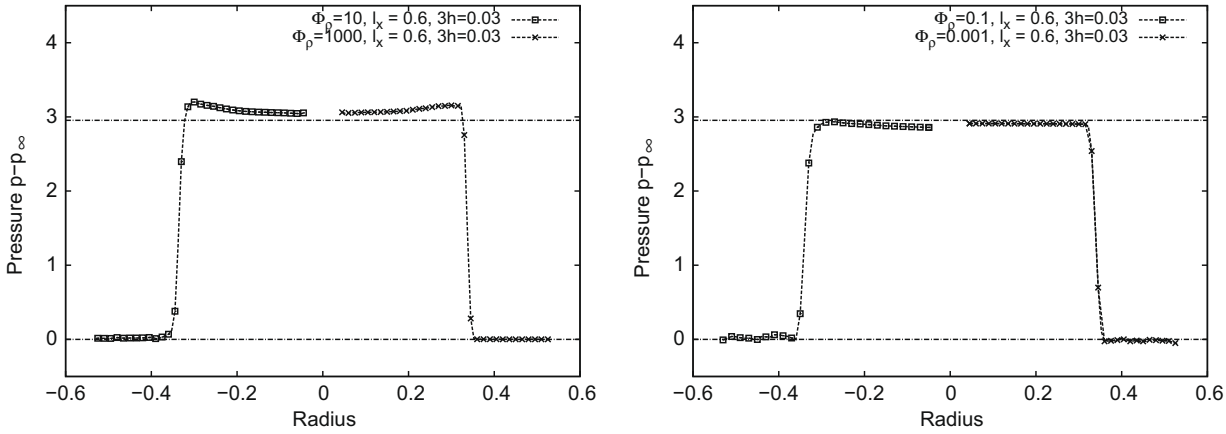

Fig. 5. Pressure drop for $l_x = 0.6$ with (a) $\phi_\rho = 10$ and $\phi_\rho = 1000$ and (b) $\phi_\rho = 0.1$ and $\phi_\rho = 0.001$.

water or a water droplet in air, respectively. Although the result is not as accurate as for the case with $\Phi_\rho = 1$, we find good agreement with and convergence to the analytic solution. Note that over- or underestimation of the pressure drop depends on the sign of the density gradient at the interface. This dependence can be explained by reference to the surface-tension model in our method. As we bias the surface-tension force towards the heavy phase at the interface, the approximation error implies an interface position slightly shifted towards the heavy phase.

4.2. Oscillating rod

A dynamic test case is the circular liquid-droplet oscillation under the action of capillary forces. Instead of starting from an initially elliptic droplet we prescribe an initial velocity field

$$U_x = U_0 \frac{x}{r_0}\left(1 - \frac{y^2}{r_0 r}\right)\exp\left(-\frac{r}{r_0}\right), \tag{27}$$

$$U_y = -U_0 \frac{y}{r_0}\left(1 - \frac{x^2}{r_0 r}\right)\exp\left(-\frac{r}{r_0}\right) \tag{28}$$

with $U_0 = 10$ and $r_0 = 0.05$ for the particles within the drop of radius $R = 0.2$. The computational domain is a box of size $L_x = L_y = 1.0$ and the droplet is placed at the center of the box. The densities of the liquid phase and the droplet are both set to $\rho_l = \rho_d = 1$, the dynamic viscosities are $\eta_l = \eta_d = 0.05$ and the surface-tension coefficient between the two phases is $\alpha = 1$. At the boundaries we apply no-slip wall boundary conditions. Fig. 6 shows the positions of the droplet particles at t = 0.0, 0.08, 0.16 and 0.26.

To show convergence of our method we simulate the oscillating droplet with different resolutions of 900, 3600 and 14,400 particles. The result of these simulations is shown in Fig. 7(a), where we compare the position of the mass center of the particles of the upper right-quarter section of the droplet.

Author's personal copy

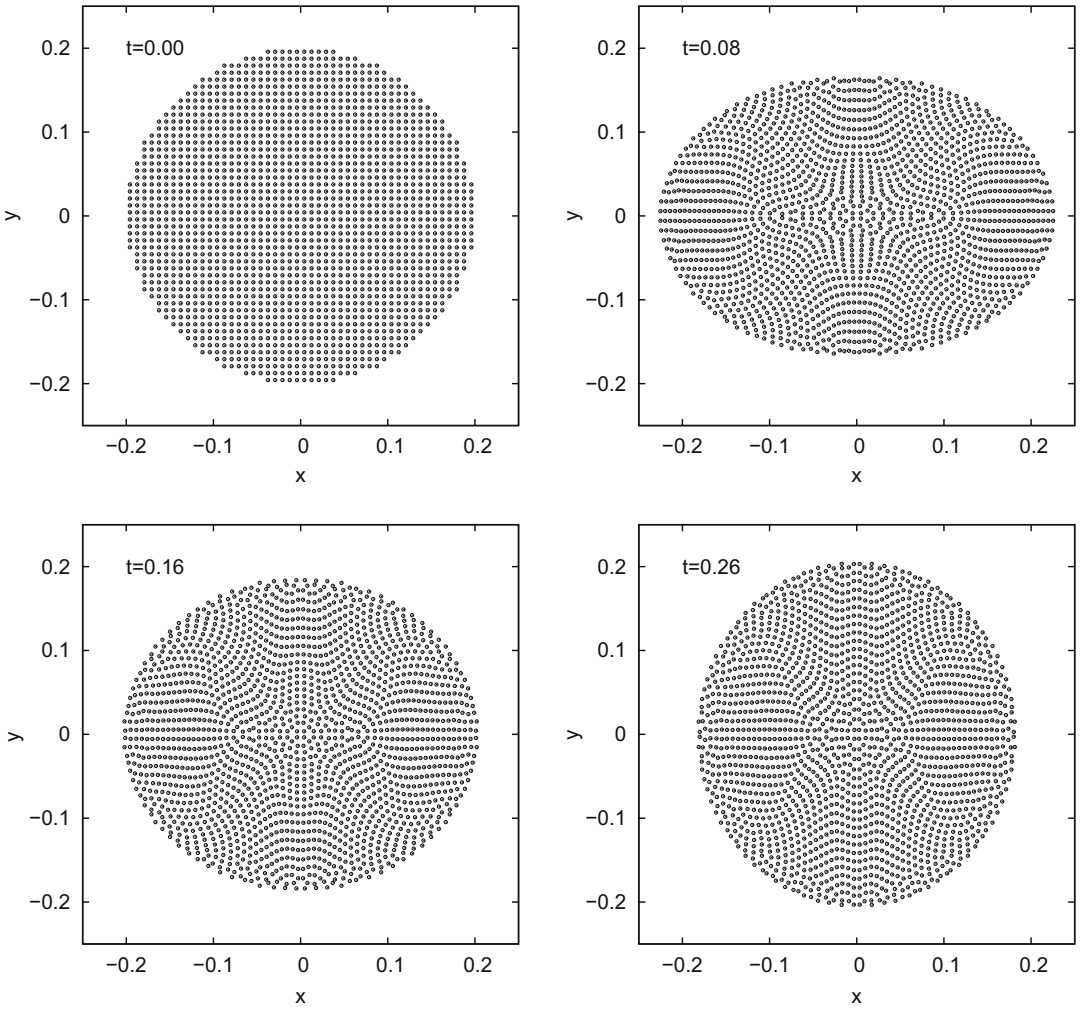

Fig. 6. Droplet oscillation with $\rho_d = \rho_l = 1$: positions of droplet particles at $t = 0.0$, 0.08, 0.16 and 0.26.

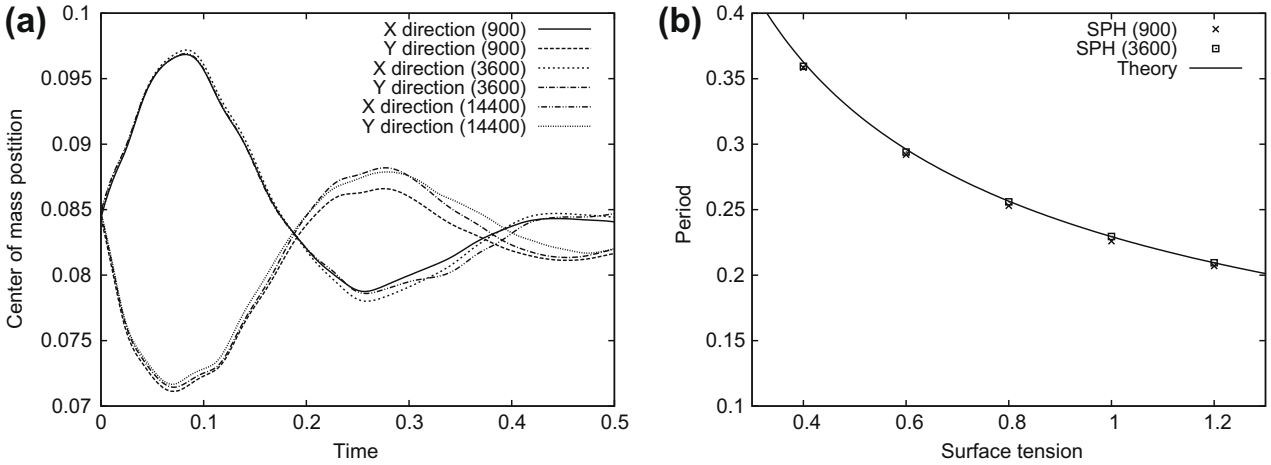

Fig. 7. (a) Droplet oscillation with $\rho_d = \rho_l = 1$: Convergence of center of mass position. (b) Droplet oscillation with $\Phi = 1000$ and $\lambda = 100$: Convergence of oscillation period.

Now we study the small-amplitude oscillations of an air–water like interface with $U_0 = 1$. For this purpose we set the density and viscosity ratio of the droplet phase and the surrounding phase to $\Phi = \rho_d/\rho_l = 1000$ and $\lambda = \eta_d/\eta_l = 100$, respectively. A study of the influence of the surface-tension coefficient on the resulting oscillation period τ is shown in Fig. 7(b). The solid line represents the theoretical relation between the surface tension α and the oscillation period $\tau = 2\pi\sqrt{\frac{R^3\rho_d}{6\alpha}}$. We find

Author's personal copy

good agreement between the analytic expression and the simulations over the entire range of studied parameters and demonstrate once again convergence of our method. As in Hu and Adams [6], the largest deviation from the theoretical values is less than 5%.

This second test case is of special importance for our new surface-tension formulation. If the simple inter-particle-averaged color gradient summation is used to obtain the curvature and normal direction, as in Hu and Adams [6], the artificial sound speed and the time-step size are determined by the surface tension and the density ratio, which leads to a much smaller Mach number (less than 0.05) and a much smaller time-step size than that obtained based on the maximum flow velocity. For the density-weighted color-gradient formulation we find that we can relax the time-step criterion implied by the surface tension (Eq. (25)) and use a suitable chosen reference density instead of the minimum density as threshold. In this example we set $\rho_{\text{ref}} = 0.1\rho_{\max}$ which allows for a 10 times larger time-step as compared to $\rho_{\min}$. The theoretical relation between the surface tension and the oscillation period can be computed accurately with a more reasonable Mach number (0.1) and significantly better efficiency, see Fig. 7(b).

4.3. Drop in shear flow

We consider a circular drop in a shear flow with a density ratio of $\Phi = 1$. The drop of size $R = 1$ is located in the middle of a periodic rectangular channel of size $L_x = L_y = 8$. A velocity of $\pm u_\infty$ is applied to the no-slip wall boundaries. The capillary number Ca and the Reynolds number Re are defined by the shear rate $G = 2u_\infty/L_y$, i.e.

$$Ca = \frac{G\eta R}{\alpha}, \quad Re = \frac{\rho G R^2}{\eta}. \tag{29}$$

In the range of parameters where a steady solution is obtained, the flow shear deforms the droplet to an ellipsoid, balancing the viscous stresses and the surface tension. As a measure of the deformation the parameter $D = (a-b)/(a+b)$ is used, which is a ratio of the transverse drop diameter a and conjugate diameter b.

Fig. 8(a) shows a snapshot of the simulation with the parameters $Ca = 0.2$, $Re = 1.0$ and a viscosity ratio of $\lambda = 100$. The calculation was performed with a smoothing length $3h = 0.25$, i.e. a total of 9216 particles. The deformation parameter is calculated with the least-square ellipse fitting method of Fitzgibbon et al. [4]. A comparison of the calculated deformations and the analytic predictions using the small-deformation theory suggested by Taylor [17] is plotted in Fig. 8(b). For both the viscosity ratios of $\lambda = 1$ and 100 we find good agreement with theory in the range of small capillary numbers. Contrary to Hu and Adams [8], the deformation parameter is slightly overpredicted, but the absolute deviation from theory using the same number of particles is smaller.

As last case we simulate a complex multi-phase problem with topology change of the interface geometry to show the capabilities of our method for technically relevant flows. For this purpose we place a three-dimensional drop of size $R = 1$ at the center of a computational domain of size $8R \times 4R \times 4R$ and move the upper and lower wall boundaries with the velocity $u_\infty = \pm 2$. Periodic boundary conditions are applied at the remaining boundaries. The shearing fluid and the drop phase have a density and viscosity ratio of $\Phi_\rho = \lambda = 1$. The other fluid properties are chosen to correspond to $Re = 1$ and $Ca = 0.25$. Fig. 9 shows the steady-state solution at $T = 25$ for a simulation with a resolution of $3h = 0.15$, i.e. a total of 1,024,000 particles. The left half of the droplet is represented with particles, the right half shows the extracted surface contour using pv-meshless [19]. The surrounding bulk phase is shown by blue particles. At $Ca = 0.25$ the shear forces are moderate compared to the surface-tension forces and the droplet deforms to a steady ellipsoid. We simulated 80,000 time-steps

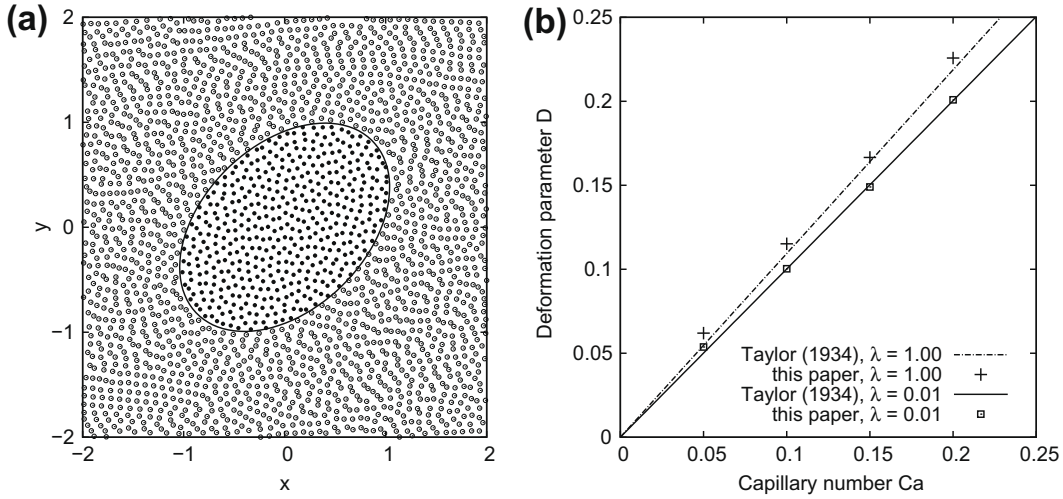

Fig. 8. (a) Positions of droplet particles and shearing fluid particles for $Ca = 0.2$, $Re = 1.0$ and $\lambda = 0.01$. (b) Drop deformation parameter D over capillary number Ca.

Author's personal copy

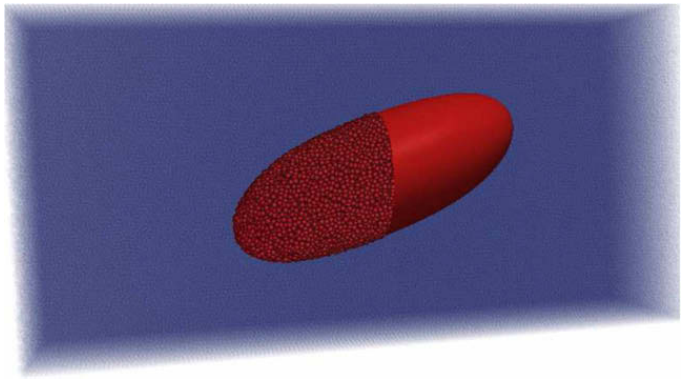

Fig. 9. Three-dimensional drop deformation in shear flow at $Re = 1$, $Ca = 0.25$ and a resolution of $3h = 0.15$ at $T = 25$.

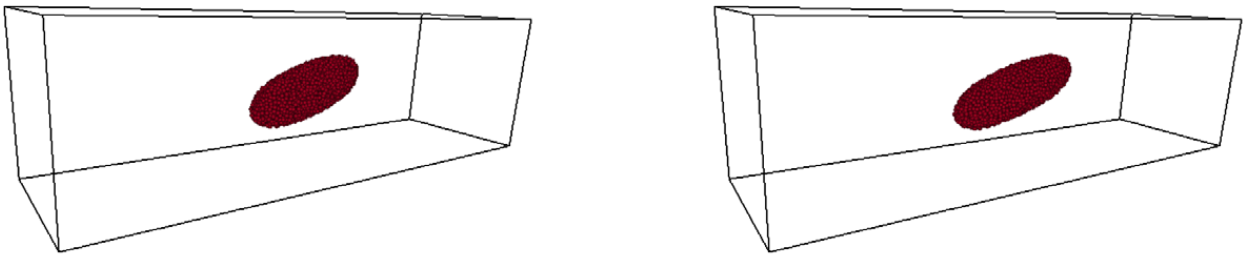

(a) Ca=0.25, left: T = 25, right: T = 50.

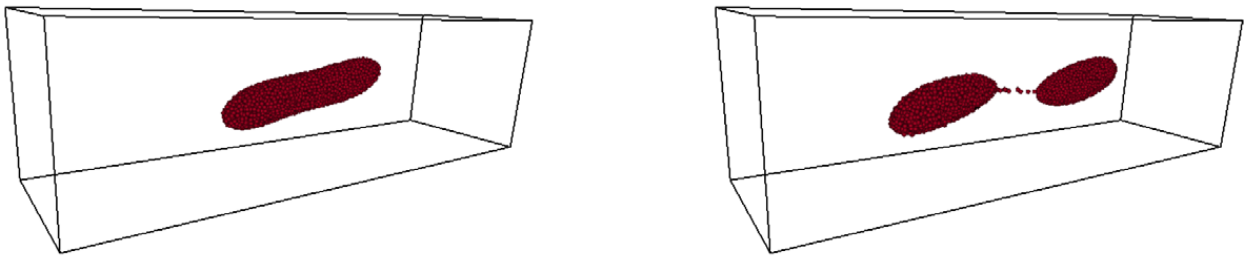

(b) Ca=0.3, left: T = 25, right: T = 50.

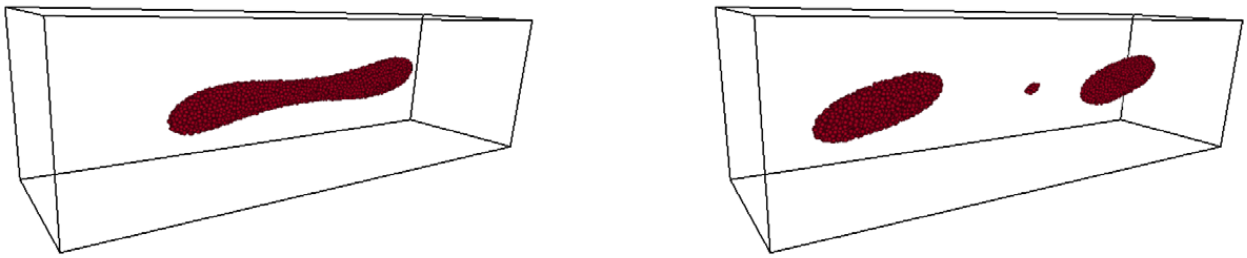

(c) Ca=0.35, left: T = 25, right: T = 50.

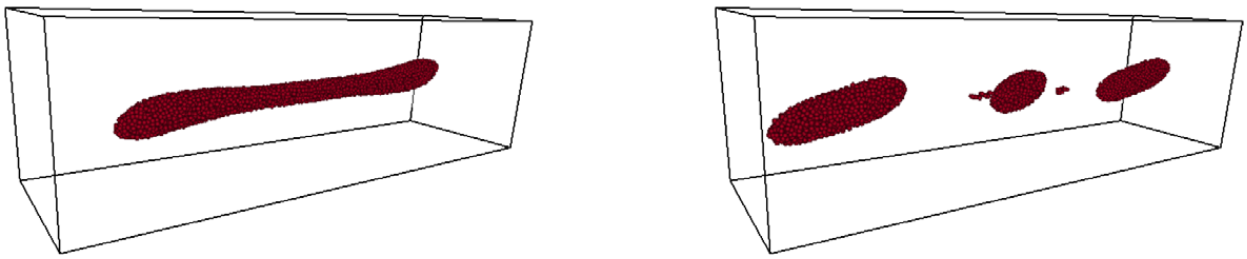

(d) Ca=0.4, left: T = 25, right: T = 50.

Fig. 10. Drop deformation and breakup in shear flow at $Re = 1$ and different capillary numbers at $T = 25$ (left figure) and $T = 50$ (right figure). After the breakup into two main daughter drops, the liquid thread in the middle is still unstable and separates two further small droplets.

Author's personal copy

of this example on a SGI Altix 4700 platform using 64 processors within about 80 h. The performance of the implemented SPH-client using the PPM library is about $2 \cdot 10^{-4}$ s/time-step/particle, which is comparable to the performance for a basic SPH code without surface-tension effects, see Sbalzarini et al. [15].

When the capillary number is increased, i.e. the surface-tension forces become less dominant, the capillary force is not strong enough to balance the viscous stress and no steady drop deformation is obtained. In Fig. 10 we show the results of the simulations with capillary numbers ranging from $Ca = 0.25$ to $Ca = 0.4$ in a channel of size $18R \times 4R \times 4R$ with a resolution of $3h = 0.3$. As a reference we show again the last example with $Ca = 0.25$ in Fig. 10(a). Above the critical state, see also Li et al. [9], droplet breakup occurs and produces two droplets, see Fig. 10(b). Further increasing the capillary number, the neck is more pronounced before breakup, and a very small third droplet between the other droplets is generated in Fig. 10(c). For high capillary numbers, the so-called "dumbbell" shape has a very long neck and a more complex breakup process occurs. In Fig. 10(d) we show that at $Ca = 0.4$ five droplets occur.

This example shows quite clear one advantage of SPH (and particle methods in general) compared to grid-based methods in studying multi-phase problems: once the studied problem is initialised, by its nature the method incorporates interface phenomena adaptively, i.e. the change of the interface geometry or even separation and merging are handled without the need of special numerical algorithms.

5. Concluding remarks

In this work, we present a novel surface-tension method for multi-phase SPH. With a new reproducing divergence approximation, we propose a new formulation for the surface curvature and modify the color gradient summation with a density weighting. While the new formulation has comparable accuracy as the formulation of Hu and Adams [6], it can achieve much faster computation for problems with large density ratio. Although demonstrated here only for the case of two different fluids distinguished by a single color function, we emphasize that an extension to handle more complex multi-phase problems is straightforward. We have validated our method with analytic solutions for steady equilibrium droplets, capillary waves and drop deformations in shear flow. We demonstrate convergence of our method and good stability properties even for long time simulations. The simulation of a complex three-dimensional problem shows the capabilities of our method in handling multi-phase problems with complex interfaces.

Acknowledgment

The authors wish to acknowledge the support of the German Research Foundation (DFG – Deutsche Forschungsgesellschaft) for funding this work within the project AD 186/6-1.

References

[1] J.U. Brackbill, D.B. Kothe, C. Zemach, A continuum method for modeling surface tension, J. Comput. Phys. 100 (2) (1992) 335–354.
[2] J.K. Chen, J.E. Beraun, T.C. Carney, A corrective smoothed particle method for boundary value problems in heat conduction, Int. J. Numer. Methods Eng. 46 (2) (1999) 231–252.
[3] P. Español, M. Revenga, Smoothed dissipative particle dynamics, Phys. Rev. E 67 (2) (2003) 026705.
[4] A. Fitzgibbon, M. Pilu, R.B. Fisher, Direct least square fitting of ellipses, IEEE Trans. Pattern Anal. Machine Intell. 21 (1999) 476–480.
[5] J. Hongbin, D. Xin, On criterions for smoothed particle hydrodynamics kernels in stable field, J. Comput. Phys. 202 (2) (2005) 699–709.
[6] X.Y. Hu, N.A. Adams, A multi-phase SPH method for macroscopic and mesoscopic flows, J. Comput. Phys. 213 (2) (2006) 844–861.
[7] X.Y. Hu, N.A. Adams, Angular-momentum conservative smoothed particle dynamics for incompressible viscous flows, Phys. Fluids 18 (10) (2006) 101702.
[8] X.Y. Hu, N.A. Adams, An incompressible multi-phase SPH method, J. Comput. Phys. 227 (1) (2007) 264–278.
[9] J. Li, Y.Y. Renardy, M. Renardy, Numerical simulation of breakup of a viscous drop in simple shear flow through a volume-of-fluid method, Phys. Fluids 12 (2) (2000) 269–282.
[10] J.J. Monaghan, Smoothed particle hydrodynamics, Rep. Prog. Phys. 68 (8) (2005) 1703–1759.
[11] J.P. Morris, Simulating surface tension with smoothed particle hydrodynamics, Int. J. Numer. Methods Fluids 33 (3) (2000) 333–353.
[12] J.P. Morris, P.J. Fox, Y. Zhu, Modeling low reynolds number incompressible flows using SPH, J. Comput. Phys. 136 (1) (1997) 214–226.
[13] S. Nugent, H.A. Posch, Liquid drops and surface tension with smoothed particle applied mechanics, Phys. Rev. E 62 (4) (2000).
[14] P.W. Randles, L.D. Libersky, Smoothed particle hydrodynamics: some recent improvements and applications, Comput. Methods Appl. Mech. Eng. 139 (1–4) (1996) 375–408.
[15] I.F. Sbalzarini, J.H. Walther, M. Bergdorf, S.E. Hieber, E.M. Kotsalis, P. Koumoutsakos, PPM – a highly efficient parallel particle-mesh library for the simulation of continuum systems, J. Comput. Phys. 215 (2) (2006) 566–588.
[16] A.M. Tartakovsky, P. Meakin, Modeling of surface tension and contact angles with smoothed particle hydrodynamics, Phys. Rev. E 72 (2) (2005).
[17] G.I. Taylor, The formation of emulsions in definable fields of flow, Proc. Roy. Soc. London Ser. A (1934) 501–523.
[18] Y. Zhu, P.J. Fox, Smoothed particle hydrodynamics model for diffusion through porous media, Transport Porous Media 43 (3) (2001) 441–471.
[19] J. Biddiscombe, D. Graham, P. Maruzewski, Interactive visualization and exploration of SPH data, in: Proceedings of 2nd SPHERIC international workshop, Madrid (Spain), May 2007, pp. 47–50.

A.4. A CONSERVATIVE SPH METHOD FOR SURFACTANT DYNAMICS

Rightslink Printable License https://s100.copyright.com/App/PrintableLicenseFrame.jsp?publisherI...

ELSEVIER LICENSE
TERMS AND CONDITIONS

Feb 04, 2013

This is a License Agreement between Stefan Adami ("You") and Elsevier ("Elsevier") provided by Copyright Clearance Center ("CCC"). The license consists of your order details, the terms and conditions provided by Elsevier, and the payment terms and conditions.

All payments must be made in full to CCC. For payment instructions, please see information listed at the bottom of this form.

Supplier	Elsevier Limited The Boulevard,Langford Lane Kidlington,Oxford,OX5 1GB,UK
Registered Company Number	1982084
Customer name	Stefan Adami
Customer address	Technische Universität München Garching, 85748
License number	3081820136497
License date	Feb 04, 2013
Licensed content publisher	Elsevier
Licensed content publication	Journal of Computational Physics
Licensed content title	A conservative SPH method for surfactant dynamics
Licensed content author	S. Adami,X.Y. Hu,N.A. Adams
Licensed content date	1 March 2010
Licensed content volume number	229
Licensed content issue number	5
Number of pages	18
Start Page	1909
End Page	1926
Type of Use	reuse in a thesis/dissertation
Portion	full article
Format	both print and electronic
Are you the author of this Elsevier article?	Yes
Will you be translating?	No
Order reference number	
Title of your thesis/dissertation	Modeling and Simulation of Multiphase Phenomena with SPH
Expected completion date	Apr 2013
Estimated size (number of pages)	120
Elsevier VAT number	GB 494 6272 12
Permissions price	0.00 EUR

1 von 5 04.02.2013 10:28

VAT/Local Sales Tax	0.0 USD / 0.0 GBP
Total	0.00 EUR
Terms and Conditions	

INTRODUCTION

1. The publisher for this copyrighted material is Elsevier. By clicking "accept" in connection with completing this licensing transaction, you agree that the following terms and conditions apply to this transaction (along with the Billing and Payment terms and conditions established by Copyright Clearance Center, Inc. ("CCC"), at the time that you opened your Rightslink account and that are available at any time at http://myaccount.copyright.com).

GENERAL TERMS

2. Elsevier hereby grants you permission to reproduce the aforementioned material subject to the terms and conditions indicated.

3. Acknowledgement: If any part of the material to be used (for example, figures) has appeared in our publication with credit or acknowledgement to another source, permission must also be sought from that source. If such permission is not obtained then that material may not be included in your publication/copies. Suitable acknowledgement to the source must be made, either as a footnote or in a reference list at the end of your publication, as follows:

"Reprinted from Publication title, Vol /edition number, Author(s), Title of article / title of chapter, Pages No., Copyright (Year), with permission from Elsevier [OR APPLICABLE SOCIETY COPYRIGHT OWNER]." Also Lancet special credit - "Reprinted from The Lancet, Vol. number, Author(s), Title of article, Pages No., Copyright (Year), with permission from Elsevier."

4. Reproduction of this material is confined to the purpose and/or media for which permission is hereby given.

5. Altering/Modifying Material: Not Permitted. However figures and illustrations may be altered/adapted minimally to serve your work. Any other abbreviations, additions, deletions and/or any other alterations shall be made only with prior written authorization of Elsevier Ltd. (Please contact Elsevier at permissions@elsevier.com)

6. If the permission fee for the requested use of our material is waived in this instance, please be advised that your future requests for Elsevier materials may attract a fee.

7. Reservation of Rights: Publisher reserves all rights not specifically granted in the combination of (i) the license details provided by you and accepted in the course of this licensing transaction, (ii) these terms and conditions and (iii) CCC's Billing and Payment terms and conditions.

8. License Contingent Upon Payment: While you may exercise the rights licensed immediately upon issuance of the license at the end of the licensing process for the transaction, provided that you have disclosed complete and accurate details of your proposed use, no license is finally effective unless and until full payment is received from you (either by publisher or by CCC) as provided in CCC's Billing and Payment terms and conditions. If full payment is not received on a timely basis, then any license preliminarily granted shall be deemed automatically revoked and shall be void as if never granted. Further, in the event that you breach any of these terms and conditions or any of CCC's Billing and Payment terms and conditions, the license is automatically revoked and shall be

void as if never granted. Use of materials as described in a revoked license, as well as any use of the materials beyond the scope of an unrevoked license, may constitute copyright infringement and publisher reserves the right to take any and all action to protect its copyright in the materials.

9. Warranties: Publisher makes no representations or warranties with respect to the licensed material.

10. Indemnity: You hereby indemnify and agree to hold harmless publisher and CCC, and their respective officers, directors, employees and agents, from and against any and all claims arising out of your use of the licensed material other than as specifically authorized pursuant to this license.

11. No Transfer of License: This license is personal to you and may not be sublicensed, assigned, or transferred by you to any other person without publisher's written permission.

12. No Amendment Except in Writing: This license may not be amended except in a writing signed by both parties (or, in the case of publisher, by CCC on publisher's behalf).

13. Objection to Contrary Terms: Publisher hereby objects to any terms contained in any purchase order, acknowledgment, check endorsement or other writing prepared by you, which terms are inconsistent with these terms and conditions or CCC's Billing and Payment terms and conditions. These terms and conditions, together with CCC's Billing and Payment terms and conditions (which are incorporated herein), comprise the entire agreement between you and publisher (and CCC) concerning this licensing transaction. In the event of any conflict between your obligations established by these terms and conditions and those established by CCC's Billing and Payment terms and conditions, these terms and conditions shall control.

14. Revocation: Elsevier or Copyright Clearance Center may deny the permissions described in this License at their sole discretion, for any reason or no reason, with a full refund payable to you. Notice of such denial will be made using the contact information provided by you. Failure to receive such notice will not alter or invalidate the denial. In no event will Elsevier or Copyright Clearance Center be responsible or liable for any costs, expenses or damage incurred by you as a result of a denial of your permission request, other than a refund of the amount(s) paid by you to Elsevier and/or Copyright Clearance Center for denied permissions.

LIMITED LICENSE

The following terms and conditions apply only to specific license types:

15. **Translation**: This permission is granted for non-exclusive world **English** rights only unless your license was granted for translation rights. If you licensed translation rights you may only translate this content into the languages you requested. A professional translator must perform all translations and reproduce the content word for word preserving the integrity of the article. If this license is to re-use 1 or 2 figures then permission is granted for non-exclusive world rights in all languages.

16. **Website**: The following terms and conditions apply to electronic reserve and author websites:
Electronic reserve: If licensed material is to be posted to website, the web site is to be password-protected and made available only to bona fide students registered on a relevant course if:
This license was made in connection with a course,

This permission is granted for 1 year only. You may obtain a license for future website posting,
All content posted to the web site must maintain the copyright information line on the bottom of each image,
A hyper-text must be included to the Homepage of the journal from which you are licensing at http://www.sciencedirect.com/science/journal/xxxxx or the Elsevier homepage for books at http://www.elsevier.com , and
Central Storage: This license does not include permission for a scanned version of the material to be stored in a central repository such as that provided by Heron/XanEdu.

17. **Author website** for journals with the following additional clauses:

All content posted to the web site must maintain the copyright information line on the bottom of each image, and the permission granted is limited to the personal version of your paper. You are not allowed to download and post the published electronic version of your article (whether PDF or HTML, proof or final version), nor may you scan the printed edition to create an electronic version. A hyper-text must be included to the Homepage of the journal from which you are licensing at http://www.sciencedirect.com/science/journal/xxxxx . As part of our normal production process, you will receive an e-mail notice when your article appears on Elsevier's online service ScienceDirect (www.sciencedirect.com). That e-mail will include the article's Digital Object Identifier (DOI). This number provides the electronic link to the published article and should be included in the posting of your personal version. We ask that you wait until you receive this e-mail and have the DOI to do any posting.

Central Storage: This license does not include permission for a scanned version of the material to be stored in a central repository such as that provided by Heron/XanEdu.

18. **Author website** for books with the following additional clauses:
Authors are permitted to place a brief summary of their work online only.
A hyper-text must be included to the Elsevier homepage at http://www.elsevier.com . All content posted to the web site must maintain the copyright information line on the bottom of each image. You are not allowed to download and post the published electronic version of your chapter, nor may you scan the printed edition to create an electronic version.

Central Storage: This license does not include permission for a scanned version of the material to be stored in a central repository such as that provided by Heron/XanEdu.

19. **Website** (regular and for author): A hyper-text must be included to the Homepage of the journal from which you are licensing at http://www.sciencedirect.com/science/journal/xxxxx. or for books to the Elsevier homepage at http://www.elsevier.com

20. **Thesis/Dissertation**: If your license is for use in a thesis/dissertation your thesis may be submitted to your institution in either print or electronic form. Should your thesis be published commercially, please reapply for permission. These requirements include permission for the Library and Archives of Canada to supply single copies, on demand, of the complete thesis and include permission for UMI to supply single copies, on demand, of the complete thesis. Should your thesis be published commercially, please reapply for permission.

21. **Other Conditions**:

v1.6

If you would like to pay for this license now, please remit this license along with your payment made payable to "COPYRIGHT CLEARANCE CENTER" otherwise you will be invoiced within 48 hours of the license date. Payment should be in the form of a check or money order referencing your account number and this invoice number RLNK500949011.
Once you receive your invoice for this order, you may pay your invoice by credit card. Please follow instructions provided at that time.

Make Payment To:
Copyright Clearance Center
Dept 001
P.O. Box 843006
Boston, MA 02284-3006

For suggestions or comments regarding this order, contact RightsLink Customer Support: customercare@copyright.com or +1-877-622-5543 (toll free in the US) or +1-978-646-2777.

Gratis licenses (referencing $0 in the Total field) are free. Please retain this printable license for your reference. No payment is required.

Author's personal copy

Journal of Computational Physics 229 (2010) 1909–1926

Contents lists available at ScienceDirect

Journal of Computational Physics

journal homepage: www.elsevier.com/locate/jcp

A conservative SPH method for surfactant dynamics

S. Adami *, X.Y. Hu, N.A. Adams

Lehrstuhl für Aerodynamik, Technische Universität München, 85748 Garching, Germany

ARTICLE INFO

Article history:
Received 1 April 2009
Received in revised form 5 November 2009
Accepted 9 November 2009
Available online 17 November 2009

Keywords:
SPH
Insoluble/soluble surfactant
Surface diffusion
Interfacial flow
Surface tension
Marangoni effects

ABSTRACT

In this paper, a Lagrangian particle method is proposed for the simulation of multiphase flows with surfactant. The model is based on the multiphase smoothed particle hydrodynamics (SPH) framework of Hu and Adams (2006) [1]. Surface-active agents (surfactants) are incorporated into our method by a scalar quantity describing the local concentration of molecules in the bulk phase and on the interface. The surfactant dynamics are written in conservative form, thus global mass of surfactant is conserved exactly. The transport model of the surfactant accounts for advection and diffusion. Within our method, we can simulate insoluble surfactant on an arbitrary interface geometry as well as interfacial transport such as adsorption or desorption. The flow-field dynamics and the surfactant dynamics are coupled through a constitutive equation, which relates the local surfactant concentration to the local surface-tension coefficient. Hence, the surface-tension model includes capillary and Marangoni-forces. The present numerical method is validated by comparison with analytic solutions for diffusion and for surfactant dynamics. More complex simulations of an oscillating bubble, the bubble deformation in a shear flow, and of a Marangoni-force driven bubble show the capabilities of our method to simulate interfacial flows with surfactants.

© 2009 Elsevier Inc. All rights reserved.

1. Introduction

Multiphase systems occur in a wide range of technical or biological applications. The dynamics of such systems are much more complex than that of single-phase systems. Depending on the characteristic length scales, surface-tension forces at an interface may dominate inertia effects and thus have a strong influence on the overall flow evolution. Surface-tension effects can be differentiated into the capillary force and the Marangoni-force. The former is proportional to the local curvature and minimizes the interface area, the latter accounts for surface-tension gradients along the interface (Scriven and Sternling [2]).

Surface-active agents (surfactants) offer the possibility to manipulate or even control the dynamics of multiphase systems. By their nature, surfactant molecules adhere to a fluid interface and reduce the local surface tension as they form a buffer zone between the two phases. The surfactant at an interface is advected with the interfacial motion and may diffuse along the surface. Consequentially, surface-tension gradients can develop and influence the flow evolution. Besides the insoluble case, where all molecules are confined to the interface, the dynamics of the surfactant can be coupled with the adjacent phases. Depending on the bulk concentration and the local interface concentration, adsorption and desorption may transport surfactant molecules between the bulk phase and the interface.

Surfactants are widely used in technological and biological applications. Due to the presence of surfactant, e.g. in a mixture of water and air, very small droplets can be formed which is useful to drug delivery, water purification and other applications. Even more important is the presence of surfactant in pulmonary alveoli, whose liquid-lining layer can function only

* Corresponding author. Tel.: +49 89 289 16122; fax: +49 89 289 16139.
E-mail addresses: stefan.adami@aer.mw.tum.de (S. Adami), Xiangyu.Hu@aer.mw.tum.de (X.Y. Hu).

0021-9991/$ - see front matter © 2009 Elsevier Inc. All rights reserved.
doi:10.1016/j.jcp.2009.11.015

Author's personal copy

with a substance that reduces surface tension (Pattle [3], Clements [4]). A simple estimate of the pressure in the liquid layer of an alveolar structure with a characteristic length scale of about 100 μm and the Young–Laplace equation shows that a pure water–air interface ($\sigma_0 \approx 0.07$ N/m) would cause endexpiratory alveolar collapse and atelectasis (Von Neergard [5]). Moreover, surfactant molecules are believed to contribute also to pulmonary defence mechanisms and local immunomodulation (Hamm et al. [6]).

A numerical model describing interface dynamics including surfactants needs to handle the phase singularity at the interface and solve the surfactant evolution equation on the interface. Also, an evolution equation for the surfactant in the bulk solution needs to be coupled with the interfacial dynamics. As a consequence, the surfactant dynamics and the flow field cannot be solved independently from each other. Another important issue is the conservative formulation of the governing equations, in particular with respect to the mass of surfactant. These requirements render the modeling of multiphase flows with interfaces including surfactant effects a challenging task which has been studied already since about 20 years.

Early numerical investigations of the effect of surfactants in multiphase systems were limited to the insoluble case, where the transport of molecules between the bulk phase and the interface is neglected. The models were mainly used to investigate the effect of surfactants on drop deformation in a shear flow. Stone and Leal [7] solved the time-dependent convective-diffusion equation for surfactant transport on an interface using the boundary-integral method. Including the effect of surfactant solubility, Milliken and Leal [8] studied the deformation and breakup of a drop in an axial extensional flow with their extended boundary-integral method, but they did not present a general method for simulating arbitrary interfaces with soluble surfactants. While these works were restricted to two-dimensional problems, Yon and Pozrikidis [9] developed a fully three-dimensional finite volume method combined with the boundary-element method to study shear flows past a viscous drop. Whereas these methods described the interface in a discrete way, many following works used a continuous interface representation to account for interface dynamics. Xu and Zhao [10] used the Eulerian level-set method, where the moving interface is formulated as zero level-set on a Cartesian grid. They considered the interface to be convected passively by the flow, i.e. they prescribed the flow field and solved the surfactant dynamics on the interface without feedback to the flow field.

With respect to its importance for realistic long-time simulations and for accuracy reasons, the surfactant mass conservation property was of special interest in subsequent works. James and Lowengrub [11] presented a fully coupled, axisymmetric, incompressible Navier–Stokes solver based on the "volume of fluid" (VOF) method and simulated insoluble surfactant dynamics on a moving interface. Different from previous works, they tracked the surfactant mass instead of solving the evolution equation for the concentration. Also, the surface area is tracked in this method instead of a reconstruction from the volume fraction. As consequence, for long-time simulations and strong interface deformations the reconstruction of the interface might be inconsistent with both the volume fraction and the surface area. Xu et al. [12] used a level-set method for interfacial Stokes flows to investigate the effect of insoluble surfactants on single drops and droplet interactions. Conservation of surfactant material on the interface was enforced numerically by a rescaling operation, since the method itself was not formulated in conservative variables.

Recently, Lai et al. [13] proposed an immersed-boundary method to simulate the interfacial problems with insoluble surfactant. Their main achievement is a new discretization for the surfactant concentration equation and a Lagrangian tracking of the interface, which allows for numerical conservation of the total mass of surfactant.

An important increase of considered complexity in the contaminated and moving interface problem was achieved by Zhang et al. [14]. They solved the fully coupled flow field and surfactant dynamics on the interface and in the bulk phase. The flux of surfactant on the interface was assumed to be balanced by adsorption and desorption. But this front-tracking method does not conserve the total mass of surfactant. Muradoglu and Tryggvason [15] also used the front-tracking method to simulate interfacial flows with soluble surfactant, but assumed that the mass transfer between the bulk phase and the interface occurs within a thin adsorption layer. They considered the axisymmetric motion and deformation of a viscous drop moving in a circular tube and demonstrated first-order convergence of the surfactant mass error.

Another class of methods use finite elements to simulate free surface flows with surfactant transport, e.g. Liao et al. [16] and McGough and Basaran [17]. Such approaches do not satisfy discrete conservation of surfactant mass at the interface, which can be of particular importance for the long-time simulations of realistic applications.

In this article, we present a numerical method that includes all main relevant surfactant dynamics in an incompressible Navier–Stokes solver based on the smoothed particle hydrodynamics (SPH) method. This Lagrangian formulation for multiphase problems requires no special interface capturing or tracking and can handle complex geometries as well as topology changes. We introduce the surfactant dynamics in conservative form and use mass fluxes to consider the exchange of surfactant between the interface and the bulk phase. Within the thin interface layer, we solve a diffusion equation for the surfactant and due to our Lagrangian method advection is naturally included. Furthermore, we use different constitutive equations for the surface-tension correlation to demonstrate the general applicability of our method. We validate the method by comparisons with analytic solutions and grid convergence studies and show the exact conservation of surfactant mass on the interface and in the bulk phase. Finally, we study some more complex multiphase problems such as the oscillating bubble experiment, the bubble deformation in shear flow and the Marangoni-force driven bubble.

In the next section, the governing equations for the flow field and the surfactant dynamics are presented and the numerical algorithm summarizing also the main aspects of the SPH particle method is described in Section 3. The diffusion model in the bulk phase as well as on the interface and the coupling between them is validated and tested in Section 4. Some complex simulations are presented in Section 5 and finally, concluding remarks are given in Section 6.

Author's personal copy

2. Governing equations

The isothermal Navier–Stokes equations are solved on a moving Lagrangian frame

$$\frac{d\rho}{dt} = -\rho\nabla\cdot\mathbf{v}, \tag{1}$$

$$\frac{d\mathbf{v}}{dt} = \mathbf{g} + \frac{1}{\rho}\left[-\nabla p + \mathbf{F}^{(v)} + \mathbf{F}^{(s)}\right], \tag{2}$$

where ρ, p, $\mathbf{v}$ and $\mathbf{g}$ are material density, pressure, velocity and body force, respectively. $\mathbf{F}^{(v)}$ denotes the viscous force and $\mathbf{F}^{(s)}$ is the interfacial surface force.

In SPH, incompressible flow is usually modelled by the weakly-compressible approach, in which a stiff equation of state (EOS) is used to relate the pressure to the density, i.e.

$$p = p_0\left(\frac{\rho}{\rho_0}\right)^{\gamma} + b, \tag{3}$$

with $\gamma = 7$, the reference pressure p_0, the reference density ρ_0 and a parameter b. These parameters and the artificial speed of sound are chosen following a scale analysis presented by Morris et al. [18] which determines the threshold of the admissible density variation.

The viscous force $\mathbf{F}^{(v)}$ then simplifies to the incompressible formulation

$$\mathbf{F}^{(v)} = \eta\nabla^2\mathbf{v}, \tag{4}$$

where η is the dynamic viscosity. Following the continuum-surface-tension model (CSF), the surface force can be expressed as the gradient of the surface stress tensor with the surface-tension coefficient α

$$\mathbf{F}^{(s)} = \nabla\cdot[\alpha(\mathbf{I}-\mathbf{n}\otimes\mathbf{n})\delta_\Sigma] = -(\alpha\kappa\mathbf{n} + \nabla_s\alpha)\delta_\Sigma. \tag{5}$$

The capillary force $\alpha\kappa\mathbf{n}\delta_\Sigma$ is calculated with the curvature κ, the normal vector of the interface $\mathbf{n}$ and the surface-delta function δ_Σ. This expression describes the pressure jump condition normal to an interface. In case of surface tension variations along the interface (e.g. due to non-uniform temperature or surfactant concentration) the Marangoni-force $\nabla_s\alpha\delta_\Sigma$ results in a tangential stress acting along the interface (∇_s is the surface gradient operator).

The evolution of surfactant on the interface is governed by an advection–diffusion equation with a source term accounting for the surfactant transport between the bulk and the phase interface, e.g. adsorption and desorption,

$$\frac{d\Gamma}{dt} = \nabla_s\cdot\mathbf{D_s}\nabla_s\Gamma + \dot{S}_\Gamma, \tag{6}$$

where Γ, $\mathbf{D_s}$ and $\dot{S}_\Gamma$ are the interfacial surfactant concentration, the diffusion coefficient matrix (in case of isotropic diffusion $\mathbf{D_s} = D_s\cdot\mathbf{I}$) and the source term, respectively.

After integration over the domain, Eq. (6) gives the variation of the total mass m_s of the interfacial surfactant

$$\frac{dm_s}{dt} = \frac{1}{dt}\int_V \Gamma\delta_\Sigma dV = \int_V \nabla_s\cdot\mathbf{D_s}\nabla_s\Gamma\delta_\Sigma dV + \int_V \dot{S}_\Gamma\delta_\Sigma dV. \tag{7}$$

The source term $\dot{S}_\Gamma$ specifies the surfactant mass flux between the bulk phase and the interface. As widely used in the literature, the transport of surfactant is assumed to follow Langmuir kinetics (see Borwankar and Wasan [19])

$$\dot{S}_\Gamma = k_1 C_s(\Gamma^\star - \Gamma) - k_2\Gamma, \tag{8}$$

where k_1 and k_2 are the adsorption and desorption coefficients and C_s is the volumetric concentration of surfactant in the fluid phase immediately adjacent to the interface. The maximum equilibrium surfactant concentration is given by $\Gamma^\star$, which is only reached by Γ in the limit of large concentration C_s.

Assuming that each surfactant molecule can move freely in the bulk phase, the transport of surfactant can be described by the advection–diffusion equation

$$\frac{dC}{dt} = \nabla D_\infty\nabla C. \tag{9}$$

Here, D_∞ denotes the bulk diffusion coefficient and C is the volumetric surfactant concentration in the liquid. After integration over the domain the rate of change of the total surfactant mass in the liquid M_s is obtained by

$$\frac{dM_s}{dt} = \int_V D_\infty\nabla^2 C dV - \int_V \dot{S}_\Gamma\delta_\Sigma dV. \tag{10}$$

The second term on the right side of Eq. (10) is equal to the second term on the right hand side of Eq. (7), hence ensures global mass conservation.

Author's personal copy

To close our model, we relate the interfacial surfactant concentration Γ to the surface-tension coefficient α by a constitutive equation. In this paper, the model of Otis et al. [20] defined by two piecewise linear functions is used

$$\alpha(\Gamma) = \begin{cases} \alpha_0 + (\alpha^\star - \alpha_0)\frac{\Gamma}{\Gamma^\star}, & \Gamma \leqslant \Gamma^\star \\ \alpha^\star - \alpha_2\left(\frac{\Gamma}{\Gamma^\star} - 1\right), & \Gamma^\star < \Gamma \leqslant \Gamma_{\max}. \end{cases} \tag{11}$$

In Eq. (11), α_0 is the reference surface tension of the clean surface and $\alpha^\star$ is the reduced surface tension at the maximum equilibrium surfactant concentration $\Gamma^\star$. The second part of the function is defined up to the maximum possible surfactant concentration $\Gamma_{\max}$ where the surface tension α changes proportionally with factor α_2 to the non-dimensional concentration $\Gamma/\Gamma^\star$. $\Gamma_{\max}$ is the maximum dynamic concentration of surfactant obtainable on dynamic compression of the interface, see [20].

Note that the use of other relations, such as the Frumkin isotherm or the Langmuir model [21,14,9,22,23], is straightforward.

The governing equations are non-dimensionalized using reference values for the velocity u_0, the length scale l_0, the density ρ_0 and the bulk concentration C_∞. The non-dimensional characteristic numbers are

$$Re = \frac{\rho_0 u_0 l_0}{\eta}, \quad Ca = \frac{\eta u_0}{\alpha_0}, \quad Bo = \frac{\rho g l_0^2}{\alpha_0}, \tag{12}$$

$$Pe_s = \frac{u_0 l_0}{D_s}, \quad Pe_\infty = \frac{u_0 l_0}{D_\infty}, \quad Da = \frac{\Gamma^\star}{C_\infty l_0}, \tag{13}$$

where Re, Ca, Bo, Pe_s, Pe_∞ and Da are the Reynolds number, the capillary number, the Bond number, the Peclet number based on D_s, the Peclet number based on D_∞ and the Damköhler number [15].

3. Numerical method

The governing equations are discretized using the multiphase SPH method of Hu and Adams [1]. Each particle represents a Lagrangian element of fluid, carrying all local phase properties. With updating the positions of the particles, this method accounts for advection as the governing equations are formulated in terms of material derivatives.

3.1. Multiphase flow solver

According to Hu and Adams [1], we calculate the density of a particle i each timestep from a summation over all neighboring particles j

$$\rho_i = m_i \sum_j W_{ij} = \frac{m_i}{V_i}. \tag{14}$$

Here, m_i denotes the particle mass, $W_{ij} = W(\mathbf{r}_i - \mathbf{r}_j, h)$ is a kernel function with smoothing length h and V_i is the volume of particle i. This summation allows for density discontinuities and conserves mass exactly. Based on the studies of Morris et al. [18], we use the quintic spline function with compact support of $3h$ as kernel function.

The pressure term in the momentum equation is approximated as

$$\frac{d\mathbf{v}_i^{(p)}}{dt} = -\frac{1}{\rho_i}\nabla p_i = -\frac{1}{m_i}\sum_j \left(V_i^2 p_i + V_j^2 p_j\right)\frac{\partial W}{\partial r_{ij}}\mathbf{e}_{ij}, \tag{15}$$

with the weight-function gradient $\frac{\partial W}{\partial r_{ij}}\mathbf{e}_{ij} = \nabla W(\mathbf{r}_i - \mathbf{r}_j)$. Note that this form conserves linear momentum exactly since exchanging indices i and j in the sum leads to an opposite pressure force. The viscous force is derived from the inter-particle-averaged shear stress with a combined viscosity. A simplification for incompressible flows gives

$$\frac{d\mathbf{v}_i^{(v)}}{dt} = \nu_i \nabla^2 \mathbf{v}_i = \frac{1}{m_i}\sum_j \frac{2\eta_i\eta_j}{\eta_i + \eta_j}\left(V_i^2 + V_j^2\right)\frac{\mathbf{v}_{ij}}{r_{ij}}\frac{\partial W}{\partial r_{ij}}, \tag{16}$$

where $\nu_i = \eta_i/\rho_i$ is the local kinematic viscosity of particle i, $\mathbf{v}_{ij} = \mathbf{v}_i - \mathbf{v}_j$ is the relative velocity of particle i and j and $r_{ij} = |\mathbf{r}_i - \mathbf{r}_j|$ is the distance of the two particles.

The calculation of the interface curvature to determine the surface tension can be avoided. For this purpose, in the continuous surface force model (CSF) the surface force is rewritten as the gradient of a stress tensor. The gradient of the color function c_i is used as approximation of the surface-delta function δ_Σ. This color function defines to which phase particle i belongs, i.e. $c_i = 0$ for phase 1 and $c_i = 1$ for phase 2. Since this function has a unit jump across the phase interface, the particle-averaged gradient ∇c_i of particle i

Author's personal copy

$$\nabla c_i = \frac{1}{V_i}\sum_j \left[V_i^2 c_i + V_j^2 c_j\right]\frac{\partial W}{\partial r_{ij}}\mathbf{e}_{ij} \tag{17}$$

has a delta-function-like distribution. Hence, the interface stress between phases 1 and 2 is obtained as

$$\Pi_i^{(s)} = \alpha_i \frac{1}{|\nabla c_i|}\left(\frac{1}{d}\mathbf{I}|\nabla c_i|^2 - \nabla c_i \nabla c_i\right), \tag{18}$$

where d denotes the spatial dimension and α is the surface tension coefficient between the phases 1 and 2. Finally, the particle-averaged gradient of this stress term gives the particle acceleration due to surface tension

$$\frac{d\mathbf{v}_i^{(s)}}{dt} = \frac{1}{m_i}\sum_j \frac{\partial W}{\partial r_{ij}}\mathbf{e}_{ij}\cdot\left(V_i^2\Pi_i^{(s)} + V_j^2\Pi_j^{(s)}\right). \tag{19}$$

3.2. Surfactant kinetics

Using the color function to distinguish different phases in the system, particles with a non-vanishing color-function gradient approximate the singularity at an interface as a narrow transition band, see Fig. 1. As only particles with at least one neighbor of a different phase have a non-vanishing color-function gradient, the thickness of this transition band is of the size of $3h$ at each side of the interface. Within this narrow band of particles, the governing equations for the interfacial phenomena (6)–(8) are solved locally for each individual particle. Hence, using the color gradient function as surface-delta function, an interfacial particle i contributes to the interface area by

$$A_i = V_i|\nabla c_i| \tag{20}$$

(in two dimensions, A_i and V_i are the interface length and the particle area). Corresponding to the individual interface area fraction, each particle carries a fraction of interfacial mass of surfactant m_{si}. The evolution of the surfactant mass fraction of a single particle due to adsorption and desorption is given by

$$\frac{dm_{si}^{(s)}}{dt} = \dot{S}_{\Gamma_i}A_i = \left[k_1 C_\infty\left(\Gamma^\star - \Gamma_i\right) - k_2\Gamma_i\right]A_i, \tag{21}$$

where the subscript (s) indicates the effects due to adsorption and desorption. To assure the numerical stability for particles with small interface area, the interfacial surfactant concentration is calculated from a kernel average

$$\Gamma_i = \frac{\sum_j m_{sj}W_{ij}}{\sum_j A_j W_{ij}}, \tag{22}$$

where summation is on all neighboring interface particles, i.e. all neighboring particles which are within the narrow transition band.

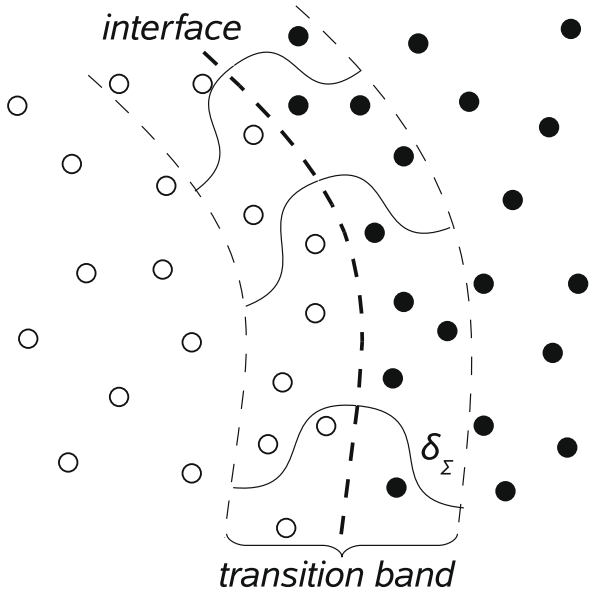

Fig. 1. Sketch of the transition band at an interface with the surface delta function δ_Σ and particles of two different phases. The width of the transition band is equal to the compact support of the kernel function on each side of the interface, i.e. in total $6h$.

Author's personal copy

As we solve the surfactant equations in conservative form, the total mass of surfactant is conserved exactly. Due to particle motion it may happen, that interface particles leave the transition band and transport surfactant material away from the interface. To ensure exact conservation of surfactant mass in the system, we must treat these particles k that leave the interface transition band in a special way. Their fraction of interfacial mass of surfactant m_{sk} is mapped back to a particle i that remains within the transition band by

$$\Delta m_{si}^{map} = \sum_k m_{sk} \frac{W_{ki}}{\sum_l W_{kl}}, \tag{23}$$

where the smoothing function W_{ki} serves as weighting factor. To satisfy the consistency condition, this weight is normalized with $\sum_l W_{kl}$. Here, the summation is on all particles I of the intersection of neighbors of k and the remaining interface particles.

3.3. Bulk diffusion

The diffusion in the bulk phase has a similar form as the viscous force in the momentum equation for an incompressible flow. Hence, the SPH approximation of the diffusion equation in conservative form follows in analogy to Eq. (16) as:

$$\frac{dM_{si}}{dt} = \sum_j \frac{2D_{\infty i} D_{\infty j}}{D_{\infty i} + D_{\infty j}} \left(V_i^2 + V_j^2\right) \frac{C_{ij}}{r_{ij}} \frac{\partial W}{\partial r_{ij}}, \tag{24}$$

where M_{si} is the mass of surfactant in the bulk phase of particle i, $D_{\infty i}$ and $D_{\infty j}$ are the bulk diffusion coefficients of particle i and j and $C_{ij} = C_i - C_j$ is the concentration difference. Note that the average diffusion coefficient in Eq. (24) ensures the zero-flux condition between two phases if one diffusion coefficient is zero. Each time-step, after updating the particle surfactant mass and particle volume, the local bulk concentration is calculated from

$$C_i = \frac{M_{si}}{V_i}. \tag{25}$$

3.4. Interfacial diffusion

Following Bertalmío et al. [24], the interfacial diffusion Eq. (6) can be expressed as

$$\frac{d\Gamma}{dt} = \nabla_s \cdot \mathbf{D_s} \nabla_s \Gamma = \frac{1}{|\nabla c|} \nabla \cdot [\mathbf{P_s} \mathbf{D_s} \nabla \Gamma |\nabla c|], \tag{26}$$

where $\mathbf{P_s} = \mathbf{I} - \mathbf{n} \otimes \mathbf{n}$ is the operator, which projects the gradient of the surfactant concentration $\nabla\Gamma$ tangentially to the interface (i.e. the surface gradient operator $\nabla_s\Gamma$). This formulation solves the interfacial diffusion on a surface of a finite width and thus is well suited for the interfacial modelling within the smoothed particle hydrodynamics framework.

Discretizing Eq. (26) with SPH, we calculate the term in the brackets on the RHS ($\lambda = \mathbf{P_s} \mathbf{D_s} \nabla \Gamma |\nabla c|$) for each particle and use the general SPH summation formula to calculate the divergence of λ. Finally, the material derivative of the interfacial surfactant mass fraction by interfacial diffusion is

$$\frac{dm_{si}^{(d)}}{dt} = \sum_j \left(\lambda_{\mathbf{i}} V_i^2 + \lambda_{\mathbf{j}} V_j^2\right) \frac{\partial W}{\partial r_{ij}} \mathbf{e}_{ij}. \tag{27}$$

Particles on the fringes of the interface transition band might have only one neighboring particle of a different phase. Hence, the simple normalized color gradient could lead to a wrong approximation of the interface normal direction. As a remedy, we calculate the normal vector by a weighted summation of the color gradients of the interfacial neighbors j

$$\mathbf{n_i} = \frac{\sum_j \nabla c_j A_j}{\left|\sum_j \nabla c_j A_j\right|}. \tag{28}$$

Here, the interfacial area fraction A_j is used as weighing factor since the color gradient of the interface nearest particle is a better approximation of the normal direction (see Section 4.2, Fig. 4(b)).

As a consequence of the finite transition region, the general SPH discretization does not everywhere give an accurate estimate of the surfactant gradient. The neighbors of a particle adjacent to the interface do not all belong to the interface and must therefore be excluded from the gradient calculation. Following Chen et al. [25], a corrected gradient calculation at position $\mathbf{x_i}$ yields

$$\nabla \Gamma(\mathbf{x_i}) = \left[\sum_j (\mathbf{x_i} - \mathbf{x_j}) V_j^2 \nabla W_{ij} V_j\right]^{-1} \cdot \sum_j (\Gamma_i - \Gamma_j) V_j^2 \nabla W_{ij} V_j. \tag{29}$$

Author's personal copy

This formulation is valid for all situations where the gradient $\nabla\Gamma(\mathbf{x_i})$ of particle i is calculated with at least two neighboring particles in the transition band. The implementation of Eq. (29) is for both two and three dimensions straightforward since only a $d \times d$ matrix inversion has to be performed.

During time integration, due to particle motion in the transition band around the interface a non-uniform and non-smooth surfactant concentration profile normal to the interface may develop. In the limit of an infinitely high resolution, this unphysical effect vanishes as the width of the transition region tends to zero. Nevertheless, to increase the accuracy especially for lower resolution simulations, we introduce a smoothing of the surfactant concentration normal to the interface. Instead of using a reinitialization as presented by Sbalzarini et al. [26], we adopt the directed-diffusion approach to introduce artificial normal diffusion within the transition band. For this purpose, Eq. (26) is extended with the artificial normal diffusion as

$$\frac{d\Gamma}{dt} = \nabla_s \cdot \mathbf{D_s}\nabla_s\Gamma = \frac{1}{|\nabla c|}\nabla \cdot [\mathbf{P_s}\mathbf{D_s}\nabla\Gamma|\nabla c| + \mathbf{P_n}\mathbf{D_n}\nabla\Gamma|\nabla c|], \tag{30}$$

where $\mathbf{P_n} = \mathbf{n} \otimes \mathbf{n}$ and $\mathbf{D_n} = D_n\mathbf{I}$ are the normal projection matrix and the normal diffusion coefficient matrix.

3.5. Coupling between the bulk phase and the interface

The evolution of surfactant on the interface and in the bulk phase is coupled by the source term $\dot{S}_\Gamma A$, thus global conservation of mass is ensured. If one fluid phase is insoluble for surfactant but has an interface containing surfactant, a special treatment of its interface particles is needed. Physically, the bulk surfactant concentration C_k and the interfacial surfactant concentration Γ_k of such a particle k are zero. But as these particles contribute to the surfactant dynamics within the transition band, the bulk concentration must be extrapolated from the interface particles of the adjacent phase. Accordingly, the calculated surfactant mass flux of these particles must be taken into account on the opposite bulk particles. Mathematically, the mass exchange between an interface particle k (of an insoluble phase) and a bulk particle i (of the opposite soluble phase) is represented as

$$\Delta\left(\frac{dM_{si}}{dt}\right) = -\sum_k \dot{S}_{\Gamma_k} A_k \frac{A_i}{\sum_l A_l}, \tag{31}$$

where the fraction of the interface area A_i is used as weight. For consistency this weight is normalized with the sum of the fractions of the interface areas $\sum_l A_l$. Here, the summation is on all particles l, which are in the surfactant soluble phase and in the neighborhood of particle k (within the support domain of the kernel function).

3.6. Time-step criteria

The equations presented above are integrated in time with an explicit predictor – corrector scheme. All quantities are updated in every substep. For stability reasons the global time-step is chosen based on several time-step criteria [27,28]. Within the weakly-compressible SPH formulation, following [27,28,1] the time-step must satisfy the CFL-condition (Courant–Friedrichs–Lewy-condition) based on the maximum artificial sound speed and the maximum flow speed

$$\Delta t \leqslant 0.25\frac{h}{c_{\max} + |u_{\max}|}, \tag{32}$$

the viscous condition

$$\Delta t \leqslant 0.125\frac{h^2}{\nu}, \tag{33}$$

the body force condition

$$\Delta t \leqslant 0.25\left(\frac{h}{|\mathbf{g}|}\right)^{1/2}, \tag{34}$$

the surface tension condition

$$\Delta t \leqslant 0.25\left(\frac{\rho h^3}{2\pi\alpha}\right)^{1/2} \tag{35}$$

and the diffusion condition

$$\Delta t \leqslant 0.125\frac{h^2}{D}. \tag{36}$$

Therefore, the global time-step is evaluated through the minimum between Eqs. (32)–(36).

Author's personal copy

4. Validation

To validate our modeling and implementation of the diffusion effects and surfactant kinetics with SPH we consider several two-dimensional test cases isolating each single effect. Provided that an analytic solution is available, we compare our results and test for convergence.

4.1. Bulk diffusion

In a first test we calculate the diffusion of a scalar species in a bulk liquid phase. For the computational domain we choose a square of fluid surrounded by solid walls with a length of $l_x = l_y = 0.1$ m in each direction. The diffusion coefficient of the liquid phase is taken to be $D = 4 \times 10^{-6}$ m^2/s. Using an initial exponential distribution of the concentration field $C(x,t)$

$$C(x, t = 0) = \exp\left[\frac{-(x - x_0)^2}{4DT_0}\right], \tag{37}$$

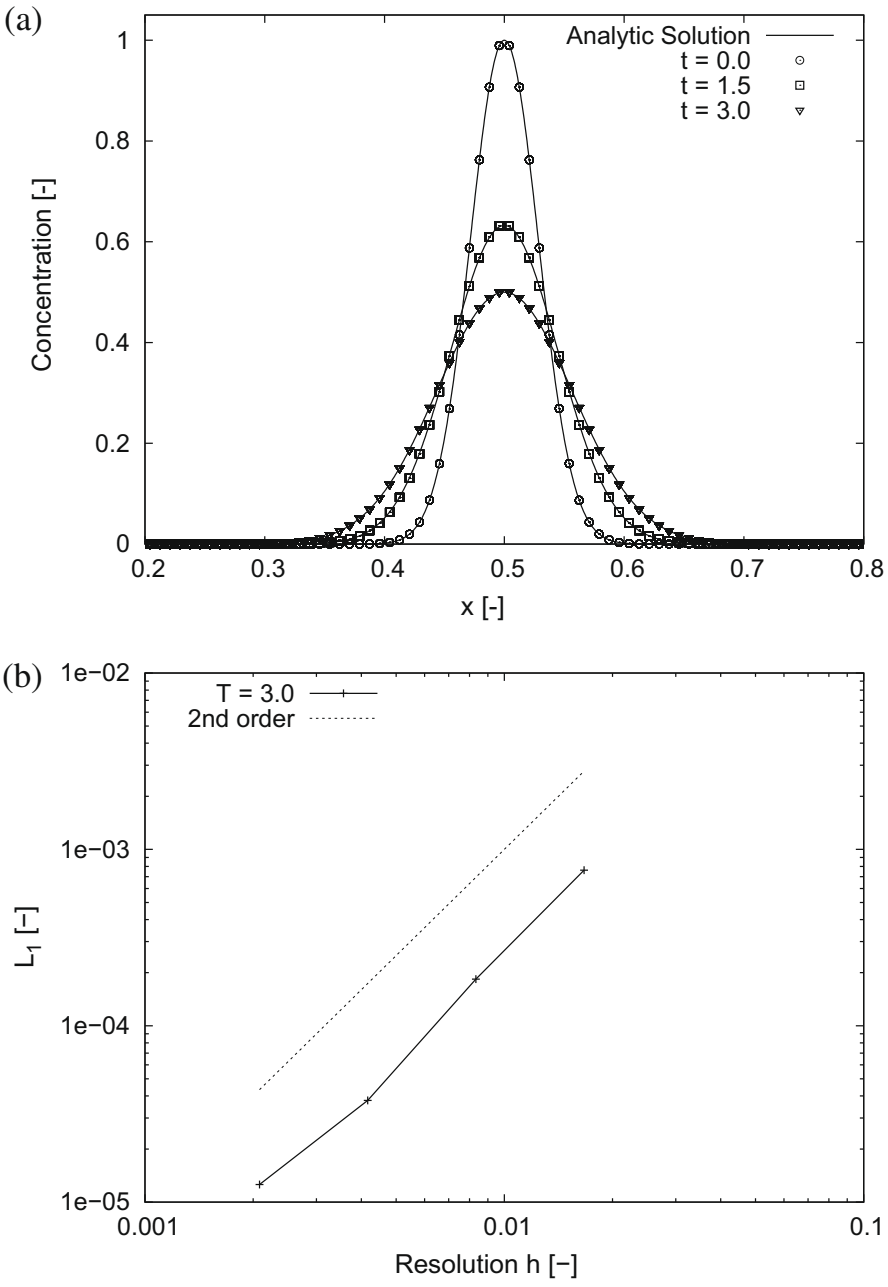

Fig. 2. (a) Concentration profiles of bulk diffusion at $t = 0.0$, 1.5 and 3.0; solid line: analytic solution, symbols: SPH results. (b) L_1 error with respect to smoothing length h for the bulk diffusion test (see Section 4.1).

Author's personal copy

the analytic solution of the diffusion problem follows from:

$$C(x,y,t) = \frac{A}{\sqrt{t+T_0}} \exp\left[\frac{-(x-x_0)^2}{4D(t+T_0)}\right], \tag{38}$$

where $T_0 = 1s,\ A = 1\ \mathrm{kg\ m^{-3}\ s^{1/2}}$ and $x_0 = l_x/2$.

Fig. 2(a) shows the evolution of the concentration profiles at $t = 1.5$ and 3. The solid lines represent the exact analytic solution and the symbols denote the results of a simulation with smoothing length $h = 8.\bar{3} \times 10^{-3}$. The time and spatial values are made dimensionless with the reference values T_0 and l_x, respectively. Even though this resolution is relatively poor, the calculated profiles are in very good agreement with the analytic solution. To evaluate the accuracy of our calculation quantitatively we define the error norm L_1

$$L_1 = \frac{\sum_j |C_j - C(x_j,t)|}{C_\infty N}, \tag{39}$$

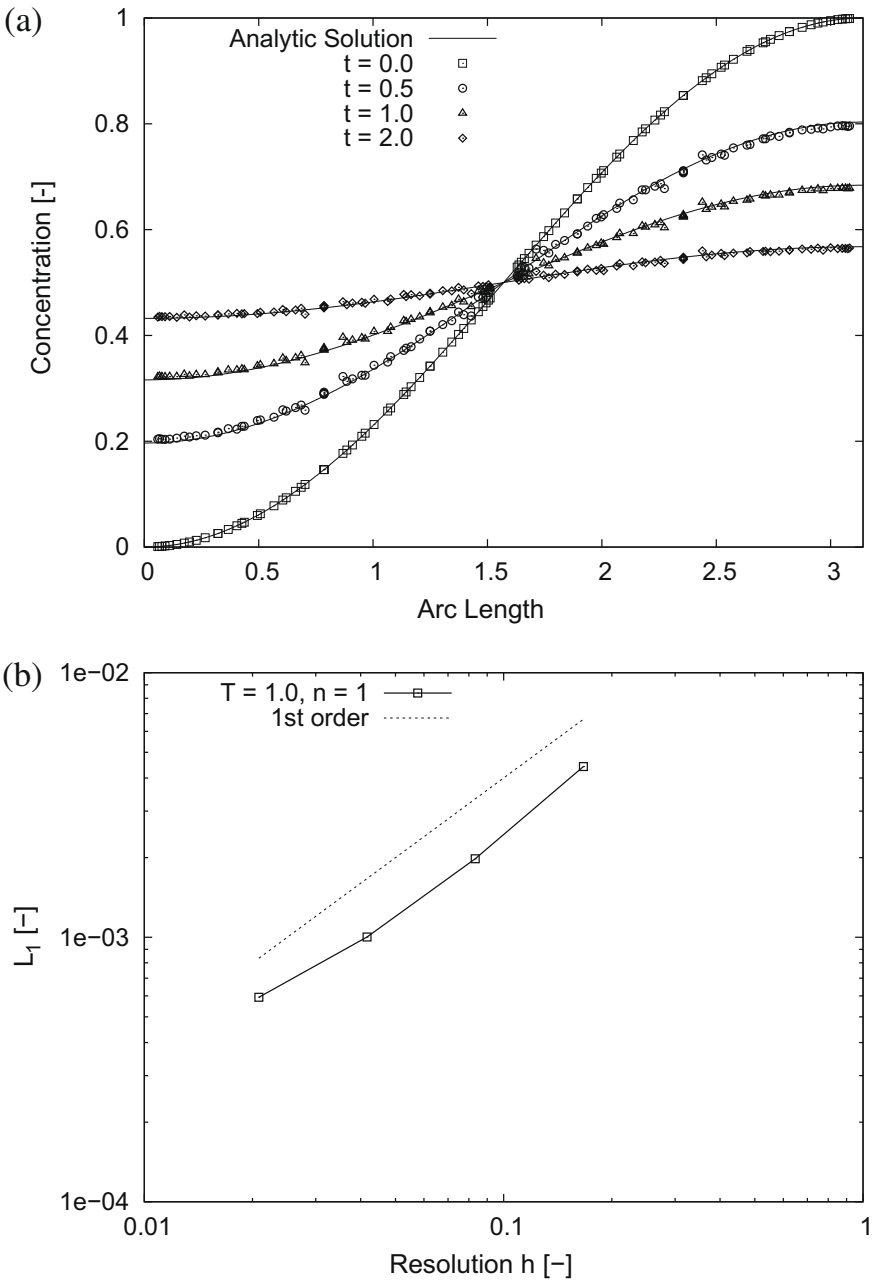

Fig. 3. (a) Concentration profiles of interfacial diffusion at $t = 0$, 0.5, 1.0 and 2.0; solid line: analytic solution, symbols: SPH results. (b) L_1 error with respect to smoothing length h for the interfacial diffusion test (see Section 4.2).

Author's personal copy

which is the normalized particle-averaged deviation from the analytic solution. Here, N denotes the total number of particles. In Fig. 2(b) the error norm L_1 is plotted with respect to the smoothing length h. As expected, with increasing resolution the error decreases and converges approximately with second order.

4.2. Surface diffusion

For validation of the surface diffusion model we calculate the temporal evolution of an initially non-uniformly distributed surfactant concentration profile on an interface. We put a drop with radius $R = 1 \times 10^{-3}$ m into a liquid environment (centered in a Cartesian coordinate system) and initialize the interfacial surfactant concentration with the solution from Xu et al. [10] at $t = 0$

$$\Gamma(\Theta, t) = \frac{\Gamma_\infty}{2}[\exp(-t)\cos(\Theta) + 1]. \tag{40}$$

Here, Θ is the counterclockwise angle of the interface with respect to the x-axis.

Fig. 3(a) shows the prediction of the interfacial concentration profiles with our SPH-model compared to the analytic solution at several timesteps. The calculations were performed with a smoothing length $h = 5 \times 10^{-3}$ m, a surface diffusivity of $D = 1 \times 10^{-6}$ m^2/s for both the tangential and normal diffusion and a maximum surfactant concentration $\Gamma_\infty = 3 \times 10^{-6}$ kg/m^2. The reference values used to non-dimensionalize the results are $T_\infty = 1$ s,Γ_∞ and $l_\infty = R$. The calculated profiles only show very small discrepancies from the analytic solution. These errors converge with about first-order, see Fig. 3(b).

To clarify the influence of the interface-normal approximation, in a next step we neglect the diffusivity on the interface ($D_s = 0$) and simulate the surfactant concentration evolution on a steady air–water interface. Physically, the profile is expected to remain at the initial condition. The left profile in Fig. 4(a) shows the surfactant profile after $t = 5$ using the normalized color gradients as normal direction $\mathbf{n}_i = \nabla c_i/|\nabla c_i|$. The profile is not smooth and differs strongly from the initial condition. This problem arises from the fact, that the particles are initially positioned on a Cartesian grid and that the circular interface is not represented accurately. Consequently, the color gradients do not represent the correct normal direction, which is shown in the left plot of Fig. 4(b). Note that the length of the vectors is adjusted for clarity.

We solved this problem with the introduction of the averaged normal calculation with Eq. (28). The corresponding surfactant profile and normals are shown in the right plots in Fig. 4(a) and (b). The initial surfactant profile is preserved and the normal diffusion does not introduce artificial surface diffusion.

4.3. Surfactant kinetics

Now we test our implementation of the interfacial surfactant transport and the coupling between the bulk phase and the interface. For this purpose, the adsorption of surfactant molecules to an initially clean interface is investigated. A bubble of size $R = 1 \times 10^{-3}$ m is exposed to a liquid phase with a constant surfactant concentration of $C(x, t = 0) = C_0 = 1$ kg/m^3.

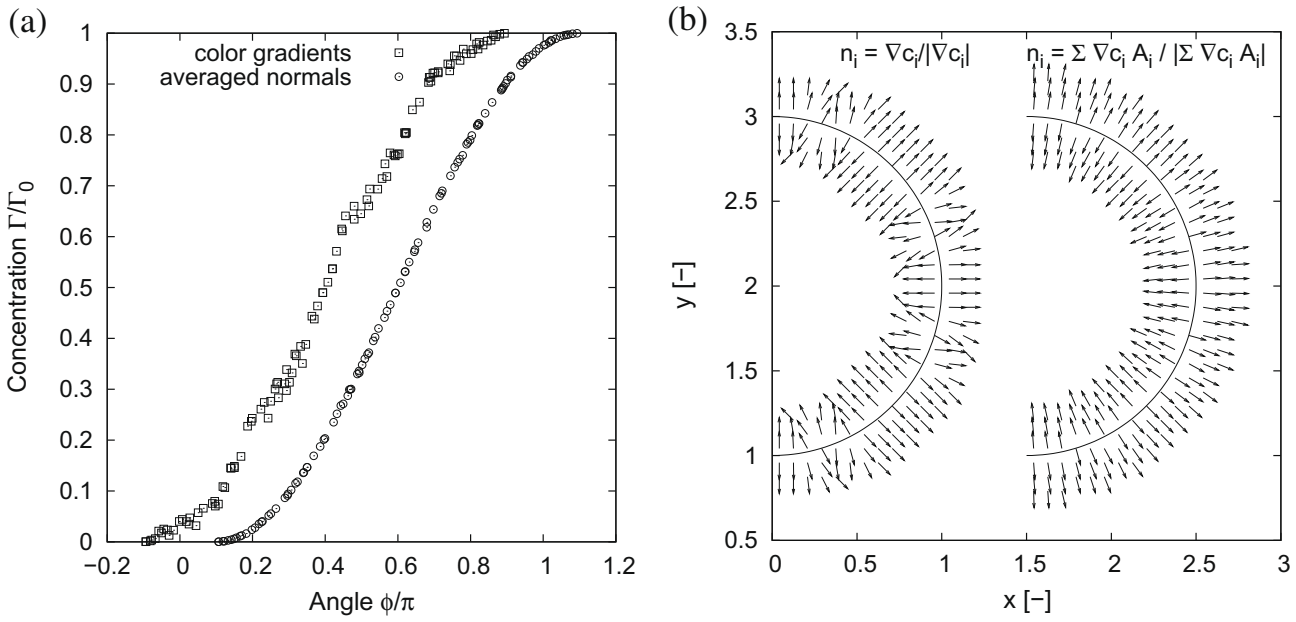

Fig. 4. (a) Non-dimensional surfactant concentration profile at $t = 5$ with $D_n = 1$ and $h = 0.125$ for the two normal formulations (curves are shifted for clarity). (b) Comparison of interface normals formulation; left: calculation with $\mathbf{n}_i = \nabla c_i/|\nabla c_i|$, right: calculation with Eq. (28).

Author's personal copy

Assuming the bulk phase to be very large and the diffusion process to be infinitely fast, the bulk surfactant concentration is homogeneous in space and constant in time. Hence, the bulk surfactant concentration directly underlying the interface is constant as well. From Eq. (8) using the parameters $k_1 = 1\ \mathrm{kg/m^3/s}$, $k_2 = 0.1 \times 1/\mathrm{s}$ and $\Gamma^\star = 0.005\ \mathrm{kg/m^3}$ an equilibrium interfacial surfactant concentration can be obtained as

$$\frac{\Gamma_{eq}}{\Gamma^\star} = \frac{k_1 C}{k_1 C + k_2} \approx 0.91, \tag{41}$$

where the adsorption and desorption rates balance each other, and the interfacial surfactant concentration remains constant. The first line in Fig. 5(a) shows the result of a simulation of a fixed air bubble in a surfactant rich water surrounding ($1 : D_\infty = \infty$). Here, time is non-dimensionalized with the reference time $t_\infty = 1/k_2$. As a reference, the broken horizontal line shows the analytic equilibrium state.

Now we include diffusion effects, i.e. the surfactant kinetics from Eq. (8) depend also on the local volume concentration of surfactant at the interface $C_{r=R}$. The diffusion coefficient in the bulk liquid phase is set to $D_\infty = 1 \times 10^{-6}\ \mathrm{m^2/s}$, which corresponds to a Peclet number of $Pe_\infty = 0.1$ (using the velocity scale $u_\infty = l_\infty k_2$). The second line in Fig. 5(a) shows the evolution

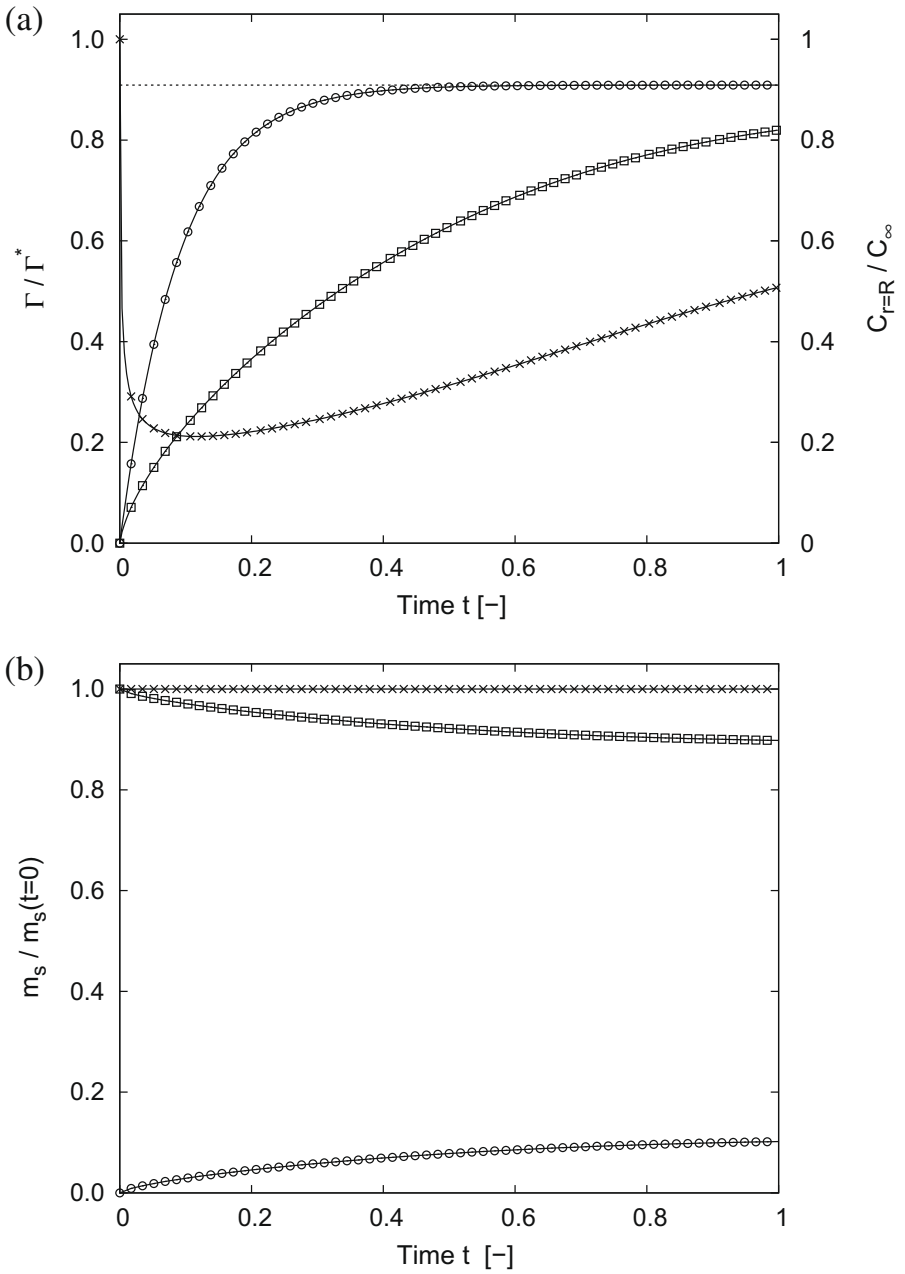

Fig. 5. (a) Surfactant transport to a steady interface, comparison between adsorption-limited $Pe_\infty = \infty$ and diffusion-limited $Pe_\infty = 0.1$ case. (b) Mass of surfactant on the interface and in the liquid phase over time.

Author's personal copy

of the interfacial surfactant concentration including the coupling with the liquid phase ($2 : Pe_\infty = 0.1$). The corresponding evolution of the bulk concentration in the subsurface region directly underneath the interface is also plotted in this figure ($3 : C_{r=R}, Pe_\infty = 0.1$). Since the adsorbed surfactant material is taken from the liquid phase, the bulk concentration $C_{r=R}$ decreases, and at the same time the interfacial concentration Γ does not increase as fast as in the infinite diffusion case. From $t \approx 0.2$ the bulk concentration increases again, caused by diffusion of surfactant in the liquid phase and a reduced surfactant flux between the interface and the bulk phase. The evolution of surfactant mass on the interface and in the liquid phase over time is shown in Fig. 5(b). As can be expected, with an increasing surfactant mass on the interface the surfactant mass in the liquid phase decreases. The total amount of surfactant in the system is conserved.

5. Results and discussion

With the results presented above we have shown the validity and accuracy of our model. In the following, we perform more complex two-dimensional simulations with coupled effects.

5.1. Oscillating bubble

Following Otis et al. [20], we simulate the dynamic surface tension of an air–water-like interface with surfactant. As in this problem the densities of the two phases do not determine the evolution, we assume the "air" and "water" phase to have a density ratio of 10 only to facilitate computation. The viscosities of the two phases are chosen such that the ratio of the kinematic viscosities is comparable to the realistic case. Due to this smaller density difference, we avoid too small timesteps and decrease the computational time, see Hu and Adams [1].

As in the experiment, an air bubble is exposed to a liquid environment containing surfactant molecules. Enforcing an oscillating of the bubble, the dynamics of the surfactant transportation can be investigated. In our SPH method we perform the bubble oscillation by changing the mass of the air particles. This resembles the blowing and suction of air in the experiment. Consequently, the density of the particles changes and the pressure force drives the bubble to change its size. Starting from a droplet with initial radius of $r_{\max} = 0.02$ m at an equilibrium surfactant concentration $\Gamma^\star = 3 \times 10^{-6}$ kg/m^2, the size of the air–water interface is oscillated sinusoidally with the period T and the evolution of the surfactant concentration on the interface is calculated. In the first set of simulations we assume adsorption-limited surfactant dynamics. Thus the bulk surfactant concentration is constant since the diffusion in the liquid phase is considered to be infinitely fast. The surfactant dynamics from Eq. (8) are extended to the insoluble and the squeeze-out regime, see Otis et al. [20]. In the second regime ($\Gamma^\star \leqslant \Gamma < \Gamma_{\max}$) the interface is insoluble, i.e. the concentration changes only by interface deformation,

$$\frac{dm_s}{dt} = \frac{d(\Gamma A)}{dt} = 0. \tag{42}$$

Reaching the maximum surfactant concentration $\Gamma_{\max}$, the surfactant molecules are packed as tightly as possible in the interface and further compression results in an squeeze-out of molecules back to the bulk phase.

Fig. 6(a) shows the surface-tension loops for various adsorption depths $\tilde{k} = k_1 C/k_2$ at a Biot number of $Bi = k_2 T = 1$ for the adsorption-limited case. At a very low adsorption depth the minimum possible surface tension is never reached during an oscillation cycle. This is due to the fact, that in the bulk phase there are not enough surfactant molecules available to accumulate at the interface. Increasing the adsorption depth, this limit is overcome and the nearly-zero surface tension occurs in the loop. Furthermore, the hysteresis increases with increasing adsorption depth.

Morris et al. [29] showed that under some conditions "pseudo-film collapse" occurs in the dynamic surface-tension loops. Similarly to the true film collapse at the lowest possible surface tension, in this case the surface tension remains relatively constant near the equilibrium $\alpha^\star$ even though the interface is further compressed. As they showed in their experiments, this is not a numerical artifact but a physically realistic behavior. Following the experimental investigations, we have checked if our model recovers this phenomenon correctly. A variation of the Biot number at a fixed adsorption depth is given in Fig. 6(b). As seen in the experiments, with increasing Biot number the maximum occurring surface tension within the loop decreases. At very high desorption rates the "pseudo-film collapse" is observed.

Comparisons with experiments have shown, that under certain conditions the adsorption-limited model tends to predict a wrong transient behavior, i.e. the assumption of a constant bulk surfactant concentration does not hold in all situations. As a remedy, Morris et al. [29] consider the diffusion-limited surfactant dynamics. With this model they are able to reproduce the experimental observations of Schürch et al. [30] and get even better agreement with the steady-state oscillations than with the adsorption-limited model. Using Eqs. (7) and (10), we can simulate with our SPH method the fully coupled interfacial surfactant dynamics with the bulk diffusion. As an example, Fig. 7 shows the concentration evolution in the bulk subsurface region directly underneath the interface and the surface-tension loop for the dynamic cycling with the parameters $Bi = 10,\ \tilde{k} = 10,\ Da = 1$ and $Pe = 1$. Due to the transient bulk concentration available at the interface, the maximum surface tension in the loop increases as well as the minimum surface tension decreases. Furthermore an increase of the hysteresis is observed. Our simulations confirm the findings of Morris et al., who were the first to simulate the influence of the diffusion process in the bulk phase on the dynamic cycling based on a one-dimensional model.

Author's personal copy

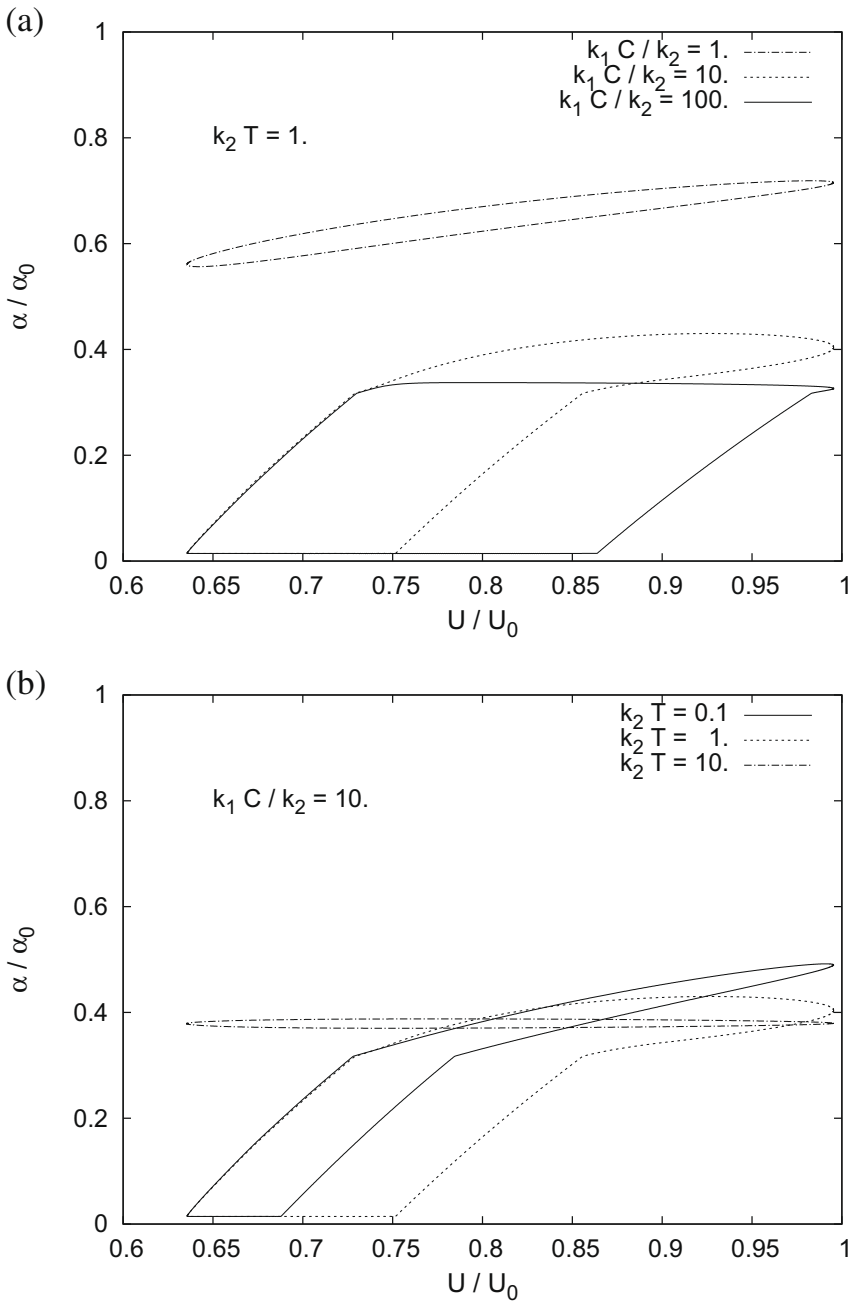

Fig. 6. Stationary surface-tension loops. (a) $k_2T = 1,\ k_1C/k_2 = 1,\ 10$ and 100 (b) $k_1C/k_2 = 10,\ k_2T = 0.1,\ 1$ and 10.

5.2. Drop in shear flow

We consider a circular drop in a shear flow with $\rho_a = \rho_w = 1000\ \mathrm{kg/m^3}$ and $\lambda = \eta_a/\eta_w = 0.01$. Initially we assume the interface to be clean of any surfactant and keep the surface tension coefficient constant during the whole calculation. The drop of size $R_0 = 1 \times 10^{-3}$ m is located in the middle of a periodic rectangular channel of size $l_x = l_y = 8R_0$ with a wall velocity of $\pm u_\infty$. In this case, the capillary number Ca and the Reynolds number Re are redefined by the shear rate $G = 2u_\infty/l_y$, i.e.

$$Ca = \frac{G\eta R_0}{\alpha}, \quad Re = \frac{\rho G R_0^2}{\eta}. \tag{43}$$

The reference length to non-dimensionalize spatial variables in this example is $l_\infty = R_0$. Caused by the flow shear, the drop deforms to an ellipsoid balancing the viscous stresses and surface tension. Here, we only consider subcritical Reynolds- and capillary numbers where the drop deforms to a steady ellipsoid, see Li et al. [31]. Above the critical state breakup occurs, where in the case of surfactants at the interface Marangoni effects can play an important role, see Timmermans and Lister [32] or Ambravaneswaran and Basaran [33].

Author's personal copy

Fig. 8(a) shows a snapshot of the simulation when $Ca = 0.1$ and $Re = 1.0$. The calculation was performed with a non-dimensional smoothing length $h = 8.\bar{3} \times 10^{-2}$, i.e. a total of 9216 particles. The deformation parameter is calculated with the least-square ellipse fitting method of Fitzgibbon et al. [34] using the interface particles to denote the shape of the droplet. A comparison of the current calculated deformations and the analytic predictions using the small-deformation theory suggested by Taylor [35] is plotted in Fig. 8(b). Even though we slightly overpredict the deformation, the agreement is good. Comparable results are presented in Hu and Adams [1], who simulated the same case but with a higher viscosity ratio of one.

Starting from the clean drop in a shear flow as a reference simulation, we consider now an initially circular droplet in the presence of an insoluble surfactant on the interface. That means that the bulk surfactant concentration in the two phases vanishes everywhere for the entire simulation time and the interfacial surfactant mass is distributed only over the particles within the transition band at the interface. The constitutive equation for the surface-tension coefficient α as function of the surfactant concentration Γ reduces in this example to

$$\alpha = \alpha_0\left(1 - \beta\frac{\Gamma}{\Gamma^\star}\right), \tag{44}$$

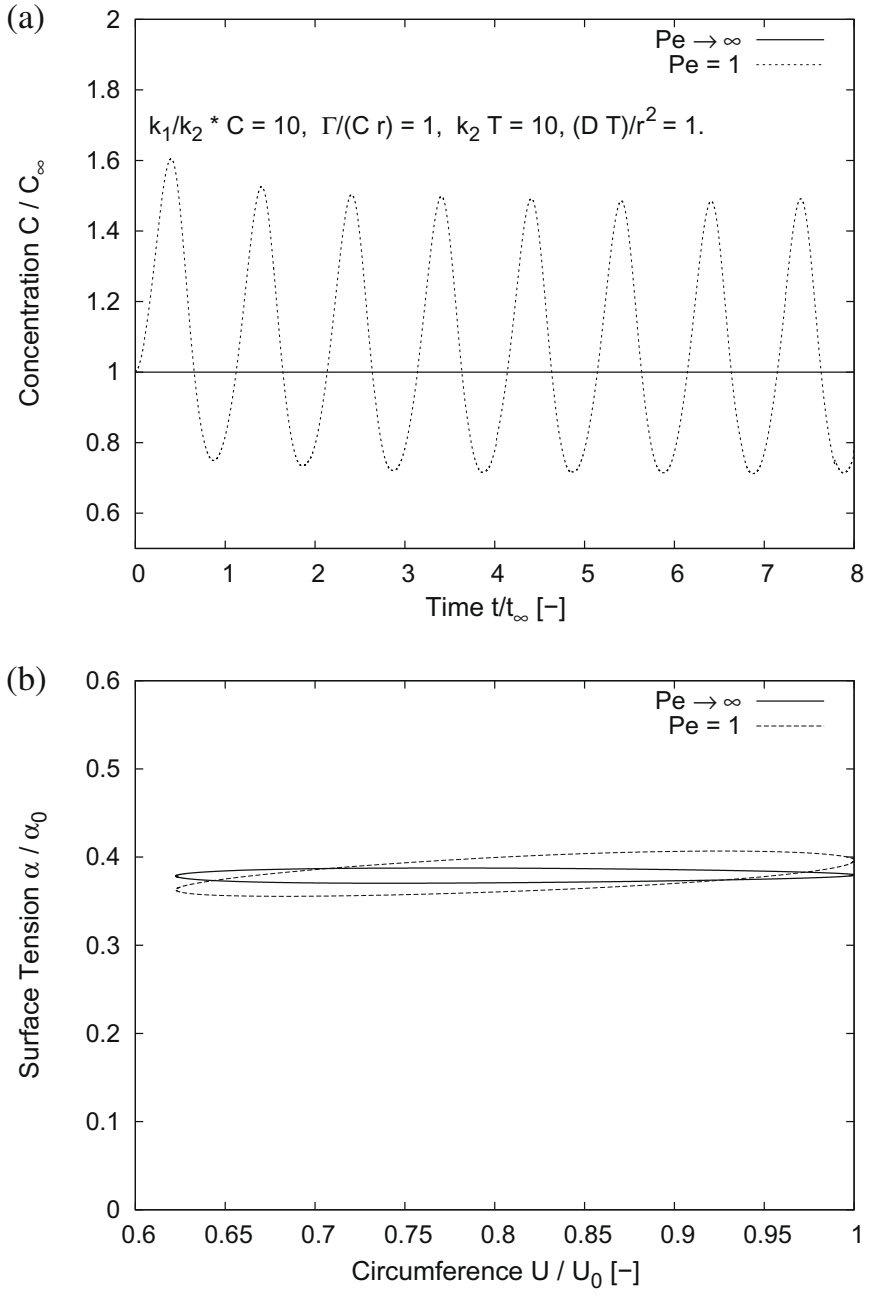

Fig. 7. Comparison between the adsorption-limited ($Pe \to \infty$) and the diffusion-limited model ($Pe = 1$). (a) Evolution of the surfactant concentration in the bulk subsurface region directly underneath the interface. (b) Corresponding surface-tension loops.

Author's personal copy

where β is a parameter. Fig. 9(a) and (b) shows the deformed interface and the velocity vector plot at steady-state for the case without surfactant ($\beta = 0$) and with insoluble surfactant ($\beta = 0.5,\ Pe = 1$) at $Re = 1,\ Ca = 0.1$ and $\lambda = 0.01$. The deformation parameters for the two cases are calculated to be $D = 0.107$ and $D = 0.130$.

Considering an insoluble surfactant present on the interface, we observe an increase of the bubble deformation of about 20%. The bubble inclination angle with respect to the x-axis at steady-state decreases slightly. The parameters in Eq. (44) are chosen such that initially the surfactant concentration and the surface tension for both the clean drop and the insoluble case are the same.

Note that in this example we used the very simple linear relation between α and Γ with the parameter β being the slope of this function ($\beta = d\alpha/d\Gamma$). Of course more complex constitutive equations and other parameter ranges of β can be used, but our focus is to investigate the influence of surface diffusion and variable surface tension. Varying β would not change the basic characteristics of the problem, an increasing β e.g. would only amplify the increase in deformation caused by an insoluble surfactant present at the interface.

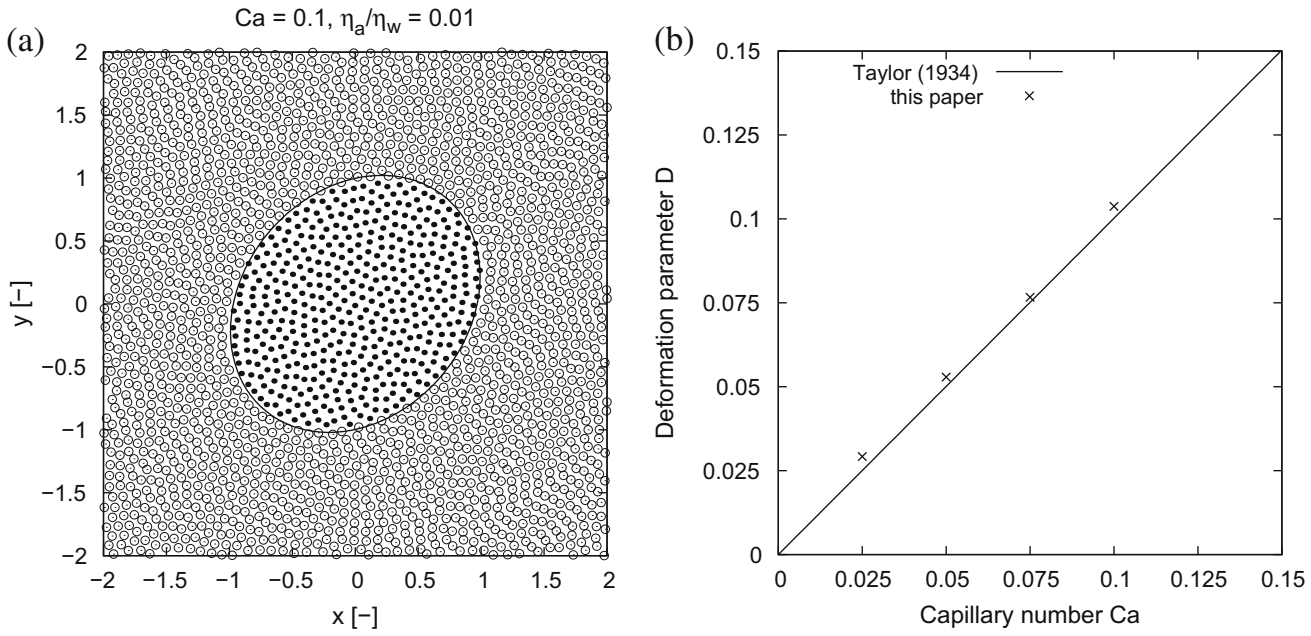

Fig. 8. (a) Positions of air particles (black dots) and shearing water particles (open circles) for $Ca = 0.1$, $Re = 1.0$ and $\lambda = 0.01$. (b) Drop deformation parameter D over capillary number Ca for $\lambda = 0.01$.

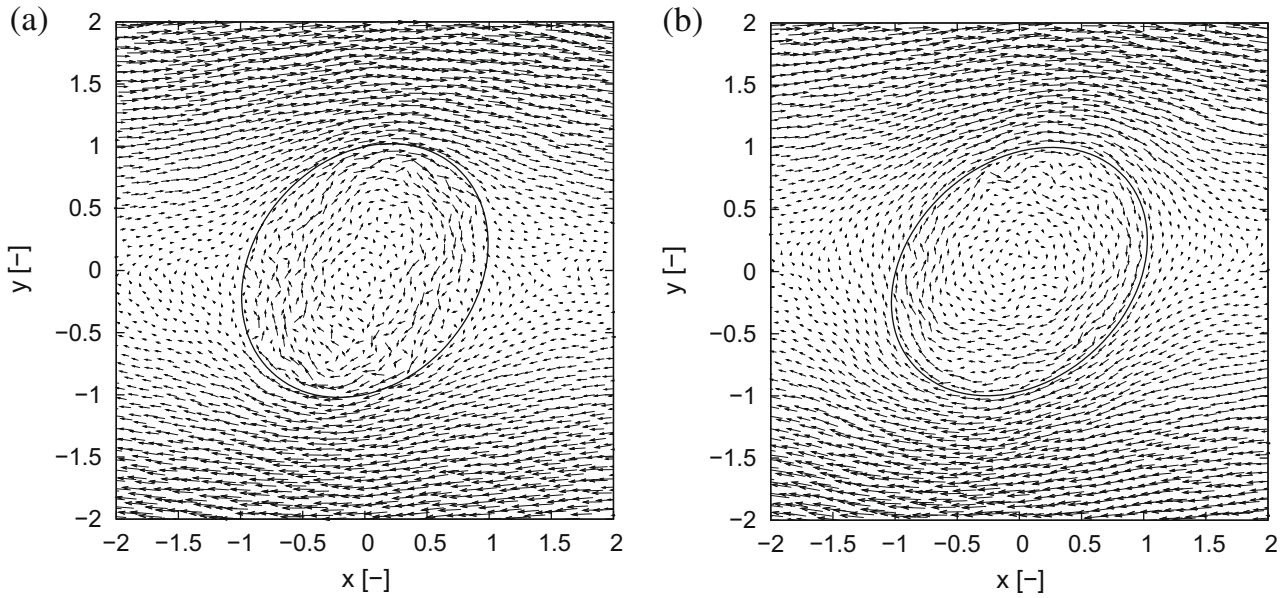

Fig. 9. Interface position and velocity vector plot of a drop in a shear flow at $Re = 1,\ \lambda = 0.01$ and $Ca = 0.1$. (a) Clean droplet ($\beta = 0.0$). (b) Insoluble surfactant on the interface ($\beta = 0.5,\ Pe = 1$).

Author's personal copy

To study in more detail the influence of surfactants present on the interface of a shearing drop, we consider the tangential velocity along the interface and the surfactant profile. Fig. 10 shows these distributions against the polar angle ϕ measured around the drop's transverse diameter for the three simulated cases of a clean interface ($\beta = 0$), a low diffusive ($\beta = 0.5,\ Pe = 1.0$) and a high diffusive ($\beta = 0.5,\ Pe = 0.1$) surfactant on the interface.

The distribution of the surfactant concentration at steady-state forms two local maxima at the tips of the deformed drop, see Fig. 10(b). With lower Peclet numbers ($Pe = 0.1$) surface diffusion of the surfactant becomes more dominant and produces a nearly constant profile. Hence, the drop deformation and tangential velocity converge to the clean interface results in the limit of an infinite surface diffusion.

Contrary to Lee and Pozrikidis [22], we do not observe any region where the tangential velocity of the clean interface is negative, see Fig. 10(a). The drop rotates continuously in clockwise direction with a maximum non-dimensional tangential velocity of approximately one (non-dimensionalized with $u_{ref} = GR$). To the knowledge of the authors, so far no experiment provides evidence for the correct flow pattern of this example. But from our simulations with Lagrangian particles we do not see neither particles moving with a negative tangential velocity nor four stagnation points on the interface, as reported in [22]. Including surfactant effects with $Pe = 1$, the oscillations of the tangential velocity around $GR/2$ decrease. Comparing the velocity vector plots in Fig. 9 shows how the diffusive surfactant on the interface affects the flow field within the droplet

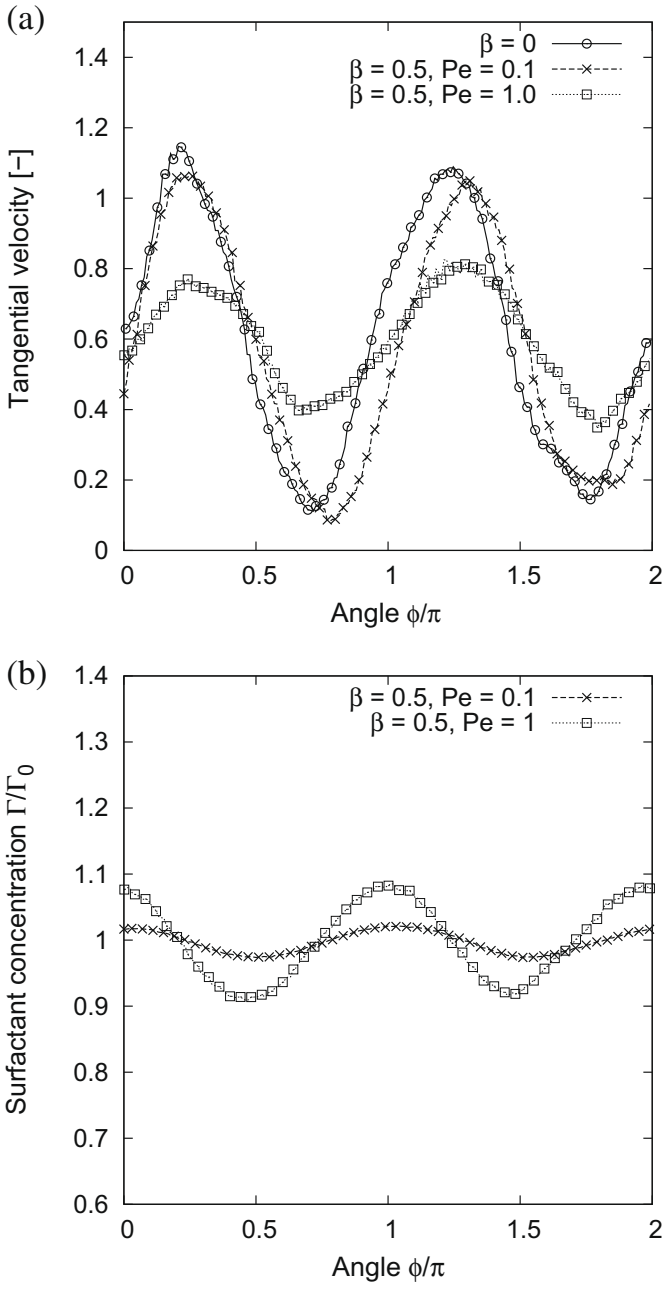

Fig. 10. Effect of surfactant on the steady deformation of a drop in a shear flow at $Re = 1, \lambda = 0.01$ and $Ca = 0.1$. (a) Distribution of tangential velocity for the cases $\beta = 0.$, $\beta = 0.5,\ Pe = 0.1$ and $\beta = 0.5,\ Pe = 1.0$. (b) Distribution of the interfacial surfactant concentration for $Pe = 0.1$ and $Pe = 1$.

Author's personal copy

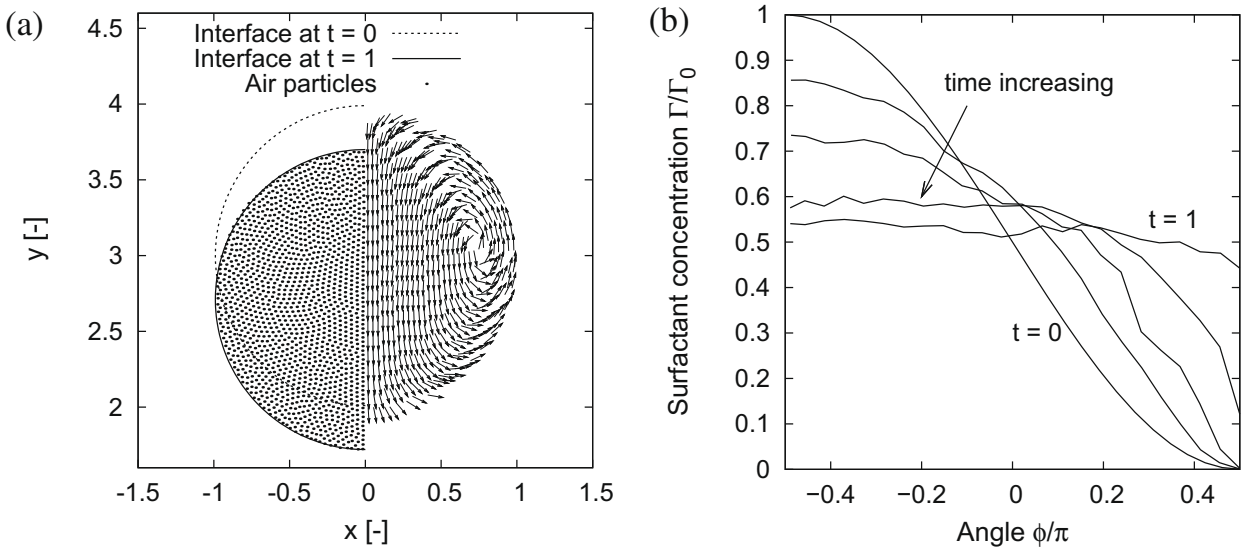

Fig. 11. Interface positions (left) and velocity field (right) for an initially non-uniform surfactant covered bubble moving due to the Marangoni effect.

and in the bulk phase. The drop with the contaminated interface rotates more like a rigid body with a continuous nearly uniform tangential velocity, which is in agreement with the results of the surfactant enriched drop in a shear flow presented in [22].

From a Lagrangian point of view it is easy to explain, that the interface of a surfactant enriched insoluble drop in a shear flow at steady-state necessarily has to rotate continuously in one direction. Assuming that there are regions on the interface where the tangential velocity is negative, particles would move towards these stagnation points. As an example for such a flow situation we refer to Lee and Pozrikidis [22] (Figs. 8 and 9), who showed the streamline pattern for a clean drop in a shear flow with four stagnation points. As a consequence, particles would leave the interface band at these regions. Without diffusion, the insoluble surfactant is transported along the interface only by advection. Whenever a particle leaves the interface region, the insoluble surfactant must stay on the interface. Hence, finally all surfactant would be concentrated at the point where the particles leave the interface region. Since this singularity is incompatible with a stable drop or ellipsoid, this flow pattern cannot exist when the interface contains insoluble surfactant.

5.3. Marangoni-force driven motion

When surfactants are present at an interface, surface-tension gradients can develop and influence the flow physics, see e.g. Pawar and Stebe [36]. Here, we do not study the Marangoni effect on the flow physics of a problem in detail. We solely intend to show that our proposed method incorporates this effect. Therefore, we simulate the Marangoni-force driven motion of a bubble. We consider a bubble with the initially non-uniform distributed surfactant concentration on the interface given by $\Gamma = \Gamma_0(1 + \tanh(4(\Theta/\pi - 0.5)))$. The density and viscosity ratio of the initially quiescent bubble and bulk phase are both $\rho_1/\rho_2 = \lambda = 1$. The diffusion coefficient D_s is set to zero, i.e. the Peclet number is infinite. A similar test case but in three dimensions and with a different density and viscosity ratio is presented in Zhang et al. [14].

According to Eq. (44) and the variation of surfactant along the interface, the interfacial surface-tension gradient $\nabla_s\alpha$ is non-zero and produces a motion of the bubble caused by the Marangoni effect. Interfacial particles at low surface tension are forced to advect towards regions of higher surface tension smoothing out the surfactant concentration distribution. On the left side of Fig. 11(a) the initial interface position and the final steady-state location of the bubble particles are shown. As the bottom part of the bubble contains initially more surfactant, the Marangoni-force induced motion along the interface produces a counterclockwise rotation in the bubble phase and thus moves down. The vector plot of the velocities of the particles within the bubble (see right plot in Fig. 11(a)) shows the counterclockwise rotation of the interface and the downward motion of the drop center. The corresponding surfactant profiles along the interface during the bubble motion are shown in Fig. 11(b). The surfactant is transported along the interface by advection resulting in lowering the maximum concentration and producing an uniform profile. Hence, the surface tension finally is constant over the interface and the bubble rests at a steady position.

6. Concluding remarks

We have developed a fully Lagrangian particle method for simulating incompressible interfacial flows with surfactant dynamics. The surfactant transport model accounts for exchange between the bulk phase and the interface (adsorption, desorption, squeeze-out) as well as diffusion on the interface and within the bulk phase. In our numerical scheme, the

Author's personal copy

different transportation phenomena can be considered simultaneously or separately, depending on the problem statement. In the present model the mass of surfactant is conserved exactly in the fluid phases and on interfaces. We have shown the validity of our method by several convergence studies and have performed several more complex simulations demonstrating the capabilities of this grid-free method. In this work we have only presented results of two-dimensional examples. The extension of the SPH-model for three-dimensional flows along the lines given in this paper is straightforward.

Acknowledgments

The authors wish to acknowledge the support of the German Research Foundation (DFG – Deutsche Forschungsgesellschaft) for funding this work within the Project AD 186/6-1.

References

[1] X. Hu, N. Adams, A multi-phase SPH method for macroscopic and mesoscopic flows, J. Comput. Phys. 213 (2) (2006) 844–861.
[2] L. Scriven, C. Sternling, The Marangoni effects, Nature 187 (4733) (1960) 186–188.
[3] R. Pattle, Properties, function, and origin of the alveolar lining layer, Nature 175 (4469) (1955) 1125–1126.
[4] J. Clements, Surface tension of lung extracts, Proc. Soc. Exp. Biol. Med. 95 (1) (1957) 170–172.
[5] K. Von Neergard, Neue Auffassung über einen Grundbegriff der Atemmechanik, Z. Ges. Exp. Med. 66 (1929) 373–393.
[6] H. Hamm, H. Fabel, W. Bartsch, The surfactant system of the adult lung: physiology and clinical perspectives, J. Mol. Med. 70 (8) (1992) 637–657.
[7] H. Stone, L. Leal, The effects of surfactants on drop deformation and breakup, J. Fluid Mech. 220 (1990) 161–186.
[8] W. Milliken, L. Leal, The influence of surfactant on the deformation and breakup of a viscous drop: the effect of surfactant solubility, J. Colloid Interf. Sci. 166 (2) (1994) 275–285.
[9] S. Yon, C. Pozrikidis, A finite-volume/boundary-element method for flow past interfaces in the presence of surfactants with application to shear flow past a viscous drop, Comput. Fluids 27 (8) (1998) 879–902.
[10] J.-J. Xu, H.-K. Zhao, An Eulerian formulation for solving partial differential equations along a moving interface, J. Sci. Comput. 19 (1) (2003) 573–594.
[11] A. James, J. Lowengrub, A surfactant-conserving volume-of-fluid method for interfacial flows with insoluble surfactant, J. Comput. Phys. 201 (2) (2004) 685–722.
[12] J.-J. Xu, Z. Li, J. Lowengrub, H. Zhao, A level-set method for interfacial flows with surfactant, J. Comput. Phys. 212 (2) (2006) 590–616.
[13] M. Lai, Y. Tseng, H. Huang, An immersed boundary method for interfacial flows with insoluble surfactant, J. Comput. Phys. 227 (15) (2008) 7279–7293.
[14] J. Zhang, D. Eckmann, P. Ayyaswamy, A front tracking method for a deformable intravascular bubble in a tube with soluble surfactant transport, J. Comput. Phys. 214 (1) (2006) 366–396.
[15] M. Muradoglu, G. Tryggvason, A front-tracking method for computation of interfacial flows with soluble surfactants, J. Comput. Phys. 227 (4) (2008) 2238–2262.
[16] Y. Liao, O. Basaran, E. Franses, Effects of dynamic surface tension and fluid flow on the oscillations of a supported bubble, Colloid. Surf. A: Physicochem. Eng. Asp. 282 (2006) 183–202.
[17] P. McGough, O. Basaran, Repeated formation of fluid threads in breakup of a surfactant-covered jet, Phys. Rev. Lett. 96 (5) (2006) 054502.
[18] J.P. Morris, P.J. Fox, Y. Zhu, Modeling low reynolds number incompressible flows using SPH, J. Comput. Phys. 136 (1) (1997) 214–226.
[19] R.P. Borwankar, D.T. Wasan, The kinetics of adsorption of surface active agents at gas–liquid surfaces, Chem. Eng. Sci. 38 (10) (1983) 1637–1649.
[20] D.R. Otis, E.P. Ingenito, R.D. Kamm, M. Johnson, Dynamic surface tension of surfactant TA: experiments and theory, J. Appl. Physiol. 77 (6) (1994) 2681–2688.
[21] C. Chang, E. Franses, Adsorption dynamics of surfactants at the air/water interface: a critical review of mathematical models, data, and mechanisms, Colloid. Surf. A 100 (1995) 1–45.
[22] J. Lee, C. Pozrikidis, Effect of surfactants on the deformation of drops and bubbles in Navier–Stokes flow, Comput. Fluids 35 (1) (2006) 43–60.
[23] G. Tryggvason, B. Bunner, A. Esmaeeli, D. Juric, N. Al-Rawahi, W. Tauber, J. Han, S. Nas, Y.J. Jan, A front-tracking method for the computations of multiphase flow, J. Comput. Phys. 169 (2) (2001) 708–759.
[24] M. Bertalmío, L.-T. Cheng, S. Osher, G. Sapiro, Variational problems and partial differential equations on implicit surfaces, J. Comput. Phys. 174 (2) (2001) 759–780.
[25] J.K. Chen, J.E. Beraun, T.C. Carney, A corrective smoothed particle method for boundary value problems in heat conduction, Int. J. Numer. Meth. Eng. 46 (2) (1999) 231–252.
[26] I. Sbalzarini, A. Hayer, A. Helenius, P. Koumoutsakos, Simulations of (an) isotropic diffusion on curved biological surfaces, Biophys. J. 90 (3) (2006) 878–885.
[27] J.J. Monaghan, Smoothed particle hydrodynamics, Rep. Prog. Phys. 68 (8) (2005) 1703–1759.
[28] Y. Zhu, P. Fox, Smoothed particle hydrodynamics model for diffusion through porous media, Transport Porous Med. 43 (3) (2001) 441–471.
[29] J. Morris, E. Ingenito, L. Mark, R. Kamm, M. Johnson, Dynamic behavior of lung surfactant, J. Biomech. Eng. 123 (2001) 106–113.
[30] S. Schurch, D. Schurch, T. Curstedt, B. Robertson, Surface activity of lipid extract surfactant in relation to film area compression and collapse, J. Appl. Physiol. 77 (2) (1994) 974.
[31] J. Li, Y.Y. Renardy, M. Renardy, Numerical simulation of breakup of a viscous drop in simple shear flow through a volume-of-fluid method, Phys. Fluids 12 (2) (2000) 269–282.
[32] M. Timmermans, J. Lister, The effect of surfactant on the stability of a liquid thread, J. Fluid Mech. 459 (2002) 289–306.
[33] B. Ambravaneswaran, O. Basaran, Effects of insoluble surfactants on the nonlinear deformation and breakup of stretching liquid bridges, Phys. Fluids 11 (1999) 997.
[34] A. Fitzgibbon, M. Pilu, R.B. Fisher, Direct least square fitting of ellipses, IEEE Trans. Pattern Anal. Mach. Intell. 21 (1999) 476–480.
[35] G. Taylor, The formation of emulsions in definable fields of flow, Proc. Roy. Soc. Lond. Ser. A (1934) 501–523.
[36] Y. Pawar, K. Stebe, Marangoni effects on drop deformation in an extensional flow: the role of surfactant physical chemistry. I. Insoluble surfactants, Phys. Fluids 8 (1996) 1738.

B. BIBLIOGRAPHY

[1] D. Adalsteinsson and J.A. Sethian. Transport and diffusion of material quantities on propagating interfaces via level set methods. *J. Comput. Phys.*, 185(1):271–288, 2003.

[2] S. Adami, X.Y. Hu, and N.A. Adams. Simulating dynamic surface tension of lung surfactant using SPH. In *Symp. Prot. Artif. Respir.*, Aachen, Germany, 2008.

[3] S. Adami, X.Y. Hu, and N.A. Adams. Simulations of multiphase phenomena using Smoothed Particle Hydrodynamics (SPH). In *Work. Turbul. Hydrodyn. Instab. Excell. Clust. Universe*, Garching, Germany, 2008.

[4] S. Adami, X.Y. Hu, and N.A. Adams. A conservative SPH method for interfacial flows with surfactant dynamics. In *Proc. 4th ERCOFTAC SPHERIC Work.*, Nantes, France, 2009.

[5] S. Adami, X.Y. Hu, and N.A. Adams. Surfactant dynamics with SPH. In *Proc. 1st Int. Conf. Math. Comput. Biomed. Engrg*, Swansea, UK, 2009.

[6] S. Adami, X.Y. Hu, and N.A. Adams. 3D drop deformation and breakup in simple shear flow considering the effect of insoluble surfactant. In *Proc. 8th Euromech. Fluid Mech. Conf.*, Bad Reichenhall, Germany, 2010.

[7] S. Adami, X.Y. Hu, and N.A. Adams. 3D drop deformation and breakup in simple shear flow considering the effect of insoluble surfactant. In *Proc. 5th ERCOFTAC SPHERIC Work.*, Manchester, UK, 2010.

[8] S. Adami, X.Y. Hu, and N.A. Adams. A conservative SPH method for surfactant dynamics. *J. Comput. Phys.*, 229(5):1909–1926, 2010.

[9] S. Adami, X.Y. Hu, and N.A. Adams. A new surface-tension formulation for multi-phase SPH using a reproducing divergence approximation. *J. Comput. Phys.*, 229(13):5011–5021, 2010.

[10] S. Adami, X.Y. Hu, and N.A. Adams. A soft-tissue model coupled with fluid dynamics using SPH. In *Proc. 5th ERCOFTAC SPHERIC Work.*, Manchester, UK, 2010.

[11] S. Adami, X.Y. Hu, and N.A. Adams. Tipstreaming of a drop in simple shear flow in the presence of surfactant. In *Gall. Fluid Motion, 63rd Annu. Meet. Am. Phys. Soc. Fluid Dyn.*, Long Beach, California, USA, 2010.

[12] S. Adami, X.Y. Hu, and N.A. Adams. A fully coupled 3D transport model in SPH for multi-species reaction-diffusion systems. In *Proc. 6th ERCOFTAC SPHERIC Work.*, Hamburg, Germany, 2011.

[13] S. Adami, X.Y. Hu, and N.A. Adams. A Generalized Wall Boundary Condition for Smoothed Particle Hydrodynamics. *J. Comput. Phys.*, 231:7057–7075, 2012.

[14] S. Adami, X.Y. Hu, and N.A. Adams. Contact line hydrodynamics with SPH. In *Proc. 7th ERCOFTAC SPHERIC Work.*, Prato, Italy, 2012.

[15] S. Adami, X.Y. Hu, and N.A. Adams. Numerical investigation of complex multi-phase flows with Lagrangian particle methods. In S. Wager, A. Bode, H. Satzger, and M. Brehm, editors, *High Perform. Comput. Sci. Eng.* Verlag der Bayerischen Akademie der Wissenschaften, 2012.

[16] S. Adami, X.Y. Hu, and N.A. Adams. Simulating 3D turbulence with SPH. In *Proc. 2012 Summer Program, Cent. Turbul. Res.* Stanford, California, USA, 2012.

[17] S. Adami, X.Y. Hu, and N.A. Adams. A transport-velocity formulation for Smoothed Particle Hydrodynamics. *J. Comput. Phys.*, 241:292–307, 2013.

[18] S. Adami, X.Y. Hu, and N.A. Adams. A transport-velocity formulation for Smoothed Particle Hydrodynamics. In *Proc. 8th ERCOFTAC SPHERIC Work.*, Trondheim, Norway, 2013.

[19] S. Adami, X.Y. Hu, and N.A. Adams. Simulating 3D turbulence with SPH. In *Proc. 8th ERCOFTAC SPHERIC Work.*, Trondheim, Norway, 2013.

[20] S. Adami and H.J. Kaltenbach. Sensitivity of the wave-steepening in railway tunnels with respect to the friction model. In *BBAA VI Int. Colloq. Bluff Bodies Aerodyn. Appl.*, Milano, Italy, 2008.

[21] S. Adami, I. Mahle, X.Y. Hu, N.A. Adams, and M. Wendel. Simulating dynamic surface tension of lung surfactant using SPH. In *Proc. 3rd ERCOFTAC SPHERIC Work.*, Lausanne, Switzerland, 2008.

[22] A. Alke and D. Bothe. 3D Numerical Modeling of Soluble Surfactant at Fluidic Interfaces Based on the Volume-of-Fluid Method. *Fluid Dyn. Mater. Process.*, 5(4):345–372, 2009.

[23] M.P. Allen and D.J. Tildesley. *Computer simulation of liquids*. Oxford University Press, New York, 1989.

[24] C. Antoci, M. Gallati, and S. Sibilla. Numerical simulation of fluid–structure interaction by SPH. *Comput. Struct.*, 85(11-14):879–890, 2007.

[25] T. Belytschko and Y. Krongauz. On the completeness of meshfree particle methods. *Int. J. Numer. Methods Eng.*, 43(5):785–819, 1998.

[26] W. Benz and E. Asphaug. Simulations of brittle solids using smooth particle hydrodynamics. *Comput. Phys. Commun.*, 87(1-2):253–265, 1995.

[27] M. Bergdorf, I.F. Sbalzarini, and P. Koumoutsakos. A Lagrangian particle method for reaction-diffusion systems on deforming surfaces. *J. Math. Biol.*, 61(5):649–63, 2010.

[28] R.P. Borwankar and D.T. Wasan. The kinetics of adsorption of surface active agents at gas-liquid surfaces. *Chem. Eng. Sci.*, 38(10):1637–1649, 1983.

[29] J.U. Brackbill, D.B. Kothe, and C. Zemach. A continuum method for modeling surface tension. *J. Comput. Phys.*, 100(2):335–354, 1992.

[30] J.K. Chen, J.E. Beraun, and T.C. Carney. A corrective smoothed particle method for boundary value problems in heat conduction. *Internat. J. Numer. Methods Engrg.*, 46(2):231–252, 1999.

[31] P.W. Cleary. Modelling confined multi-material heat and mass flows using SPH. *Appl. Math. Model.*, 22(12):981–993, 1998.

[32] A. Colagrossi. Numerical simulation of interfacial flows by smoothed particle hydrodynamics. *J. Comput. Phys.*, 191(2):448–475, November 2003.

[33] S.J. Cummins and M. Rudman. An SPH Projection Method. *J. Comput. Phys.*, 152(2):584–607, 1999.

[34] R.A. Dalrymple and B.D. Rogers. Numerical modeling of water waves with the SPH method. *Coast. Eng.*, 53(2-3):141–147, 2006.

[35] A.K. Das and P.K. Das. Equilibrium shape and contact angle of sessile drops of different volumes—Computation by SPH and its further improvement by DI. *Chem. Eng. Sci.*, 65(13):4027–4037, 2010.

[36] A.K. Das and P.K. Das. Incorporation of diffuse interface in smoothed particle hydrodynamics : Implementation of the scheme and case studies. *Int. J. Numer. Methods Fluids*, 2010.

[37] T Das, S Das, and S Chakraborty. Influences of streaming potential on cross stream migration of flexible polymer molecules in nanochannel flows. *J. Chem. Phys.*, 130(24):244904, 2009.

[38] M. De Leffe, D. Le Touze, and B. Alessandrini. Normal flux method at the boundary for SPH. In *Proc. 4th SPHERIC Work.*, pages 150–157, 2009.

[39] W. Dehnen and H. Aly. Improving convergence in smoothed particle hydrodynamics simulations without pairing instability. *Mon. Not. R. Astron. Soc.*, 15(June):1–15, 2012.

[40] J.M. Domínguez, A.J.C. Crespo, D. Valdez-Balderas, B.D. Rogers, and M. Gómez-Gesteira. New multi-GPU implementation for Smoothed Particle Hydrodynamics on heterogeneous clusters. *Comput. Phys. Commun.*, 184:1848–1860, 2013.

[41] D.A. Edwards, H. Brenner, and D.T. Wasan. *Interfacial transport processes and rheology*. 1991.

[42] M. Ellero, M. Kröger, and S. Hess. Viscoelastic flows studied by smoothed particle dynamics. *J. Non-Newtonian Fluid Mech.*, 105:35–51, 2002.

[43] A. Fakhari and M. H. Rahimian. Investigation of deformation and breakup of a moving droplet by the method of lattice Boltzmann equations. *Int. J. Numer. Methods Fluids*, 64(8):827–849, 2010.

[44] K. Feigl, D. Megias-Alguacil, P. Fischer, and E.J. Windhab. Simulation and experiments of droplet deformation and orientation in simple shear flow with surfactants. *Chem. Eng. Sci.*, 62(12):3242–3258, 2007.

[45] M. Ferrand, D. Laurence, B.D. Rogers, and D. Violeau. Improved time scheme integration approach for dealing with semi analytic bounday conditions in SPARTACUS2D. In *Proc. 5th SPHERIC Work.*, pages 98–105, 2010.

[46] M. Ferrand, D.R. Laurence, B.D. Rogers, D. Violeau, and C. Kassiotis. Unified semi-analytical wall boundary conditions for inviscid, laminar or turbulent flows in the meshless SPH method. *Int. J. Numer. Methods Fluids*, 71:446–472, 2013.

[47] G. Fourey and G. Oger. SPH/FEM coupling to simulate fluid-structure interactions with complex free-surface flows. In *Proc. 5th ERCOFTAC SPHERIC Work.*, Manchester, UK, 2010.

[48] U. Ghia, K.N. Ghia, and C.T. Shin. High-Re solutions for incompressible flow using the Navier-Stokes equations and a multigrid method. *J. Comput. Phys.*, 48(3):387–411, 1982.

[49] R.A. Gingold and J.J. Monaghan. Smoothed particle hydrodynamics -Theory and application to non-spherical stars. *Mon. Not. R. Astron. Soc.*, 181:375, 1977.

[50] J.P. Gray, J.J. Monaghan, and R.P. Swift. SPH elastic dynamics. *Comput. Methods Appl. Mech. Eng.*, 190(49-50):6641–6662, 2001.

[51] N. Grenier, M. Antuono, A. Colagrossi, D Le Touze, B. Alessandrini, and D. Le Touzé. An Hamiltonian interface SPH formulation for multi-fluid and free surface flows. *J. Comput. Phys.*, 228(22):8380–8393, 2009.

[52] S. Hawgood and J.A. Clements. Pulmonary surfactant and its apoproteins. *J. Clin. Invest.*, 86(1):1–6, 1990.

[53] A. Hérault, G. Bilotta, and R.A. Dalrymple. SPH on GPU with CUDA. *J. Hydraul. Res.*, 48:74–79, 2009.

[54] S.E. Hieber and P. Koumoutsakos. A Lagrangian particle method for the simulation of linear and nonlinear elastic models of soft tissue. *J. Comput. Phys.*, 227(21):9195–9215, 2008.

[55] S.E. Hieber and P. Koumoutsakos. An immersed boundary method for smoothed particle hydrodynamics of self-propelled swimmers. *J. Comput. Phys.*, 227(19):8636–8654, 2008.

[56] C.W. Hirt and B.D. Nichols. Volume of fluid (VOF) method for the dynamics of free boundaries. *J. Comput. Phys.*, 39(1):201–225, 1981.

[57] X.Y. Hu, S. Adami, and N.A. Adams. Formulating surface tension with reproducing divergence approximation for multi-phase SPH. In *Proc. 4th ERCOFTAC SPHERIC Work.*, Nantes, France, 2009.

[58] X.Y. Hu, S. Adami, I. Mahle, and N.A. Adams. Numerical modeling of the dynamic behavior of lung surfactant using smoothed particle dynamics. In *World Congr. Comput. Mech.*, Venice, Italy, 2007.

[59] X.Y. Hu and N.A. Adams. A multi-phase SPH method for macroscopic and mesoscopic flows. *J. Comput. Phys.*, 213(2):844–861, 2006.

[60] X.Y. Hu and N.A. Adams. Angular-momentum conservative smoothed particle dynamics for incompressible viscous flows. *Phys. Fluids*, 18(10):101702, 2006.

[61] X.Y. Hu and N.A. Adams. An incompressible multi-phase SPH method. *J. Comput. Phys.*, 227(1):264–278, 2007.

[62] X.Y. Hu and N.A. Adams. A constant-density approach for incompressible multiphase SPH. *J. Comput. Phys.*, 228(6):2082–2091, 2009.

[63] R. Issa, E.S. Lee, D. Violeau, and D.R. Laurence. Incompressible separated flows simulations with the smoothed particle hydrodynamics gridless method. *Internat. J. Numer. Methods Fluids*, 47(10-11):1101–1106, 2005.

[64] A.J. James and J. Lowengrub. A surfactant-conserving volume-of-fluid method for interfacial flows with insoluble surfactant. *J. Comput. Phys.*, 201(2):685–722, 2004.

[65] J. Kordilla, A. Tartakovsky, and T. Geyer. A Smoothed Particle Hydrodynamics model for droplet and film flow on smooth and rough fracture surfaces. *Adv. Water Resour.*, 59:1–14, 2013.

[66] P. Koumoutsakos. Multiscale Flow Simulations Using Particles. *Annu. Rev. Fluid Mech.*, 37(1):457–487, 2005.

[67] B. Lafaurie. Modelling merging and fragmentation in multiphase flows with SURFER. *J. Comput. Phys.*, 113:134–147, 1994.

[68] M.C. Lai, Y.H. Tseng, and H. Huang. An immersed boundary method for interfacial flows with insoluble surfactant. *J. Comput. Phys.*, 227(15):7279–7293, 2008.

[69] J. Leduc, F. Leboeuf, and M. Lance. Improvement of multiphase model using preconditioned Riemann solvers. In *Proc. 5th ERCOFTAC SPHERIC Work.*, number 4, Manchester, UK, 2010.

[70] E. Lee, C. Moulinec, R. Xu, D. Violeau, D. Laurence, and P Stansby. Comparisons of weakly compressible and truly incompressible algorithms for the SPH mesh free particle method. *J. Comput. Phys.*, 227(18):8417–8436, 2008.

[71] Y.C. Liao, E.I. Franses, and O.A. Basaran. Deformation and breakup of a stretching liquid bridge covered with an insoluble surfactant monolayer. *Phys. Fluids*, 18:22101, 2006.

[72] L.D. Libersky and A.G. Petschek. Smooth particle hydrodynamics with strength of materials. In Harold Trease, Martin Fritts, and W Crowley, editors, *Adv. Free. Method Incl. Contrib. Adapt. Gridding Smooth Part. Hydrodyn. Method*, volume 395 of *Lecture Notes in Physics*, pages 248–257. Springer Berlin Heidelberg, Berlin, Heidelberg, 1991.

[73] L.D. Libersky, A.G. Petschek, T.C. Carney, J.R. Hipp, and F.A. Allahdadi. High Strain Lagrangian Hydrodynamics. *J. Comput. Phys.*, 109(1):67–75, 1993.

[74] S. Litvinov, M. Ellero, X.Y. Hu, and N.A. Adams. Smoothed dissipative particle dynamics model for polymer molecules in suspension. *Phys. Rev. E*, 77(6):066703, 2008.

[75] Livermore Software Technology Corporation (LSTC). LS-DYNA. *http://www.lstc.com/products/ls-dyna*, 2011.

[76] L.B. Lucy. A numerical approach to the testing of the fission hypothesis. *Astron.J.*, 82(12):1013–1024, 1977.

[77] S. Marrone, M. Antuono, A. Colagrossi, G. Colicchio, D. Le Touzé, and G. Graziani. δ-SPH model for simulating violent impact flows. *Comput. Methods Appl. Mech. Eng.*, 200(13-16):1526–1542, 2011.

[78] S. Marrone, A. Colagrossi, M. Antuono, G. Colicchio, and G. Graziani. An accurate SPH modeling of viscous flows around bodies at low and moderate Reynolds numbers. *J. Comput. Phys.*, 245:456–475, 2013.

[79] P.T. McGough and O.A. Basaran. Repeated formation of fluid threads in breakup of a surfactant-covered jet. *Phys. Rev. Lett.*, 96(5):54502, 2006.

[80] S. Meissner, L. Knels, T. Koch, E. Koch, S. Adami, X.Y. Hu, and N.A. Adams. Experimental and numerical investigation on the flow-induced stresses on the alveolar-epithelial-surfactant-air interface. In M. Klaas, E. Koch, and W. Schröder, editors, *Notes Numer. fluid Mech. Multidiscip. Des.* Springer, 2011.

[81] W.J. Milliken and L.G. Leal. The influence of surfactant on the deformation and breakup of a viscous drop: the effect of surfactant solubility. *J. Colloid Interface Sci.*, 166(2):275–285, 1994.

[82] J.J. Monaghan. On the problem of penetration in particle methods. *J. Comput. Phys.*, 82(1):1–15, 1989.

[83] J.J. Monaghan. Simulating Free Surface Flows with SPH. *J. Comput. Phys.*, 110(2):399–406, 1994.

[84] J.J. Monaghan. Smoothed particle hydrodynamics. *Reports Prog. Phys.*, 68(8):1703–1759, 2005.

[85] J.J. Monaghan. A turbulence model for Smoothed Particle Hydrodynamics. *Eur. J. Mech. - B/Fluids*, 30(4):360–370, 2011.

[86] J.J. Monaghan, H.E. Huppert, and M.G. Worster. Solidification using smoothed particle hydrodynamics. *J. Comput. Phys.*, 206(2):684–705, 2005.

[87] J.J. Monaghan and J.B. Kajtar. SPH particle boundary forces for arbitrary boundaries. *Comput. Phys. Commun.*, 180(10):1811–1820, 2009.

[88] J.J. Monaghan and A. Rafiee. A simple SPH algorithm for multi-fluid flow with high density ratios. *Int. J. Numer. Meth. Fluids*, 2012.

[89] J.P. Morris. Simulating surface tension with smoothed particle hydrodynamics. *Int. J. Numer. Methods Fluids*, 33(3):333–353, 2000.

[90] J.P. Morris, P.J. Fox, and Y. Zhu. Modeling Low Reynolds Number Incompressible Flows Using SPH. *J. Comput. Phys.*, 136(1):214–226, 1997.

[91] M. Muradoglu and G. Tryggvason. A front-tracking method for computation of interfacial flows with soluble surfactants. *J. Comput. Phys.*, 227(4):2238–2262, 2008.

[92] S. Nugent and H.A. Posch. Liquid drops and surface tension with smoothed particle applied mechanics. *Phys. Rev. E*, 62(4):4968–75, 2000.

[93] S. Osher and R. Fedkiw. *Level set methods and dynamic implicit surfaces*. Springer, New York, 2003.

[94] S. Osher and J. A. Sethian. Fronts propagating with curvature-dependent speed: Algorithms based on Hamilton-Jacobi formulations. *J. Comput. Phys.*, 79(1):12–49, 1988.

[95] W. Pan, A.M. Tartakovsky, and J.J. Monaghan. Smoothed particle hydrodynamics non-Newtonian model for ice-sheet and ice-shelf dynamics. *J. Comput. Phys.*, 242:828–842, 2013.

[96] C. Pozrikidis. *Boundary Integral and Singularity Methods for Linearized Viscous Flow*. Cambridge University Press, Cambridge, 1992.

[97] C. Pozrikidis. Interfacial Dynamics for Stokes Flow. *J. Comput. Phys.*, 169(2):250–301, 2001.

[98] D.J. Price. Smoothed Particle Magnetohydrodynamics - IV. Using the vector potential. *Mon. Not. R. Astron. Soc.*, 401(3):1475–1499, January 2010.

[99] D.J. Price. Smoothed particle hydrodynamics and magnetohydrodynamics. *J. Comput. Phys.*, 231(3):759–794, 2012.

[100] A. Prosperetti and G. Tryggvason, editors. *Computational methods for multiphase flow*. Cambridge University Press, Cambridge, 2007.

[101] T. Rabczuk, S. P. Xiao, and M. Sauer. Coupling of mesh-free methods with finite elements: basic concepts and test results. *Commun. Numer. Methods Eng.*, 22(10):1031–1065, 2006.

[102] Y.Y. Renardy, M. Renardy, and V. Cristini. A new volume-of-fluid formulation for surfactants and simulations of drop deformation under shear at a low viscosity ratio. *Eur. J. Mech. - B/Fluids*, 21:49–59, 2002.

[103] M. Robinson and J.J. Monaghan. Forced Two-Dimensional Wall-Bounded Turbulence Using SPH. In *3rd ERCOFTAC SPHERIC Work.*, Lausanne, Switzerland, 2008.

[104] M. X. Rodriguez-Paz and J. Bonet. A corrected smooth particle hydrodynamics method for the simulation of debris flows. *Numer. Methods Partial Differ. Equ.*, 20(1):140–163, 2004.

[105] E.M. Ryan, A.M. Tartakovsky, and C. Amon. A novel method for modeling Neumann and Robin boundary conditions in smoothed particle hydrodynamics. *Comput. Phys. Comm.*, 181(12):2008–2023, 2010.

[106] E.M. Ryan, A.M. Tartakovsky, K.P. Recknagle, M.A. Khaleel, and C. Amon. Pore-scale modeling of the reactive transport of chromium in the cathode of a solid oxide fuel cell. *J. Power Sources*, 196(1):287–300, 2011.

[107] I.F. Sbalzarini, J.H. Walther, M. Bergdorf, S.E. Hieber, E.M. Kotsalis, and P. Koumoutsakos. PPM - A highly efficient parallel particle-mesh library for the simulation of continuum systems. *J. Comput. Phys.*, 215(2):566–588, 2006.

[108] I.J. Schoenberg. Contributions to the problem of approximation of equidistant data by analytic functions, Part A. *Quart. Appl. Math.*, 4:45–9, 1946.

[109] L.E. Scriven and C.V. Sternling. The marangoni effects. *Nature*, 187(4733):186–188, 1960.

[110] Y. Shi, M. Ellero, and N.A. Adams. Analysis of intermittency in under-resolved smoothed-particle-hydrodynamics direct numerical simulations of forced compressible turbulence. *Phys. Rev. E*, 85(3), 2012.

[111] K. Shintate and H. Sekine. Numerical simulation of hypervelocity impacts of a projectile on laminated composite plate targets by means of improved SPH method. *Compos. Part A Appl. Sci. Manuf.*, 35(6):683–692, 2004.

[112] V. Springel and L. Hernquist. Cosmological smoothed particle hydrodynamics simulations: a hybrid multiphase model for star formation. *Mon. Not. R. Astron. Soc.*, 339(2):289–311, 2003.

[113] H.A. Stone. A simple derivation of the time-dependent convective-diffusion equation for surfactant transport along a deforming interface. *Phys. Fluids A*, 2(1):111–112, 1990.

[114] J.W. Swegle, D.L. Hicks, and S.W. Attaway. Smoothed particle hydrodynamics stability analysis. *J. Comput. Phys.*, 116:123–134, 1995.

[115] A.M. Tartakovsky and P. Meakin. Modeling of surface tension and contact angles with smoothed particle hydrodynamics. *Phys. Rev. E*, 72(2):1–9, 2005.

[116] A.M. Tartakovsky, P. Meakin, T.D. Scheibe, R. Eichlerwest, and R.M.E. West. Simulations of reactive transport and precipitation with smoothed particle hydrodynamics. *J. Comput. Phys.*, 222(2):654–672, 2007.

[117] G.I. Taylor. The formation of emulsions in definable fields of flow. *Proc. Roy. Soc. London Ser. A*, 146(858):501–523, 1934.

[118] The Acute Respiratory Distress Syndrome Network. Ventilation with lower tidal volumes as compared with traditional tidal volumes for acute lung injury and the acute respiratory distress syndrome. *N Engl J Med*, 342:1301–1308, 2000.

[119] G. Tryggvason, B. Bunner, A. Esmaeeli, D. Juric, N. Al-Rawahi, W Tauber, J Han, S Nas, and Y J Jan. A Front-Tracking Method for the Computations of Multiphase Flow. *J. Comput. Phys.*, 169(2):708–759, 2001.

[120] P. Van Liedekerke, E. Tijskens, H. Ramon, P. Ghysels, G. Samaey, and D. Roose. A particle based model to simulate plant cells dynamics. In *Proc. 4th ERCOFTAC SPHERIC Work.*, Nantes, France, 2009.

[121] A. Vázquez-Quesada, M. Ellero, and P. Español. Smoothed particle hydrodynamic model for viscoelastic fluids with thermal fluctuations. *Phys. Rev. E*, 79(5):056707, May 2009.

[122] L. Verlet. Computer "Experiments" on classical fluids. I. Thermodynamical properties of Lennard-Jones molecules. *Phys. Rev.*, 159(1):98–103, 1967.

[123] Y. Vidal, J. Bonet, and A. Huerta. Stabilized updated Lagrangian corrected SPH for explicit dynamic problems. *Int. J. Numer. Methods Eng.*, 69(13):2687–2710, 2007.

[124] R. Vignjevic and J. Campbell. A penalty approach for contact in smoothed particle hydrodynamics. *Int. J. Impact Eng.*, 23:945–956, 1999.

[125] D. Violeau and R. Issa. Numerical modelling of complex turbulent free-surface flows with the SPH method: an overview. *Int. J. Numer. Methods Fluids*, 53(2):277–304, 2007.

[126] H. Wendland. *Scattered Data Approximation*. Cambridge University Press, Cambridge, UK, 2005.

[127] M. Wörner. Numerical modeling of multiphase flows in microfluidics and micro process engineering: a review of methods and applications. *Microfluid. Nanofluidics*, 12(6):841–886, 2012.

[128] J.J. Xu, Z. Li, J. Lowengrub, and H. Zhao. A level-set method for interfacial flows with surfactant. *J. Comput. Phys.*, 212(2):590–616, 2006.

[129] J.J. Xu and H.K. Zhao. An Eulerian Formulation for Solving Partial Differential Equations Along a Moving Interface. *J. Sci. Comput.*, 19(1):573–594, 2003.

[130] R. Xu, P. Stansby, and D. Laurence. Accuracy and stability in incompressible SPH (ISPH) based on the projection method and a new approach. *J. Comput. Phys.*, 228(18):6703–6725, 2009.

[131] Z.J. Xu and P. Meakin. A phase-field approach to no-slip boundary conditions in dissipative particle dynamics and other particle models for fluid flow in geometrically complex confined systems. *J. Chem. Phys.*, 130(23):234103, 2009.

[132] S. Yon and C. Pozrikidis. A finite-volume/boundary-element method for flow past interfaces in the presence of surfactants, with application to shear flow past a viscous drop. *Comput. Fluids*, 27(8):879–902, 1998.

[133] A. Zainali, N. Tofighi, M.S. A Shadloo, and M. Yildiz. Numerical investigation of Newtonian and non-Newtonian multiphase flows using ISPH method. *Comput. Methods Appl. Mech. Eng.*, 254:99–113, 2013.

[134] J. Zhang, D.M. Eckmann, and P.S. Ayyaswamy. A front tracking method for a deformable intravascular bubble in a tube with soluble surfactant transport. *J. Comput. Phys.*, 214(1):366–396, 2006.

[135] M. Zhang. Simulation of surface tension in 2D and 3D with smoothed particle hydrodynamics method. *J. Comput. Phys.*, 229(19):7238–7259, 2010.